Probing Photoinduced Charge and Energy Transfer on the Nanoscale with Time-Resolved X-ray Spectroscopy Techniques

Dissertation
zur Erlangung des Doktorgrades
an der Fakultät für Mathematik, Informatik und Naturwissenschaften
Fachbereich Physik
Universität Hamburg

angefertigt am
Lawrence Berkeley National Laboratory
Berkeley, California, USA

vorgelegt von
Johannes Mahl

Hamburg
2022

Gutachter der Dissertation:

Prof. Dr. Nils Huse
Dr. Oliver Gessner

Zusammensetzung der Prüfungskommission:

Prof. Dr. Nils Huse
Dr. Oliver Gessner
Prof. Dr. Arwen Pearson
Prof. Dr. Michael A. Rübhausen
Prof. Dr. Gabriel Bester

Vorsitzende der Prüfungskommission:

Prof. Dr. Arwen Pearson

Datum der Disputation:

27.04.2022

Vorsitzender des Fach-Promotionsausschusses Physik:

Prof. Dr. Wolfgang J. Parak

Leiter des Fachbereichs Physik:

Prof. Dr. Günter H. W. Sigl

Dekan der Fakultät für Mathematik, Informatik und Naturwissenschaften:

Prof. Dr. Heinrich Graener

Contents

Abstract

The spatio-temporal characteristics of charge and energy transfer following photoexcitation of model solar energy harvesting systems are studied using time-resolved X-ray spectroscopy techniques. The thesis consists of two parts: First, a model system for heterogeneous light-harvesting architectures, consisting of N3 ((cis-bis(isothiocyanato)bis(2,2′-bipyridyl-4,4′-dicarboxylato)-ruthenium(II))) dye molecules adsorbed onto a nanostructured ZnO substrate, is studied using time-resolved X-ray photoelectron spectroscopy (TRXPS). The element specificity of X-ray spectroscopy techniques enables independent insight into both sides of the heterojunction, i.e., the light-absorbing N3 dye and the ZnO electrode into which photoexcited electrons are injected. The positions of both types of photoinduced charge carriers, holes remaining on the dye and injected electrons within the surface region of the ZnO electrode, are revealed on the nanometer scale by spectral variations in the XPS data. In the second part of the thesis, cupric oxide (CuO), a semiconductor (SC) used in catalysis, supercapacitors and magnetic storage media among others, is investigated with time-resolved X-ray absorption spectroscopy (TRXAS). The technique is sensitive to structural and electronic changes following photoexcitation and this study presents a framework to disentangle the two contributions to TRXAS data on solid state samples. The results are interpreted in terms of temperature effects that modify the atomic lattice structure, and they highlight the need to take these effects into account when investigating photoinduced electronic phenomena.

The groundwork for the N3-ZnO study is an XPS investigation of the bare nanocrystalline ZnO electrode. This wide-bandgap SC is used in biological and chemical sensors and photovoltaic systems in various nanostructured forms. Especially, under conditions different from ultra-high vacuum, single-crystal ZnO surfaces are known to exhibit pronounced downward band bending. This study reveals a similar situation for the technologically pertinent surface of nanostructured ZnO. Band bending in the near-surface region of the sample is detected as a shift and broadening of the photoelectron spectra. Data of the Zn3d photoline is acquired for different degrees of hydroxylation of the ZnO surface, controlled via the sample temperature. Modelling this data set with a global fit algorithm yields a (790 ± 30) meV downward band bending within a surface layer

that is less than 6 nm thick. The existence of such a strong electron confining potential has important implications for charge carrier mobility and lifetimes in photocatalytic applications. The band bending revealed for the ground state of the bare ZnO substrate also applies to the N3 dye-sensitized nanocrystalline ZnO films. For the latter system we demonstrate that the N3 adsorption does not change the surface electronic structure. Within the main study of the first part of this thesis, TRXPS is used to follow the spatial distributions of photoexcited charge carriers on the nanometer scale through the stages of charge injection, separation, and recombination in N3-ZnO. This capability is crucial to identify bottlenecks in heterogeneous light-harvesting systems. Two complementary TRXPS data sets are acquired: The C1s and Ru3d photolines, which are both exclusively associated with the N3 dye, and the Zn3d photoline stemming from the ZnO SC. The N3 chromophore is excited with 532 nm light pulses and a shift of the C1s/Ru3d spectra appears within the instrument response function (IRF) of the experiment (~70 ps), indicating the oxidation of the chromophore. The arrival of the respective photo-injected electron in the ZnO conduction band (CB), however, appears with a ~300 ps delay as a shift and broadening of the Zn3d photoline. This time delay strongly suggests an interfacial charge transfer (ICT) configuration being populated in an intermediate step between photoexcitation and charge injection into the CB. The recombination dynamics between holes remaining on the dye and injected electrons range from ns to μs timescales. An additional transient downward band bending of (100 ± 20) meV is observed at the ZnO surface within a width of less than 6 nm. These results are deduced from the time-resolved broadening and shift of the Zn3d line, modelled within the same depth-resolving analysis framework used in the bare ZnO study. Additionally, the position of the hole is determined to be in the range of 0.3-1.2 nm above the ZnO surface. This matches the expected location of the HOMO hole density of the N3 dye. This information is accessible through the additional shift of the C1s/Ru3d lines that occurs on top of the shift due to altered ZnO band bending. The potential difference between electron donor and acceptor is described within a parallel plate capacitor model. The significant downward band bending in both ground and excited states leads to strong electron confinement in the near-surface region after injection into the CB. Correspondingly, electron transport needs to proceed near the SC surface, opening new recombination pathways that likely contribute to shortcomings of nanostructured ZnO electrodes compared to their TiO_2 counterparts.

The second part of this thesis focuses on a ubiquitous side effect in pump-probe experiments on solid state samples: laser-induced sample heating. In a proof-of-principle study, a framework to deconvolute lattice contributions from electronic effects in TRXAS is applied to laser-induced changes in the oxygen K-edge X-ray absorption of CuO. The transient signals following 532 nm excitation can be fully described within a one-dimensional heat deposition and diffusion model within the precision of the experiment. The model is calibrated using a series of steady-state, temperature-resolved XAS data. The method produces a spatio-temporal lattice temperature profile on an absolute scale with a temporal and spatial sensitivity on the order of tens of picoseconds and tens of nanometers. This profile is the result of an initial laser-induced temperature profile that is propagated in time by iteratively using Fick's Law of diffusion to describe heat dissipation. Both, heat deposition and dissipation, can be estimated in a one-dimensional approach along the surface normal given a significantly larger pump than probe diameter at the sample surface. The resulting thermal conductivity of (1.3 ± 0.4) $\mathrm{Wm^{-1}K^{-1}}$ for the CuO sample is in good agreement with the literature value for CuO powder (1.013 $\mathrm{Wm^{-1}K^{-1}}$). A caveat becomes apparent when modelling TRXAS data following 355 nm excitation, where a comparatively short laser penetration depth causes pronounced temperature gradients that require extrapolation of the temperature-resolved data, which cannot fully describe the observed TRXAS effects.

Zusammenfassung

Die räumlichen und zeitlichen Eigenschaften von photo-induziertem Ladungs- und Energietransfer in Modellsystemen fuer die Umwandlung von Solarenergie werden mittels zeitaufgelöseten Röntgenspektroskopiemethoden untersucht. Die Dissertation besteht aus zwei Teilen: Ein Modellsystem für heterogene Lichtsammelarchitekturen, bestehend aus N3 ((cis-bis(isothiocyanato)bis(2,2′-bipyridyl-4,4′-dicarboxylato)-ruthenium(II))) Farbstoffmolekülen, die auf ein nanostruckturiertes ZnO Substrat adsorbiert sind, wird mittels zeitaufgelöster Röntgenphotoelektronenspektroskopie (TRXPS) untersucht. Die Elementselektivität von Röntgenspektroskopien ermöglicht unabhängige Einblicke in beide Seiten der Heterostrucktur, d.h. des lichtabsorbierenden N3 Farbstoffes und der ZnO Elektrode, in welche die lichtangeregten Elektronen injeziert werden. Die Positionen beider Ladungsträgertypen, Löcher, die auf dem Farbstoff bleiben, und injezierte Elektronen innerhalb der Oberflächenregion der ZnO Elektrode, werden auf der Nanometerskala mittels spektraler Veränderungen der XPS Daten sichtbar gemacht. Im zweiten Teil der Dissertation wird Kupfer(II)-oxid (CuO), ein Halbleiter der unter anderem in der Katalyse, Superkondensatoren und magnetischen Speichermedien Anwendung findet, mittels zeitaufgelöster Röntgenabsorptionsspektroskopie (TRXAS) untersucht. Diese Messmethode ist auf lichtinduzierte struckturelle und elektronische Veränderungen empfindlich und diese Studie presentiert eine Methodik zur Unterscheidung dieser zwei Beiträge zu TRXAS Daten von Festkörperproben. Die Ergebnisse werden im Sinne von Temperatureffekten interpretiert, welche die atomare Gitterstrucktur beeinflussen, und heben die Notwendigkeit hervor diese Effekte bei der Untersuchung von lichtinduzierten elektronischen Phänomenen in Betracht zu ziehen.

Die Grundlage der Studie des N3-ZnO ist eine XPS Untersuchung der blanken, nanokristallinen ZnO Elektrode. Dieser Halbleiter mit großer Bandlücke wird in biologischen und chemischen Sensoren, sowie in der Photovoltaik in verschiedenen nanotstruckturierten Formen verwandt. Besonders unter nicht-ultrahochvakuum Bedingungen sind kristalline ZnO Oberflächen bekannt für deutlich nach unten gebogene elektronische Bänder. Diese Studie zeigt, dass die technologisch relevanten Nanostruckturen des ZnO eine ähnliche Situation aufweisen. Gebogene Bänder nahe der

Probenoberfläche äußern sich durch Verschieben und Verbreitern der Photoelektronenspektren. Daten der Zn3d Photolinie werden für verschiedene Grade von Oberflächenhydroxilierung aufgenommen, welche durch die Probentemperatur gesteuert wird. Eine Modellierung dieses Datensatzes mittels eines globalen Fitalgorithmus ergibt um (790 ± 30) meV nach unten gebogene Bänder in einer weniger als 6 nm breiten Oberflächenregion. Eine derart ausgeprägte räumliche Einschränkung der Elektronen hat wichtige Auswirkungen auf die Mobilität und Lebenszeit der Ladungsträger in photokatalytischen Anwendungen. Die Bandverbiegung des blanken ZnO Substrates im Grundzustand trifft auch auf das mit N3 sensitisierte nanokristalline ZnO zu. Für letzteres System wird gezeigt, dass die Adsorption von N3 die elektronische Strucktur der Oberfläche nicht verändert. Innerhalb des Haupteils dieses ersten Teils der Dissertation wird TRXPS genutzt, um der räumlichen Verteilung von lichtangeregten Ladungsträgern in N3-ZnO auf der Nanoskala durch die Phasen von Ladungsinjektion, -separation und -rekombination zu folgen. Dies stellt eine entscheidende Fähigkeit dar, um Engpässe in heterogenen Lichtsammelsystemen zu identifizieren. Hierfür werden zwei sich ergänzende TRXPS Datensätze aufgenommen: Die C1s und Ru3d Photolinien, die ausschließlich dem N3 Farbstoff zuzuordnen sind, und die Zn3d Photolinie, die vom ZnO Halbleiter stammt. Der N3 Chromophor wird mit 532 nm Lichtpulsen angeregt, worauf eine Verschiebung der C1s/Ru3d Spektren innerhalb der Instrumentenantwortfunktion des Experiments (~70 ps) eintritt, die auf die Oxidation des Chromophor hinweist. Die Ankunft der entsprechenden lichtinjezierten Elektronen im Leitungsband des ZnO tritt allerdings mit einer Verzögerung von ~300 ps als eine Verschiebung und Verbreiterung der Zn3d Photolinie auf. Diese Zeitverzögerung deutet stark auf einen Ladungstransferzustand an der Grenzfläche als Ursache für die Verzögerung zwischen Lichtanregung und Ladungsträgerinjektion in das Leitungsband hin. Die Rekombinationsdynamiken von Löchern, die auf dem Farbstoff verbleiben, und injezierten Elektronen finden auf Zeitskalen zwischen Nano- und Mikrosekunden statt. Die Oberfläche des ZnO zeigt ein zusätzliches, transientes Verbiegen der Bänder von (100 ± 20) meV innerhalb einer weniger als 6 nm dicken Schicht. Diese Ergebnisse werden von der zeitaufgelösten Verbreiterung und Verschiebung der Zn3d Photolinie abgeleitet, welche mithilfe der selben tiefenauflösenden Methode modelliert wird, die in der Studie des blanken ZnO verwandt wurde. Zusätzlich wird die Position des Lochs in Bezug auf die Oberfläche des ZnO als 0.3-1.2 nm bestimmt. Dies stimmt mit der erwarteten Lage der HOMO Lochdichte des N3 Farbstoffes überein. Diese Information is durch eine

Verschiebung der C1s/Ru3d Linien zugänglich, welche zusätzlich zur Verschiebung durch Bandverbiegung des ZnO auftritt. Diese Potentialdifferenz zwischen Elektronendonor und -akzeptor wird mittels eines parallelen Plattenkondensators modelliert. Die deutliche, nach unten gerichtete Verbiegung der Bänder im Grund- sowie im angeregten Zustand führt zu einer stark ausgeprägten räumlichen Einschränkung der Elektronen innerhalb der oberflächennahen Region nach Injektion in das Leitungsband. Dementsprechend muss der Elektronentransport nahe der Halbleiteroberfläche stattfinden, was neue Rekombinationsmöglichkeiten eröffnet und wahrscheinlich zur verminderten Effizienz von Elektroden aus nanostrucktuierten ZnO im Vergleich zu TiO_2 beiträgt.

Der zweite Teil dieser Dissertation behandelt eine allgegenwärtige Begleiterscheinung in Pump-probe Experimenten an Festkörperproben: laserinduziertes Erwärmen der Probe. In einer Grundsatzstudie wird eine Methode zur Unterscheidung von Gitterbeiträgen und elektronischen Effekten in TRXAS auf laserinduzierte Veränderungen der Röntgenabsorption der Sauerstoff K-Kante von CuO angewandt. Die Anregung mit 532 nm führt zu transienten Signalen, die innerhalb der experimentellen Streuung der Daten vollständig durch ein eindimensionales Modell der Wärmedeponierung und -diffusion dargestellt werden können. Das Modell basiert auf einer Reihe von temperaturaufgelösten XAS Daten. Diese Methode produziert ein zeitlich und räumlich aufgelöstes Gittertemperaturprofil auf einer absoluten Skala, welches empfindlich auf Änderungen auf einer Größenordnung von zehn Pikosekunden und zehn Nanometern ist. Dieses Profil resultiert aus einem anfänglichen laserinduziertem Temperaturprofil, das durch iterative Benutzung des Fick'schen Gesetzes in der Zeit propagiert wird, um die Wärmedissipation zu beschreiben. Sowohl Wärmedeponierung als auch -dissipation können näherungsweise in einem eindimensionalen Ansatz entlang der Oberflächennormale beschrieben werden, da der Durchmesser des Pump- deutlich größer als der des Probe-pulses auf der Probenoberfläche ist. Die daraus resultierende Wärmeleitfähigkeit der CuO Probe von (1.3 ± 0.4) $Wm^{-1}K^{-1}$ stimmt gut mit dem Literaturwert von puderförmigen CuO (1.013 $Wm^{-1}K^{-1}$) überein. Eine Einschränkung wird durch die Modellierung von TRXAS Daten nach Anregung mit 355 nm deutlich. Die vergleichsweise kurze Lasereindringtiefe führt hier zu starken Temperaturgradienten. Dies erfordert eine Extrapolation der temperaturaufgelösten Daten, mithilfe welcher die beobachteten TRXAS Effekte nicht vollständig beschreiben werden können.

List of Publications

I

Strong Potential Gradients and Electron Confinement in ZnO Nanoparticle Films: Implications for Charge-Carrier Transport and Photocatalysis
Johannes Mahl, Oliver Gessner, Johannes V. Barth, Peter Feulner, and Stefan Neppl
ACS Applied Nano Materials **4**, 12213–12221 (published in November 2021)
DOI: https://doi.org/10.1021/acsanm.1c02730

II

Nanoscale Confinement of Photo-Injected Electrons at Hybrid Interfaces
Stefan Neppl*, Johannes Mahl*, Friedrich Roth, Giuseppe Mercurio, Guosong Zeng, Francesca M. Toma, Nils Huse, Peter Feulner, and Oliver Gessner (* authors contributed equally)
Journal of Physical Chemistry Letters **12**, 11951-11959 (published in December 2021)
DOI: https://doi.org/10.1021/acs.jpclett.1c02648

III

Decomposing Electronic and Lattice Contributions in Optical Pump – X-Ray Probe Transient Inner-Shell Absorption Spectroscopy of CuO
Johannes Mahl, Stefan Neppl, Friedrich Roth, Mario Borgwardt, Catherine Saladrigas, Benjamin Toulson, Jason Cooper, Tahiyat Rahman, Hendrik Bluhm, Jinghua Guo, Wanli Yang, Nils Huse, Wolfgang Eberhardt, and Oliver Gessner
Faraday Discussions **216**, 414-433 (published in January 2019)
DOI: https://doi.org/10.1039/C8FD00236C

Eidesstattliche Versicherung / Declaration on Oath

Hiermit versichere ich an Eides statt, die vorliegende Dissertationsschrift selbst verfasst und keine anderen als die angegebenen Hilfsmittel und Quellen benutzt zu haben.

Hamburg, den 03.03.2022

Johannes Mahl

1 Introduction

Solar light harvesting technology plays a central role in the transition to a sustainable energy future. The potential of solar power is best illustrated by putting its scale into perspective. Approximately 120,000 TW of solar power are incident on the earth's surface at any given moment.[1] The corresponding solar energy accumulated within less than one and a half hours is equal to the global primary energy supply per year of 606 EJ or $\sim 1.68 \cdot 10^5$TWh (2019).[2] This vast amount of energy is increasingly tapped with the annually installed photovoltaic power production capacity increasing to 138.2 GW in 2020, a plus of 18% compared to the year before.[3] In terms of the installation cost per kWh in a centralized power plant scenario, renewable energy sources have become comparable to fossil fuels for electricity generation.[4] Regarding the price per kWh produced, solar power is already competitive with fossil fuels.[5] The electricity sector accounts for 20% of the primary energy consumption which is 418 EJ or ~1.16 TWh (2019).[6] Oil (40.4%), natural gas (16.4%) and coal (9.5%) still make up ~67% of the primary energy consumption.[6] While oil is used mainly for transport, natural gas is mostly used within the industrial and residential sectors, and coal mostly in industrial processes. For some transport, such as air travel, and industrial applications requiring energy densities similar to fossil fuels, a promising route is producing gasoline-range (C_5-C_{11}) synthetic fuels, via hydrogenation of CO_2[7,8] or a modified Fischer-Tropsch mechanism[9] for example. These fuels are carbon-neutral when utilizing renewable energy, green hydrogen and CO_2 from direct air capture.[10] And they can be used to mitigate greenhouse gas emissions from industrial processes or power generation involving fossil fuels where higher CO_2 concentrations than in air are present. All these chemical transformations usually involve charge-transfer processes in materials that act as electrodes and/or catalysts. On a microscopic scale effective charge migration with minimal losses to competing channels depends on local electronic potentials. In light-triggered applications specifically, the timely separation of photoinduced charge carriers is key to minimize losses right after light absorption.[11,12] A full spatio-temporal understanding of photoinduced charge carrier dynamics with the aim of increased device efficiency is an impactful research topic concerning electricity, hydrogen, and synthetic fuel generation because increased device efficiency would reduce land usage and cut costs per installed kW. Improvements will make photovoltaic and photocatalytic technologies more widely available and are necessary to enable green hydrogen and carbon-neutral synthetic fuels at an industrial scale.

With single-junction silicon-based cells approaching the Shockley-Queisser Efficiency Limit[13,14] of ~34%, hetero- and multi-junction cell designs have received increasing attention and currently achieve a maximum efficiency of 47%.[15] The general idea of these systems is to combine materials to improve the overall absorption characteristics either by covering an increased portion of the solar spectrum or enhancing the photoconversion efficiency. This is routinely realized by combining a wide bandgap SC, such as TiO_2 or ZnO, with smaller bandgap materials or sensitizers, such as nanoparticles (NPs), quantum dots or molecules.[16–19] This approach maximizes the converted energy per unit area with the goal of translating this surplus into a higher overall device efficiency. Therefore, it is imperative to develop a sound understanding of charge separation, migration, and recombination, especially within the interfacial regions of the different system components. As SCs are the most widely used material class and central to this study, the next chapter starts by introducing basic SC terminology (section 2.1) such as the nomenclature of energy levels and potential differences in SCs. In general, recombination of the photo-generated charges is a central loss mechanism in hetero- and multi-junction systems. Counteracting this tendency requires a fast spatial separation of electron and hole as well as maintaining sufficient separation between them throughout the migration to their respective electrodes, both of which can strongly depend on interfacial electronic fields and potential differences. Band bending (section 2.2) between the surface and the bulk electronic levels within a SC represents a local electronic potential variation that is key for the charge carrier dynamics upon photoexcitation: Upward band bending (towards the surface or interface) drives mobile electrons into the bulk while downward band bending confines them in the near-surface region and vice versa for holes. Hence, the SC band bending constitutes one factor determining whether photo-generated charge pairs are efficiently spatially separated in heterojunctions. Section 2.3 introduces a heterojunction model system, consisting of the N3 dye molecule[20] and a nanoporous ZnO film – the sample studied in the first part of this work. The N3-ZnO interfacial energy alignment is discussed in the broader context of the working principle of (dye-sensitized) solar cells with a focus on the generation of photo-currents. In photocatalytic applications,[21,22] the spatial separation of photo-generated charges is often desired and enables two simultaneous half-cycle reactions, i.e. oxidation and reduction. Depending on the specific catalytic process, this separation can help mitigate recombination of the product gases and corrosion of the electrodes as well as charge recombination prior to chemical reactions. Photoinduced charge carriers themselves influence the band bending, which is referred to as the surface photovoltage (SPV) effect (section 2.4). Improving photovoltaic and photocatalytic applications requires the ability to follow charge carrier positions with sufficient spatial and temporal resolution in order to make design changes to suppress undesired processes. The ideal experimental method would enable this capability under *in operando* conditions of a device and for different excitation parameters.

The photoexcitation itself would be most accurately replicated by a solar simulator. However, experiments based on constant illumination cannot provide sufficient insights into time-dependent processes that are needed for a comprehensive understanding of the underlying physical mechanisms. In order to study elementary electronic processes in matter, pump-probe methods are widely-used time-resolved spectroscopic techniques.[23] A pump pulse excites the sample into a non-equilibrium state and is followed by a probe pulse to retrieve information on the state of the sample that is averaged only over the probe pulse duration with additional temporal broadening by the pump pulse duration. As the delay between pump and probe pulse is variable and precisely adjustable, information on the ground state (at negative delays), around the excitation (at near-zero delays), and the ensuing dynamics and kinetics of pump-induced changes (at positive delays) is accessible. Generally, the overall data acquisition time is proportional to the number of recorded pump-probe delays and the repetition rate at which the pump-probe experiment can be operated. The repetition rate typically lies in the kHz to MHz regime and should be low enough to ensure that any pump-induced dynamics have decayed before the next pump pulse excites the sample, in order to avoid accumulation or saturation effects.

The choice of probe spectroscopy determines the observable effects of the photoexcitation. The photon energy of the probe pulse selects the accessible probed transitions. Many spectroscopic techniques use ultraviolet (UV), visible or infrared light to probe transitions from the valence to the conduction band in solids and transitions between valence electronic, vibrational and/or rotational energy levels. X-ray spectroscopy, on the other hand, utilizes transitions of core-electrons into the unoccupied density of bound states or the ionization continuum. Since the localized core-electrons have distinct, element-specific binding energies, individual elements can be addressed. In addition to this element specificity, the binding energies of core-electrons depend to a varying degree on the chemical environment of their corresponding element. This is referred to as chemical sensitivity. These two characteristics of any X-ray spectroscopy allow accessing information on the electronic structure of valence bands from the perspective of each constituting element. Pairing pump-probe spectroscopy with pulsed X-ray light sources creates experimental tools that can follow time-dependent and local photoinduced changes of valence charge distributions, electronic potentials, oxidation states and local structure. Such a method is especially useful for investigating hetero- and multi-junction systems because the individual system components will contain different elements and/or different (chemical) environments for identical elements. Targeting suitable elements results in distinct probe signals uniquely associated with each component.

The unique capacity of time-resolved X-ray spectroscopy is realized in two experimental laser pump – synchrotron probe setups with picosecond time resolution (chapter 3). The two X-ray spectroscopy techniques used as probes in this thesis are X-ray photoelectron spectroscopy (XPS, historically called electron spectroscopy for chemical analysis, ESCA)[24,25] and X-ray absorption spectroscopy (XAS).[26] Briefly, XPS analyzes photoelectrons ejected from the sample by absorption of X-ray photons of an energy larger than the electron binding energy and sample material work function. This barrier is modified by (local) surface electronic effects[27,28] such as surface dipoles. Because of these interactions, local electronic potentials and their transient changes[27,28] are mapped onto the electron kinetic energy spectrum. Before reaching the surface, the photoelectron may inelastically scatter, the likelihood of which is expressed by its inelastic mean free path (IMFP). In the soft X-ray regime, typical IMFP values vary between a few Ångstrom (Å) and a few nanometers depending on the material and the electron kinetic energy. The latter, can be adjusted via the X-ray photon energy and therefore, the surface sensitivity is tunable, making XPS and TRXPS[29] ideal tools to investigate electronic potentials at surfaces and interfaces in equilibrium and during charge transfer processes. Indeed, TRXPS is an established technique to study band bending at interfaces and surfaces via SPV effects.[30–40] Section 3.1 discusses the TRXPS experimental setup involving the electronic synchronization of the pump laser and data acquisition, detection scheme and data structure.

While XPS accesses valence electron dynamics exclusively through core level shifts, XAS is inherently sensitive to transitions between initial and final (core-excited) states. Generally, sample absorption is characterized by the logarithm of the ratio between the radiation incident on and transmitted through the sample. XAS in transmission mode is best suited for samples with a transmission of about 1/e. For thicker samples, with insufficient transmission, core-hole relaxation products such as fluorescence and Auger electrons provide proxy signals for the X-ray absorption strength. For very dilute element concentrations the fluorescence yield is advantageous as well. Both techniques, XAS and XPS, provide surface sensitivity, given primarily by the X-ray penetration depth in case of XAS and the IMFP in XPS, the latter technique providing tunable surface sensitivity in the nanometer range. Section 3.2 briefly describes the total fluorescence yield (TFY) detection scheme of the TRXAS setup and available data acquisition modes utilizing different parts of the X-ray pulse train of the synchrotron. It highlights a particular improvement to the data normalization that significantly increases the signal-to-noise ratio of the technique. This improvement is achieved by adding a second data acquisition channel that allows to simultaneously record ground- and excited-state TRXAS signals, measured with X-rays that are produced by the same electron bunch in the synchrotron ring. This capability effectively decouples photoinduced effects from artefacts that can be induced by charge fluctuations between different electron bunches and corresponding intensity fluctuations in the associated X-ray pulses.

Chapter 5 contains the published results of this cumulative thesis. Section 5.2 presents new insight, gained by TRXPS, into the spatio-temporal dynamics of photoinduced charge transfer at the interface between N3 dye molecules and a nanocrystalline ZnO film. The model hybrid system N3-ZnO is excited with a 532 nm pump pulse that is absorbed by the dye chromophore. The photoinduced HOMO-to-LUMO transition (from the highest occupied to the lowest unoccupied molecular orbital) is realized by a charge transfer from the metal center to the molecule ligand. The following electron injection into the ZnO substrate is delayed compared to other SC electrodes.[41–48] The nature of this intermediate state has been debated to be either a triplet state within the dye, populated by intersystem crossing (ISC),[49–52] or an ICT configuration.[41–44,47] Furube *et al.*[41] found ultrafast IR absorption signatures of the oxidized molecule, as well as a delayed appearance of free ZnO CB electrons, pointing toward the ICT configuration as the likely scenario. Němec *et al.*[42] found a similar result accessing free SC CB electrons (multiplied with their mobilities) via ultrafast THz conductivity and using optical spectroscopy to probe the electron donor side. In the competing ISC model, strong coupling between intramolecular modes retains the electron on the dye and a thermalized triplet metal-to-ligand charge-transfer (MLCT) state precedes the electron injection into the SC CB.[52] TRXPS gives access to both sides of the charge transfer within a single experiment. The results presented here on the C1s/Ru3d and Zn3d photoelectron regions are directly attributable to the electron donating or accepting sides, respectively. Photolines associated with the oxidized molecule exhibit a shift to higher binding energies by ~80 meV that appears within the instrument response function of ~70 ps. The existence of an ICT configuration is clearly observed in the delayed appearance of free charge carriers in the ZnO CB on a timescale of ~300 ps. These photoinduced charge carriers lead to a transient increase in downward band bending by (100 ± 20) meV to a total of ~890 meV, enhancing their confinement in a <6 nm deep surface-near region. The results are confirmed by two independent Zn3d time-series data sets acquired at photon energies of ~320 and ~614 eV. The spatial distribution of photo-injected electrons is directly connected to the electronic potentials via the Poisson equation. This allows converting spectral changes of the TRXPS Zn3d photoline into spatial distributions of the photo-injected ZnO CB electrons. The corresponding data analysis method is detailed in section 4.4. Similarly, spatial information on the hole remaining on the chromophore can be retrieved from the ~80 meV IRF-limited C1s/Ru3d shift in excess of the band bending change. This shift represents the potential difference between molecule and ZnO surface and, within in a parallel plate capacitor model, translates into a 0.3-1.2 nm distance between electron holes and SC surface (section 4.1). This combination of insights showcases the ability of TRXPS to follow the timescales and energetics of photoinduced charge transfer with spatial sensitivity within a single experimental scheme. Besides adsorbate-SC systems,[45] TRXPS has been successfully used to study purely molecular interfaces,[53,54] as well as metal NP-SC heterojunctions.[55] The work, on charge transfer in the N3-ZnO system, is supported by a temperature-dependent steady-state XPS investigation of the ground-state surface electronic structure of the bare (unsensitized) nanocrystalline ZnO substrate (section 5.1). In this study, the surface hydroxylation of the ZnO sample is controlled via the sample temperature to vary and thereby reveal the band bending in the near-surface region. The sintered ~15 nm diameter NPs forming the film show downward band bending similar to the single-crystal surface.[56,57] The entire data set is best described by an underlying band bending of cubic polynomial shape with a maximum value of (790 ± 30) meV at the surface and an upper boundary for its spatial extent into the material of 6 nm, where the bands reach their bulk value. In this XPS as well as in the TRXPS study, the spatial extent of the band bending is on the nanometer length scale, with its 1/e-equivalent value roughly matching the IMFP of the Zn3d photoelectrons. Therefore, the measured Zn3d spectrum consists of contributions originating from different depths within the ZnO whose kinetic energies vary according to the depth-dependent band bending. The corresponding mathematical framework that connects the overall spectrum and individual components is described in section 4.4 and within the publication re-printed in section 5.1.[58] Generally, steeper band bending within the surface region of the SC leads to increased broadening of photoelectron spectra and smaller apparent shifts compared to the maximum potential energy changes at the surface. Such effects have been exploited to gain spatial sensitivity along the surface normal at solid/liquid interfaces.[59–61] The approach of varying the band bending by an experimental parameter to study its shape and amplitude is especially useful for nanostructured materials. Angle-resolved photoelectron spectroscopy (ARPES) can give similar insights into single-crystal samples,[56,57] but not irregular nanostructured samples as they lack the necessary long-range structural order.

In most solid-state pump-probe experiments, the deposition of energy in the sample by the pump pulse via electronic excitation is followed by a conversion to heat via electron-phonon and phonon-phonon coupling. The second part of this thesis focuses on laser-induced heating (section 4.2) and the subsequent heat dissipation (section 4.3) in solid-state samples. A framework is developed to model the overall magnitude of the heating effect and its decay dynamics in pump-probe experiments on solid-state samples. The goal is to gain insight into the relevant experimental parameters and to enable the distinction of these temperature-related signatures from laser-induced electronic effects in future experiments. The technique used in this case is TRXAS, which is highly sensitive to structural changes of the sample as a consequence of temperature changes, and at the same time, to laser-induced electronic effects. The X-ray absorption of a sample is recorded as a function of the incoming X-ray photon energy. The response contains resonantly excited electronic transitions into bound or unbound states as well as X-ray absorption into the ionization continuum for X-ray energies larger than the binding energy of the targeted electronic orbitals. The local electronic and chemical structure around the targeted element influences the absorption around the onset of continuum absorption, i.e. the near-edge X-ray absorption fine structure (NEXAFS). Complementary, the geometrical lattice structure dominates the extended X-ray absorption fine structure (EXAFS) region starting several tens of eV above the onset of the continuum. Spectral interferences in the EXAFS region can be isolated and analyzed via Fourier transformation to extract nearest neighbor distances. These modulations stem from the outgoing electron wave packet which is partially backscattered by the neighboring atoms and interferes with itself. While this makes EXAFS an interesting technique to study laser-induced lattice effects in detail, the NEXAFS region reveals the interplay of laser-induced heat energy transfer and electronic effects in solids.

Existing TRXAS[26] literature has so far made qualitative comparisons of XAS data acquired at a variety of temperatures and time delays.[62–64] Lin *et al*. studied non-radiative recombination in PbI_2 via TRXAS and confirmed temperature effects as the underlying reason through a complementary ultrafast electron diffraction study.[63] Hayes *et al.* acquired TRXAS as well as ultrafast near-IR absorption data on hematite (α-FeO_3). In both experiments any effects at pump-probe delays larger than 100 ps can be attributed to lattice effects.[62] Finally, Schultze *et al*. followed lattice dynamics in silicon via bandgap modulations arising on the femtosecond timescale.[64] While these studies identify the natural timescales of their corresponding effects in great detail[64] and verify the lattice origins of the observed effects with complementary experimental techniques,[62,63] the study on CuO presented in this thesis (section 5.3) provides quantitative modelling of heat deposition and dissipation for the entire cycle of laser-induced heating and subsequent cooling. A series of independently acquired steady-state temperature-resolved XAS data is used to calibrate the effects within the TRXAS data. This study exploits known X-ray penetration and escape depths, as well as laser penetration depths to infer a depth-resolved (see sections 4.4 and 5.3) temperature distribution with a resolution of tens of nanometers throughout the TRXAS time series. As the laser pump pulse spot size is significantly larger than the X-ray probe spot size, the radial temperature distribution in the probed sample volume is expected to be homogeneous. Therefore, a one-dimensional depth-resolved model is adequate to describe the heat dissipation (section 4.3) following laser excitation. In the case of excitation with 532 nm light, dominant TRXAS effects are explained by lattice heating within the signal-to-noise of the measurement. The results of this fit model are a thermal conductivity of (1.3 ± 0.4) $Wm^{-1}K^{-1}$, matching the literature value of CuO powder (1.013 $Wm^{-1}K^{-1}$),[65] and an initial surface temperature of (120 ± 11) °C, which is reasonably close to the estimate of 157 °C based on the laser parameters as described in section 4.2. The limitations of the chosen model become apparent in a second data set where laser excitation with a wavelength of 355 nm leads to a relatively small laser penetration depth and consequently to high temperature gradients close to the surface. Here, the expected initial surface temperature is much larger than the highest temperature used in the steady-state temperature-resolved XAS calibration measurements and TRXAS data is not fully explained by extrapolated temperature-resolved XAS data.

The thesis concludes (chapter 6) by summarizing the presented work and providing an outlook on future experiments building on the frameworks presented. The emphasis is on moving towards *in operando* environments by combining TRXPS and ambient-pressure XPS to study fully functional photovoltaic and photocatalytic cells under working conditions.

2 Theoretical Background

This chapter provides the necessary background for understanding the results presented in chapter 5, specifically the steady-state potential study of the hydroxylated ZnO surface region and laser-induced charge redistribution study on the N3-ZnO system. Firstly, basic SC terminology is laid out in section 2.1. Building on these basics, section 2.2 describes band bending in SCs, affecting the energy alignment at the SC surface or interface with other materials, such as NPs, and quantum dots, and for molecular adsorbates such as the N3 dye on the nanocrystalline ZnO surface. Section 2.3 describes the N3-ZnO functional heterogeneous interface as the central part of a model dye-sensitized solar cell (DSSC) design. The general mechanism of how DSSCs function is described with a focus on the timescales of photoinduced generation and separation of charge carriers at the N3-ZnO interface specifically. Lastly, laser-induced changes of band bending, i.e. surface photovoltage (SPV) effects, are discussed in section 2.4. In the N3-ZnO system, SPV occurs as a consequence of laser-induced charge carrier injection from the N3 dye into the ZnO CB. Both, equilibrium band bending and SPV effects, are crucial for charge carrier separation. Moreover, the maximum retrievable energy difference per absorbed photon depends on the (interfacial) energy level alignment. Spatially, charges can either be pinned at the interface or pushed into the bulk. Sufficient spatial separation is a necessary to avoid losses via charge recombination.

2.1 Basics of Semiconductor Terminology

The electronic properties of a SC depend significantly on the number of impurities, such as dopant atoms, or other defects per volume. Typically, these densities range between 10^{15} and $10^{18}/\text{cm}^3$ corresponding to roughly 10^{-8} to 10^{-5} of atoms. This characteristic is in contrast to (semi-)metals and insulators whose electrical properties are not significantly influenced by impurity densities of this magnitude. There is a qualitative difference to metals, as their conductivity as a function of temperature decreases, while it increases for SCs around room temperature. The difference to insulators is only quantitative: Diamond without doping behaves as an insulator (with a bandgap of E_{gap} = 5.5 eV), while sufficient doping makes it semiconducting.

In the absence of any thermal energy, the energy levels of an intrinsic SC (no impurities) are depicted in Figure 1a. Available electronic states are divided between the completely filled valence band (VB) and completely empty CB. The VB maximum E_V and the CB minimum E_C are separated by the bandgap E_{gap} in which there are no allowed electronic states. Hence, E_{gap} represents the minimum amount of energy required to lift an electron from the valence into the conduction band. CB electrons contribute to the electrical conductivity of the SC. There are two conceptually different definitions of the vacuum level E_{vac}. The local E_{vac} corresponds to the energy of an electron at rest, i.e. with zero kinetic energy with respect to the surface, located just outside the surface of a solid. This relatively loose definition alludes to a distance large enough for the electron to be subjected to the full impact of a surface dipole, usually a few nanometers,[28] but small compared with the distance from any other surface with a potentially different local vacuum level. This is in contrast to the vacuum level at infinity $E_{vac}(\infty)$ referring to the energy of an electron at rest far away from any solid surface.[28] This distinction is especially relevant for photoelectron spectroscopy where surface dipole effects are distinguishable from other observables modifying E_{vac}. $E_{vac}(\infty)$, on the other hand, is experimentally not readily accessible and has mostly theoretical implications. The energy difference between E_{vac} and the lowest unoccupied state is called electron affinity $EA = E_{vac} - E_C$. The energy difference between E_{vac} and the highest occupied state is called ionization energy $IE = E_{vac} - E_V$.

Figure 1b (c) depicts the situation for a SC doped with impurity atoms. These atoms function as electron donors (acceptors), if they carry more (fewer) valence electrons than the lattice atoms they

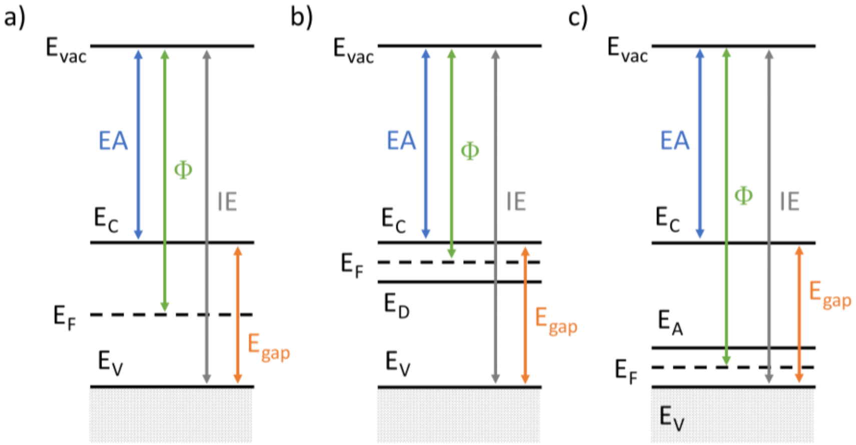

Figure 1: Energy levels in a) intrinsic, b) n-type and c) p-type doped SCs. The CB minimum E_C and VB maximum E_V are separated by the bandgap of size E_{gap}. E_F is the Fermi level and E_D and E_A are the donor and acceptor levels, respectively. See text for explanations.

replace. Doping an intrinsic SC with electron donors (acceptors) makes it n-type (p-type) with donor states E_D (acceptor states E_A), in the top (bottom) half of the bandgap. Generally, in an n-type SC electrons are the most prevalent type of charge, therefore called majority charge carriers, and holes are minority charge carriers, while their roles are flipped in a p-type SC. The Fermi level E_F, or electrochemical potential, can conceptually be described as the energy level that has a 50% chance of being occupied in thermodynamic equilibrium. It is the thermodynamic work required to add one electron to a solid-state system. While at E_C and E_V there are available electronic states, generally, for E_F this is not the case in a non-degenerate SC. E_F depends on the density of states, doping concentration, carrier concentration and temperature of the material. It is a statistical value that generally lies between E_V and E_C, and more specifically between E_D and E_C in an n-type (Figure 1b) or between E_V and E_A in a p-type SC (Figure 1c). The work function Φ is the difference between E_F and E_{vac}. All quantities defined with respect to E_{vac}, i.e. Φ, EA, IE, are positive valued and are meaningful only at the surface of the material.

The combination of different SC layers allows the creation of a variety of different electronic functional interfaces, consisting of either a combination of differently doped versions of the same SC material (homojunctions) or different SCs (heterojunction). The properties of such junctions mainly depend on the energy band alignment at the interface. Generally, three types of heterojunctions are distinguished as displayed in Figure 2. In a straddling gap (type I, Figure 2a) the wider gap ($E_{gap,1}$) of one SC completely encompasses the smaller gap ($E_{gap,2}$) of the other SC, such that $E_{C,1} > E_{C,2}$ and $E_{V,1} < E_{V,2}$. If there is partial overlap of $E_{gap,1}$ and $E_{gap,2}$ a staggered gap (type

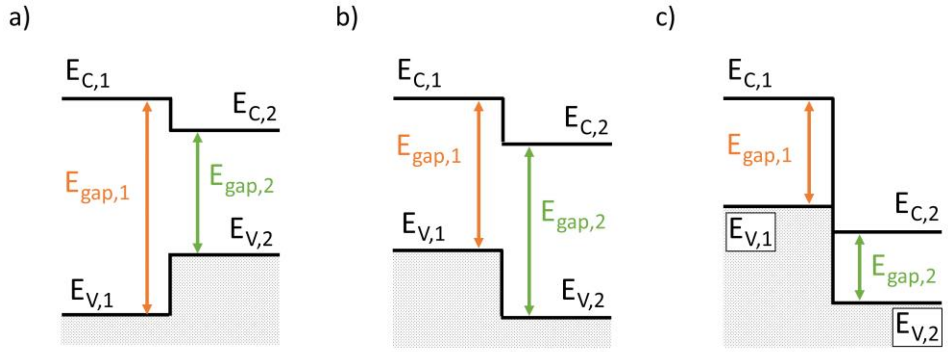

Figure 2: Energy level alignment at different heterojunction SC interfaces. a) A straddling gap (type I) interface involves material 2 with a smaller bandgap ($E_{gap,2}$) that lies entirely within the wider bandgap ($E_{gap,1}$) of material 1. b) A staggered gap (type II) appears when both E_C and E_V of one material lie energetically below E_C and E_V of the other material with an overlapping bandgap. c) A broken gap (type III) is formed when there is no overlap in bandgap as the E_C of one material is energetically below the other material's E_V.

II, Figure 2b) is formed. Here, $E_{C,1}$ and $E_{V,1}$ lie energetically above $E_{C,2}$ and $E_{V,2}$, respectively. In a broken gap (type III, Figure 2c) scenario, there is no energetic overlap between the bandgap of material 1 and 2 such that $E_{C,2}$ lies not only below $E_{C,1}$but also $E_{V,1}$. The energy bands away from the junction are assumed as flat in Figure 2. However, in reality their functional shape is determined by Poisson's equation, as described in detail in the following section 2.2. These junctions, as well as SC-metal, or SC-molecule junctions, are building blocks for more complex electronic structures, such as transistors, light emitting diodes, photovoltaic cells, etc. They enable the trapping or movement of charge carriers often controllable via an external voltage bias.

2.2 Band Bending and Interfacial Electric Fields at Semiconductor Interfaces

All energy levels, excluding E_F, of the SC bulk and surface are not necessarily aligned in thermal equilibrium. Band bending refers to a continuous shift of energy levels approaching the surface of a SC. This is a consequence of spatially varying charge densities in the surface region compared to the bulk material. The direction and magnitude, together with the spatial extent of the band bending has critical impact on the functionality of photocatalytic devices and heterogeneous interfaces used in light-harvesting devices, as schematically shown in Figure 3. Consider the difference between a super-bandgap excitation in a SC with downward and upward band bending towards the interface. In the first case (Figure 3a), the electron is confined within the surface region and may move laterally with respect to the surface normal. In the second case (Figure 3b), the injected electron will be pushed away from the interface and migrate into the SC bulk. These two scenarios lead to a focus

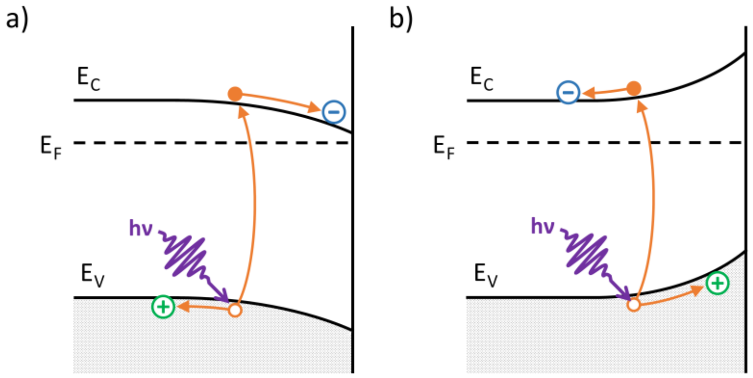

Figure 3: Effect of band bending on distribution of photo-generated charges. Absorption of a photon (violet) with an energy greater than the SC bandgap creates a super-bandgap excitation with an electron (blue) in the CB and a hole (green) in the VB. a) Downward band bending leads to the hole being pushed into the SC bulk and the electron in the CB towards the surface. b) Upward band bending reverses the situation such that the electron migrates into the bulk and the hole is confined at the surface.

on defect states in either the bulk or the surface region of the SC in terms of device optimization. This is key information, as the electronic structure of the bulk is mainly determined by defects and dopant atoms incorporated during the growth and production processes, whereas the surface electronic structure, additionally, can be modified after production by sputtering, annealing, ozone cleaning, adsorption of individual atoms or molecules, chemical treatment, or coating with macroscopic layers of material.

In photocatalytic devices, light with a photon energy larger than the SC bandgap will excite a valence electron into the CB, leaving behind a hole, i.e. positive charge, in the VB. After such super-bandgap excitation, the direction of the band bending will determine which charge carrier type will migrate to the surface as described in Figure 3. While holes facilitate the oxidative part, electrons are needed for the reductive part of the photocatalytic reaction. The magnitude of band bending, thus, directly influences the efficiency of the respective subreactions.[66–68]

In general, band bending can appear at metal-SC interfaces, be caused by external electric fields, or by the existence of surface states and the presence of adsorbates.[69] The following descriptions of each of them will be limited to the case of an n-type SC as is the case for ZnO. Note that adsorbates on SC surfaces are discussed separately and in more detail in section 2.3 as this case is including the N3-ZnO interface studied in the TRXPS experiments.

Metal-semiconductor interface

Schottky, Mott and Davydov independently developed the band bending concept studying metal-SC interfaces, specifically as a framework to describe their rectifying behavior.[70–74] If the work function of the metal Φ_M differs from the work function of the SC Φ_{SC}, charge will redistribute between the two after bringing them into electrical contact until equilibrium is reached, i.e. their Fermi levels are aligned. Generally, on the SC side such charged surface regions are called space charge layers (SCL) and typically extend from the nanometer range up to a few micrometers into the bulk. This redistribution of charges results in an electrostatic dipole potential in the SCL called built-in potential. If $\Phi_M > \Phi_{SC}$ (Figure 4a), electrons from the SC will flow into the metal, leading to a charge surplus on the metal side and charge depletion in the SCL (Figure 4c).[69] This so-called

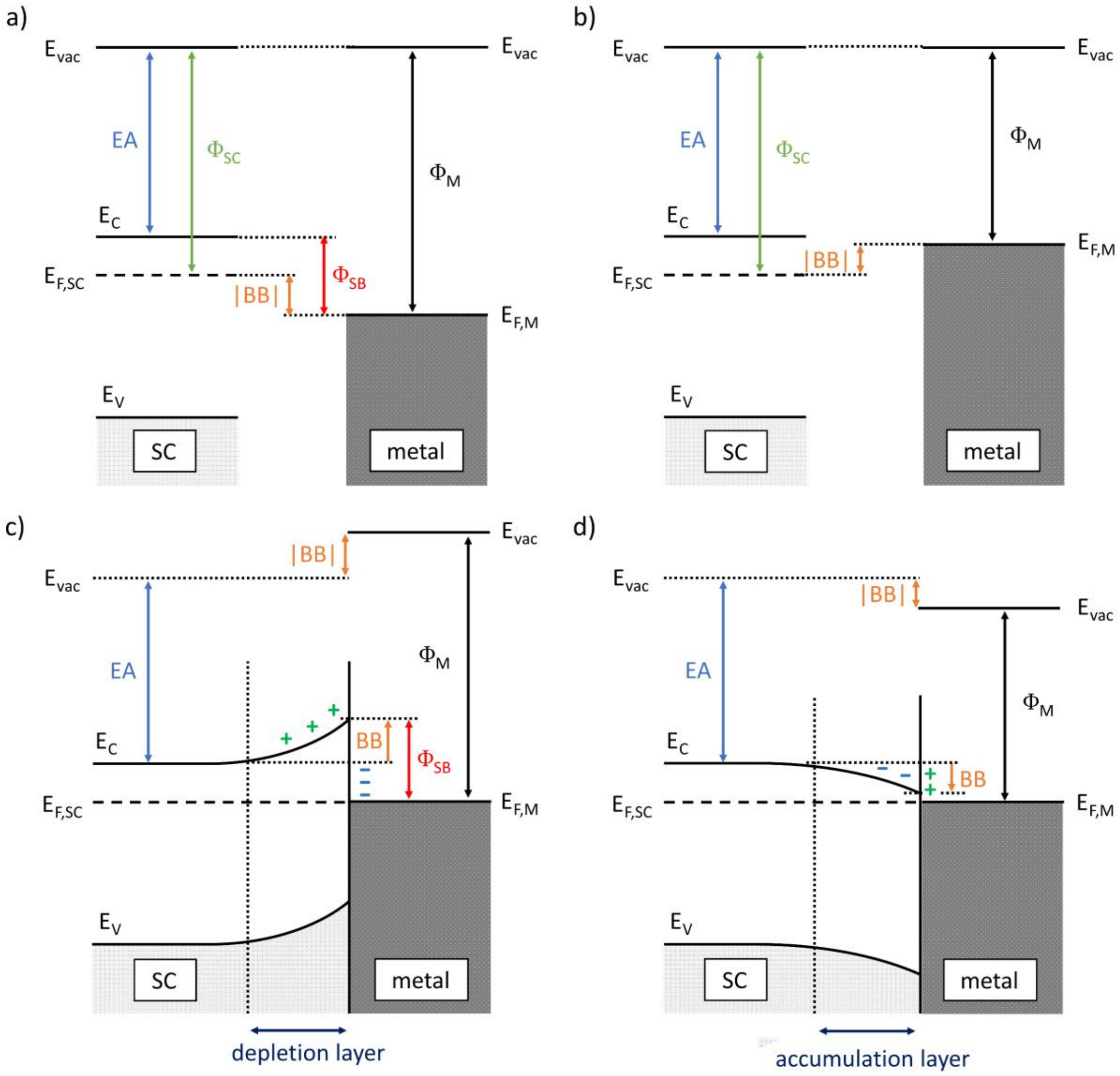

Figure 4: Energy diagrams of n-type SC-metal junctions. The independent energy levels before contact are shown for a metal with a work function Φ_M larger (a) and smaller (b) than the SC work function Φ_{SC}. After contact of the two components, charge redistribution at the interface facilitates the equalizing of SC and metal Fermi levels, i.e. $E_{F,SC}$ and $E_{F,M}$, respectively. c) In the case of $\Phi_M > \Phi_{SC}$ electrons (blue) flow from the SC to the metal leaving behind empty donor states (green) in a depletion layer in the SC. The SC bands are bent upwards and any backflow of electrons from the metal to the SC CB would have to overcome the Schottky barrier. The height of the Schottky barrier is given by $\Phi_{SB} = \Phi_M - EA$ within the Schottky-Mott model. d) If $\Phi_M < \Phi_{SC}$, electrons flow from the metal to the SC where they accumulate near the surface. In both cases the amount of band bending ($|BB|$) is defined by the difference in work functions of the two materials.

depletion layer gets its name from the relative absence of the majority carriers (i.e. electrons in an n-type SC). The charge depletion is realized by now empty donor states having transferred their electron to the metal. Every such electron transfer increases the potential (“Schottky”) barrier, for remaining SC electrons towards the interface. This transfer of charge leads to upward band bending within the SC with the empty donor states lying above E_F. The Schottky barrier height is equal to the difference between E_F and E_C at the SC surface and, within the Schottky-Mott model, given by $\Phi_{SB} = \Phi_M - EA$. Significant deviations from this rule occur depending on the exact nature of the materials and the interface.[75–77] As the charge imbalance in the SC is mediated by minority charge carriers, the width of the depletion layer is dependent on the donor state density. On the other hand, if $\Phi_M < \Phi_{SC}$ (Figure 4b), electrons from the metal are transferred into the SC giving rise to an accumulation layer (Figure 4d). Here, excess majority charge carriers lead to downward band bending. As there is no barrier at the interface, this configuration is called an ohmic contact. Typically, the width of an accumulation layer is smaller than that of a depletion layer, as the spatial density of the (mobile) majority charge carriers is not limited by the (immobile) available donor states per volume. The SCL is the region in which charge densities differ from the bulk. The generally low free charge carrier density in SCs, compared to metals, leads to less efficient screening of charges. This can be viewed as the underlying reason of the macroscopic extent of band bending and the SCL. The amount of band bending ($|BB|$ in Figure 4), i.e. the difference between surface and bulk energy levels, is given by the absolute difference of the work functions of metal and SC before electrical contact.

External electric fields

The low concentration of free charge carriers in SCs also gives rise to inefficient screening of external electric fields. An external electric field can therefore penetrate the SC and lead to band bending.[78] Consider a flat metal plate mounted parallel to an n-type SC connected to ground. To exclude other sources of band bending, it is assumed that the work functions of the metal plate and the SC are identical, and that there are no SC surface states. The flat bands of the SC remain flat, if no voltage is applied to the metal plate. Positive (negative) voltages on the metal lead to electron accumulation (depletion) in the SCL, causing downward (upward) band bending in the SC surface region.

Surface states

The lattice periodicity of the SC bulk is broken at its surface resulting in unpaired electrons at the surface, i.e. half-filled orbitals also called dangling bonds. The unreconstructed Si(111) surface, for example, has one dangling bond per surface atom.[79] The corresponding states form surface bands are generally located within the bandgap and can have metallic or semiconducting/insulating character. As in the bulk, metallic surface state bands are filled up to E_F, while in semiconducting and insulating ones a bandgap is separating a filled from an empty band. Since surface states usually have large densities (ca. $10^{15}/\text{cm}^2$), a small change of E_F within a surface band results in a large surface charge. On the other hand, the dopant density of states in the bulk parallel to the surface is typically comparatively small (between ca. 10^8 and $10^{12}/\text{cm}^2$).[69] Charge conservation must be fulfilled between the surface itself and the near-surface region, which has bulk like characteristics. Because of the difference in density of states E_F shifts only marginally with respect to the surface band. This is referred to as Fermi level pinning (to the surface band). Equilibrium between bulk and surface requires their Fermi levels to be aligned. This alignment is achieved by charge transfer between surface and bulk, if necessary, leading to the bands bending towards the surface while E_F in the surface band will move only slightly.[79] To describe this charge transfer process and its effect on the local potentials in more detail, a half filled and centered surface band located in the middle of the surface bandgap is assumed. In the case of an intrinsic SC, the bulk E_F is also in the middle of the bandgap. Therefore, no charge transfer takes place and VB and CB are flat throughout the material.[69] In an n-type SC the bulk E_F is located between E_D and E_C whereas it is pinned in the middle of the surface band at the surface as shown in Figure 5a. For electrons in donor states above E_F it is energetically favorable to migrate into empty surface states. Figure 5b depicts the ensuing negatively charged surface (Q_{SS}) and positively charged SCL (Q_{SC}). The charge redistribution between surface and bulk goes along with an electrostatic dipole potential in the SCL. This built-in

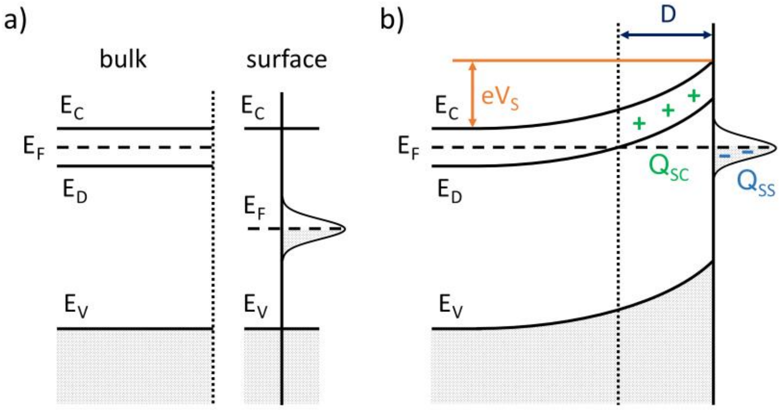

Figure 5: Upward band bending in an n-type SC induced by surface states. a) The material's energy levels are shown for the conceptual case of no electrical contact between bulk and surface, including a differing E_F. b) In reality, the equilibrium case has one consistent E_F achieved through charge transfer. A surplus in electrons in the surface band (Q_{SS}) is screened by positive charges in the SCL (Q_{SC}) such that $Q_{SS} = -Q_{SC}$. The magnitude of the band bending (orange vertical arrow) is proportional to the corresponding built-in potential $V(z)$ (see eq. (1) in text) evaluated at the surface ($z = 0$): $eV_S = e \cdot V(z = 0)$, where e is the electron charge.

potential is represented by upward bent valence, donor and conduction bands toward the surface in Figure 5b. Assuming a constant concentration of ionized donor states N_D in the SCL, the built-in potential is defined by

$$V(z) = V_{bulk} - \frac{2\pi N_D}{\epsilon}(z-d)^2\,, \tag{1}$$

where d is the thickness of the SCL, $0 < z < d$ is the distance from the surface, ϵ is the dielectric constant of the SC and V_{bulk} is the position of the band far away from the surface.[80] Note that after multiplying the potential with the electron charge e (with negative sign) the upward band bending of the n-type SC becomes apparent. For most materials, the defect density at the surface differs from the bulk defect concentration. Non-homogeneous defect densities lead to higher order built-in potentials. For NPs the amount of maximally achievable band bending generally increases with the particle size.[81] However, in the presence of a varying defect density between the surface and bulk of the NP considerable band bending is possible even within individual NPs of small sizes.[82] As an example, in a 20 nm diameter TiO_2 NP a maximal band bending of 250 meV has been reported.[83]

The above description and Figure 5 refer to a depletion layer as the SCL, named for the relative absence of the majority carriers in it. This is the standard case (Figure 6b), however two other

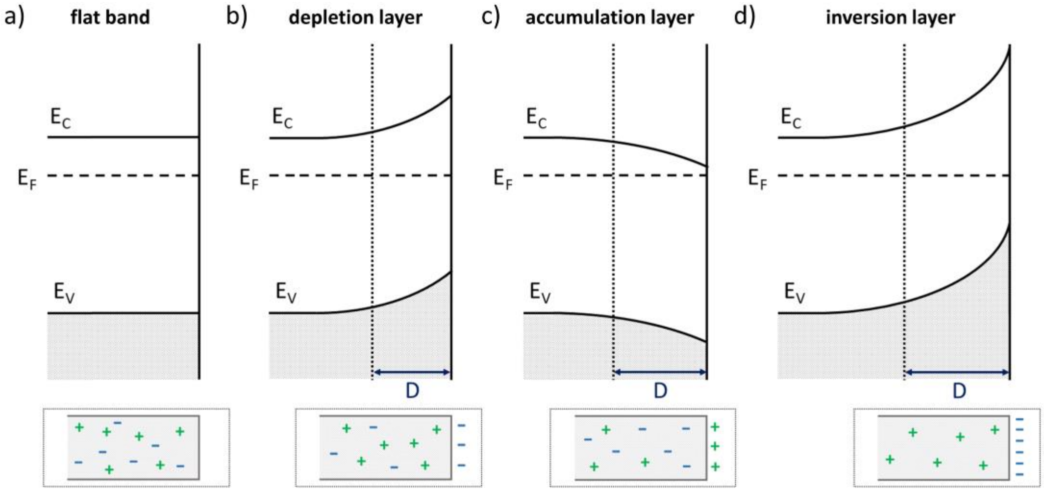

Figure 6: Overview of all possible surface-state-induced band bending scenarios for a (bulk) n-type SC depending on the charge distribution between surface and SCL. a) In the absence of any surface states or charges there is no band bending and majority (“−”) and minority (“+”) charge carriers have bulk like distributions all the way to the surface, as shown in the schematic at the bottom. b) Negative surface charges, e.g., from dangling bonds, are screened by positive charges within the SCL originating from empty donor levels pulled above E_F by upward band bending. c) Positive surface charges, e.g., from an adsorbate, are screened by negative charges accumulating in the SCL and downward band bending is present. d) High negative surface charge densities lead to screening effects sufficient to locally reverse majority and minority charge carrier type roles, generating a p-type SC as holes become the majority charge carrier in the SCL.

scenarios are possible besides the theoretical case of bulk and surface energy levels being aligned in the first place (Figure 6a).[69] An accumulation layer (Figure 6c) forms, if the surface band is energetically closer to the CB minimum than the VB maximum. In this case, electrons transfer from the surface into the bulk leading to an accumulation of majority carriers in the SCL screening positive charges at the surface. The respective downward bending is again equal to the difference between bulk and surface E_F when not in electrical contact. Lastly, in an inversion layer (Figure 6d), significantly stronger band bending than in the depletion layer (Figure 6b) is caused by minority carriers determining the electronic properties in the SCL. In this scenario the n-type SC is effectively locally turned into a p-type SC in the near-surface region. The (re-)arrangement of bulk and surface charges is qualitatively displayed at the bottom of each subfigure.

2.3 N3-ZnO Heterojunction in Dye-Sensitized Solar Cells

Atoms and molecules adsorbing to SC surfaces can influence the interfacial energetics in different ways. Physisorption of an atom consisting of positively charged core and negatively charged electrons leads to image charges within the substrate due to screening.[84] Chemisorption that includes charge redistribution between adsorbate and substrate gives rise to dipoles.[84] Similar to the metal-SC interface, this charge redistribution leads to a Helmholtz layer and affects band bending in the SC. Adsorbates can function either as electron acceptor or donors, depending on the specific interface and specific site. For the ZnO($10\overline{1}0$) surface, at low temperatures, atomic hydrogen binds to both oxygen and zinc atoms at the surface, functioning as electron donor and acceptor, respectively.[56] While this leaves the surface in a semiconducting state, at above room temperature conditions H only binds to O sites,[56] leading to surface metallization.[85,86] Here, the adsorbate-induced downward band bending is strong enough to locally pull the CB minimum below the Fermi level at the surface. Clear signatures of surface metallization are present in single-crystal ZnO($10\overline{1}0$) samples investigated via angle-resolved XPS.[56,57] As the density of states of the associated part of the CB that lies below the Fermi level is rather small, it can generally not be detected via standard XPS. However, a combination of UV/vis measurements and literature values of the nanocrystalline ZnO sample used here strongly suggests downward band bending large enough for surface metallization consistent with the single-crystal samples. See section 5.1 (re-print of ref. 58) for a more detailed explanation.

After the adsorption of N3 dye molecules[20] on this nanoscale ZnO film, the ZnO band bending stays constant.[87] Adsorption of the dye molecule on the ZnO($10\bar{1}0$) surface mainly takes place via the carboxyl groups (COOH).[45] Density functional theory (DFT) calculations show the most energetically favorable configuration consists of bonds involving three of the four carboxyl groups, in the two bipyridyl rings. Specifically, two COO^- groups are binding to Zn sites in a Zn-O-C-O-Zn geometry, with the corresponding hydrogen ions binding to nearest neighbor oxygen lattice sites, and a third carboxyl group where one O-Zn bond is replaced by a connection to an oxygen lattice site via a hydrogen bond (---) Zn-O-C-O---H-O.[45] The net zero effect of the N3 adsorption on ZnO band bending implies no effect of the newly formed bonds with Zn lattice atoms on the electric potential at the surface. Note that this situation may change in the presence of a solvent.

The N3-ZnO interface is a model system for charge transfer in heterogeneous adsorbate-SC systems, and the central part of an early DSSC[88,89] design. The standard design of photovoltaic devices consists of a SC material, most often crystalline silicon, sandwiched by the two electrodes. In the SC a photon is absorbed, and the emergent electron-hole pair is separated. The separation and migration of electron and hole to their respective electrodes is enabled by applying a voltage bias across the structure. This conversion of photons to electrical current has a maximally retrievable amount of energy per electron-hole pair that is equal to the bandgap of the employed SC. Therefore, this process by itself has unit efficiency for a photon energy matching the bandgap of the SC. With increasing photon energy the efficiency declines directly proportional to the excess photon energy exceeding the SC bandgap. All photons with energy below the SC bandgap cannot be converted to a photo-current, referred to as spectrum loss. These basic assumptions combined with the solar spectrum after passing through the atmosphere forms the basis of the Shockley-Queisser Efficiency Limit:[13] For single-junction designs the theoretical efficiency limit is ~34% at an ideal theoretical SC bandgap of 1.34 eV.[14] Other loss mechanisms included in this limit are the recombination of electron-hole pairs, and black body radiation due to increased solar cell temperature. Sources of the latter are non-radiative recombination of charge pairs and the transfer of photonic excess energy above the SC bandgap into heat via electron-phonon coupling. A common approach to overcome this efficiency limit is to combine different absorber materials separated by electric junctions in a so-called multi-junction cell design. Different parts of the solar spectrum are absorbed in different subsections of the solar cell. Typically, a wide bandgap SC is followed by one or more increasingly smaller bandgap SC layers. Photon energies above the bandgap of the first layer are absorbed while below bandgap energies are transmitted to deeper lying layers until reaching a small enough bandgap SC material where they can be absorbed. In single-junction solar cell designs, on the other hand, the main idea behind combining different materials is the quick separation of photo-generated charges to minimize recombination losses.

DSSCs are one category of single-junction solar cells combining different absorber materials. Typically, a wide bandgap SC such as TiO_2 or ZnO is combined with a dye absorbing in the visible spectrum. Figure 7a schematically shows the working principle of a DSSC based on the synthetic N3 dye, with an absorption maximum at a wavelength of 535 nm,[20] adsorbed onto ZnO. Absorption of a photon in the N3 dye molecules leads to an excitation from the highest occupied molecular orbital (HOMO) into the lowest unoccupied molecular orbital (LUMO), marked as step 1 in Figure 7a. While the HOMO is localized at the Ru metal center and the thiocyanate (NCS) groups (see Figure 7c), the LUMO is associated with the bipyridine rings of the ligands.[45] Therefore, the HOMO-to-LUMO excitation corresponds to a MLCT. The photoexcited singlet MLCT state decays on a <500 fs timescale[45] (step 2 in Figure 7a) leaving the system in an intermediate state before the electron injection into the SC.[41–48] The nature of this intermediate state has been debated to be either a triplet MLCT state[49–52] or a ICT configuration for which the TRXPS study in section 5.2 finds

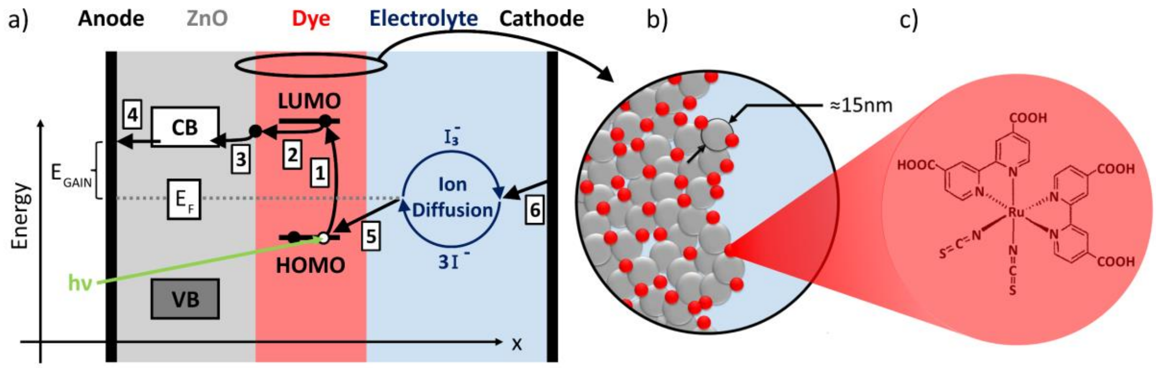

Figure 7: a) Schematic working principle of a dye-sensitized solar cell. Absorption of an incident photon leads to electron excitation from the highest occupied molecular orbital into the lowest unoccupied molecular orbital of the dye (step 1). Subsequent rapid dye ionization (step 2) is followed by injection of the electron into the SC CB (step 3). Here, the electron relaxes to the CB minimum and arrives at the working electrode (anode) with this energy (step 4). The HOMO hole is filled by electrons supplied by iodide anions (I^-) within the electrolyte (step 5). The counter electrode (cathode) supplies the iodide/triiodide redox cycle with electrons (step 6). b) A schematic of the SC-dye-electrolyte interface illustrates the nanoporous layer of sintered ZnO NPs (grey) and chemisorbed N3 dye molecules (red) immersed in the electrolyte (cyan). c) The chemical structure of the N3 molecule consists of a Ru metal center and two bipyridyl groups and thiocyanide ligands.

strong evidence: Separate signals from the dye and ZnO electrode establish clear evidence of ultrafast dye ionization and delayed injection of the photo-electron into the ZnO CB by ~300 ps agreeing with previous studies[41,42,47,87] (step 3 in Figure 7a). The injection step requires an energetic configuration between the LUMO energy (E_{LUMO}) and CB minimum at the surface ($E_C^{surface}$) such that $E_C^{surface} < E_{LUMO}$. The ZnO film is directly connected to the anode receiving the electron, thereby completing the first half of the photo-current generation process (step 4 in Figure 7a). The hole remaining in the HOMO is filled with an electron supplied by the electrolyte (step 5 in Figure 7a). Charges are transported via ion diffusion and replenished within the electrolyte via a redox cycle: $I_3^- + 2 \cdot e^- \leftrightarrow 3 \cdot I^-$.[20] Here, electrons from the cathode (step 6 in Figure 7a) enable a triiodide-to-iodide reduction reaction while the reverse oxidation reaction generates the electrons to neutralize the N3 dye HOMO hole. The total energy gained per charge pair separation E_{GAIN} equals the difference between the SC Fermi level and the electrolyte redox potential.[20]

Besides the charge transfer steps laid out in Figure 7a there are potential loss channels. In principle, every injection step as well as the electron transport within the electrode could suffer from competing recombination losses. The ICT configuration following the singlet MLCT state benefits from the carboxylate groups in the ligand binding the dye to the SC surface[90] and establishes good electronic connectivity. The latter is associated with a fast transfer timescale[91] in the femtosecond to picosecond regime, depending on the material combinations making up the interface.[20,92] Besides the delayed injection signal, the transient TRXPS signal (section 5.2) associated with the dye is sensitive to the recombination timescales. While a distinct recombination site or mechanism is hard to pinpoint, the depth-resolution shows downward band bending that should lead to electron transport near the usually more defect-rich surface within the electrode. These defects could trap otherwise (laterally) mobile charges and reduce the device performance of the N3-ZnO system compared to its TiO_2 counterpart.

The nanoporous structure of the ZnO film illustrated in Figure 7b significantly increases the available surface area and thereby the volume density of adsorbed dye molecules. This design feature enables much higher cell efficiencies compared to a flat single-crystal substrate. Because of the porous nature of the interface this DSSC design is a bulk-junction device. The originally individual NPs, with a diameter of ~15 nm (see section 5.2), are sintered to improve electrical contact, before sensitizing the film by immersing it in a solution of the N3 dye molecules in ethanol. Exact details of the sample preparation method can be found in section 5.2.

2.4 Surface Photo-Voltage in Semiconductors

Surface photo-voltage (SPV) is a photoinduced change in band bending. SPV effects can be observed in Kelvin probe measurements[93–96] and in special cases indirectly via photoluminescence which can be sensitive to the width of the SCL.[97] Photoelectron spectroscopy is a direct and the most widely used technique for accessing band bending changes.[29,69,98–102] TRXPS is sensitive to SPV effects and Figure 8 shows several important SPV mechanisms using an n-type SC with accumulation layer as an example, as this is the configuration of the ZnO substrate studied in sections 5.1 and 5.2. In this scenario, positive surface charges are screened by a negatively charged SCL. The corresponding dipole moment is pointing outwards, from bulk to surface (light blue arrow), displayed at the bottom of each subfigure. Super-bandgap excitation (Figure 8a) leads to a VB hole migrating away from the surface and a CB electron moving towards the surface. The respective laser-induced dipole (orange arrow shown in the middle of the bandgap) is opposing the existing dipole and therefore flattens the bands. This transient upward band bending is indicated by the upward pointing black arrows on the right. The super-bandgap excitation is the most relevant mechanism for photon energies exceeding the bandgap due to the high density of states of the VB and CB compared to surface, doping or defect induced states. Figure 8b shows an excitation of a VB electron into the surface band, with the VB hole again being driven away from the surface. The resulting transient dipole counteracting the accumulation layer dipole and flattening the bands similar to the super-bandgap excitation case. The minimally needed photon energy for this process is $E_F - E_V^{surface}$. An excitation of a surface band electron into the CB (Figure 8c) leaves a hole at the surface with the CB electron relatively confined within the SCL depending on the magnitude of the band bending. The resulting dipole (orange arrow) is enhancing the existing dipole (light blue arrow) bending the bands further downwards. The minimally needed photon energy of $E_C^{surface} - E_F$ is relatively small in this example. Finally, a light absorbing adsorbate can inject electrons into the SC CB after laser excitation (Figure 8d). Typically, an excitation from the HOMO into LUMO within the molecule is followed by electron injection from the LUMO into the SC CB, as is the case for the N3-ZnO interface. A necessary prerequisite is suitable band alignment such that $E_C^{surface} <$

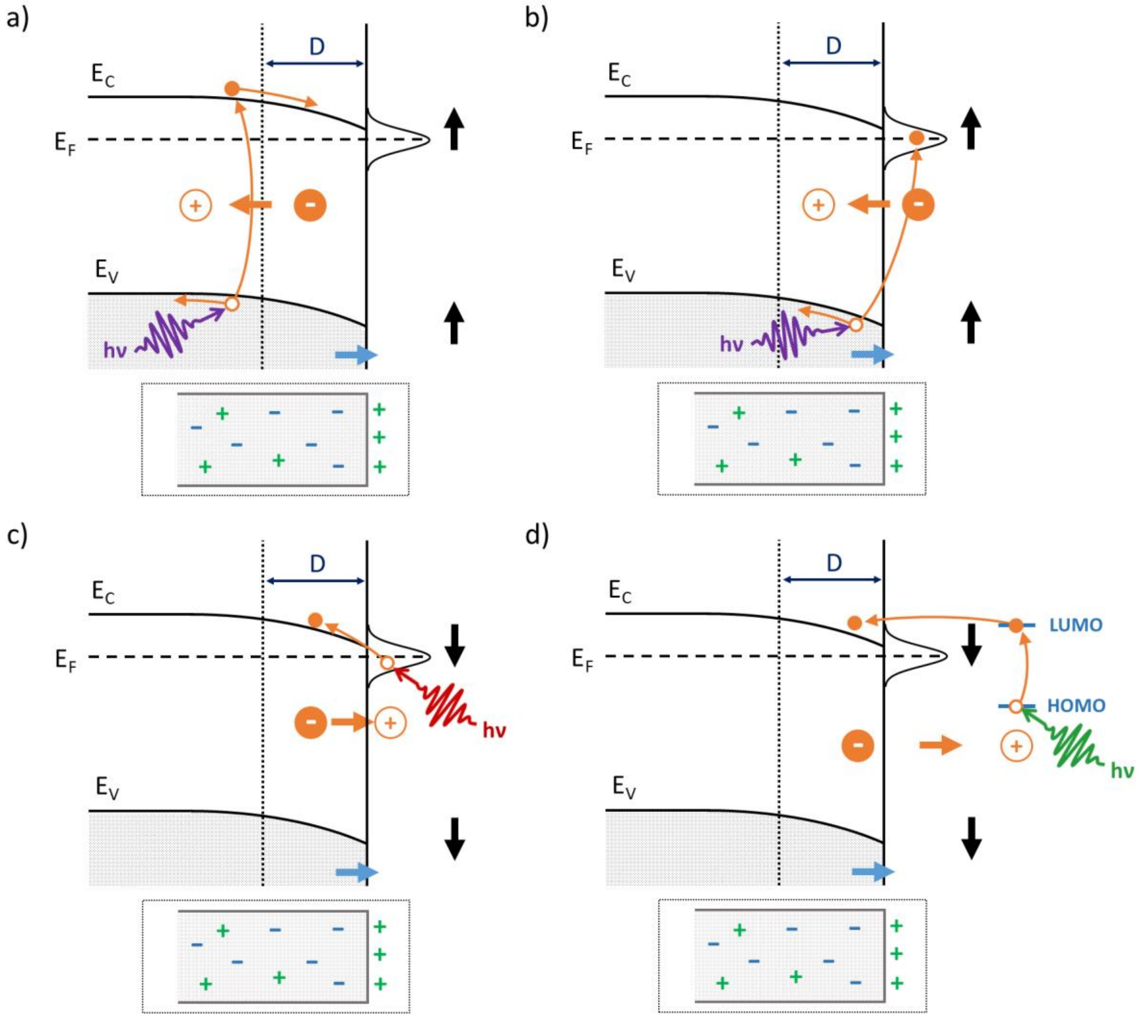

Figure 8: Laser excitation scenarios leading to SPV in an n-type SC with an accumulation layer of width D. The equilibrium charge distribution in the near-surface region is shown at the bottom of each subfigure along with the associated dipole (light blue arrow) pointing from bulk to surface. a) Super-bandgap, b) VB to surface band, c) surface band to CB excitations and d) adsorbate excitation followed by electron injection into the CB each create an additional transient dipole (orange arrow) between laser-generated charges (orange circles). This dipole can either reduce the existing dipole, as in a) and b), and flatten the bands (upward pointing black arrows) or enhance the existing dipole, as in c) and d), bending the bands further downwards (downward pointing black arrows). See text for details.

E_{LUMO} where E_{LUMO} is the LUMO energy position. The similarity between Figure 8c and d highlights the importance of distinguishing the two mechanisms. If an adsorbate-SC electron injection mechanism is investigated, the blank SC substrate should also be interrogated with the same experimental parameters as the adsorbate-SC sample to exclude surface band to CB electron transfer or other sub-bandgap processes as competing possible scenarios. Notably, for the N3-ZnO experiment discussed in section 5.2, the corresponding bare ZnO reference measurement with the same experimental parameters exhibits no detectable surface band to CB electron transfer or any other sub-bandgap effect.

Generally, the laser-induced CB electrons in the SCL can be considered relatively immobile along the surface normal, but laterally free to move, although under the influence of Coulomb forces from the laser-generated hole at the surface. The hole can be mobile within the VB (Figure 8a and b), or either laterally mobile or confined in the surface band or the adsorbate (Figure 8c and d) depending on their exact nature.

3 Experimental Setups

This chapter describes key components and concepts of the two time-resolved experimental schemes employed, i.e. TRXPS and TRXAS. Both time-resolved X-ray spectroscopy experiments use a picosecond laser to generate the pump pulse and soft X-ray radiation from the Advanced Light Source (ALS) located at Lawrence Berkeley National Laboratory as a probe pulse. The data acquisition and the laser pulses are synchronized to the X-ray source via the ALS master clock and run with adjustable repetition rates of up to ~500 kHz. The X-ray pulse train combined with the time-resolved detection of X-ray photoelectron (TRXPS) or X-ray fluorescence (TRXAS) signals allows the implementation of a “single-pump multiple-probe” scheme. This approach leads to higher data acquisition rates where data for a large number of delays in the ns to µs regime are acquired simultaneously. Data with a time-resolution on the picosecond scale is acquired by varying the pump-probe delay. The best achievable time resolution is limited by $\left(\tau_{\mathrm{pump}}{}^2 + \tau_{\mathrm{probe}}{}^2\right)^{1/2}$ where τ_{pump} and τ_{probe} are the pulse durations of pump and probe pulse, respectively. In the presented experiments, the ALS probe pulses with a length of ~70 ps (FWHM) are effectively determining the temporal resolution.

The TRXPS experiment, set up at beamline 11.0.2.2 of the ALS, is briefly described in section 3.1, including the temporal structure of the X-ray pulse train, electronic synchronization of laser and data acquisition to the X-ray source, and X-ray photoelectron data collection. More detailed information on the TRXPS experiment can be found in the works of Shavorskiy *et al.*,[103] Neppl *et al.*,[101] and Neppl and Gessner.[29]

The TRXAS setup uses the same laser source and scheme to electronically synchronize the laser and data acquisition to the ALS. The detected signals, however, as well as experimental setups and used ALS beamline differ from the TRXPS setup. In the TRXAS results presented in section 5.3 the total fluorescence yield data is detected at beamline 8.0.1.2 of the ALS. Section 3.2 gives a brief introduction to the experimental setup focusing on the data acquisition scheme and a significant improvement to the data normalization, implemented during the course of this work. Specifically, the data acquisition is adjusted such that laser-excited and reference spectra are recorded using X-ray pulses originating from the same electron bunches within the synchrotron ring. This self-referencing scheme improves the TRXAS signal-to-noise ratio by eliminating fluctuations in the X-ray fluence caused by the intermittent refilling of individual electron bunches during the standard top-off operation mode of the ALS. A more detailed description of the setup beyond this aspect can be found in a study by Neppl *et al.*,[104] which describes a proof-of-principle experiment on photoinduced dynamics in Cu_2O.

3.1 Time-Resolved X-ray Photoelectron Spectroscopy

A schematic overview of the TRXPS setup is shown in Figure 9a.[105] The electron bunches (violet) within the ALS synchrotron ring create X-rays (blue) when passing through the beamline 11 undulator. The electron bunches are arranged in a pattern of a higher charge camshaft bunch surrounded by a gap and a multi-bunch region. The multi-bunches have a spatial separation that corresponds to a 2 ns delay between individual bunches while orbiting the synchrotron ring with close to the speed of light. Their energy loss is compensated within radiofrequency cavities driven by a 500 MHz master clock. As the electron bunch pattern defines the temporal characteristics of the X-ray pulse train, the ALS master clock is used to synchronize both the optical laser source as well as the data acquisition to the X-ray source. This electronic synchronization scheme enabling synchrotron based optical pump – X-ray probe schemes is similar to implementations at the Advanced Photon Source[106] and Swiss Light Source.[107] The 500 MHz master clock signal passes through a 1/6 frequency divider such that the resulting ~83 MHz frequency is equal to the repetition rate of the optical laser oscillator. Leakage from one of the oscillator mirrors provides a signal of the oscillator pulse train. The oscillator signal together with the ALS-derived ~83 MHz signal is fed into a clock synchronizer unit provided by the laser manufacturer. This unit locks the phase of the oscillator pulse train to the ALS by dynamically controlling the position of one of the laser oscillator cavity mirrors via a piezo motor. The jitter of this phase-locked loop typically ranges from the sub-ps to the few-ps regime. The pump-probe delay is adjusted in 5 ps steps using a phase shifter unit with a maximum delay of ~5 ns. The experiment repetition rate as well as the coarse timing between X-rays and laser is set via the second branch of the synchronization electronics. The ~83 MHz signal passes through a programmable frequency divider (PFD). The user-defined division sets the laser repetition rate as the PFD output signal which is used to pick a pulse from the oscillator pulse train

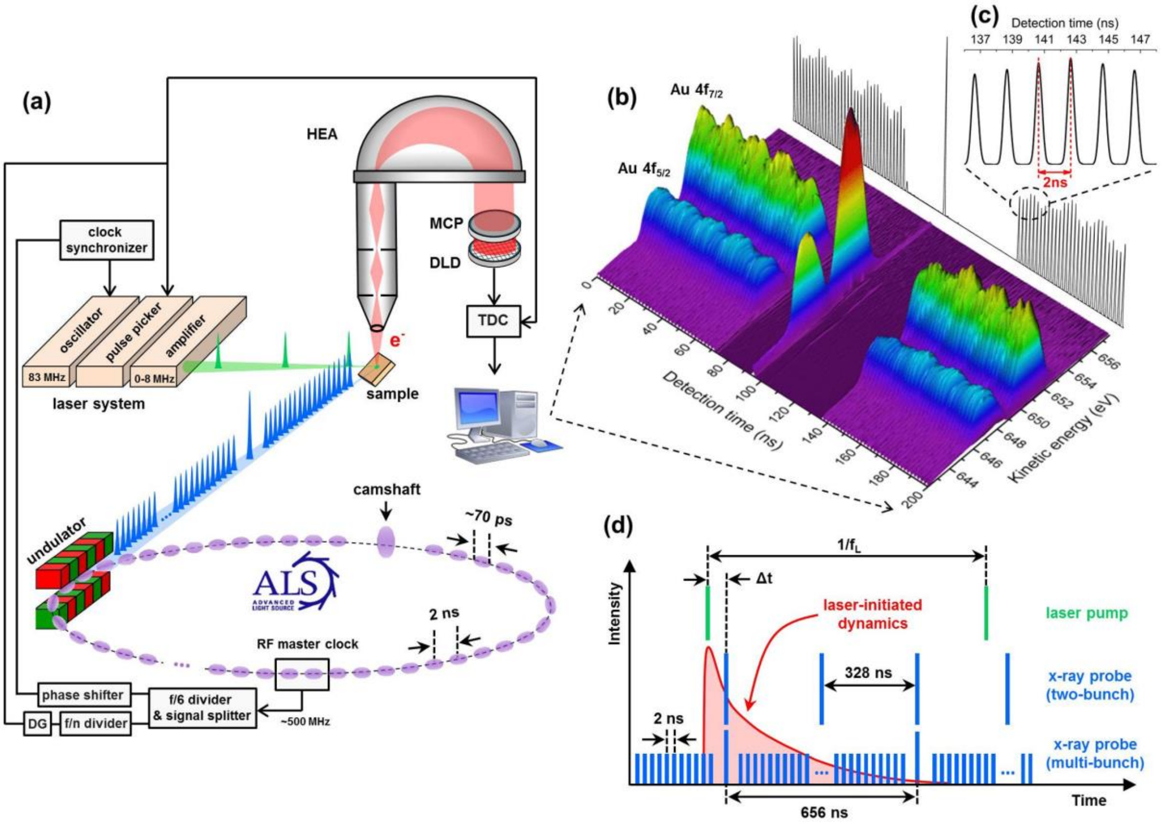

Figure 9: Overview of the TRXPS experimental setup. a) Schematic of X-ray (blue pulses) source (ALS), optical laser (green pulses) system, and photoelectrons (red). The electronic synchronization of the laser source to the ALS master clock establishes a controllable time delay between the two light sources. See text for detailed explanation. The hemispherical electron analyzer (HEA) is equipped with a time- and position-sensitive delay line detector (DLD) acquiring the X-ray photoelectron signal. b) Exemplary TRXPS data of the Au4f photoline of a gold foil is shown as a function of photoelectron kinetic energy and photoelectron detection time. Every X-ray pulse creates the typical Au4f doublet that is most clearly seen for the so-called camshaft signal (at ca. 100 ns detection time) surrounded by a gap. Cutting the TRXPS data at an individual photoelectron kinetic energy reveals its temporal structure shown as a black line behind the TRXPS three-dimensional false color plot. c) The 2 ns spacing in the so-called multi-bunch region stems from the electron bunch filling pattern of the ALS shown in d). The setup can be used in both the two-bunch (top) and multi-bunch (bottom) operating mode of the ALS. Reprinted with permission from Elsevier.[105]

for amplification and output. A fast photodiode sensitive to all available X-ray and laser photon energies is able to resolve the individual X-ray pulses. First, coarse temporal overlap between the optical and X-ray pulses is adjusted via the photodiode signal using an oscilloscope. Subsequently, the SPV effect (section 2.4) on a SC such as Si or GaAs is used to determine the precise timing of the laser relative to the X-ray pulse train. More technical details of establishing temporal overlap of laser and X-ray source are described in references 101 and 103.

The X-rays produced in the beamline 11 undulator are incident on the sample where they create X-ray photoelectrons (red). The photoelectrons are filtered by their kinetic energy within a hemispherical electron analyzer (HEA), amplified within a stack of two micro-channel plates (MCP) and detected using a time- and position-sensitive delay line detector (DLD).[108] The hit positions indicate the electron kinetic energy within the energy window selected via voltages applied to the HEA. The time of arrival of the detected X-ray photoelectrons is recorded and digitized by a time-to-digital converter (TDC). The trigger for the TDC stems from the PFD signal used by the laser pulse picker. An exemplary time- and energy-resolved Au4f X-ray photoelectron data set is shown in Figure 9b. The typical doublet structure of the Au4f spectrum can be best seen in the camshaft data with a relative detection time of just below 100 ns. The color-coded three-dimensional plot shows the gap around the camshaft spectrum followed by multi-bunch regions on both sides. The temporal structure of the TRXPS data is shown as a black line behind the color-coded plot for a selected X-ray photoelectron kinetic energy. Figure 9c emphasizes the multi-bunch region where photoelectron signals from different X-ray pulses are clearly distinguishable. With this combination of picosecond time-resolved pump-probe scheme and microsecond range data acquisition, extended ranges of photoinduced dynamics can be captured simultaneously. The best achievable time resolution is predominantly determined by the ~70 ps FWHM X-ray pulses. Figure 9d schematically shows the laser pulse pattern (green) and its associated photoinduced dynamics (red). Both the multi-bunch mode (bottom) as well as the two-bunch mode (top) of the ALS can be used in the TRXPS experiment. In the two-bunch mode, two electron bunches with charges of 4-5 times of the camshaft and a spacing of ~328 ns circle the ring. Notice, that the temporal width of individual photoelectron signals, such as in Figure 9c, depends on the XPS signal intensity and the time-of-flight spread discussed in more detail in references 29 and 103.

The 1064 nm laser system has integrated doubling (532 nm) and tripling (355 nm) stages. The user-selected wavelength is passed through a telescope enlarging the spot size and then focused to between 50 and 250 µm (FWHM) on the sample, typically selected to be significantly larger than the X-ray spot size. Spatial overlap of the two light sources is established with a photodiode that is sensitive to all relevant laser as well as soft X-ray energies. A sharp edge on top of the photo-sensitive area of the diode allows the determination of the beam positions via so-called knife-edge scans. The laser beam pointing is precisely adjusted by moving the last optical mirror before the experimental chamber, which is attached to a piezo-actuated mirror mount.

3.2 Time-Resolved X-ray Absorption Spectroscopy

An experimental scheme of the TRXAS setup is shown in Figure 10. The employed laser and X-ray sources, their synchronization, and the procedure to establish their spatial overlap are identical to the TRXPS setup described in section 3.1. Coarse temporal overlap is established again via a fast photodiode signal. Fine-tuning takes place via a pump-probe delay scan at a fixed X-ray photon energy displaying a relatively large photoinduced effect such as CuO at ~529.5 eV. This section focuses on the TRXAS data collection scheme and specifically on a new data normalization technique significantly improving the signal-to-noise ratio. A more detailed description of other aspects of the setup can be found in a prior proof-of-principle publication by Neppl *et al.*[104]

Figure 10a shows the X-ray beam incident on the sample where it is absorbed and leads to fluorescence and Auger electron decay processes. The TFY signal is amplified and detected by a MCP assembly connected to a TDC.[109] The temporal structure of the TFY signals follows the X-ray pulse pattern which in turn depends on the electron bunches inside the synchrotron ring: A sequence of multi-bunches with a spacing of 2 ns is interrupted by a ~60 ns wide gap that contains only the more intensely filled camshaft bunch, 20 ns after the last multi-bunch. The resulting X-ray pattern repeats every ~656 ns, corresponding to a ~1.5 MHz repetition rate for X-rays from any one given electron bunch. An exemplary time- and X-ray photon energy-resolved data set of the O1s absorption edge of a TiO_2 NP film is displayed in Figure 10b. The simultaneously collected total electron yield (TEY) spectrum is shown in black behind the color-coded plot of the time-resolved TFY data. The intensity of the camshaft TFY spectrum at a timestamp of ~165 ns is scaled down by a factor of 1/2 to enable better comparison with the multi-bunch region. The gap surrounding the camshaft signal described above is clearly visible between time stamps of ~145 to ~205 ns. Because of the rendering of the three-dimensional plot the multi-bunch TFY signals seemingly overlap while in fact the individual multi-bunch spectra are experimentally resolved. Figure 10c shows a typical timing configuration of the laser and X-ray pulses within the data acquisition window. The experimental pump-probe delay is adjusted such that the laser pump pulse precedes the camshaft X-ray pulse. This allows to probe picosecond dynamics quickly with the high intensity camshaft pulse while dynamics on timescales of tens of nanoseconds and above are probed with the following X-ray pulse train. However, there is no signal in the first 40 ns after the first probe pulse because of the

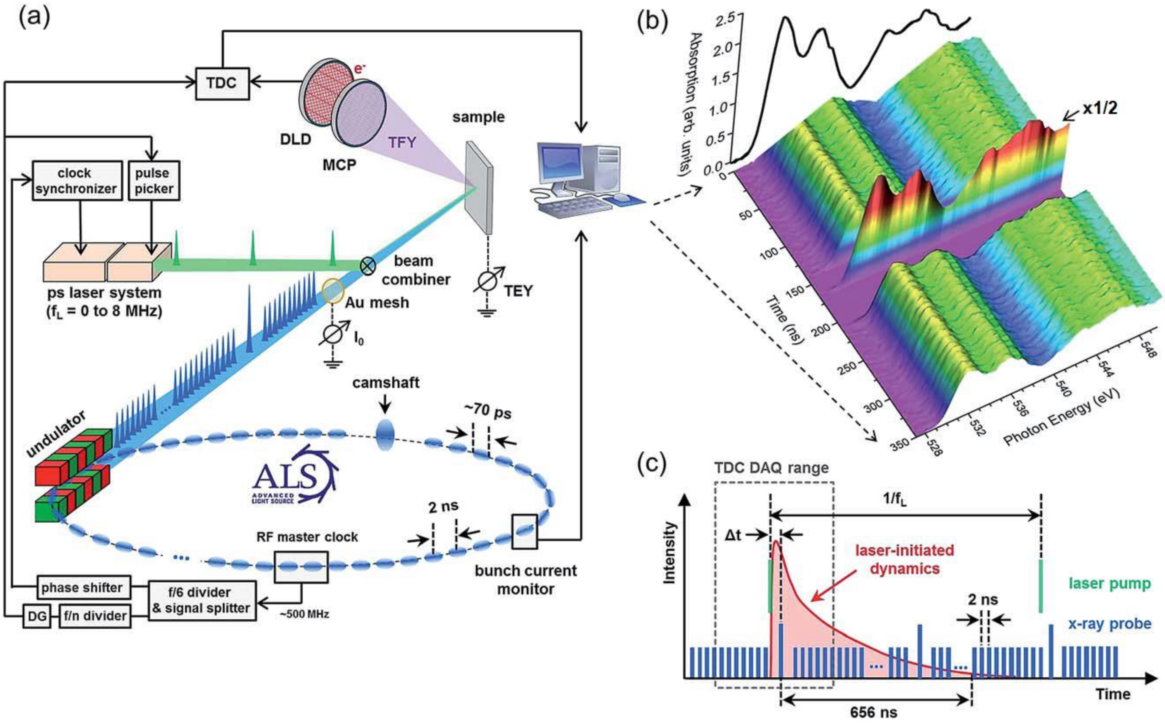

Figure 10: Overview of time-resolved X-ray absorption setup. a) A schematic shows key components of the experiment including the ALS synchrotron ring, X-ray generation, pump laser source, and data acquisition method. Total fluorescence yield (TFY) signals are collected with a micro-channel plate (MCP) and delay-line detector (DLD). See text for more details. b) Exemplary time- and photon-energy-dependent TFY spectra of the O1s edge of a TiO_2 NP film. The color-coded three-dimensional plot shows individual multi-bunch spectra surrounding the higher amplitude camshaft signal at a timestamp of around 170 ns. The fast electronic readout enables the clear distinction of individual TFY signals and association to their respective pump-probe delays. Note that the perspective and rendering of the data plot creates an apparent merging of the separated multi-bunch signals. TRXAS data is corrected for slow X-ray beam intensity fluctuations and the photon-energy-dependent X-ray transmission of the beamline by a reference photocurrent measurement on a gold mesh inserted into the X-ray beam. The more surface-sensitive total electron yield (TEY) spectrum of the sample (black solid line) is recorded simultaneously with the time-resolved TFY data. c) Timing schematic of the laser-pump (green)/multiple X-ray probe (blue) spectroscopy during ALS multi-bunch operating mode. Reproduced from ref. 104 with permission from the Royal Society of Chemistry.

gap following the camshaft bunch schematically shown in Figure 10c. This gap in the acquired TRXAS data can be avoided by placing the laser pump pulse within the X-ray multi-bunch train.

Both configurations, with the laser pulse placed before the camshaft or within the multi-bunch train, benefit from the improved dual-channel data normalization scheme developed in the course of this work. Figure 11 compares the single-channel (Figure 11a) and dual-channel (Figure 11b) data normalization schemes. In both cases, the laser pulse (green) induces a transient effect (red, dotted) modifying the pumped TRXAS signal (red). These transient effects are captured by subtracting a reference signal (violet) spectrum from the individual pumped signal (red) spectra, thereby creating

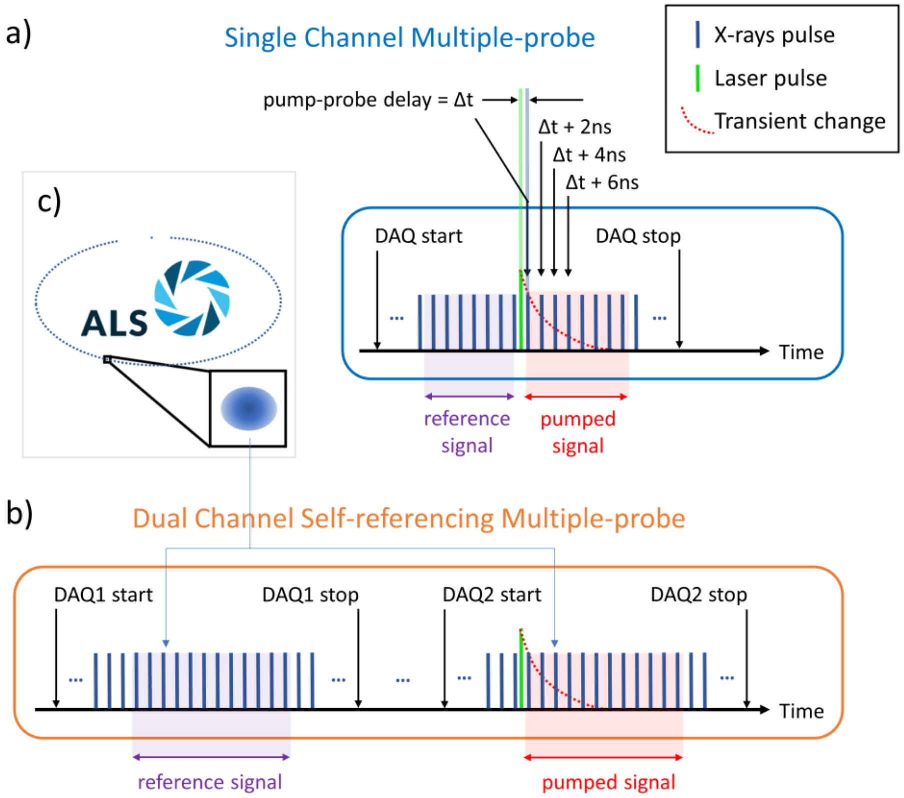

Figure 11: Overview of single- (a) and dual-channel (b) multiple-probe TRXAS data acquisition schemes. The laser pump pulse (green) induces a transient change (dotted red curve) detectable in TRXAS data associated with the X-ray pulses (blue) following the laser. Their time delays with respect to the laser pulse are $\Delta t_N = \Delta t + N \times 2$ ns, where Δt is the time-delay of the first X-ray pulse and $N \in \mathrm{N}_0$. a) The single-channel data acquisition scheme records the reference signal (violet) before and the pumped signal (red) after the laser pulse using consecutive X-ray pulses that stem from different electron bunches within the synchrotron ring. b) The dual-channel data acquisition scheme allows collection of reference and pumped signals originating from the same synchrotron electron bunches, one of which is shown schematically in c). This self-referencing signal eliminates the sensitivity of TRXAS data to variations in X-ray fluence from different electron bunches, thereby significantly improving the TRXAS signal-to-noise ratio. To this end, two separate data acquisition channels are used with a relative delay equal to the roundtrip time of an electron bunch within the synchrotron ring.

a difference spectrum for each delay Δt_N. In the single-channel data acquisition scheme (Figure 11a) the reference signal is acquired just before the laser pulse is incident on the sample. Averaging of the reference signal provides some reduction of noise in the difference spectra. This version of the data acquisition scheme, however, is subject to significant systematic variations in the recorded difference spectra due to the operating mode of the synchrotron. Reference and pumped signals stem from X-ray pulses generated by different electron bunches in the synchrotron ring. These electron bunches are continuously refilled (“topped up”), to counteract scattering losses of electrons due to imperfect vacuum in the synchrotron ring. Refilling specific electron bunches manifests itself as a step-function-like change of the corresponding X-ray pulse intensity, thus creating an artefact in the TRXAS data of the time delay associated with this X-ray pulse.[104] Either an individual bunch or every 4th bunch within the ring is topped up approximately every ~10 s. Multiple refilling events occur per TRXAS data point as typical data acquisition times are around 60 s per X-ray photon energy step. The ALS provides time-stamped data of the charge of each electron bunch. Normalizing the TRXAS spectra using the electron bunch charge data smooths these artefacts and improves the signal-to-noise ratio of the difference spectra as described in detail in ref. 104. However, the electron bunch data itself has finite accuracy and invariably a residual error remains within this single-channel data acquisition scheme.

Within this work, a self-referencing scheme (Figure 11b) has been implemented that eliminates this problem. Here, a second data acquisition channel, with a relative delay of one electron bunch roundtrip time, is added to enable acquisition of reference and pumped signals stemming from the same electron bunch (shown schematically in Figure 11c) in the synchrotron ring. Any refilling of electron bunches affects pumped and reference signals equally. Note that normalization of TRXAS spectra with electron bunch charge data can still be applied and smooths the overall individual spectra, enabling a more accurate comparison to literature data. Importantly however, the difference spectra used to evaluate photoinduced effects (such as the exemplary transient effect shown in Figure 11) are inherently independent of changes in charge across different synchrotron electron bunches when using the dual-channel self-referencing technique. This technique has been used to acquire the TRXAS data presented in section 5.3.

4 Methods for Data Analysis

This chapter provides more detail on the data analysis methods employed to generate the results presented in chapter 5 beyond the general data analysis description in the respective publications. Section 4.1 demonstrates how transient interfacial dipoles can be accessed via TRXPS. The section starts by describing accessible physical quantities within XPS, specifically for a molecule-SC system such as the N3-ZnO sample. The influence of a surface dipole, such as the photoinduced interfacial dipole between N3 adsorbate and ZnO substrate surface, is discussed in detail. Finally, the magnitude of the interfacial dipole is used, together with other experimental and sample parameters, to estimate the dipole distance, i.e. the distance between the adsorbate hole and SC surface, and the associated interfacial electric field. Section 4.2 describes laser-induced heat deposition in solids and gives temperature estimates for several technologically pertinent metal oxide SCs dependent on experimental parameters such as laser wavelength, spot size, and fluence. Whether a signature of the laser-induced temperature jumps should be expected in X-ray probe signals depends on electron-phonon coupling timescales and experimental parameters such as sample scanning speed, laser pulse duration and repetition rate. Section 4.3 describes the time-resolved modelling of the dissipation of laser-deposited heat and the resulting temperature gradients in ultra-high vacuum conditions. This section represents the central piece of the fitting algorithm to describe energy transfer within the TRXAS study on CuO. Finally, section 4.4 details a framework for leveraging spectral changes in high energy resolution data to gain additional spatial insight into SPV and temperature effects in TRXPS and TRXAS experiments, respectively. To achieve this, measured spectra are represented as a linear combination of individual depth-dependent components. In the TRXAS data these components differ in temperature, while in the (TR)XPS experiment their binding energy varies according to the SC band bending.

4.1 Interfacial Dipoles in X-ray Photoelectron Spectroscopy

In XPS, electrons are ejected from the sample after absorbing X-ray photons with sufficient energy. Generally, an electron will be ejected, if the X-ray photon energy is larger than the sum of the electron binding energy (measured relative to the Fermi energy) and the material work function. Any energy in excess of this barrier represents the electron kinetic energy at the sample.[27] An XPS energy level diagram for the generic case of a SC substrate with downward band bending V_{BB} and an adsorbate is shown in Figure 12a. Photoelectrons from a substrate core level $E(sub.)$ (green) and an adsorbate core level $E(ads.)$ (yellow) are probed with X-rays of the same photon energy (violet arrows). The kinetic energy of the resulting photoelectrons near the SC surface, i.e. $E_{kin}^{SC}(sub.)$ and $E_{kin}^{SC}(ads.)$, are defined by

$$h\nu = E_B(sub.) + \Phi^{SC} + E_{kin}^{SC}(sub.) + E_F - E_V^{surface} \, , \tag{2}$$

or

$$h\nu = E_B(sub.) + \Phi^{SC} + E_{kin}^{SC}(sub.) + E_F - \left(E_V^{bulk} + V_{BB}\right) , \tag{3}$$

and

$$h\nu = E_B(ads.) + \Phi^{SC} + E_{kin}^{SC}(ads.) \, , \tag{4}$$

respectively, where $h\nu$ is the X-ray photon energy, Φ^{SC} the SC work function, $E_B(sub.)$ and $E_B(ads.)$ their respective binding energies, and E_V^{bulk} and $E_V^{surface}$the VB maximum positions within the bulk and at the surface of the SC, respectively. Note that the binding energy for the SC is given relative to the top of the VB,[110] while for the adsorbate it is given relative to the Fermi level of the combined adsorbate-SC system. The sign of V_{BB} is the same as for all other energy levels, i.e. V_{BB} is negative in Figure 12. Interestingly, the detected kinetic energies of both substrate and adsorbate, i.e. $E_{kin}^{D}(sub.)$ and $E_{kin}^{D}(ads.)$, are referenced to the detector work function Φ^D and thus independent of Φ^{SC}. This can be rationalized by taking into account the so-called contact potential $\Phi^{contact} = \Phi^{SC} - \Phi^D$, established between sample and detector upon electrical contact. This is the typical situation in XPS experiments as both sample and detector are connected to a common ground. Thus, kinetic energies defined with respect to sample and detector surfaces can be converted via $E_{kin}^{D} = E_{kin}^{SC} + \Phi^{contact}$. Since any change in Φ^{SC} affects the photoelectron kinetic energy at the sample and the contact potential with opposite signs, there is no net effect of Φ^{SC} on the detected kinetic energy. Using eq. (2) to (4) and the contact potential yields a detected substrate photoelectron kinetic energy of

$$E_{kin}^{D}(sub.) = h\nu - E_B(sub.) - \Phi^D - E_F + E_V^{surface} \, , \tag{5}$$

or

$$E^D_{kin}(sub.) = h\nu - E_B(sub.) - \Phi^D - E_F + E_V^{bulk} + V_{BB}\,, \tag{6}$$

and a detected adsorbate photoelectron kinetic energy of

$$E^D_{kin}(ads.) = h\nu - E_B(ads.) - \Phi^D\,. \tag{7}$$

Figure 12b shows the effects of a surface dipole δ on the energy level alignment as is the case for the photoinduced electron injection of the N3 dye adsorbate on the nanocrystalline ZnO SC substrate. δ and all quantities changing as a result of its presence are marked in red. The surface

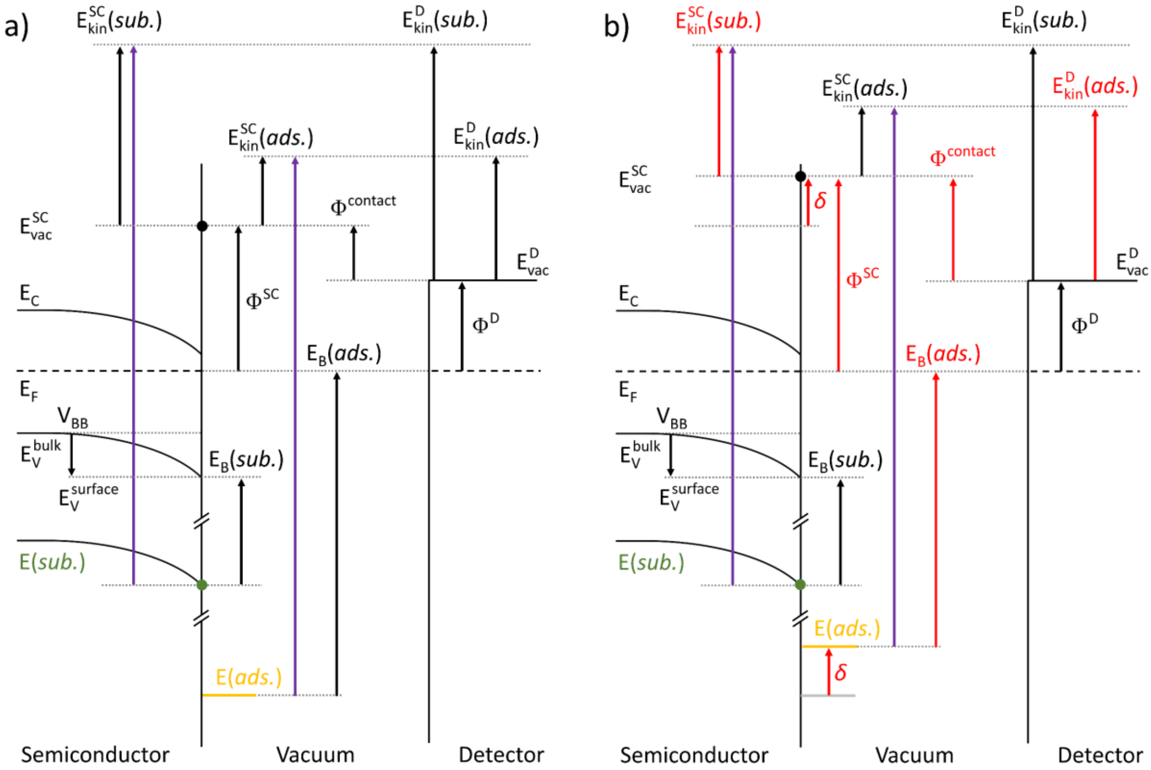

Figure 12: (TR)XPS energy level diagram of an adsorbate/substrate sample without (a) and with (b) a surface dipole δ. a) The exemplary substrate (*E(sub.)*, green) and adsorbate (*E(ads.)*, yellow) energy levels are probed with an X-ray photon (violet) of the same energy each. The resulting photoelectron kinetic energies, $E^{SC}_{kin}(sub.)$ and $E^{SC}_{kin}(ads.)$, are referenced to the SC vacuum level E^{SC}_{vac} right outside its surface. The contact potential $\Phi^{contact} = \Phi^{SC} - \Phi^{D}$ is used to convert between sample and detector kinetic energies. Consequently, the experimentally accessible kinetic energies, measured by the detector, $E^{D}_{kin}(sub.)$ and $E^{D}_{kin}(ads.)$, depend on the detector work function Φ^D. b) The presence of a surface dipole δ modifies the SC vacuum level at the surface and all states directly bound to it, such as the adsorbate states including *E(ads.)*. The surface dipole and all energy levels changed by it are shown in red. Importantly, while near the SC surface $E^{SC}_{kin}(sub.)$ is affected by the surface dipole and $E^{SC}_{kin}(ads.)$ is unaffected, the situation is reversed for the measured kinetic energies where $E^{D}_{kin}(sub.)$ is constant and $E^{D}_{kin}(ads.)$ changes. This is due to $\Phi^{contact}$ being affected by δ. See text for more details.

dipole directly influences the SC vacuum level and all adsorbate energy levels, including $E(ads.)$ and consequently all associated quantities referenced to the constant E_F, i.e. Φ^{SC}, $\Phi^{contact}$, $E_{kin}^{SC}(sub.)$, $E_B(ads.)$, and $E_{kin}^{D}(ads.)$.

Crucially, while $E_{kin}^{D}(ads.)$ is affected by δ, $E_{kin}^{D}(sub.)$ is not.[111,112] Therefore, measuring TRXPS data of both, substrate and adsorbate, specifically shifts S in the photoelectron spectra of the substrate level $S\left[E_{kin}^{D}(sub.)\right]$ and adsorbate level $S\left[E_{kin}^{D}(ads.)\right]$, allows to isolate δ gaining quantitative insight into electric fields at the surface. To this end, $S\left[E_{kin}^{D}(sub.)\right]$ is used to establish a baseline from signatures that affect all sample energy levels equally, such as band bending changes. Note that broadening effects may lead to an apparent shift that differs from the actual band bending which needs to be isolated as described in section 4.4. Any differential shift

$$\Delta S = S\left[E_{kin}^{D}(ads.)\right] - S\left[E_{kin}^{D}(sub.)\right] \qquad (8)$$

observed in adsorbate TRXPS data after correcting for the band bending baseline, constitutes an interfacial potential drop (IPD) represented by δ in Figure 12. In the case of the N3-ZnO experiment, photoexcitation leads to a transient δ consisting of a hole remaining on the adsorbate and an electron injected into the ZnO substrate. In a first order approach, the screening of the injected electron within the SC can be approximated as metal-like. This leads to an effective dipole distance that is insensitive to the exact position of the injected electron within the substrate. As previously shown for static interfacial fields,[84] the IPD can be described as a voltage drop across a parallel plate capacitor when assuming (locally) flat surfaces. In this model, the electric field is

$$E = \Delta S / d_{IPD} \, , \qquad (9)$$

where d_{IPD} is the distance between the idealized plates, i.e. the SC surface and the adsorbate hole. The general relation valid for all capacitors

$$C = Q / \Delta S \, , \qquad (10)$$

where Q is the stored charge, ΔS the voltage drop, and C the capacitance, can be combined with the parallel-plate capacitor relation

$$C = \varepsilon_0 \varepsilon_r A / d_{IPD} \, , \qquad (11)$$

where ε_0 is the vacuum permittivity, ε_r the relative permittivity of the medium between the two plates, and A the area of each individual plate, to calculate the dipole distance as

$$d_{IPD} = \Delta S \varepsilon_0 \varepsilon_r A/Q = \Delta S \varepsilon_0 \varepsilon_r/\rho \ , \tag{12}$$

where ρ is the surface charge density $\rho = Q/A$. As the idealized plates consist of individual dipoles that interact with each other,[84] a correction factor, is introduced such that

$$d_{IPD} = \left(1 + f_{dep}\right) \Delta S \varepsilon_0 \varepsilon_r A/Q = \left(1 + f_{dep}\right) \Delta S \varepsilon_0 \varepsilon_r/\rho \ , \tag{13}$$

where f_{dep} is the depolarization factor. For a square array of uniformly arranged charge pairs it is given by $f_{dep} \cong 9\alpha(\rho/e)^{3/2}/(4\pi\varepsilon_0)$,[84] where α is the polarizability of the adsorbed molecules and e is the elementary charge. The surface charge density can be defined as

$$\rho = P_{ex}\, P_{in}\, \rho_M = \sigma_{ads}(\lambda_{laser})\, N_{ph}\, P_{in}\, \rho_M, \tag{14}$$

where P_{ex} is the adsorbate excitation probability, which is the product of the laser wavelength dependent absorption cross-section of the adsorbate $\sigma_{ads}(\lambda_{laser})$ and the number of photons per laser pulse per unit area N_{ph}, P_{in} is the likelihood of electron injection following excitation, and ρ_M is the number of adsorbed molecules per surface area. Inserting eq. (14) into eq. (13) yields a dipole distance of

$$d_{IPD} = \left(1 + f_{dep}\right) \Delta S \varepsilon_0 \varepsilon_r / \left(\sigma_{ads}(\lambda_{laser})\, N_{ph}\, P_{in}\, \rho_M\right) . \tag{15}$$

Within this model, the position of the photoinduced adsorbate charge with respect to the substrate surface, their area density, as well as the interfacial electric field are quantitatively accessible through shifts in X-ray photoelectron spectra.

4.2 Laser-Induced Heating in Pump-Probe Experiments

Studying excited electronic states using pulsed lasers introduces the side effect of depositing thermal energy in the sample as a consequence of electronic relaxation following the optical excitation. In the case of SCs, the mechanism determining the timescale of electron relaxation is generally carrier-phonon coupling[113,114] often described by the two-temperature model.[115–117] An exception is faster relaxation due to carrier-carrier scattering[114,118] caused by high carrier densities. In any case, electron-phonon coupling is determining the onset of increasing lattice temperatures typically in the picosecond regime.[114] However, the coupling strength varies significantly for different samples and is often found to positively correlate with laser fluence.[119–121] For example, Graphene has an electron phonon-coupling time of tens of fs,[122] single-walled carbon nanotubes of 10-400 fs,[123,124] Si of

60 fs,[64] Gold NPs,[119,125] nanorods,[126] thin films,[127,128] and bulk[129] exhibit timescales of ~500-800 fs, copper 1 ps,[120] WSe_2 of 1.83 (and 19) ps,[130] and bismuth(111) of 5-6 ps.[131] As a rule of thumb, thermal effects should be checked for in experiments with 10 fs and slower time resolution, while single femtosecond and faster time-resolved experiments, should generally not be directly affected.

Time-resolved experiments with non-replenishing samples may show thermal signatures if the time between consecutive pump pulses is shorter than the time required for the sample to dissipate the deposited thermal energy. For replenishing samples, such as solid-state samples scanned using a manipulator or particles suspended in liquid jets, the sample scanning/jet speed v_{sample}, laser repetition rate f_{rep} and laser spot size (diameter) d_{laser} in the direction of sample movement determine whether two consecutive laser pulses will hit the same sample spot/particle via $f_{rep} \geq v_{sample}/d_{laser}$. Strictly speaking, in the case of liquid jets, the particle diameter should be added to the laser diameter, however it is usually several orders of magnitude smaller than the laser spot size and can be omitted. Typical parameters for experiments described in this thesis are sample scan speeds on the order of 100 μm to 1 mm per second, laser spot sizes of around 100 μm and laser repetition rates of 100 kHz. Therefore, 10^4 to 10^5 laser pulses will hit any given sample spot and thermal considerations become highly relevant.

It is worth noting that even for condensed matter experiments with ideal parameters regarding thermal effects these considerations should not generally be cast aside: In liquid jet experiments v_{sample} can reach 100 m/s,[132] making the cutoff for f_{rep} = 1 MHz assuming d_{laser} = 100 μm. Currently the field of high harmonic generation is still dominated by Titanium:Sapphire based ultrafast lasers operating far below this threshold, usually in the kHz regime. However, the push to ever higher data acquisition rates requires higher repetition rates which are available via fiber[133] and thin disk[134,135] lasers and have been used for high harmonic generation.[136–140] Noteworthy examples are a 10.7 MHz, 31 fs pulse duration, 76 W average power system for high harmonic generation at 27.7 eV,[136] a 20.8 MHz system producing up to the 17th harmonic of a 1030 nm central wavelength, 35 fs pulse duration pump with 20 W average power,[139] and an Ytterbium based system with 154 MHz repetition rate using a driving laser with 120 fs pulse duration and 80 W average power.[140] The situation is similar for cutting edge X-ray free electron lasers where most free-electron lasers currently operate in the kHz regime, but next generation facilities aim at the 100 kHz to MHz regime. The European XFEL already has a MHz intra-bunch repetition rate despite its overall 27 kHz repetition rate. To fully exploit these gains in repetition rate, the pump laser repetition rate is required to match the rate of the probe pulse. Once the threshold of more than one laser pulse per individual particle is exceeded in liquid jet experiments the subsequent thermal relaxation can be expected to be slower compared to bulk solid-state samples as the thermal conductivity of the liquid surrounding the absorbing particle is small. At normal pressure and T = 25 °C, water e.g. has a thermal conductivity of 0.6062 $\mathrm{Wm^{-1}K^{-1}}$, acetone of 0.161 $\mathrm{Wm^{-1}K^{-1}}$, ethanol of 0.167 $\mathrm{Wm^{-1}K^{-1}}$, and methanol of 0.202 $\mathrm{Wm^{-1}K^{-1}}$,[141] whereas metals and SCs typically have values that are approximately two to three orders of magnitude higher.

Thermal effects are rarely discussed in (ultrafast) pump-probe experiments even though comparatively moderate fluences/pulse energies can be expected to lead to significant temperature jumps within the sample. To demonstrate this, the laser-induced temperature jump ΔT is estimated for the transition metal oxides α-Fe_2O_3 (hematite), Cu_2O, CuO, ZnO and anatase TiO_2. Assume a laser pulse with photon energy E_{photon} is incident onto the sample as depicted in Figure 13a. Neglecting defect states located within the bandgap, $E_{photon} > E_{gap}$ is necessary for photon absorption within the sample material as shown in the inset on the left in Figure 13. The volume for which the temperature jump is calculated is a cylinder with the circular cross section of $\pi/4\cdot(\mathrm{FWHM})^2$, where FWHM is the full-width-at-half-maximum of the symmetric laser spot on the

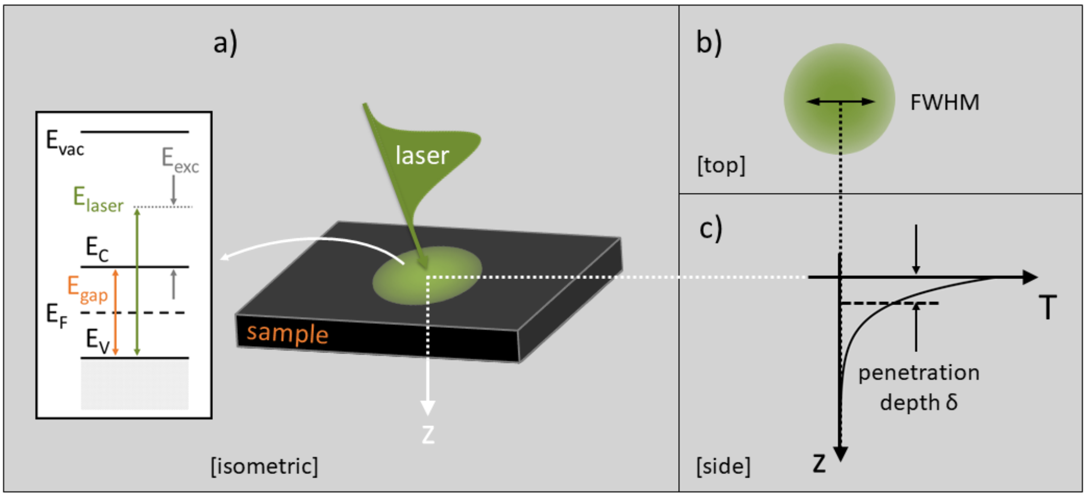

Figure 13: Overview of relevant parameters for laser-induced sample heating. a) Schematic of a laser pulse incident on a SC sample. b) Top view of the circular laser pulse indicating its FWHM spot size on the sample surface. c) Side view showing the amount of deposited heat $Q(z)$, as a consequence of absorbed laser light, as a function of depth z. The penetration depth δ is the 1/e value of the depth-dependent laser intensity as it propagates along z. The inset on the left shows the relevant energies, specifically the bandgap (E_{gap}), laser photon (E_{photon}), and maximum photonic excess energy above the bandgap $E_{\mathrm{exc}} = E_{\mathrm{photon}} - E_{\mathrm{gap}}$.

sample surface (Figure 13b). The depth of the cylinder is chosen as the laser wavelength-dependent penetration depth δ_{laser} (Figure 13c). The intensity of the laser light as a function of depth z within the material follows the Beer-Lambert law $I_{laser}(z) = I_0\exp[-z/\delta_{laser}(\lambda)]$. As the amount of absorbed intensity is proportional to the derivative of the intensity itself (dI/dz), it is proportional to the same exponential profile as the intensity. Consequently, the deposited heat energy $Q(z)$ and temperature differential $\Delta T(z)$ are also proportional to $I_{laser}(z)$ as is shown in the side view in Figure 13c. To get a general sense of the magnitude of the laser heating effect, the average laser-induced temperature jump is calculated within the cylinder described above. The total amount of deposited heat within the volume $Q_{cylinder}$ is connected to the temperature jump ΔT within the same volume via

$$Q_{cylinder} = m \cdot C \cdot \Delta T\ , \tag{16}$$

where m is the mass and C is the specific heat capacity of the material. Using the definition of density $\rho = m/V$ and the dimensions of the cylinder described above yields

$$Q_{cylinder} = V \cdot \rho \cdot C \cdot \Delta T\ = \frac{\pi}{4}(FWHM)^2 \cdot \delta \cdot \rho \cdot C \cdot \Delta T\ . \tag{17}$$

Because of the lateral two-dimensional Gaussian beam profile and the exponential decay from the surface (z = 0) into the bulk of the laser intensity and therefore also of $Q(z)$, the heat deposited within the cylinder simplifies to

$$Q_{cylinder} = \iint_{FWHM} \int_0^{\delta} Q(z,A)\, dz\, dA = \frac{1}{2}\int_0^{\delta} Q(z)\, dz = \frac{1}{2}\frac{e-1}{e} Q_{total}\ , \tag{18}$$

where Q_{total} is the total heat deposited by the laser. Combining eq. (17) and (18) yields the laser-induced temperature jump as

$$\Delta T = \frac{2}{\pi}\frac{e-1}{e}\frac{Q_{total}}{(FWHM)^2 \cdot \delta \cdot \rho \cdot C}\ . \tag{19}$$

Two extreme cases for the relation between Q_{total} and the laser pulse energy E_{pulse} can be considered, concerning electron relaxation from the CB minimum to the VB maximum. Minimal laser-induced heat deposition (ΔT_{min}) occurs for radiative electron hole recombination. In this case, E_{exc} (see inset Figure 13) is the only contributor to laser-induced sample heating. On the other hand, maximum heat deposition (ΔT_{max}) is the consequence of a fully non-radiative electron hole recombination over the bandgap leading to

$$Q_{total,min} = \frac{E_{photon} - E_{gap}}{E_{gap}} \cdot E_{pulse} \tag{20}$$

and

$$Q_{total,max} = E_{pulse}\ . \tag{21}$$

The respective temperature jumps

$$\Delta T_{min} = \frac{2}{\pi}\frac{e-1}{e} \cdot \frac{E_{photon} - E_{gap}}{E_{gap}} \cdot \frac{E_{pulse}}{(FWHM)^2 \cdot \delta \cdot \rho \cdot C} \tag{22}$$

and

$$\Delta T_{max} = \frac{2}{\pi}\frac{e-1}{e} \cdot \frac{E_{pulse}}{(FWHM)^2 \cdot \delta \cdot \rho \cdot C} \tag{23}$$

are the two extreme cases for the mean temperature jump in the cylindrical volume defined by laser penetration depth and FWHM of the laser. Table 1 contains the necessary material parameters, i.e. bandgap (E_{gap}), density (ρ), specific heat (C) and penetration depth (δ) for 355 nm (top row in each field) and 532 nm (bottom row) laser excitation, and the results for laser-induced temperature jumps for the two cases ΔT_{max} and ΔT_{min}. In these latter two columns the top rows refer to the λ = 355 nm case and bottom rows to λ = 532 nm, where E_{photon} and δ are adjusted accordingly. Ranges of values, indicated by "-" within a row, account for varying literature bandgap values. For ease of scaling the results to specific experimental parameters the estimates are based on 100 mW laser power assuming a spot size of 100 × 100 µm^2 and a laser repetition rate of 100 kHz. These parameters correspond to a pulse energy of 1 µJ and a fluence of 12.7 mJ/cm^2. The estimates assume instant deposition of the laser energy, i.e. an infinitesimally short laser pulse and no reflection of the laser pulse on the sample surface. The resulting ΔT values in the last two columns of Table 1 can be used to estimate the magnitude of any expected temperature-induced effects such as described for TRXAS on CuO in detail in section 5.3.

Additional potentially irreversible effects are (partial) melting of the sample and other phase changes. As these effects play no role in the presented CuO study, they will only be discussed briefly. The melting point of the individual transition metal oxides is given in the second column as a boundary to compare ΔT values to. Note that surface melting is expected to start at lower temperatures than the literature (bulk) melting points[157] and that the curvature of NPs lowers the onset of melting.[158] Phase changes can occur in α-Fe_2O_3,[159] Cu_2O and CuO,[160] ZnO,[161] and TiO_2,[162]

Table 1: Temperature jumps ΔT following laser excitation with 355 nm or 532 nm wavelength light in selected transition metal oxides assuming a 100 mW laser pulse with a 100 kHz repetition rate and Gaussian beam with FWHM spot size of 100 × 100 μm^2. The relevant material parameters bandgap (E_{gap}) at room temperature (RT), density (ρ), specific heat (C) and penetration depth (δ) for laser excitation with 355 nm (top row in each field) and 532 nm (bottom row) light are provided. ΔT_{max} and ΔT_{min} refer to conversion of the entire photon energy and excess photon energy above bandgap, respectively. Ranges, indicated by "-" within a row, account for different literature bandgap values. See text above for details on the calculation of ΔT_{max} and ΔT_{min}. Literature references are provided in square brackets.

Material	**Melting point [°C]**	**E_{gap} (at RT) [eV]**	**Density ρ [g/cm^3]**	**$C(T)$ (T=300K) [J/mol/K]**	**δ [nm] {355nm} {532nm}**	**ΔT_{max} [K] {355nm} {532nm}**	**ΔT_{min} [K] {355nm} {532nm}**
α-Fe_2O_3	1565[141]	2.2[142] indirect	5.25[141]	104.2[149]	23.9[154] 105.8	491.4 111.0	182.5 6.2
Cu_2O	1235[141]	2.1[143,144]	6.0[141]	62.7[150]	22.6[146] 352.8	677.1 43.4	270.9 4.3
CuO	1446[141]	1.9[145] 1.2[146]	6.31[141]	42.4[151]	21.2[146] 124.5	564.3 96.1	257.9-370.8 17.7-46.6
ZnO	1975[141]	3.4[147] 3.2[141]	5.6[141]	41.1[152]	470.8[155] 5291.9	30.2 2.7	0.9-2.6 -
TiO_2 Anatase	1843[141]	3.0[148] indirect	4.23[141]	55.4[153]	478.8[156] -	28.6 -	4.1 -

depending on temperature and the available partial oxygen pressure surrounding the sample, via release of oxygen from the lattice effectively changing the metal to oxygen ratio. In the case of TiO_2 the conversion from Anatase to Rutile is another effect to consider.[163]

Generally, larger photon energies and shorter penetration depths will lead to higher ΔT within the pumped sample volume. This effect is especially pronounced for λ = 355 nm in α-Fe_2O_3, Cu_2O and CuO. On the other hand, matching the photon energy to the sample bandgap, combined with large penetration depths and a radiative decay (ΔT_{min}) produces minimal temperature jumps, as can be seen for λ = 355 nm in ZnO and TiO_2. The effect of matching photon energy and bandgap, specifically, leads to a large relative discrepancy between ΔT_{max} and ΔT_{min}. ZnO and TiO_2 are practically transparent to λ = 532 nm light as the photon energy (2.33 eV) is smaller than their bandgaps.

This estimate is fully applicable to bulk solid-state materials. For NPs with a diameter comparable to or smaller than the penetration depth, the temperature jump will be smaller as the laser pulse will not be fully absorbed in the NP. However, it should also be noted that averaging within a depth ranging from the surface to the penetration depth underestimates ΔT at the surface. Similarly, the averaging in lateral direction underestimates ΔT at the center of the laser spot. Beyond melting or other phase changes it depends on the individual experiment whether laser-induced temperature jumps will create a signature in the probe signal. The result of jumps of up to hundreds of degrees Kelvin as a result of relatively moderate laser parameters of 1 µJ pulse energy distributed over a 100 x 100 μm^2 FWHM spot underlines the relevance of these considerations. High repetition rate experiments are expected to be especially sensitive as well as experiments with a time-resolution not significantly smaller than the electron-phonon coupling timescale of the sample.

In principle, temperature changes can also lead to a (de-)population of (donor) acceptor states depending on their respective energy separation from the (conduction) valence band. In this context, laser-induced heating may potentially experimentally resemble a laser-induced electronic excitation of electrons from donor states into the CB or from the VB into acceptor states. This is relevant for ultraviolet and X-ray photoelectron spectroscopies. A temperature-dependent number of free charge carriers also potentially affects microwave conductivity, THz, and IR probes directly or indirectly via changes in the sample conductivity.

4.3 Transport and Dissipation of Laser-Induced Heat in Solids

This section describes the mechanisms of heat transport following the initial energy deposition by the laser in a solid-state sample. Generally, the transport of thermal energy away from a solid surface is possible via heat convection through fluids in contact with the solid surface, heat radiation emitted from the surface, and heat conduction within the solid itself, as well as through dissipation via a phase change of the solid.

Heat convection in gases that are in contact with the sample surface is mediated by temperature differences within the gas. The associated density differences in turn lead to a material flow from high to low density regions effectively transporting thermal energy. A necessary precondition for this is the collision of gas atoms or molecules with each other. In this context, the mean free path between collisions λ_{MFP} for three different kinds of flow regimes can be distinguished relative to the diameter of the experimental vacuum chamber $d_{chamber}$. In the viscous or continuous flow regime ($\lambda_{MFP} < d_{chamber}$),[164] pressures of >1 mbar of air lead to significant absorption of soft X-rays and therefore, experiments are usually not feasible in this regime. Ambient pressure experiments investigating gas-solid and liquid-solid interfaces are typically conducted at pressures between 1 and 10^{-3} mbar and fall into the Knudson flow regime ($\lambda_{MFP} \approx d_{chamber}$),[164] where the thermal conductivity of gases is significantly changed.[164] Most X-ray experiments, including the ones presented here, are carried out in ultra-high vacuum (UHV). At pressures of $<10^{-7}$ mbar, the particle flow is in the molecular regime ($\lambda_{MFP} \gg d_{chamber}$)[164] with a $\lambda_{MFP} > 10^3$ m effectively rendering the mechanism of heat convection negligible.[164]

Heat radiation requires neither a surrounding medium nor a temperature differential between two bodies and is therefore always present. The radiative heat loss can be estimated by computing the radiation of a black body via the Stefan-Boltzmann law

$$\mathrm{P} = \sigma \cdot \mathrm{A} \cdot \mathrm{T}^4 \,, \tag{24}$$

where P is the total radiated power, $\sigma = 5.67 \cdot 10^{-8}\ \mathrm{Wm^{-2}K^{-4}}$ is the Stefan-Boltzmann constant, A is the surface area, and T is the surface temperature. Using the numbers from Table 1 and taking into account that temperatures directly at the surface are higher than these estimates, T = 1000 °C is assumed for an order of magnitude estimate of the total radiated energy of a sample following laser excitation. The respective total radiated power is ~149 kW/m^2 or 1.17 mW from a circular 100 × 100 µm^2 area representing the FWHM laser spot size. As a time window to compute the total amount of radiated energy in, 100 ns is chosen as most of the amplitude of laser-induced TRXAS effects decayed at this point (see Fig. 3 of section 5.3 or ref. 165). However, within the first 100 ns the emitted energy is equal to $1.17 \cdot 10^{-10}$ J. Therefore, compared to an overall laser pulse energy of 1 µJ, the fraction of radiated energy is equal to $\sim 10^{-4}$ which can be neglected, in our case, as the experimental sensitivity is in the low percent regime.

Phase changes, as discussed above, are irreversible and would therefore alter any spectra acquired in a straightforward and noticeable way. This was observed in temperature-resolved measurements on CuO used to calibrate the TRXAS results presented in section 5.3. At temperatures around 200 °C and above, the CuO surface was first partially then fully converted to Cu_2O. The monitored O1s XAS of CuO and Cu_2O are markedly different.[104] Therefore, only temperature-resolved XAS spectra up to 145 °C were used in the presented study in section 5.3. These kinds of effects were also continuously checked for and excluded for the CuO sample during TRXAS data collection.

Consequently, heat conduction is the only relevant contribution to thermal dissipation in UHV experiments discussed in the framework of this thesis. Heat dissipation in solids is described by the heat equation. It is mathematically identical to Fick's 2nd law generally describing diffusion phenomena:

$$\frac{\partial Q}{\partial t} = \nabla(k\nabla Q)\,, \tag{25}$$

where Q is the heat distribution in the material as a function of location $\vec{\mathrm{x}}$ and time t, and k is the thermal conductivity. As the material density and the thermal conductivity as a function of location are constant, the equation simplifies to

$$\frac{\partial Q}{\partial t} = k\Delta Q\,, \tag{26}$$

where $\Delta = \nabla^2$ is the Laplacian. While analytical solutions can be found for certain, relatively simple starting conditions of Q, in more complex cases the evolution of Q can be found numerically by solving eq. (26) iteratively for small increments of t.[166] In the case of heat dissipation after laser-induced heating in the context of pump-probe experiments, the starting conditions can be simplified from the general, multi-dimensional case. The temperature profile immediately following exposure to a Gaussian laser pulse is exponential along the surface normal z and Gaussian in radial directions. As optical and X-ray penetration depths are in the nanometer range and beam sizes typically in the micrometer range, the shape of the pumped and probed sample volumes usually resemble the shape of a disk. Laterally, the pump pulse is typically adjusted to be significantly larger than the probe pulse to create an approximately homogeneous excitation density within the probe pulse area. Therefore, the lateral temperature profile in the probed area is relatively constant and decays much slower compared to the surface normal direction z. Consequently, heat conduction can be estimated as a one-dimensional diffusion process along z within an insulated cylinder (ignoring lateral heat loss) by[167–169]

$$\frac{\delta Q(t,z)}{\delta t} = -k \cdot A\frac{\delta T(t,z)}{\delta z}\,, \tag{27}$$

where $\delta Q(t,z)$ is the amount of thermal energy transferred through a cross-sectional area A per time δt, k is the thermal conductivity, and T the depth- and time-dependent temperature profile. In general, the thermal conductivity of a material varies as a function of temperature, but for many practical applications with limited temperature ranges, such as in the experiment presented here, it may be approximated as constant.

The temperature distribution at time zero $T(t=0,z)$ is proportional to the derivative of the depth-dependent laser intensity $I_{laser}(z)=I_0\exp(-z/\delta_{laser}(\lambda))$, where δ_{laser} is the laser penetration depth. The amplitude of the resulting exponential function is the initial temperature increase after laser excitation at the surface $\Delta T(t=0,z=0)$ which leads to the following temperature profiles. Non-radiative recombination across the bandgap leads to a maximally observable temperature profile of

$$T_{max}(t=0,z)=\frac{\left(1-R(\lambda)\right)\cdot E_{pulse}}{2\cdot\rho\cdot A\cdot C(T)\cdot\delta_{laser}(\lambda)}\cdot e^{-\frac{z}{\delta_{laser}(\lambda)}}+T_{ref}\ , \qquad (28)$$

while radiative recombination across the bandgap leads to the minimal temperature profile of

$$T_{min}(t=0,z)=\frac{\left(1-R(\lambda)\right)\cdot E_{pulse}}{2\cdot\rho\cdot A\cdot C(T)\cdot\delta_{laser}(\lambda)}\frac{E_{photon}-E_{gap}}{E_{photon}}\cdot e^{-\frac{z}{\delta_{laser}(\lambda)}}+T_{ref}\ . \qquad (29)$$

Here $R(\lambda)$ is the sample reflectivity, E_{pulse} is the laser pulse energy, E_{photon} is the photon energy, E_{gap} is the SC bandgap, $\delta_{laser}(\lambda)$ the 1/e laser penetration depth, ρ the sample density, A the FWHM laser spot size and $C(T)$ the specific heat capacity. The sample equilibrium temperature T_{ref} is added to the laser induced temperature jump to convert to an absolute temperature scale $T(t=0,z)$. Any recombination of partly radiative and partly non-radiative decay across the bandgap would lead to a temperature profile with an amplitude between T_{max} and T_{min}.

4.4 Depth Resolution via Decomposition of Pump-Probe Spectral Signals

The effects of a laser-induced perturbation can potentially be probed with depth-resolution if the length scale of the perturbation is matched by the surface sensitivity of the probe scheme. For the two experiments described in this thesis this is the case: In the TRXAS study on CuO the penetration depth of the laser determines the length scale of the temperature gradient along the surface normal of the sample. The effective probing depth of the oxygen K-edge X-ray absorption measurement in fluorescence yield mode matches the temperature gradient on a ~100 nm scale. In the TRXPS experiment on N3-ZnO, the spatial extent of the ZnO bending matches the IMFP of the detected photoelectrons on the ~1 nm scale. An additional necessary prerequisite is a sufficiently large magnitude of the temperature and band bending induced effects in the TRXAS and TRXPS spectra, respectively. If all these prerequisites are met, a general framework to extract depth-resolved information can be utilized.

This framework consists of a spectral deconvolution of the detected probe signal into contributions originating from different depths z_n. The detected spectrum $S_d(E, t = t_i)$ at a certain pump-probe delay t_i can be approximated by a modelled spectrum $S_m(E, t = t_i)$ via a linear combination

$$S_m(E, t = t_i) = \sum_{n=0}^{N} F_{ph}(E, \mathrm{par}[t_i, z_n]) \cdot X_{abs}(z_n) \cdot D_{out}(z_n)\,, \tag{30}$$

where $F_{ph}(E, \mathrm{par}[t_i, z_n])$ describes the spectral shape of contributions from depth z_n, E is the energy axis of the spectrum, i.e. its independent variable, $\mathrm{par}[t_i, z_n]$ are modelling parameters, $X_{abs}(z_n)$ the amount of absorbed X-ray intensity at depth z_n relative to the total incident X-ray intensity, and $D_{out}(z_n)$ the amount of probe signal originating from depth z_n that escapes the sample and is detected, i.e. not absorbed or scattered, relative to the emitted amount of probe signal from depth z_n. The depth-dependent X-ray intensity $I_X(z)$ is given by the Beer-Lambert law: $I_X(z) = I_{X,0} \cdot e^{-\delta(h\nu)z}$, where $I_{X,0}$ is the incident X-ray intensity, $\delta(h\nu)$ is the X-ray energy dependent penetration depth and z is the depth coordinate along the surface normal. The absorbed X-ray intensity at depth z is equal to $-d/dz\, I_X(z) = \delta(h\nu) \cdot I_{X,0} \cdot e^{-\delta(h\nu)z}$ such that the absorbed intensity relative to the incident intensity is $X_{abs}(z = z_n) = \delta(h\nu) \cdot e^{-\delta(h\nu)z}$. $D_{out}(z_n)$ depends on the type of probed signal. Both, $X_{abs}(z_n)$ and $D_{out}(z_n)$ implicitly contain the incident and exit angle with respect to surface normal, respectively. This applies for well-defined flat sample surfaces whereas for nanocrystalline samples angles may vary considerably throughout the probe pulse depending on the local surface topology.

In the case of the time- and temperature-resolved XAS method, $F_{ph}(E, \mathrm{par}[t_i, z_n])$ is the temperature-dependent XAS spectrum, E the incoming X-ray energy, $\mathrm{par}[t_i, z_n]$ are the initial surface temperature and the thermal conductivity. Figure 14a shows an exemplary temperature profile in CuO immediately after a 532 nm laser pump leads to a transient 100 °C temperature differential in the surface region with a 28 °C sample equilibrium temperature. The dashed vertical line at 124.5 nm corresponds to the laser penetration depth at 532 nm.[146] Colored vertical lines at 0, 50, 100 and 500 nm indicate the depths of exemplary temperature-dependent O K-edge XAS data, i.e. $F_{ph}(E, \mathrm{par}[t_i, z_n])$, shown with the same color code in Figure 14b. The inset displays the

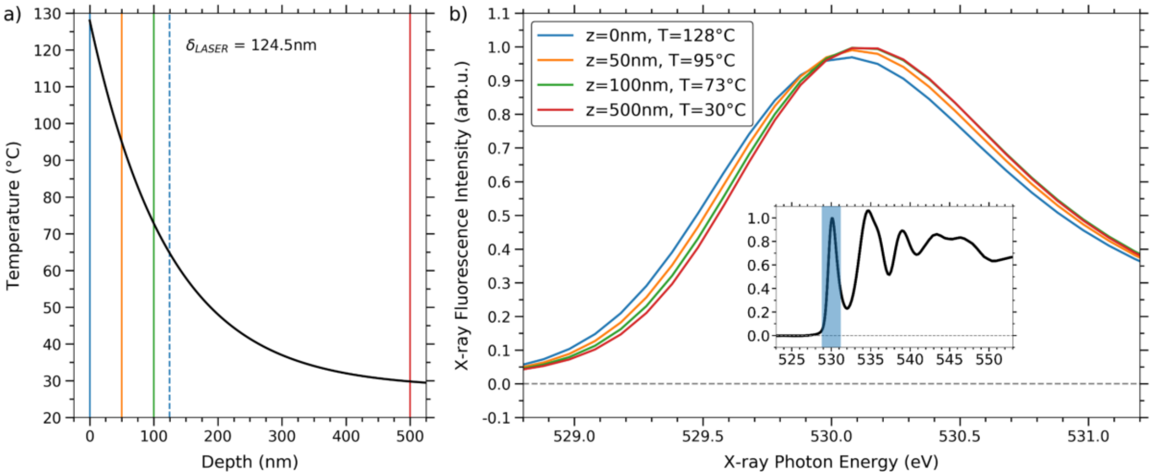

Figure 14: Components of the temperature- and time-resolved XAS modeling. a) Calculated temperature profile in CuO induced by laser heating at time zero. The dashed vertical line at the penetration depth of 124.5 nm for 532 nm laser light represents the 1/e value of the 100 °C temperature differential added to a 28 °C equilibrium sample temperature. Colored, solid vertical lines at surface (z = 0) and depths of 50, 100 and 500 nm correspond to XAS temperature profiles shown in b) with the same color code. The entire recorded O K-edge CuO X-ray absorption spectrum is shown in the inset with the blue background indicating the energy window of the first resonance shown in the main figure b).

complete recorded XAS spectrum at the equilibrium temperature with the blue background highlighting the X-ray energy region shown in Figure 14b. In the linear combination according to eq. (30), the temperature-resolved spectra are weighted with the product of $X_{abs}(z_n)$ and $D_{out}(z_n)$. If $I_{D,0}$ is the total amount of X-ray fluorescence originating from depth z directed towards the detector, then the fraction exiting the sample surface is $I_{D,0} \cdot e^{-\delta(h\nu)z}$, where $\delta(h\nu)$ is the X-ray energy dependent penetration depth. The iterative computation of the depth-dependent temperature profile for times t_i following the initial temperature distribution (Figure 14a) utilizes the heat dissipation model described in section 4.3.

The TRXPS experiment is sensitive to band bending in the SCL of the SC as contributions $F_{ph}(E, \text{par}[t_i, z_n])$ from different depths z are shifted in terms of photoelectron binding energy E according to the depth-dependent band bending. The fit parameters $\text{par}[t_i, z_n]$ are the width of the SCL and amplitude of the band bending which determine the amount of broadening and shift of the overall detected TRXPS spectrum. $D_{out}(z_n)$ (Figure 15a) is the likelihood of a photoelectron leaving the sample determined by its photon energy dependent IMFP. Typical X-ray penetration depths are large in comparison to the IMFP.[170] Therefore, X_{abs} barely varies within the range of depths producing detectable signal and eq. (30) can be simplified by neglecting X_{abs} for most XPS use cases. Figure 15b illustrates exemplary depth-dependent contributions to the overall spectrum for

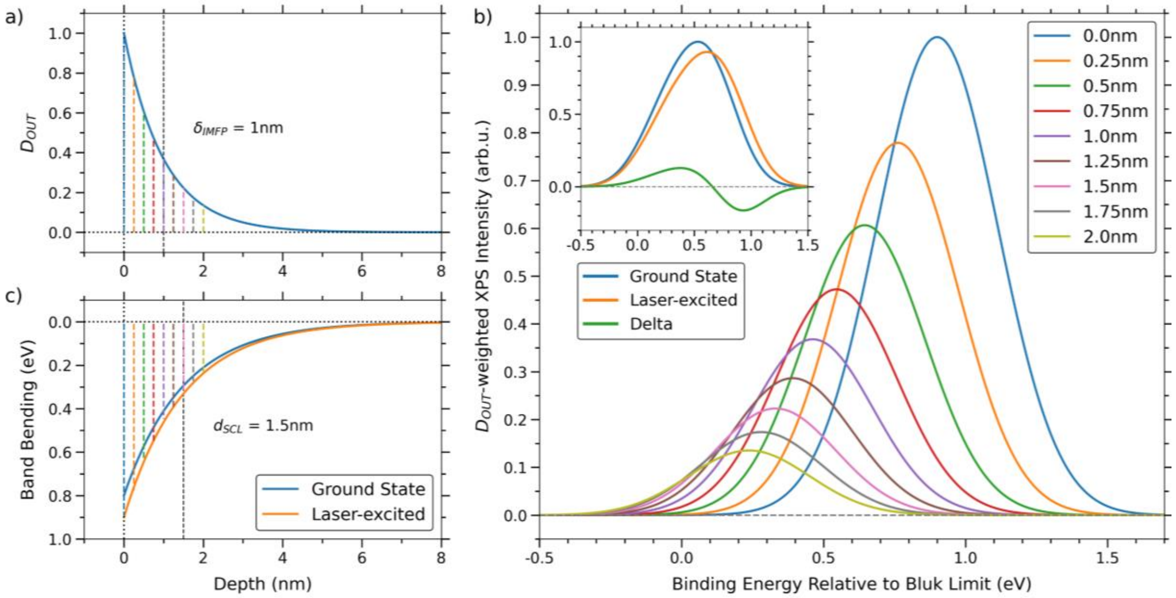

Figure 15: Overview of band bending-dependent and time-resolved XPS modeling: a) Likelihood of electron detection D_{out} as a function of depth with an exemplary 1/e value of 1 nm (IMFP, dashed line). b) Depth-dependent photoelectron contributions from first two nanometers from the sample surface in 0.25 nm steps. Individual contributions (area) are weighted by their IMFP-dependent D_{out}. Their depth-dependent center energy positions are determined by the band bending, shown in c), after laser excitation. The inset in b) shows results of linear combination of all depth-dependent contributions for the ground state (blue), laser-excited (orange), and their residual (green) spectrum that can be compared to acquired experimental data.

the first two nanometers from the surface in 0.25 nm steps. The different areas of the depth-dependent F_{ph} contributions are the result of weighting with the X-ray photoelectron detection likelihood D_{out}, an exponential function with a 1/e value equal to the IMFP. A value of 1 nm is assumed for the IMFP, representative of experiments in the soft X-ray regime. Generally, the IMFP is a function of the electron's kinetic energy and is routinely calculated using the TTP-2M model.[171,172] The F_{ph} spectral shape is equal to the XPS spectrum detected at flat-band condition. A Gaussian spectrum with a relatively narrow FWHM of 500 meV is assumed to be observed under flat-band conditions to clearly illustrate the depth-dependent spectral effects. The center binding energy positions of F_{ph} are determined by the laser-excited (orange) band bending shown in Figure 15c. Dashed vertical lines with the same color coding as in Figure 15b show the depth from which the photoelectrons are originating. The ground-state downward band bending (blue) has an amplitude of 790 meV with the laser-excitation adding another 100 meV (orange) as is the case for the TRXPS N3-ZnO study in section 5.2. The width of the SCL with a 1/e value of 1.5 nm also corresponds to the scenario of the nanocrystalline ZnO film studied. The zero position (dotted horizontal line) of the detected energy level position in Figure 15c is determined by its bulk limit and corresponds to the of the zero position of the photoelectron energy axis (vertical, dotted line in Figure 15b). The relatively large absolute band bending values and the relatively narrow flat-band spectra clearly illustrate the spectral shifting and broadening effects of the band bending to the overall spectra (inset in Figure 15b).[82]

The inset in Figure 15b shows the ground-state (blue) and laser-excited (orange), i.e. $S_m(E, t = t_i)$, spectra resulting from the described linear combination including depths up to 10 nm. In this case, spectral contributions were calculated in 0.05 nm steps. The difference spectrum (green), calculated by subtracting the laser-excited state from ground-state spectrum, includes features of both laser-induced broadening and shifting of the ground-state photoline. In particular, the effect of broadening is apparent from the amplitude difference between ground-state and laser-excited spectra. These modelled data S_m can be fit to experimentally detected data S_d by varying the band bending parameters $\mathrm{par}[t_i, z_n]$. The corresponding residual $RSS(t = t_i)$ represents the accuracy of this fit procedure for the data at pump-probe delay t_i.

In both cases, TRXAS and TRXPS, this fit procedure is repeated for all pump probe delays in order to create an aggregate residual sum square RSS over all times t_i (pump-probe delays) and energies E (in each individual spectrum)

$$RSS = \sum_{i=0}^{M} RSS(t = t_i) = \sum_{i=0}^{M} \int \left(S_d(E, t = t_i) - S_m(E, t = t_i)\right)^2 \mathrm{dE} \tag{31}$$

that is minimized until the fit converges. Notice that N, determining the maximal depth z_N, should be chosen large enough such that varying it does not significantly affect the outcome of the modelling procedure. The same holds for the granularity of the step size, i.e. the difference $z_n - z_{n-1}$, which can be varied as a function of depth according to the magnitude of spectral changes in F_{ph} in order to minimize the use of computational resources. Convergence of the fit provides the experimentally derived $\mathrm{par}[t_i, z_n]$ values, i.e. the initial surface temperature $T(t = 0, z = 0)$ and thermal conductivity k for the TRXAS method, and the SCL width d_{SCL} and SPV amplitude for TRXPS.

5 Results

5.1 Strong Potential Gradients and Electron Confinement in ZnO Nanoparticle Films: Implications for Charge-Carrier Transport and Photocatalysis

ZnO can be produced in a variety of different nanostructures.[173,174] It is used for catalysis,[175,176] sensors,[177,178] UV detectors,[179] and lasers.[180–182] Especially in sensing and (photo-)catalysis applications the effects of adsorbates on the electronic potentials of nanostructured ZnO surfaces play an important role. Ozawa and Mase have studied the adsorption of atomic hydrogen, water, and methane on crystalline ZnO surfaces using angle-resolved XPS.[56,57] The ability to resolve photoelectron spectra in k-space enables the isolation of e.g. hydrogen-induced modifications of the surface electronic structure. The Zn$(10\bar{1}0)$ and the polar oxygen terminated Zn$(000\bar{1})$ surface show an H-induced band that lies energetically below E_F pointing to surface metallization. The dispersion of these bands is parabolic in $k_\parallel$ with no dispersion in $k_\perp$. H-adsorbed Zn$(10\bar{1}0)$ and Zn$(000\bar{1})$ surfaces therefore represent a 2D electron gas (2DEG).[57] The Zn-terminated polar Zn(0001) surface on the other hand shows no surface metallization. Its surface Zn atoms are bound to three O atoms of the layer below. Adsorbed H atoms bind to these second layer O atoms, effectively replacing and removing the surface Zn atom. This process leads to Zn clusters which may absorb some of the charge introduced by H adsorption thus reducing the electron accumulation and original downward band bending.[57]

For the technologically more pertinent nanostructured ZnO the prevalent structure of their surfaces is not generally clear. While Zn$(10\bar{1}0)$ is the thermodynamically most stable ZnO surface, the large curvature of nanoparticles may lead to significantly increased defect densities. Studying the surface electronic structure of NPs via angle-resolved XPS is not feasible as nanostructured samples lack the necessary long-range order of single crystalline samples. However, band bending information is accessible by varying the surface hydroxylation and monitoring spectral changes of the Zn3d photoline. The spatial extent of the band bending is found to be ~6 nm. The depth-resolving data analysis method is enabled by varying the band bending as a function of adsorbate surface coverage and is described in section 4.4. Briefly, steeper band bending within the surface region of the SC leads to increased broadening of photoelectron spectra and smaller apparent shifts compared to the maximum potential energy changes at the surface. The approach of varying the band bending via an experimental parameter, such as the surface coverage by an adsorbate, is shown to be a useful method to extent the study of interfacial band bending to nanostructured materials.

The following publication is reprinted with permission from *ACS Appl. Nano Mater*. 2021, 4, 11, 12213–12221. Copyright 2021 American Chemical Society.

ACS APPLIED NANO MATERIALS

Strong Potential Gradients and Electron Confinement in ZnO Nanoparticle Films: Implications for Charge-Carrier Transport and Photocatalysis

Johannes Mahl, Oliver Gessner, Johannes V. Barth, Peter Feulner, and Stefan Neppl*

Cite This: *ACS Appl. Nano Mater.* 2021, 4, 12213−12221 Read Online

ACCESS | Metrics & More | Article Recommendations | Supporting Information

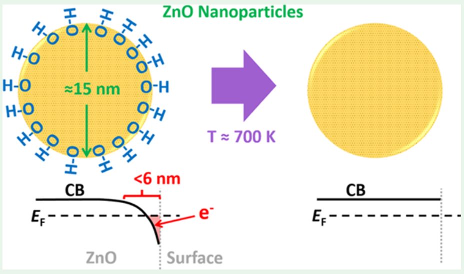

ABSTRACT: Zinc oxide (ZnO) nanomaterials are promising components for chemical and biological sensors and photocatalytic conversion and operate as electron collectors in photovoltaic technologies. Many of these applications involve nanostructures in contact with liquids or exposed to ambient atmosphere. Under these conditions, single-crystal ZnO surfaces are known to form narrow electron accumulation layers with few nanometer spatial penetration into the bulk. A key question is to what extent such pronounced surface potential gradients can develop in the nanophases of ZnO, where they would dominate the catalytic activity by modulating charge-carrier mobility and lifetimes. Here, we follow the temperature-dependent surface electronic structure of nanoporous ZnO with photoemission spectroscopy to reveal a sizable, spatially averaged downward band bending for the hydroxylated state and a conservative upper bound of <6 nm for the spatial extent of the associated potential gradient. This nanoscale confinement of conduction-band electrons to the nanoparticle film surface is crucial for a microscopic understanding and further optimization of charge transport and photocatalytic function in complex ZnO nanomaterials.

KEYWORDS: *nanoparticle films, zinc oxide, band bending, electron confinement, photoemission spectroscopy, surface metallization*

■ INTRODUCTION

Nanoscale zinc oxide (ZnO) attracts broad interest in fundamental research and for industrial applications, as it can be economically and sustainably synthesized in a vast variety of shapes, ranging from spherical particles, pillars, discs, and ribbons, to more complex and extended architectures such as tetrapods or cauliflowers.[1] This design flexibility is the main reason for its success in nanoelectronics, chemical/biological sensors, photocatalytic remediation, as well as energy conversion and storage schemes.[1−3] The crystalline phase, orientation, and aspect ratio in these nanostructures can further be tailored to meet specific application demands, facilitating rational device optimization.[4]

However, aside from these prospects, ZnO materials also exhibit a complex defect chemistry, which often complicates the prediction and microscopic interpretation of their function in electronic and catalytic applications.[1] For example, it is still controversial what types of impurities are responsible for its native n-type conductivity and what role these defect states play in mediating chemical reactions.[5−7] Most defects are formed preferentially near the surface and are therefore believed to dominate the electronic and catalytic response of metal-oxide nanomaterials. The electronic structure of ZnO interfaces is therefore governed by intrinsic and adsorbate-induced donor/acceptor states, which can disturb the local charge balance near the surface, giving rise to the formation of space charge layers (SCLs). The depth-dependent potential $V_{bb}(z)$ associated with this charge imbalance modifies all energy levels in the near-surface region of the semiconductor, commonly referred to as the "band bending" (bb) effect.[8] Depending on the characteristics of this bb, the resultant potential energy landscape can either be a driving force for efficient electron−hole pair separation or for the localization of one charge-carrier type near the surface, which are both critical gateways for boosting (photo-)chemical reaction yields.[8] In particular, the weaker photocatalytic performance of rutile TiO_2 single crystals compared to the anatase phase has been explained by the smaller surface bb present at rutile surfaces.[9] Although bb is beneficial for many applications, it is usually considered to be negligibly small in nanomaterials.[8,9] Here, we demonstrate that under hydroxylated conditions, sizeable bb can develop in nanostructured ZnO, which strongly impacts its interfacial electronic structure.

Many applications of ZnO nanostructures, especially in dye-sensitized photovoltaics, require the material to be in contact with liquids or involve exposure to ambient humidity.

Received: August 31, 2021
Accepted: October 29, 2021
Published: November 11, 2021

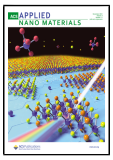

https://doi.org/10.1021/acsanm.1c02730

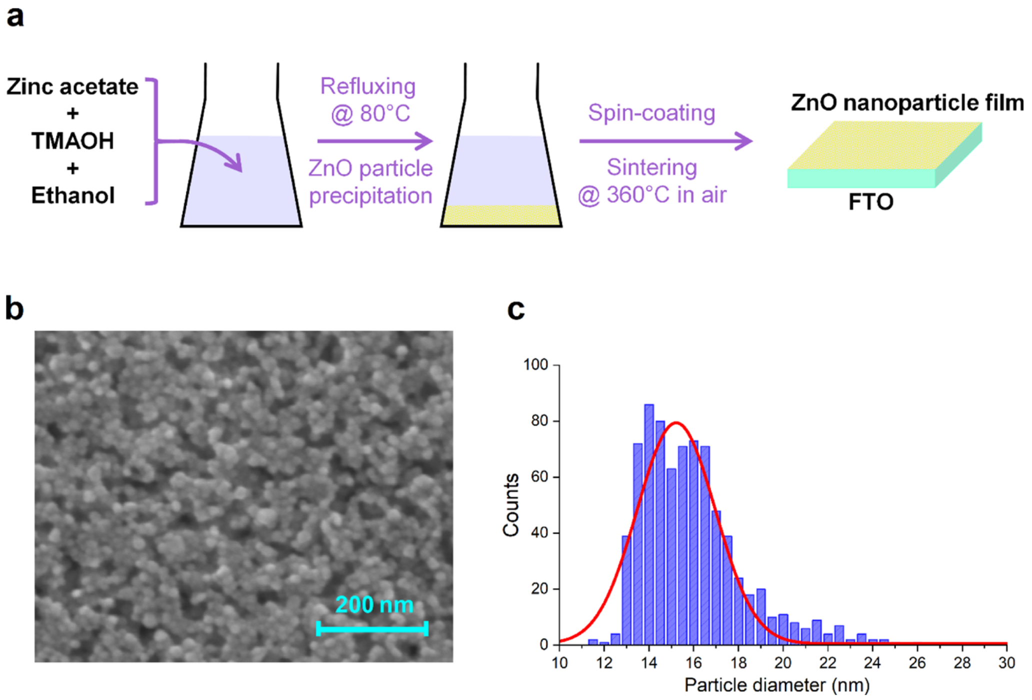

Figure 1. Preparation and characterization of the ZnO nanoparticle films. (a) Illustration of the ZnO nanoparticle film fabrication procedure (see the Experimental Section for details). (b) Typical SEM image of the ZnO nanoparticle films. (c) Typical particle size distribution extracted from the SEM images.

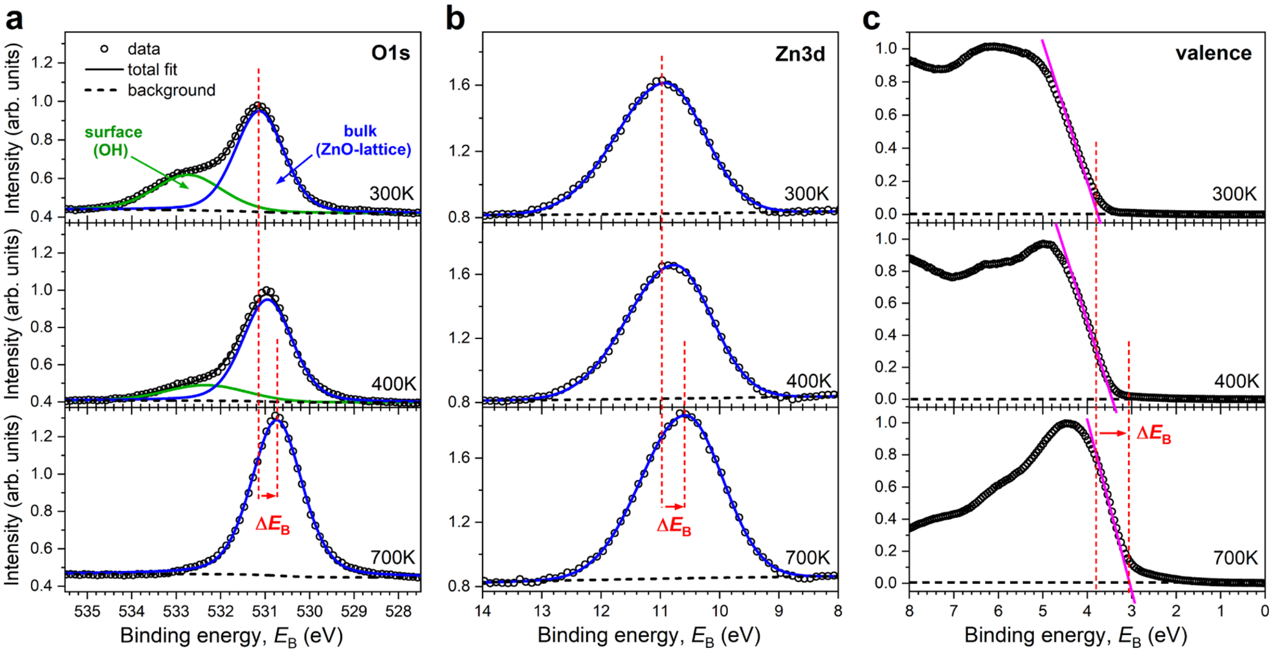

Figure 2. Temperature-dependent XPS and UPS spectra of a ZnO nanoparticle film. (a) O 1s XPS spectra obtained for the initially hydroxylated sample at 300 K (top) and after annealing to 400 K (middle) and 700 K (bottom) in UHV. The O 1s photoemission is decomposed into a ZnO-bulk (blue solid lines) and surface hydroxyl (OH) contribution (green solid lines). (b) Zn 3d XPS spectra. (c) UPS valence band spectra. The position of the valence band maximum (VBM) at the surface is determined by linear extrapolation of the low binding energy edge (magenta solid lines) to the baseline. UPS and XPS spectra are recorded with photon energies of $h\nu$ = 21.2 eV and $h\nu$ = 1253.6 eV, respectively. Red dashed lines highlight the temperature-induced shifts to lower binding energies (ΔE_B-O 1s: 470 meV; ΔE_B-Zn 3d: 380 meV; ΔE_B-VBM: 790 meV).

Extensive research on single-crystal ZnO has demonstrated that these conditions lead to a hydroxylation of the ZnO surfaces. The associated surface hydroxyl groups are mainly formed between ZnO surface oxygen atoms and intermediate protons generated, for example, during the dissociative adsorption of water, alcohols, or hydrogen.[10−19] They induce shallow donor states that easily release electrons into the ZnO conduction band (CB).[20−23] This adsorbate-mediated surface transfer doping generates positively charged donors at the surface, and accumulates negative charge within the SCL. The underling interfacial charge rearrangement leads to a downward bending of all energy levels near the surface, and may even trigger semiconductor-to-metal phase transitions when the CB minimum (CBM) is shifted below the Fermi level.[10,24,25]

Despite enormous research efforts, however, it remains unclear to what extent nanosized ZnO structures are able to accommodate significant interfacial potential gradients.[8,26,27] For ZnO nanomaterials exposed to different gases, or subject to different surface treatments, indications for both upward and downward bb have been reported, suggesting that the bb character results from the interplay between adsorbate−adsorbate and surface−adsorbate interactions.[14,28−33] Detailed, quantitative information on the polarity, magnitude, and shape of $V_{\mathrm{bb}}(z)$ under well-controlled conditions is therefore necessary to obtain a comprehensive understanding of the catalytic function of ZnO nanostructures on a microscopic level. Unfortunately, common spectroscopic techniques established for the characterization of extended, single-crystal semiconductors lack sensitivity to the shape of $V_{\mathrm{bb}}(z)$ as a function of the depth z below the surface, or yield ambiguous results when applied to nanoporous or amorphous samples.[8]

Here, we follow the temperature-controlled evolution of the near-surface electronic structure of ZnO nanoparticle films (∼15 nm average particle diameter) with X-ray photoelectron spectroscopy (XPS) and ultraviolet photoemission spectroscopy (UPS) under UHV conditions. The ZnO nanoparticle films are prepared via an established sol−gel method (see Figure 1)[34] and have previously been successfully used in the fabrication of ZnO-based dye-sensitized solar cells.[35,36] Our results provide conclusive evidence for a significant, ∼0.8 eV spatially averaged downward bb for the initially hydroxylated surface of the nanostructure, with a <6 nm maximum spatial penetration of the associated potential gradient into the bulk of the nanoparticle film. These findings are crucial for understanding and improving charge-carrier transport in interconnected metal-oxide nanoparticle networks and their (photo-) catalytic performance.

■ RESULTS AND DISCUSSION

Figure 2a compares O 1s XPS spectra acquired from the hydroxylated ZnO nanostructure, as loaded at room temperature (top panel), as well as after annealing to T_S = 400 K (middle panel) and to T_S = 700 K (bottom panel). The presence of surface OH-groups is verified by the high binding energy O 1s component at E_B = 532.7 eV (green).[12,13] The total O 1s photoemission is described by a pair of Gaussian peaks with fixed E_B separation (1.6 eV) and constrained full width at half-maximum (FWHM). Assuming a flat substrate, and taking the 2.3 Å average thickness of hydroxyl monolayers on low-index ZnO surfaces as a reference,[13,37] the 38% hydroxyl contribution to the total O 1s emission [in combination with the 1.57 nm inelastic mean free path (IMFP) of the O 1s photoelectrons[38] translates into an OH-coverage of ∼3 monolayers. Including the impact of the corrugated nanostructure surface on the relative O 1s XPS signal strengths within a single-sphere approximation leads to a ∼50% smaller estimate for the OH-coverage (see the Supporting Information).[39] Because both approximations yield OH coverages that are larger than the "saturation" coverage of one monolayer and the real surface topography of the ZnO nanoparticle films lies in between these limiting scenarios, the measured O 1s peak intensity ratio is fully consistent with a complete hydration of the sample surface at room temperature. Upon annealing to T_S = 700 K, the OH-related O 1s peak decreases below the detection limit, indicating the transition to a surface hydroxyl-free ZnO nanostructure. This threshold temperature range for complete OH removal is in good agreement with XPS results from both polar and nonpolar ZnO crystal surfaces,[12,13] temperature-dependent conductivity measurements,[40] and thermal desorption studies on ZnO powders.[41]

As indicated by the red dashed lines in Figure 2a,b, the loss of OH-groups is accompanied by rigid shifts of the O 1s and Zn 3d photoemission lines to lower E_B. The same trend is observed for the VBM as indicated by the UPS spectra in Figure 2c. The intersection of a linear fit to the leading edge of the VB photoemission and the instrument baseline yields a binding energy of $E_{\mathrm{VBM}}^{\mathrm{surf}}$ = 3.74 ± 0.02 eV for the VBM at the surface of the hydroxylated nanostructure (uncertainties are standard errors of several independent measurements). Note that this binding energy is significantly larger than the band gap E_g = 3.30 ± 0.01 eV of the nanoporous ZnO film (Figure S1, Supporting Information). Generally, for a nondegenerated n-type semiconductor, a scenario where $E_{\mathrm{VBM}}^{\mathrm{surf}}$ exceeds the material band gap is only compatible with a downward bending of the electronic bands near the surface (Figure S3, Supporting Information).[8] Thus, the combination of the large VBM binding energy relative to the Fermi level and the intrinsic n-type behavior of bulk ZnO[42] is an unambiguous signature for downward bb toward the surface of the nanostructure.[10−13] Annealing the sample shifts the VBM at the surface closer to the Fermi level, saturating at a minimum value of $E_{\mathrm{VBM}}^{\mathrm{surf}}$ = 2.95 ± 0.02 eV for $T_S \gtrsim$ 600 K.

Figure 3 summarizes the temperature-dependent evolution of several key parameters characterizing the electronic structure of the ZnO nanoparticle surface. Distinct trends are observed with decreasing OH coverage (a): both $E_{\mathrm{VBM}}^{\mathrm{surf}}$ (b) and the Zn 3d peak (d) shift gradually to lower E_B, which can be attributed to a reduction of downward bb. Additionally, the work function (c) increases as a function of T_S, which is expected for a diminishing positive charge at the surface associated with the quenching of OH-related donors upon desorption at elevated temperatures.[14] A similar correlation between OH coverage, work function and $E_{\mathrm{VBM}}^{\mathrm{surf}}$ has been found for ZnO single crystals upon controlled exposure to hydrogen, water, and methanol.[10−12,14] In particular, the work function of 3.85 eV determined here for the as-loaded nanoparticle film is almost identical to the value reported for completely hydrogen-terminated low-index ZnO surfaces,.[11,14] Due to the high sensitivity of the ZnO work function to the presence of OH groups at the surface, this is additional confirmation of a fully hydroxylated initial state of the investigated nanoparticle films at room temperature.

Closer inspection of Figure 3b,d,e reveals that the Zn 3d XPS peak experiences only roughly half the E_B-shift compared to the UPS-derived $E_{\mathrm{VBM}}^{\mathrm{surf}}$, which is accompanied by a distinct narrowing of its lineshape. The microscopic origin of these effects is illustrated in Figure 4a−c: whenever the XPS probing depth is similar to the spatial extent of the SCL below the surface, the spectral distribution of the overall Zn 3d photoemission is modulated by the interfacial potential

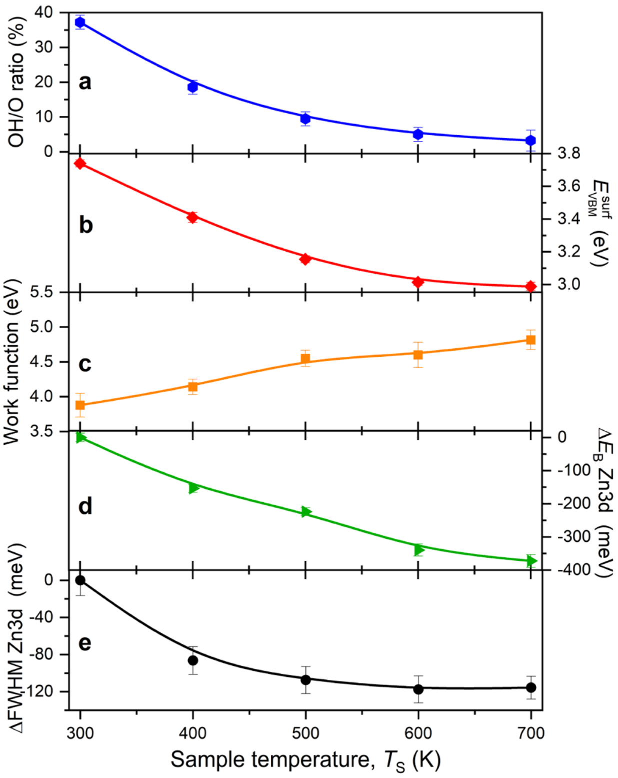

Figure 3. Temperature-dependent evolution of the surface electronic structure. (a) Contribution of the surface-hydroxyl component to the total O 1s photoemission as a function of sample temperature. (b) Position of the VBM at the surface with respect to the Fermi level. (c) Work function derived from the low-energy cutoffs of the UPS spectra. (d) Binding energy of the Zn 3d photoemission line. (e) Zn 3d peak width (FWHM). Solid lines are guides to the eye. Error bars denote the standard error of the fitted parameters.[43]

gradient $V_{bb}(z)$. Therefore, starting from a downward bb scenario as illustrated in Figure 4c, temperature-driven band flattening (a,b) will be reflected in a narrowing of the Zn 3d XPS peak width and a shift of its center toward lower binding energies, as experimentally observed. This combined effect of photoelectron escape depth and spatial $V_{bb}(z)$ progression on shaping the observed Zn 3d signal is also responsible for the difference in energy shifts determined by UPS and XPS. In the more surface-sensitive UPS measurements of E_{VBM}^{surf}, photoelectrons originate almost exclusively from the topmost layer.[44] In contrast, the probing depth (defined as 3× IMFP) in the Zn 3d XPS experiments is ∼3 × 2.35 nm,[38] which leads to significant averaging of photoelectron signals with different binding energies emerging from different depths and thus to a smaller overall energy shift of the entire XPS spectrum, as illustrated in Figure 4a,b.

Based on the discussion presented so far, we interpret the saturation behavior of the temperature-dependent spectral signatures in Figure 3 as a transition from an initial downward bb situation in the as-loaded ZnO nanoparticle film, toward flatband conditions for the dehydrated state at $T_S \gtrsim 600$ K (see schematic illustration in Figure 4d). In this context, the difference between E_{VBM}^{surf} at $T_S = 300$ K and $T_S = 700$ K directly yields the maximum downward bb at the surface $V_{bb}^{surf} = 0.79 \pm 0.03$ eV for the fully hydroxylated ZnO nanostructure, which allows us to determine the position of the CBM in the bulk of the ZnO nanoparticles to be $E_{CBM}^{bulk} = V_{bb}^{surf} + E_g - E_{VBM}^{surf} = 350$ meV above the Fermi level (see Figure S3, Supporting Information). Applying Boltzmann statistics and the effective mass approximation for the CB occupancy, we estimate the bulk carrier density of the nanoparticle film to be $n_b = N_C \times e^{-E_{CBM}^{bulk}/k_BT} \approx 4 \times 10^{12}\,\mathrm{cm}^{-3}$, where $N_C \approx 3 \times 10^{18}$ cm^{-3} is the effective CB density of states in ZnO.[13] Such comparatively low values for n_b are in reasonable agreement with carrier densities expected for high-quality ZnO films[45] and align with the core−shell structure proposed for ZnO nanoparticles, that is, a crystalline and stoichiometric bulk region surrounded by a highly defective surface.[31]

Temperature-driven bb modifications have recently been observed for various OH-terminated metal-oxide single-crystals.[12,13,46] In these systems, the transition from electron-accumulation-type SCLs to the flatband limit occurred in an intermediate temperature range and was followed by the emergence of electron-depletion-type SCLs featuring upward bb at higher temperatures.[12,13,46] In general, it is difficult to unequivocally infer flatband conditions solely based on energy shifts in photoemission spectra.[47,48] In this context, the additional information revealed by the temperature-dependent Zn 3d XPS peak width is essential. As indicated in Figure 3a−c, the flatband situation is characterized by the narrowest XPS lineshape. In contrast, the onset of sizable upward bb at higher temperatures would inevitably add spectral broadening.[42,43] It is therefore important to note that not only the energy shifts but also the FWHMs of the Zn 3d peak for the last two annealing steps (600 and 700 K) are indistinguishable within the error margins (see Figure 2d,e). This favors flatband energy level alignment rather than electron depletion within the SCL during the final heat treatment employed in our study. Note that the UPS-determined VBM position also remains unchanged for T_S = 600−700 K within the experimental uncertainty (Figure 3b). This quantity tracks any change in the surface potential even more sensitively due to the small probing depth inherent to the UPS method.[44]

Because the correlation between the Zn 3d peak shift and its line-narrowing encodes the spatial characteristics of the bb potential, we adopt an XPS peak envelope reconstruction algorithm to retrieve quantitative information on the $V_{bb}(z)$ depth profile from the T_S-dependent Zn 3d E_B-shifts and FWHM variations.[19,47,48] In this approach, the spectral distribution $D(E_B)$ of the total Zn 3d emission is modeled as a superposition of discrete photoelectron contributions emerging from different depths z_i below the surface (Figure 4a−c) according to

$$\begin{aligned} D(E_B) &= \sum_i D_i \\ &= \sum_{i(\forall z_i \in \mathrm{SCL})} D_0(E_B - E_0 - V_{bb}(z_i)) \times e^{-z_i/\mathrm{IMFP}} \end{aligned}$$

Here, D_i and E_0 denote the Zn 3d lineshape and peak position, respectively, in the absence of bb, that is, under flatband conditions $[V_{bb}(z) = 0]$. For the simulations, we derive these input parameters from a Gaussian fit to the Zn 3d spectrum at T_S = 700 K (Figure 2b). The relative spectral weights of the individual D_i components are defined by the exponential IMFP damping term. In all numerical calculations, the spatial sampling step size $z_{i+1} - z_i$ was set to 0.2 nm, which corresponds to the interlayer spacing of ZnO, averaged over all high-symmetry directions in the wurtzite lattice. By matching

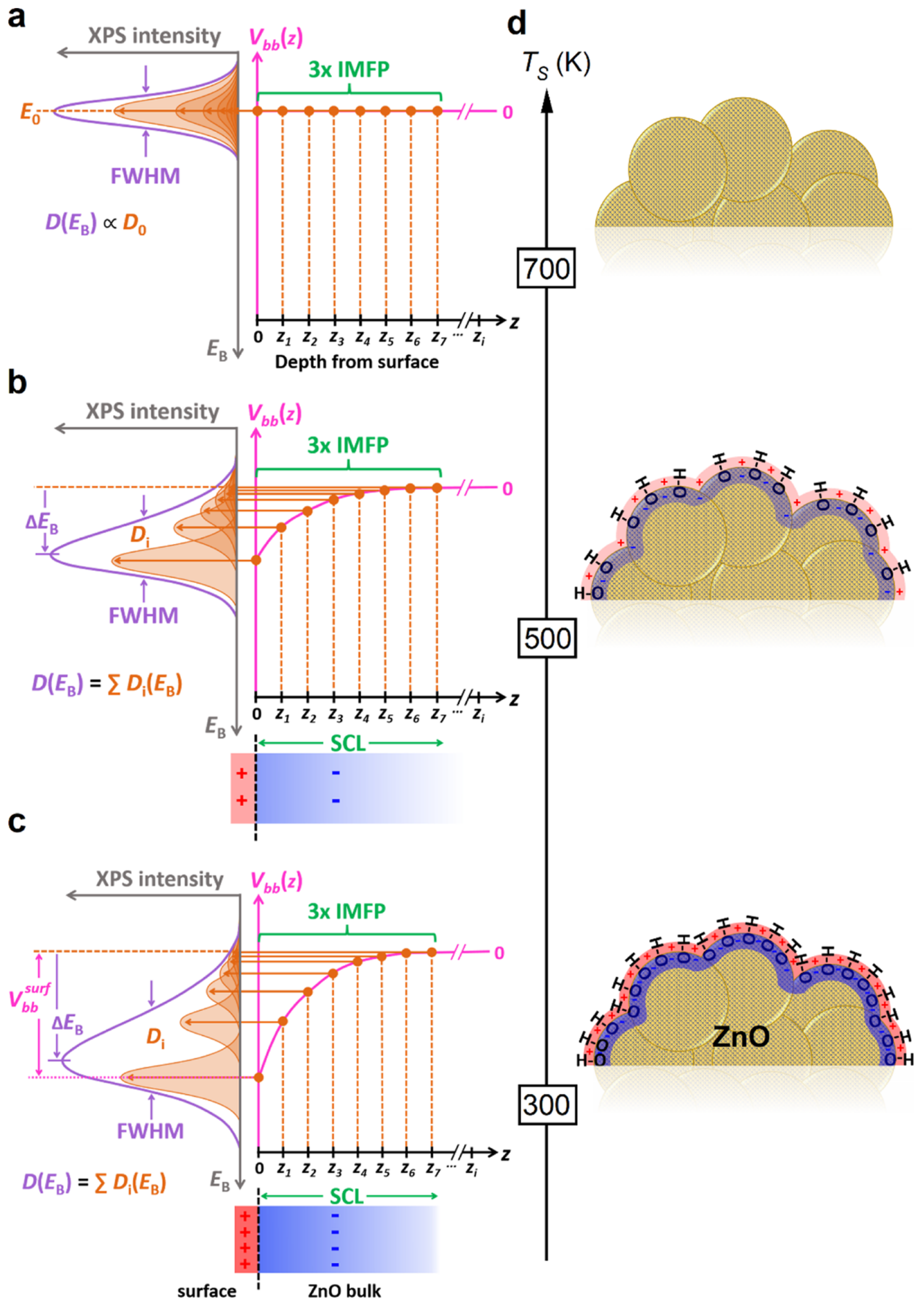

Figure 4. Correlation between Zn 3d XPS lineshape, bb, and OH coverage. (a−c) The total Zn3d XPS spectrum $D(E_B)$ is modeled as a superposition of spectral contributions D_i emerging from different depths z_i below the interface. The relative D_i intensities are weighted by the IMFP, and their central energies are governed by the local value of the bb potential $V_{bb}(z_i)$. If the XPS probing depth (= 3 × IMFP) is comparable to the spatial extent of $V_{bb}(z)$, changes in this potential are mapped onto modulations of the overall XPS lineshape. Different scenarios are illustrated: (a) flatband condition resulting in the narrowest XPS lineshape. (b) Moderate and (c) strong downward bb giving rise to additional spectral broadening. (d) Schematics illustrating the correlation between the sample temperature T_S, surface hydroxylation, and the SCL that defines $V_{bb}(z)$. Note that the oxygen in the OH groups represents a ZnO surface atom.

simulated to measured Zn 3d XPS spectra, different analytic functions describing the $V_{bb}(z)$ shape can be benchmarked against the experimental ΔFWHM-versus-ΔE_B trace, assuming that the depletion of surface donors only affects the magnitude of the downward bb potential.

These simulations are illustrated in Figure 5a, which shows fit results for a cubic potential profile, $V_{bb}(z) = V_{bb}^{surf} \times \left(\frac{z_{bb} - z}{z_{bb}}\right)^3$ for $0 \le z \le z_{bb}$, where V_{bb}^{surf} is the maximum bb value at the ZnO surface ($z = 0$) and z_{bb} is the maximum spatial extent of the bb potential into the bulk. Excellent agreement with the experimentally derived ΔFWHM-versus-ΔE_B trace (Figure 5a) and the Zn 3d XPS spectra (Figure 5b) is achieved for $z_{bb} = 5.1 \pm 0.7$ nm. Error bars represent the z_{bb}-range within which the merit function χ^2 is less than twice the minimum value, as shown in the inset of Figure 5a. We tested several functional forms of $V_{bb}(z)$, the

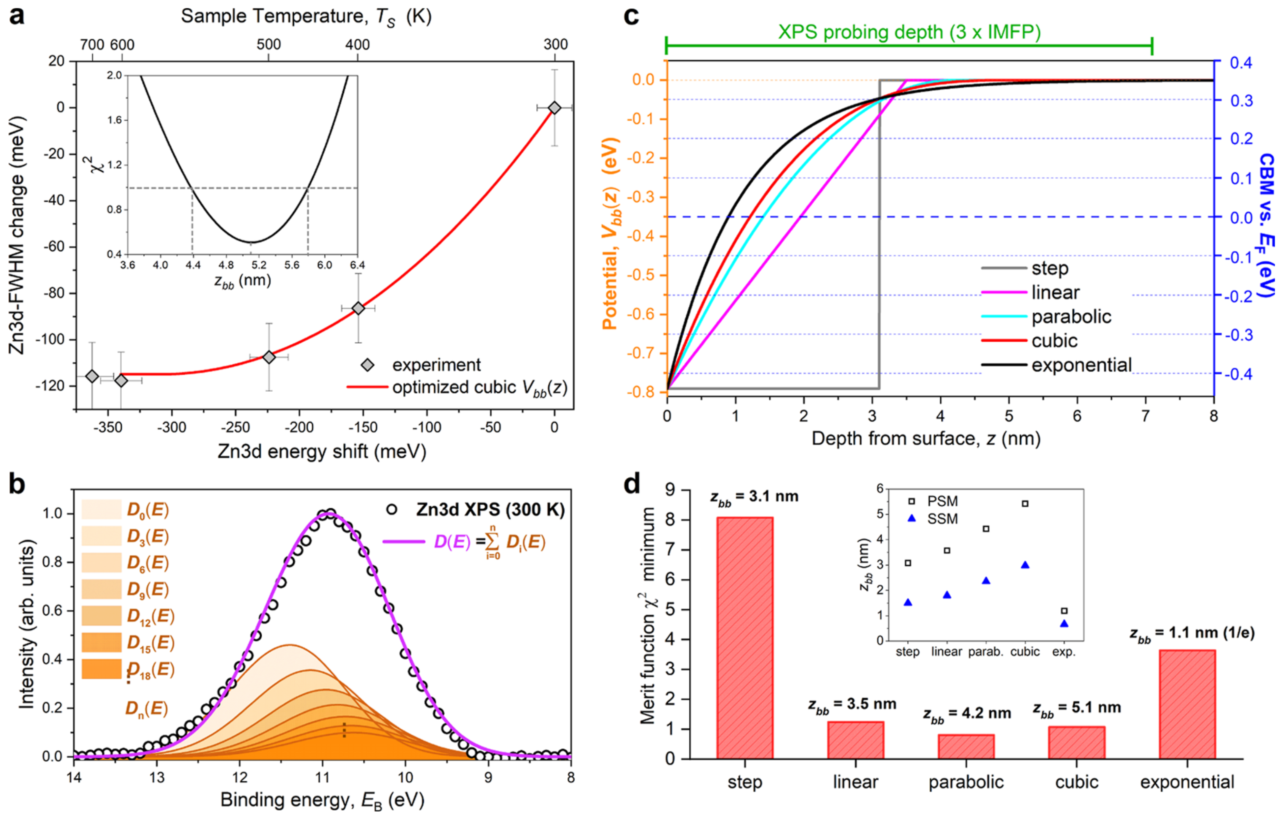

Figure 5. Quantifying the depth profile of the interfacial potential $V_{bb}(z)$. (a) Comparison of the experimentally determined correlation between the Zn 3d peak-shift and peak-narrowing to a numerical simulation based on a cubic $V_{bb}(z)$ profile. Parameter optimization restricts the maximum spatial extent of the potential to z_{bb} = 5.1 ± 0.7 nm below the surface. The nanometer sensitivity of this modeling is highlighted in the inset, showing the z_{bb}−dependence of the fit merit function. (b) Comparison of experimental (black circles) and simulated (violet solid line) Zn 3d XPS spectrum at a sample temperature T_S = 300 K. The origins of the individual XPS components D_i (orange shaded peaks) are illustrated in Figure 4a−c. (c) Comparison of analytical functions for $V_{bb}(z)$. The green bar indicates the experimental XPS probing depth of the Zn 3d photoemission. The orange energy scale references the surface potential to the bulk limit, whereas the blue energy scale refers to the position of the CBM versus the Fermi level. (d) Merit function minima of simulations based on the $V_{bb}(z)$ shapes depicted in (c). Optimized z_{bb} parameters define the depths z where the potential reaches the ZnO bulk value. Only for the exponential profile is z_{bb} defined as the $1/e$ decay constant. The inset compares z_{bb} values obtained from an analysis within a planar-surface model (PSM) and a single-sphere model (SSM).

corresponding optimized depth profiles are summarized in Figure 5c. A central finding is that the bb potential drops by more than 80% over a distance of less than 3 nm from the surface, irrespective of the exact $V_{bb}(z)$ model shape. While the existence of such strong interfacial potential gradients has been established for adsorbate-covered single-crystal ZnO surfaces,[10−14] our results strongly suggest that they can also develop in nanoscale structures.

It should be noted that the Zn 3d XPS simulations presented here are based on a planar sample geometry. Corresponding simulations within a single-sphere model (SSM) yield an even smaller spatial extent of the built-in potential (see inset of Figure 5d) due to an effectively reduced IMFP (see the Supporting Information). The interconnected nanoparticle films in our study can be assumed to exhibit surface topographies in between these two limiting cases.

The determination of the most suitable analytical approximation for $V_{bb}(z)$ is illustrated in Figure 5d. It compares the minima of the merit function for parameter-optimized simulations based on the different $V_{bb}(z)$ profiles depicted in Figure 5c. Evidently, a step-like or exponential shape can be discarded, which further demonstrates the nanometer sensitivity of our approach to $V_{bb}(z)$ depth variations. Within the experimental uncertainties, it is difficult to distinguish between a linear, parabolic, and cubic $V_{bb}(z)$ shape based on the quality of the fit results alone. However, a linear potential profile is not linked to a well-defined carrier distribution $n_e(z)$ via the Poisson equation $d^2V_{bb}(z)/dz^2 \propto n_e(z)$ and is therefore discarded. For a more detailed discussion of the parabolic and cubic potential shapes, it is instructive to consider general boundary conditions for potential gradients and underlying charge-carrier densities in isolated ∼15 nm ZnO nanoparticles. Solving the Poisson equation for spherical semiconductor particles,[27] we estimate that a uniform volume electron density of $\sim 7 \times 10^{19}$ cm^{-3} within the SCL shell is required for a parabolic $V_{bb}(z)$ to enable 0.8 eV downward bb. For comparison, a cubic $V_{bb}(z)$ can generate the same potential drop with a linear charge density increase from $n_b = 4 \times 10^{12}$ cm^{-3} in the core region to 6×10^{19} cm^{-3} near the surface of the nanoparticles (see Figure S4, Supporting Information). Integrating the charge density profiles along the depth coordinate z yields 3×10^{13} and 1.5×10^{13} cm^{-2} for the number of electrons per unit area associated with parabolic and cubic potential gradients, respectively. These values are consistent with carrier densities observed by Hall-measurements in electron accumulation layers of hydrogenated ZnO single-crystal surfaces.[49]

To explore whether electron area densities of this magnitude can be generated solely by surface-hydroxyl donor states, we build on theoretical studies of water adsorption on ZnO$(10\bar{1}0)$,[16] which represents the lowest-energy ZnO surface, and is thus expected to be a prevalent crystal orientation in ZnO nanomaterials. Density functional theory (DFT) calculations identify two H_2O molecules per ZnO$(10\bar{1}0)$ surface unit cell (0.33×0.52 nm^2) as the most stable monolayer configuration, with one H_2O moiety adsorbed molecularly, while the second dissociates. The intermediate hydrogen atom generated in the latter process combines with a surface lattice oxygen atom to form a surface OH-group with electron donor character.[16] This scenario yields an upper limit of $\sim 6 \times 10^{14}$ cm^{-2} for purely surface-hydroxyl-induced electron area densities, which is fully compatible with the interpretation of OH-mediated surface-transfer doping being the dominating source of electrons inside the SCL for the hydroxylated ZnO nanostructures. The presence of surface orientations other than $(10\bar{1}0)$, different efficiencies and pathways of generating OH groups, as well as defects with possibly compensating donor−acceptor character might explain the lower area electron densities of the ZnO nanostructure compared to the theoretical estimate discussed above.

Because most of the electrons in the ZnO SCL have been released from surface donor levels, the equilibrium electron density distribution is also expected to be graded toward the interface, shaped by Coulomb interaction and carrier diffusion processes. We therefore favor the cubic $V_{bb}(z)$ dependency as the simplest analytical description for the spatial depth evolution of the bb potential inside the ZnO nanoparticle film, albeit combinations of higher-degree polynomials might possibly yield slightly better agreement with the experiment. Interestingly, however, $V_{bb}(z)$ simulations based on single-term higher polynomial parameterizations consistently result in worse agreement with the experimental data compared to the cubic profile (Figure S5, Supporting Information). Future studies employing tunable X-ray photon energies may provide more stringent tests of such subtle microscopic details of the potential gradient.

CONCLUSIONS

In summary, we provide strong evidence for large potential gradients within the surface-near region of hydroxylated ZnO nanoparticle films, with an average spatial extent of only a few nanometers into the bulk. Based on the corrugated nature of the nanostructure surface, the ~0.8 eV downward bb revealed here should be considered as a spatially averaged property of the nanoporous film. Even though the detailed modeling of the potential profile presented here was based on average material properties, it already demonstrates the intrinsic sensitivity to the nanometer depth evolution of potential gradients below the nanoparticle film surface. In principle, this modeling to reconstruct the potential depth profile from XPS data could be extended to take the particle size distribution and porosity of the nanoparticle film into account. This would make the approach even more reliable and robust when applied to complex nanomaterials.

Recent DFT studies on hydrogenated ZnO$(10\bar{1}0)$ surfaces emphasize the local character of such adsorbate-induced potentials, with atomic-scale spatial confinement to the adsorption sites and amplitude modulations exceeding 1 eV.[14] Contrary to common belief, our experiments indicate that bb effects of this magnitude can also occur in metal-oxide nanomaterials and has therefore to be considered in the description of their surface electronic properties. Significant hydroxyl-related downward bb has also been reported for single-crystal Ag/ZnO junctions.[19] The pronounced nanophase potential gradients revealed in the study reported here might therefore be of general importance for successfully interfacing metal contacts with ZnO nanomaterials in device applications.

Finally, our results imply a partial metallization of the hydroxylated ZnO nanostructure surface because the CBM near the interface is below the Fermi level (Figure 5c).[50] The possibility to control and tailor such surface-conductive channels is relevant for advancing the performance of ZnO-based (photo-)catalytic nanomaterials. Especially, near-surface diffusive transport of electrons through interconnected nanoparticle networks may activate surface-recombination pathways and lead to reduced device performance. On the other hand, the near-surface confinement of photogenerated electrons may promote the photocatalytic activity of ZnO nanomaterials. We note that the findings presented here suggest a microscopic picture of electron propagation that is contrary to the most common models of charge transport in nanoporous metal oxides. These usually assume depleted nanoparticles featuring upward bb, where electron transfer proceeds via particle-to-particle hopping in a random-walk fashion. The surface electronic structure of hydroxylated nanoscale ZnO discovered here might be partly responsible for the comparably low performance of this material in dye-sensitized photovoltaics.[3,51]

EXPERIMENTAL SECTION

Sample Preparation. ZnO nanoparticles with an average diameter of ~15 nm have been prepared with a sol−gel method based on a zinc acetate dihydrate.[34] Briefly, 21 mL of tetramethylammonium hydroxide (25% in methanol, Sigma-Aldrich) is added to 11 g of zinc acetate ($ZnAc_2 \cdot H_2O$, Merck) and 100 mL of anhydrous ethanol in a flask attached to a condenser. The resulting sol is refluxed at 80 °C for 30 min and then left untouched for several hours at room temperature to let the ZnO nanoparticles settle down. The solvent is decanted to adjust the concentration for spin-coating (15 mL total volume). This colloidal suspension is spin-coated (2000 rpm) onto cleaned 1×1 cm^2 mirror-like polished stainless steel or FTO substrates. The films are subsequently dried at 60 °C and sintered in air at 360 °C for 50 min to generate interconnected nanoporous networks. This procedure yields macroscopically homogeneous ZnO films while preserving a nanoscale surface topography (see Figure 1b).[52] The ~0.5 μm thick ZnO nanoparticle films were cleaned by ultrasonication in ethanol and de-ionized water and blown dry with argon before transferring them into the UHV system (base pressure $< 2 \times 10^{-10}$ mbar) for the XPS and UPS experiments. In the main text, these samples are referred to as initially hydroxylated ZnO nanoparticle films.

Photoemission Experiments. UPS spectra are recorded using He−I emission ($h\nu$ = 21.2 eV) and XPS spectra with non-monochromatized Mg Kα radiation ($h\nu$ = 1253.6 eV) from a laboratory X-ray tube in normal photoelectron emission geometry. The absolute binding energy scale is calibrated with respect to the Fermi level at E_F = 0.00 eV and the Au 4f$_{7/2}$ peak center at 84.00 eV, obtained from a sputter-cleaned gold surface. The resolution in the UPS and XPS experiments was ~150 meV and ~0.8 eV, respectively. In all measurements, the photon intensity was varied by at least 1 order of magnitude to exclude errors due to sample charging, especially for the dehydroxylated samples. Additional care was taken to rule out any impact of sample degradation upon prolonged He−I/

X-ray exposure. Taking the sampling area of the hemispherical photoelectron energy analyzer into account (SPECS; Phoibos100 operated in medium-area mode), we estimate that $\sim 10^{10}$ individual nanoparticles contribute to the measured XPS and UPS signals reported here. For each annealing step, the sample was kept at a specific temperature for 5 min. Photoemission spectra were subsequently taken at a sample temperature of 300 K. The temperature was monitored with a type-K thermocouple pressed onto one corner of the sample. Sample annealing was performed by radiative heating from the rear with two tungsten filaments. Photoemission spectra obtained after annealing to >700 K are not discussed here, as such high-temperature treatments caused instabilities within the ZnO nanoparticle film, with partial loss of adhesion to the metal/FTO substrates.

■ ASSOCIATED CONTENT

Supporting Information

The Supporting Information is available free of charge at https://pubs.acs.org/doi/10.1021/acsanm.1c02730.

> Sample characterization, energy level schematics, charge density and bb calculations for isolated nanoparticles, and SSM for XPS signal attenuation (PDF)

■ AUTHOR INFORMATION

Corresponding Author

Stefan Neppl − *Chemical Sciences Division, Lawrence Berkeley National Laboratory, Berkeley, California 94720, United States; Paul Scherrer Institut, 5232 Villigen, Switzerland;* orcid.org/0000-0003-0536-1932; Email: stefan.neppl@psi.ch

Authors

Johannes Mahl − *Chemical Sciences Division, Lawrence Berkeley National Laboratory, Berkeley, California 94720, United States*

Oliver Gessner − *Chemical Sciences Division, Lawrence Berkeley National Laboratory, Berkeley, California 94720, United States;* orcid.org/0000-0003-4709-2822

Johannes V. Barth − *Physikdepartment E20, Technische Universität München, 85747 Garching, Germany*

Peter Feulner − *Physikdepartment E20, Technische Universität München, 85747 Garching, Germany*

Complete contact information is available at: https://pubs.acs.org/10.1021/acsanm.1c02730

Notes

The authors declare no competing financial interest.

■ ACKNOWLEDGMENTS

This work was supported by the Atomic, Molecular, and Optical Sciences Program of the U.S. Department of Energy, Office of Science, Office of Basic Energy Sciences, Division of Chemical Sciences, Geosciences, and Biosciences at Lawrence Berkeley National Laboratory under contract no. DE-AC02-05CH11231. J.M. acknowledges partial support from the Advanced Light Source Doctoral Fellowship. S.N. acknowledges financial support from the Alexander-Humboldt Foundation. J.V.B. and P.F. were supported by the Deutsche Forschungsgemeinschaft (e-conversion Cluster of Excellence). We thank Friedrich Esch from the Chemistry Department of the Technical University of Munich for extracting the ZnO nanoparticle size distribution from the SEM data.

■ REFERENCES

(1) Schmidt-Mende, L.; MacManus-Driscoll, J. L. ZnO − Nanostructures, Defects, and Devices. *Mater. Today* **2007**, *10*, 40−48.

(2) Özgür, Ü.; Hofstetter, D.; Morkoç, H. ZnO Devices and Applications: A Review of Current Status and Future Prospects. *Proc. IEEE* **2010**, *98*, 1255−1268.

(3) Zhang, Q.; Dandeneau, C. S.; Zhou, X.; Cao, G. ZnO Nanostructures for Dye-Sensitized Solar Cells. *Adv. Mater.* **2009**, *21*, 4087−4108.

(4) Tian, Z. R.; Voigt, J. A.; Liu, J.; Mckenzie, B.; Mcdermott, M. J.; Rodriguez, M. A.; Konishi, H.; Xu, H. Complex and Oriented ZnO Nanostructures. *Nat. Mater.* **2003**, *2*, 821−826.

(5) Kim, Y.-S.; Park, C. H. Rich Variety of Defects in ZnO via an Attractive Interaction between O Vacancies and Zn Interstitials: Origin of n-Type Doping. *Phys. Rev. Lett.* **2009**, *102*, 086403.

(6) Look, D. C.; Farlow, G. C.; Reunchan, P.; Limpijumnong, S.; Zhang, S. B.; Nordlund, K. Evidence for Native-Defect Donors in n-Type ZnO. *Phys. Rev. Lett.* **2005**, *95*, 225502.

(7) Penfold, T. J.; Szlachetko, J.; Santomauro, F. G.; Britz, A.; Gawelda, W.; Doumy, G.; March, A. M.; Southworth, S. H.; Rittmann, J.; Abela, R.; Chergui, M.; Milne, C. J. Revealing Hole Trapping in Zinc Oxide Nanoparticles by Time-Resolved X-Ray Spectroscopy. *Nat. Commun.* **2018**, *9*, 478.

(8) Zhang, Z.; Yates, J. T. Band Bending in Semiconductors: Chemical and Physical Consequences at Surfaces and Interfaces. *Chem. Rev.* **2012**, *112*, 5520−5551.

(9) Ozawa, K.; Emori, M.; Yamamoto, S.; Yukawa, R.; Yamamoto, S.; Hobara, R.; Fujikawa, K.; Sakama, H.; Matsuda, I. Electron−Hole Recombination Time at TiO_2 Single-Crystal Surfaces: Influence of Surface Band Bending. *J. Phys. Chem. Lett.* **2014**, *5*, 1953.

(10) Ozawa, K.; Mase, K. Metallization of ZnO(100)by adsorption of hydrogen, methanol, and water: Angle-resolved photoelectron spectroscopy. *Phys. Rev. B: Condens. Matter Mater. Phys.* **2010**, *81*, 205322.

(11) Ozawa, K.; Mase, K. Comparison of the Surface Electronic Structures of H-Adsorbed ZnO Surfaces: An Angle-Resolved Photoelectron Spectroscopy Study. *Phys. Rev. B: Condens. Matter Mater. Phys.* **2011**, *83*, 125406.

(12) Heinhold, R.; Williams, G. T.; Cooil, S. P.; Evans, D. A.; Allen, M. W. Influence of Polarity and Hydroxyl Termination on the Band Bending at ZnO Surfaces. *Phys. Rev. B: Condens. Matter Mater. Phys.* **2013**, *88*, 235315.

(13) Heinhold, R.; Cooil, S. P.; Evans, D. A.; Allen, M. W. Stability of the Surface Electron Accumulation Layers on the Nonpolar $(10\bar{1}0)$ and (11-20) Faces of ZnO. *J. Phys. Chem. C* **2014**, *118*, 24575−24582.

(14) Deinert, J.-C.; Hofmann, O. T.; Meyer, M.; Rinke, P.; Stähler, J. Local Aspects of Hydrogen-Induced Metallization of the ZnO$(10\bar{1}0)$ Surface. *Phys. Rev. B: Condens. Matter Mater. Phys.* **2015**, *91*, 235313.

(15) Dulub, O.; Meyer, B.; Diebold, U. Observation of the Dynamical Change in a Water Monolayer Adsorbed on a ZnO Surface. *Phys. Rev. Lett.* **2005**, *95*, 136101.

(16) Meyer, B.; Marx, D.; Dulub, O.; Diebold, U.; Kunat, M.; Langenberg, D.; Wöll, C. Partial Dissociation of Water Leads to Stable Superstructures on the Surface of Zinc Oxide. *Angew. Chem., Int. Ed.* **2004**, *43*, 6641−6645.

(17) Newberg, J. T.; Goodwin, C.; Arble, C.; Khalifa, Y.; Boscoboinik, J. A.; Rani, S. ZnO(100) Surface Hydroxylation under Ambient Water Vapor. *J. Phys. Chem. B* **2018**, *122*, 472−478.

(18) Piper, L. F. J.; Preston, A. R. H.; Fedorov, A.; Cho, S. W.; DeMasi, A.; Smith, K. E. Direct Evidence of Metallicity at ZnO (000)−(1×1) Surfaces from Angle-Resolved Photoemission Spectroscopy. *Phys. Rev. B: Condens. Matter Mater. Phys.* **2010**, *81*, 233305.

(19) Chernysheva, E.; Srour, W.; Philippe, B.; Baris, B.; Chenot, S.; Duarte, R. F.; Gorgoi, M.; Cruguel, H.; Rensmo, H.; Montigaud, H.; Jupille, J.; Cabailh, G.; Grachev, S.; Lazzari, R. Band Alignment at Ag/ZnO(0001) Interfaces: A Combined Soft and Hard x-Ray Photoemission Study. *Phys. Rev. B* **2018**, *97*, 235430.

(20) Janotti, A.; Van de Walle, C. G. Hydrogen Multicentre Bonds. *Nat. Mater.* **2007**, *6*, 44−47.

(21) Van de Walle, C. G.; Neugebauer, J. Universal Alignment of Hydrogen Levels in Semiconductors, Insulators and Solutions. *Nature* **2003**, *423*, 626−628.

(22) Van de Walle, C. G. Hydrogen as a Cause of Doping in Zinc Oxide. *Phys. Rev. Lett.* **2000**, *85*, 1012−1015.

(23) Cox, S. F. J.; Davis, E. A.; Cottrell, S. P.; King, P. J. C.; Lord, J. S.; Gil, J. M.; Alberto, H. V.; Vilão, R. C.; Piroto Duarte, J.; Ayres de Campos, N.; Weidinger, A.; Lichti, R. L.; Irvine, S. J. C. Experimental Confirmation of the Predicted Shallow Donor Hydrogen State in Zinc Oxide. *Phys. Rev. Lett.* **2001**, *86*, 2601−2604.

(24) Wang, C.; Zhou, G.; Li, J.; Yan, B.; Duan, W. Hydrogen-Induced Metallization of Zinc Oxide $(2\bar{1}\bar{1}0)$ Surface and Nanowires: The Effect of Curvature. *Phys. Rev. B: Condens. Matter Mater. Phys.* **2008**, *77*, 245303.

(25) Wang, Y.; Meyer, B.; Yin, X.; Kunat, M.; Langenberg, D.; Traeger, F.; Birkner, A.; Wöll, C. Hydrogen Induced Metallicity on the ZnO(100)Surface. *Phys. Rev. Lett.* **2005**, *95*, 266104.

(26) Albery, W. J.; Bartlett, P. N. The Transport and Kinetics of Photogenerated Carriers in Colloidal Semiconductor Electrode Particles. *J. Electrochem. Soc.* **1984**, *131*, 315−325.

(27) Goossens, A. Potential Distribution in Semiconductor Particles. *J. Electrochem. Soc.* **1996**, *143*, L131.

(28) Al-Saadi, M. J.; Al-Harthi, S. H.; Kyaw, H. H.; Myint, M. T. Z.; Bora, T.; Laxman, K.; Al-Hinai, A.; Dutta, J. Influence of Atomic Hydrogen, Band Bending, and Defects in the Top Few Nanometers of Hydrothermally Prepared Zinc Oxide Nanorods. *Nanoscale Res. Lett.* **2017**, *12*, 22.

(29) Chen, C.-Y.; Retamal, J. R. D.; Wu, I.-W.; Lien, D.-H.; Chen, M.-W.; Ding, Y.; Chueh, Y.-L.; Wu, C.-I.; He, J.-H. Probing Surface Band Bending of Surface-Engineered Metal Oxide Nanowires. *ACS Nano* **2012**, *6*, 9366−9372.

(30) Eichel, R.-A.; Erdem, E.; Jakes, P.; Ozarowski, A.; Van Tol, J.; Hoffmann, R. C.; Schneider, J. J. Space-Charge Layer, Intrinsic "Bulk" and Surface Complex Defects in ZnO Nanoparticles — a High-Field Electron Paramagnetic Resonance Analysis. *Funct. Mater. Lett.* **2013**, *06*, 1330004.

(31) Kaftelen, H.; Ocakoglu, K.; Thomann, R.; Tu, S.; Weber, S.; Erdem, E. EPR and Photoluminescence Spectroscopy Studies on the Defect Structure of ZnO Nanocrystals. *Phys. Rev. B: Condens. Matter Mater. Phys.* **2012**, *86*, 014113.

(32) Merz, T. A.; Doutt, D. R.; Bolton, T.; Dong, Y.; Brillson, L. J. Nanostructure Growth-Induced Defect Formation and Band Bending at ZnO Surfaces. *Surf. Sci.* **2011**, *605*, L20−L23.

(33) Tay, Y. Y.; Tan, T. T.; Liang, M. H.; Boey, F.; Li, S. Specific Defects, Surface Band Bending and Characteristic Green Emissions of ZnO. *Phys. Chem. Chem. Phys.* **2010**, *12*, 6008.

(34) Bauer, C.; Boschloo, G.; Mukhtar, E.; Hagfeldt, A. Ultrafast Relaxation Dynamics of Charge Carriers Relaxation in ZnO Nanocrystalline Thin Films. *Chem. Phys. Lett.* **2004**, *387*, 176−181.

(35) Keis, K.; Bauer, C.; Boschloo, G.; Hagfeldt, A.; Westermark, K.; Rensmo, H.; Siegbahn, H. Nanostructured ZnO Electrodes for Dye-Sensitized Solar Cell Applications. *J. Photochem. Photobiol. Chem.* **2002**, *148*, 57−64.

(36) Bauer, C.; Boschloo, G.; Mukhtar, E.; Hagfeldt, A. Electron Injection and Recombination in Ru(Dcbpy)$_2$ (NCS)$_2$ Sensitized Nanostructured ZnO. *J. Phys. Chem. B* **2001**, *105*, 5585−5588.

(37) Önsten, A.; Stoltz, D.; Palmgren, P.; Yu, S.; Claesson, T.; Göthelid, M.; Karlsson, U. O. SO2 Interaction with Zn(0001) and ZnO(0001) and the Influence of Water. *Surf. Sci.* **2013**, *608*, 31−43.

(38) Tanuma, S.; Powell, C. J.; Penn, D. R. Calculations of Electron Inelastic Mean Free Paths. V. Data for 14 Organic Compounds over the 50-2000 EV Range. *Surf. Interface Anal.* **1994**, *21*, 165−176.

(39) Shard, A. G.; Wang, J.; Spencer, S. J. XPS Topofactors: Determining Overlayer Thickness on Particles and Fibres. *Surf. Interface Anal.* **2009**, *41*, 541−548.

(40) Göpel, W.; Lampe, U. Influence of Defects on the Electronic Structure of Zinc Oxide Surfaces. *Phys. Rev. B: Condens. Matter Mater. Phys.* **1980**, *22*, 6447−6462.

(41) Morishige, K. Thermal Desorption Study of Surface Hydroxyls on ZnO. *J. Chem. Soc. Faraday. Trans.* **1980**, *76*, 738.

(42) Zhang, S. B.; Wei, S.-H.; Zunger, A. Intrinsic *n* -Type versus *p* -Type Doping Asymmetry and the Defect Physics of ZnO. *Phys. Rev. B: Condens. Matter Mater. Phys.* **2001**, *63*, 075205.

(43) Cumpson, P. J.; Seah, M. P. Random Uncertainties in AES and XPS: I: Uncertainties in Peak Energies, Intensities and Areas Derived from Peak Synthesis. *Surf. Interface Anal.* **1992**, *18*, 345−360.

(44) Bourke, J. D.; Chantler, C. T. Measurements of Electron Inelastic Mean Free Paths in Materials. *Phys. Rev. Lett.* **2010**, *104*, 206601.

(45) Huang, R.; Ye, S.; Sun, K.; Kiang, K. S.; de Groot, C. H. Fermi Level Tuning of ZnO Films Through Supercycled Atomic Layer Deposition. *Nanoscale Res. Lett.* **2017**, *12*, 541.

(46) Swallow, J. E. N.; Varley, J. B.; Jones, L. A. H.; Gibbon, J. T.; Piper, L. F. J.; Dhanak, V. R.; Veal, T. D. Transition from Electron Accumulation to Depletion at β-Ga$_2$ O$_3$ Surfaces: The Role of Hydrogen and the Charge Neutrality Level. *APL Mater.* **2019**, *7*, 022528.

(47) Lichterman, M. F.; Hu, S.; Richter, M. H.; Crumlin, E. J.; Axnanda, S.; Favaro, M.; Drisdell, W.; Hussain, Z.; Mayer, T.; Brunschwig, B. S.; Lewis, N. S.; Liu, Z.; Lewerenz, H.-J. Direct Observation of the Energetics at a Semiconductor/Liquid Junction by Operando X-Ray Photoelectron Spectroscopy. *Energy Environ. Sci.* **2015**, *8*, 2409−2416.

(48) Favaro, M.; Jeong, B.; Ross, P. N.; Yano, J.; Hussain, Z.; Liu, Z.; Crumlin, E. J. Unravelling the Electrochemical Double Layer by Direct Probing of the Solid/Liquid Interface. *Nat. Commun.* **2016**, *7*, 12695.

(49) Eger, D.; Many, A.; Goldstein, Y. Quantum Properties of Strong Accumulation Layers on ZnO Surfaces. *Surf. Sci.* **1976**, *58*, 18−24.

(50) We note that the weak UPS spectral intensity of such metal states near the Fermi level, which has been observed for single-crystal ZnO surfaces near the Γ-Point in *k*-space with angular-resolved, synchrotron-based photoemission (see refs 10 and 11), is expected to be below the detection sensitivity of our measurement due to the inherent angular averaging of the photoemission signals by the corrugated surface of the ZnO nanoparticle film.

(51) Neppl, S.; Mahl, J.; Roth, F.; Mercurio, G.; Zeng, G.; Toma, F.; Huse, N.; Feulner, P.; Gessner, O. Nanoscale Confinement of Photo-Injected Electrons at Hybrid Interfaces. *J. Phys. Chem. Lett.* **2021**. under consideration in. (manuscript-ID: jz-2021-02648w).

(52) Keis, K.; Lindgren, J.; Lindquist, S.-E.; Hagfeldt, A. Studies of the Adsorption Process of Ru Complexes in Nanoporous ZnO Electrodes. *Langmuir* **2000**, *16*, 4688−4694.

Supporting Information

Strong Potential Gradients and Electron Confinement in ZnO Nanoparticle Films: Implications for Charge-Carrier Transport and Photocatalysis

Johannes Mahl[1]*, Oliver Gessner*[1]*, Johannes V. Barth*[2]*, Peter Feulner*[2] *and Stefan Neppl*[1,3]*

[1]Chemical Sciences Division, Lawrence Berkeley National Laboratory, 94720 Berkeley, USA

[2]Physikdepartment E20, Technische Universität München, 85747 Garching, Germany

[3]Paul Scherrer Institut, 5232 Villigen, Switzerland

* corresponding author: stefan.neppl@psi.ch

1. Bandgap of the ZnO nanoparticle film

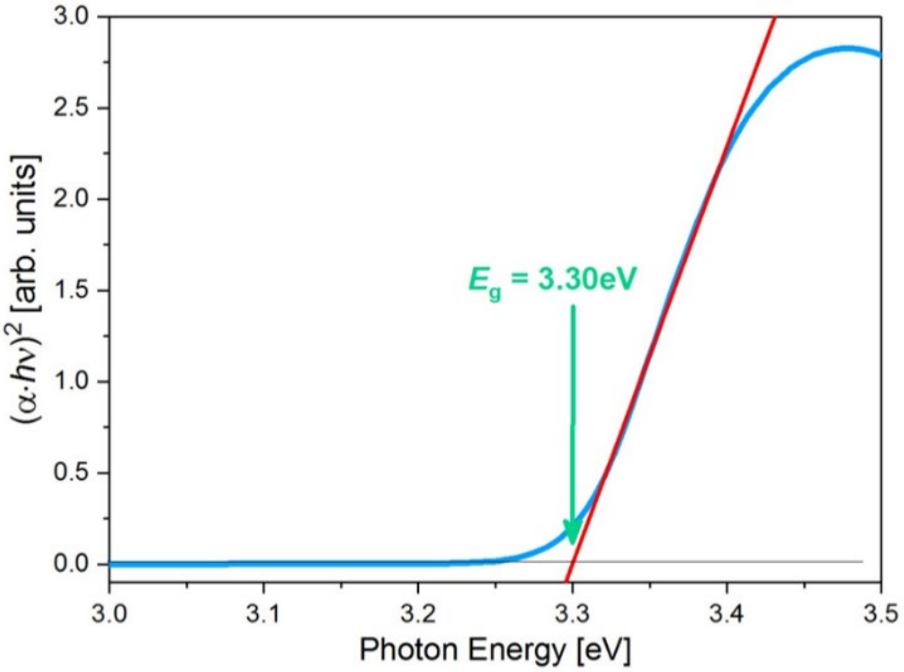

Figure S1| UV-Vis absorption spectrum of the ZnO nanoparticle film. A linear fit to the rising edge (red solid line) is used to determine the direct bandgap of E_g = 3.30 eV according to the Tauc-method.

2. Sample characterization with X-ray absorption spectroscopy

The large degree of crystallinity in the bulk of the nanoparticles is verified by O-K-edge X-ray absorption spectroscopy (Figure S2(c)). The spectrum obtained from the nanostructured film (red solid line) is very similar to the spectrum of a ZnO$(10\bar{1}0)$ single crystal (blue solid line), but is distinctly different from an amorphous ZnO reference.[1]

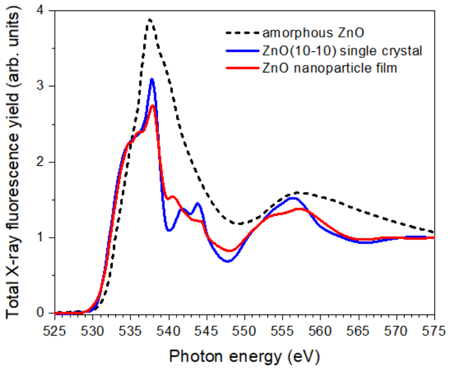

Figure S2| The oxygen K-edge X-ray absorption spectrum of the ZnO nanoparticle film (red line) is compared to a single-crystalline (blue line) and amorphous (black dashed line) reference sample.

3. Energy level band bending diagram

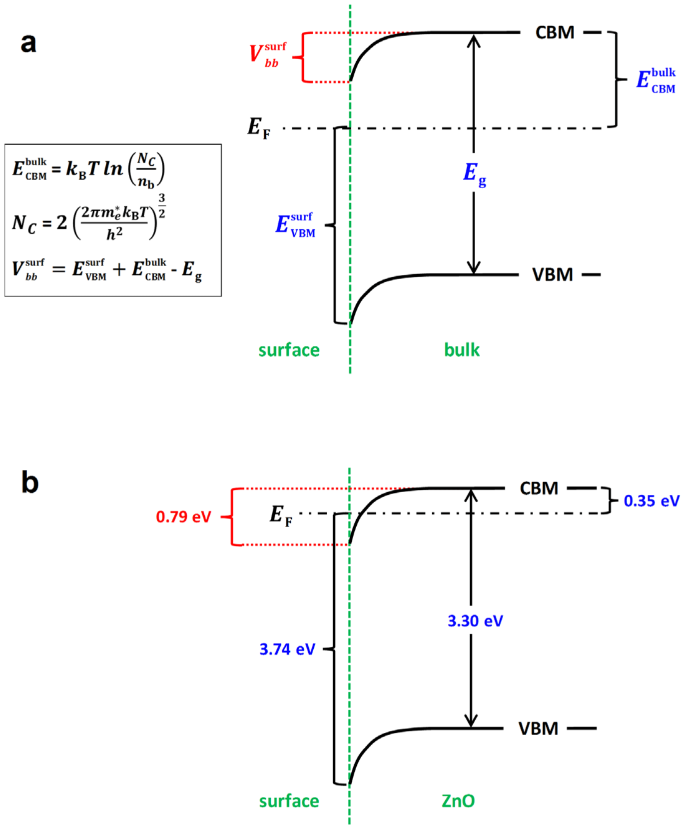

Figure S3| Energy level schematics for downward band bending. (a) Illustration of quantities to be measured and approximations commonly employed to determine the band bending at extended, single-crystal semiconductor surfaces**.** The calculation of V_{VBM}^{surf} requires knowledge of the difference E_{CBM}^{bulk} between the CBM and the Fermi level in the bulk, which can be calculated from the bulk carrier density n_b (e.g. by Hall measurements for crystalline samples) and the effective CB density of states N_C with the effective CB electron mass m_e^*. (b) Summary of values for the hydroxylated ZnO nanoparticle film as described in the main text.

4. Band bending and electron density distributions in isolated nanoparticles

The maximum possible band bending at the surface V_{bb}^{surf} for spherical ZnO nanoparticles with a diameter of 2R = 15 nm is calculated from analytical solutions of the Poisson equation.[2] For parabolic band bending, V_{bb}^{surf} as a function of electron density n_0 is given by:

$$V_{bb}^{surf} = \left(-\frac{e \cdot n_0}{6\epsilon\epsilon_0}\right) \cdot \left(1 + \frac{2(R - d_{SCL})}{R}\right) \cdot (d_{SCL})^2, \qquad \text{[Eq.1]}$$

and for cubic band bending potential by:

$$V_{bb}^{surf} = \left(-\frac{e \cdot n_0}{12\epsilon\epsilon_0\, d_{SCL}}\right) \cdot \left(R + 2(R - d_{SCL}) + \frac{3(R - d_{SCL})^2}{R}\right) \cdot (d_{SCL})^2. \qquad \text{[Eq.2]}$$

Here d_{SCL} denotes the width of the space charge layer (SCL), and $\epsilon \approx 8.5$ is the dielectric constant of ZnO. The results of Eq.1 and 2 are plotted in Figure S4(a). The integral electron densities required for a $V_{bb}^{surf} = 0.8$ eV downward band bending are indicated by the black dashed lines. The underlying charge density profiles $n_e(r)$ are shown in Figure S4(c) and (d), respectively.

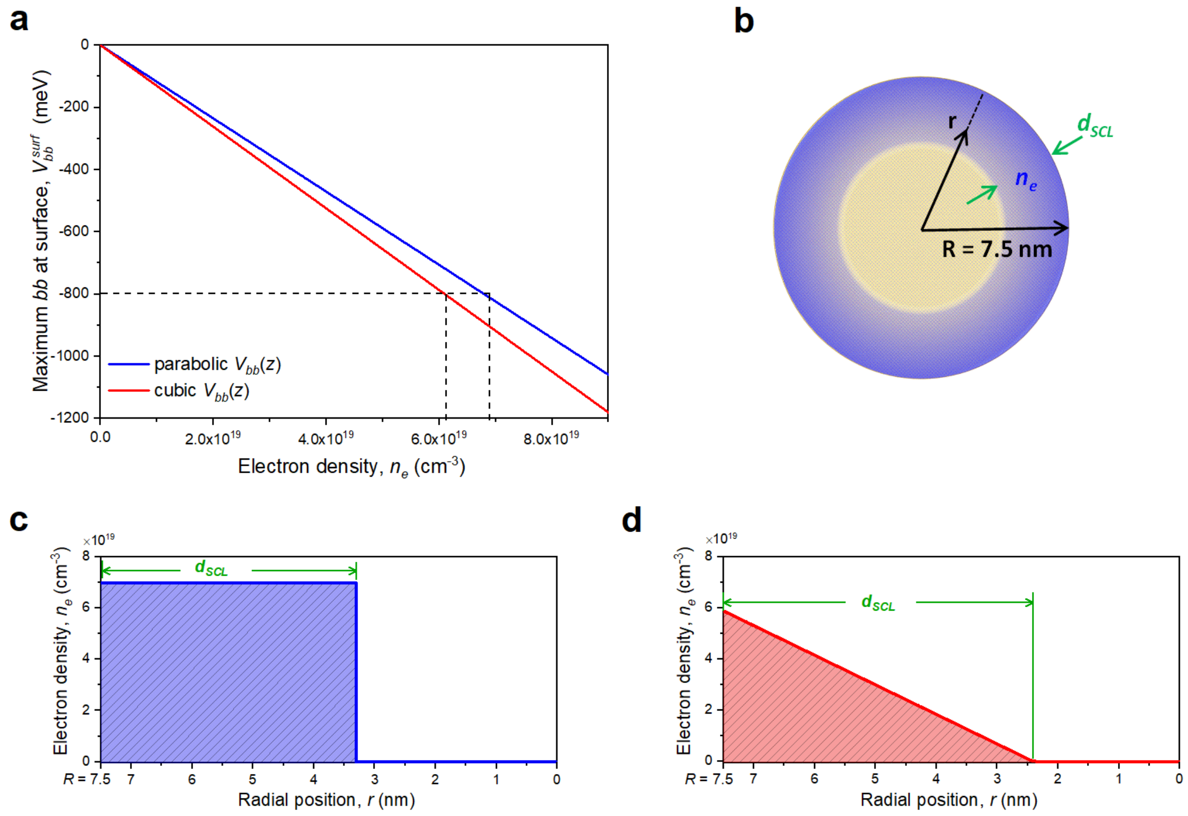

Figure S4| Band bending and charge density distribution for isolated ZnO nanoparticles. (a) Maximum band bending at the surface as a function of electron density for a parabolic (blue line) and cubic (red line) potential depth profile. (b) Illustration of parameters and coordinates for an isolated nanoparticle. (c) Depth profile of the electron charge density $n_e(r)$ producing a 0.8 eV parabolic downward band bending: $n_e(r) = n_b$ for r $\leq$ R-d_{SCL}, and $n_e(r) = n_b + n_0$ for R-$d_{SCL} \leq$ r $\leq$ R. (d) Charge density profile required for a 0.8 eV cubic downward band bending: $n_e(r) = n_b$ for r $\leq$ R-d_{SCL}, and $n_e(r) = n_b + r \cdot n_0/d_{SCL}$ for R-$d_{SCL} \leq$ r $\leq$ R. $n_b = 4 \cdot 10^{12}$ cm^{-3} is the bulk carrier density derived from the UPS data in the main text.

5. Higher-degree polynomial approximations for the band bending potential

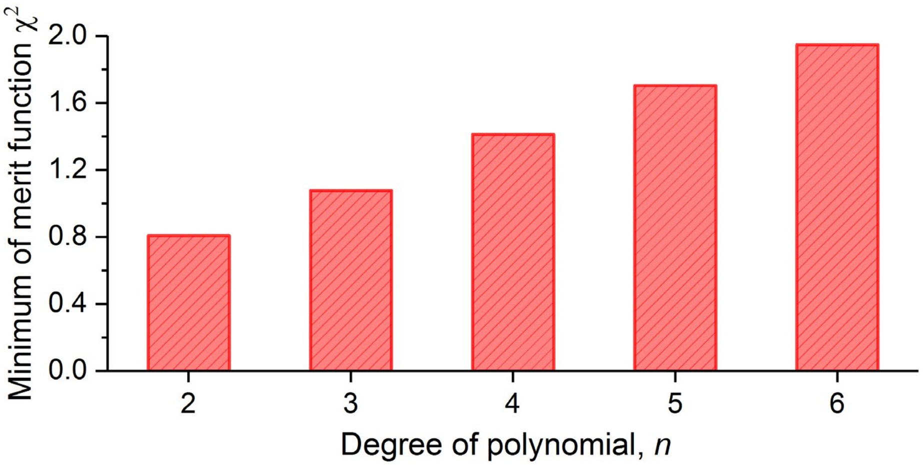

Figure S5| Higher-degree polynomial approximations for the band bending potential $V_{bb}(z)$ in the hydroxylated ZnO nanostructure (planar surface model). The merit function minima of numerical simulations based on n^{th}-degree polynomial shapes $V_{bb}(z) = V_{bb}^{surf} \times \left(\frac{z_{bb}-z}{z_{bb}}\right)^n$ are compared. A systematic trend of reduced fit quality with increasing polynomial order is observed.

6. Single-sphere model and XPS signal attenuation

The ZnO films investigated in this study exhibit a complex surface topography, which is in between the limiting cases of a planar surface and an ensemble of dispersed nanospheres. Even though the nanoparticles are interconnected by the calcination process, the electronic structure and the chemical composition within the inter-particle regions are expected to differ from bulk ZnO, e.g., due to carbonaceous residues of the organic surfactant. For simplicity, the SCL simulations presented in the main text assumed a planar surface model (PSM). However, the existence of interfacial grain boundaries, which tend to disturb the formation of extended space charge fields spanning across neighboring particles, motivates a single-sphere model[3] (SSM) as an alternative approximation for the sintered ZnO nanostructure surface.

In the following, we discuss the implications of the two models (PSM vs. SSM) for retrieving spatial information by quantitative XPS signal analysis. This is particularly relevant for the OH-layer thickness calculation of the initially hydroxylated sample, and the determination of potential depths z_{bb} within the Zn3d XPS peak reconstruction approach. In agreement with previous numerical simulations on photoelectron emission from corrugated surfaces, we find that the SSM can be reduced to the simpler PSM by introducing an effective IMFP.[4]

The main difference between the two models is illustrated in Figure 6(a,b): for a flat surface, the path length Δz inside the near-surface region (blue shaded) is constant for all photoelectrons emitted parallel to the detector axis (z-axis), while it is modulated in a plane perpendicular to the z-axis in the SSM. Combined with the constant IMFP, this gives rise to an enhanced near-surface contribution to the photoelectron signals for the SSM, which tends to overestimate, for example, adlayer thicknesses calculated with the standard exponential intensity attenuation approach.[4]

To quantify the impact of this modulation, we model the intensity of detected photoelectron signals emitted from a single spherical particle as a function of their origin within the particle. Parametrization of the problem according to Figure S6(c) leads to:

$$I(r,\alpha) \propto e^{-\frac{\Delta z(r,\alpha)}{IMFP}} \cdot |\cos\alpha \cdot \sin\alpha| \cdot \left(\frac{r}{R}\right)^2 . \qquad \text{[Eq.3]}$$

Note that only emission parallel to the detector axis is considered. The first term in Eq. 3 describes the exponential damping effect due to the IMFP, the absolute values of $\cos\alpha$ and $\sin\alpha$ account for the spherical surface and the projection onto the zx-plane, and the last term models the radial dependence of the emission intensity from a spherically symmetric electron source.

As can be inferred from Figure S6(c), $\Delta z(r,\alpha)$ is given by $\Delta z(r,\alpha) = R \cdot \cos\beta - r \cdot \cos\alpha$, where $\beta = \arcsin(\mathrm{r} \cdot \sin\alpha/R)$ since $\Delta x = r \cdot \sin\alpha = R \cdot \sin\beta$. We numerically integrate Eq.3 over the range of $0° \leq \alpha \leq 180°$ to obtain the photoemission intensity seen by the detector as a function of the radial starting position r. The results are shown as blue lines in Figure S7(a) for an IMFP of 1.57 nm corresponding to the O1s photoelectrons, and (b) for the Zn3d photoline with an the IMFP of 2.35 nm, respectively. As expected, the signal in the SSM decays more rapidly with distance from the surface compared to the PSM with the same IMFP (black lines). Interestingly, however, the SSM traces can be successfully fitted by a mono-exponential decay (red dashed lines), which suggests that the impact of the spherical shape on the overall XPS signal strength can be accounted for by introducing an effective IMFP, which turns out to be roughly half of the original IMFP.

The effective O1s IMFP of 0.85 nm would therefore reduce the initial OH-coverage to ~1.5 ML, compared to ~3 ML deduced from the PSM in the main text. However, both approximations are consistent with a fully hydroxylated surface of the ZnO nanostructure. Similarly, the smaller effective Zn3d IMFP of 1.15 nm will result in smaller values for the spatial extent z_{bb} of the band-bending potential. As shown in Figure S8, the z_{bb} values optimized with Zn3d peak simulations using the effective IMFP as input parameter are roughly a factor of two smaller compared to the PSM results – irrespective of the potential shape. Therefore, the key finding of nanoscale potential confinement in ZnO nanostructures is supported by both the SSM and the PSM approach.

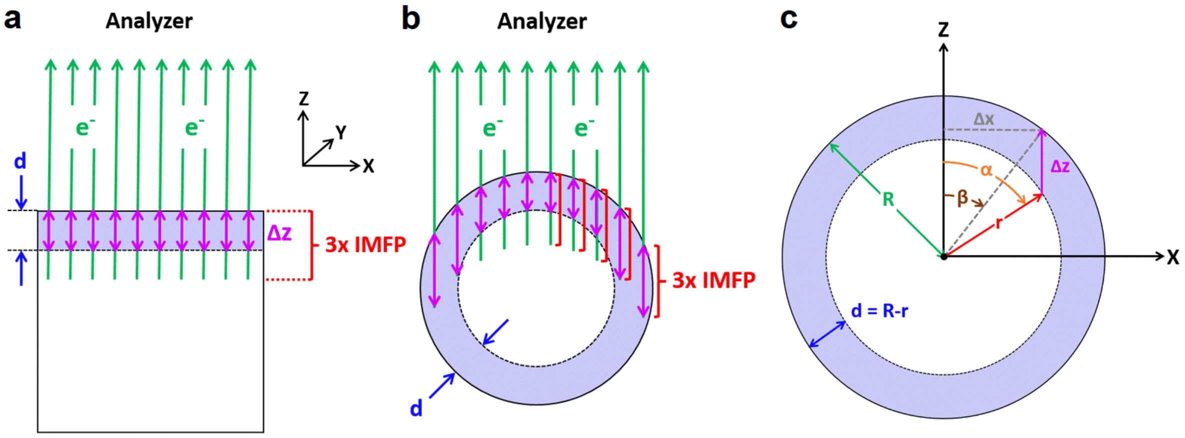

Figure S6| Comparison of XPS signal attenuation for photoelectrons emitted from a planar surface (a) and a single sphere (b). The thickness *d* defines the surface-near region in which a characteristic material property (e.g. adsorbates or band-bending potential) exists. For simplicity, only photoemission parallel to the detector axis *z* is considered. (c) Definition of the parameters and labels used in the numerical single-sphere XPS signal simulation.

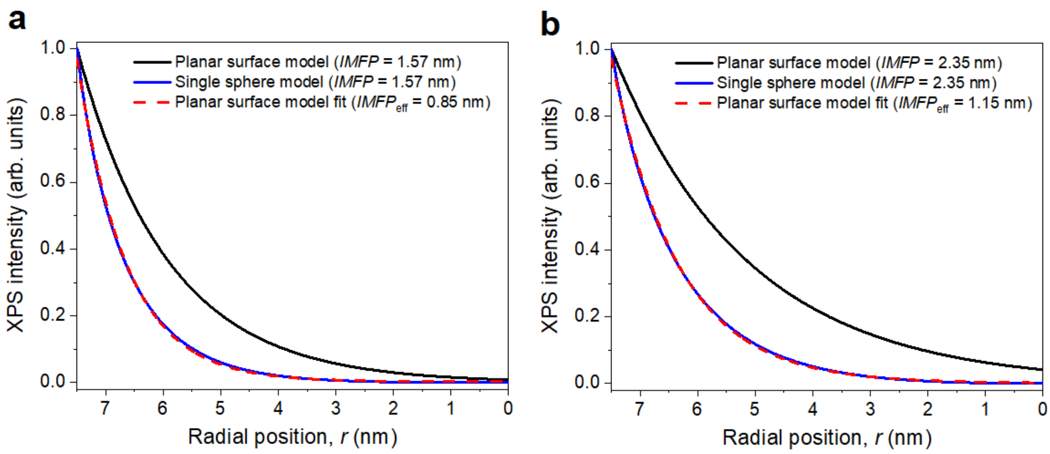

Figure S7| Simulated XPS intensity as a function of radial starting position using the IMFP of (a) O1s and (b) Zn3d (b) photoelectrons. The signal attenuation predicted by the SSM (blue lines) is compared to the signal evolution expected from a PSM with identical IMFP (black lines). Fits of the SSM trace to a mono-exponential decay function (red dashed lines) yield the effective IMFP.

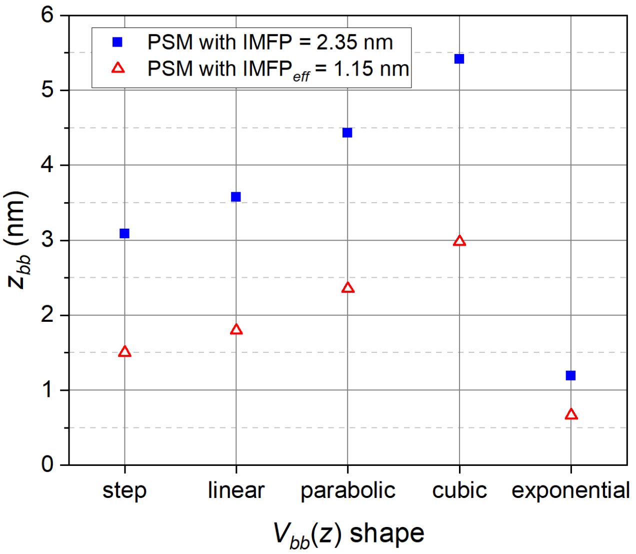

Figure S8| Comparison of the band-bending potential depth z_{bb} retrieved by numerical Zn3d XPS simulations using the standard IMFP (blue squares), and the effective IMFP (red triangles), deduced from the single sphere model.

References

(1) Cho, D.-Y.; Kim, J. H.; Na, K. D.; Song, J.; Hwang, C. S.; Park, B.-G.; Kim, Y.; Min, C.-H.; Oh, S.-J. Spectroscopic Evidence for Limited Carrier Hopping Interaction in Amorphous ZnO Thin Film. *Appl. Phys. Lett.* **2009**, *95*, 261903.

(2) Goossens, A. Potential Distribution in Semiconductor Particles. *J. Electrochem. Soc.* **1996**, *143* (6), L131–L133. https://doi.org/10.1149/1.1836900.

(3) Werner, W. S. M.; Chudzicki, M.; Smekal, W.; Powell, C. J. Interpretation of Nanoparticle X-Ray Photoelectron Intensities. *Appl. Phys. Lett.* **2014**, *104* (24), 243106. https://doi.org/10.1063/1.4884065.

(4) Shard, A. G.; Wang, J.; Spencer, S. J. XPS Topofactors: Determining Overlayer Thickness on Particles and Fibres. *Surf. Interface Anal.* **2009**, *41* (7), 541–548. https://doi.org/10.1002/sia.3044.

5.2 Nanoscale Confinement of Photo-Injected Electrons at Hybrid Interfaces

Hybrid functional materials promise enhanced electronic properties for light-harvesting applications in photovoltaics and photocatalysis. To fully realize their potential, detailed knowledge of photoinduced effects at their interfaces on microscopic length and time scales is required. Two N3-dye sensitized model systems based on ZnO and TiO_2 electrodes have been extensively studied in the time-domain. There is ongoing debate about the relatively weaker performance of ZnO compared to TiO_2. In both systems, an optical HOMO-LUMO excitation of the N3 dye leads to a MLCT singlet state of the system. Mobile charge carriers in TiO_2 appear on the sub-ps timescale[92] but they are delayed for the ZnO electrode by ~300 ps.[41,42,47,87] Two possible explanations for this intermediate state preceding the emergence of mobile CB electrons in ZnO have been suggested: intersystem crossing from the singlet to the triplet state within the dye[49–51] or an ICT configuration[41–44,47] where the electron has left the dye and resides at the dye-ZnO interface. An ultrafast TRXPS study presents evidence for the ICT scenario using constrained density functional theory to interpret transient signals of the dye.[45] Moreover, the combination of different ultrafast spectroscopic methods, accessing electron donor and acceptor side separately, presents strong evidence for the ICT.[41,42] The TRXPS study presented in this section shows dye oxidation and electron injection into the ZnO CB as two distinct events with clearly different timescales, for the first time within one experimental scheme. This further corroborates an ICT configuration as the reason underlying the delay in the charge injection from N3 dye into ZnO.

Another potential explanation for the superior performance of TiO_2 is its factor of ~10 larger permittivity compared to ZnO, leading to enhanced screening of photo-injected charges. While this electrostatic interaction between dye cation and injected electron has been suggested as detrimental,[42] there is evidence that electron mobility and other benchmarks such as dye-SC energy level alignment cannot explain the difference in performance.[47,183,184] Moreover, in a functioning DSSC the lifetime of the HOMO hole on the dye should also be reduced compared to a UHV study due to the presence of the electrolyte replenishing the missing (photo-injected) electron.

The presented study finds downward band bending within the outermost 6 nm of the ZnO nanocrystalline film that is enhanced by the photo-injected charges. The mobile charges are expected to be confined within this surface region while laterally mobile. A surface-near electron transport could potentially explain efficiency shortcomings of the ZnO-based device. Both, the usually more defect-rich surface region (compared to the bulk) as well as close proximity to the electrolyte could present trapping sites or open additional loss channels.

While pump-probe spectroscopy using ultrashort pulses provides temporal insight into charge transfer processes, retrieving spatially and temporally resolved information and especially the combination of the two is even more desirable. Ambient pressure XPS in the tender X-ray regime has been used to investigate liquid-solid interfaces relevant for photo-electrochemical cells (PEC) where it can access the crucial electronic potentials of electrolyte and SC electrode. Depth-resolved insights into the electrochemical double layer and type and width of SC band bending on the ~10 nm scale are accessible by varying the applied bias over the interface.[59–61] While section 5.1 demonstrates that soft X-ray XPS can access nanometer length scales of band bending in nanostructured ZnO, the work presented in this section is extending this method to the time-resolved domain. The retrieved spatio-temporal information on the photoinduced charge transfer at the N3-ZnO interface includes the position of the photo-generated hole on the N3 dye relative to the interface, and the electron injected into the ZnO CB, as well as the timescales associated with the injection from the ICT configuration into the ZnO CB, and eventually, the subsequent recombination of the CB electron with the dye HOMO hole.

The following publication is reprinted with permission from *J. Phys. Chem. Lett.* 2021, 12, 49, 11951–11959. Copyright 2021 American Chemical Society.

THE JOURNAL OF
PHYSICAL CHEMISTRY
LETTERS
A JOURNAL OF THE AMERICAN CHEMICAL SOCIETY

Nanoscale Confinement of Photo-Injected Electrons at Hybrid Interfaces

Stefan Neppl,[#] Johannes Mahl,[#] Friedrich Roth, Giuseppe Mercurio, Guosong Zeng, Francesca M. Toma, Nils Huse, Peter Feulner, and Oliver Gessner*

Cite This: J. Phys. Chem. Lett. 2021, 12, 11951−11959

ABSTRACT: A prerequisite for advancing hybrid solar light harvesting systems is a comprehensive understanding of the spatiotemporal dynamics of photoinduced interfacial charge separation. Here, we demonstrate access to this transient charge redistribution for a model hybrid system of nanoporous zinc oxide (ZnO) and ruthenium bipyridyl chromophores. The site-selective probing of the molecular electron donor and semiconductor acceptor by time-resolved X-ray photoemission provides direct insight into the depth distribution of the photoinjected electrons and their interaction with the local band structure on a nanometer length scale. Our results show that these electrons remain localized within less than 6 nm from the interface, due to enhanced downward band bending by the photoinjected charge carriers. This spatial confinement suggests that light-induced charge generation and transport in nanoscale ZnO photocatalytic devices proceeds predominantly within the defect-rich surface region, which may lead to enhanced surface recombination and explain their lower performance compared to titanium dioxide (TiO_2)-based systems.

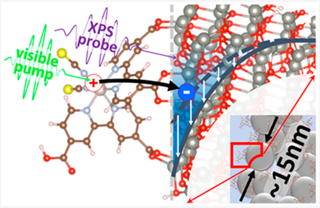

Nanostructured metal oxide semiconductor materials coupled to light-harvesting adsorbates are key components in sunlight-to-power and sunlight-to-fuel conversion schemes. Examples include photochemical cells for solar water-splitting and hybrid photovoltaics based on heterojunctions between molecular, quantum-dot, or nanoplasmonic sensitizers and transition metal oxide semiconductor electrodes.[1−6] These systems combine superior solar light absorption in the adsorbates with high photocatalytic activity of the substrates and the heterogeneous design enables spatial separation of oxidation and reduction half-reactions. Yet, observed efficiencies consistently lack, often substantially, behind theoretical limits. Understanding the photoinduced electron transfer and relaxation dynamics between sensitizers and semiconductor acceptors is crucial for advancing photocatalytic efficiency. This challenge encompasses the full photocatalytic reaction cycle: ultrafast charge injection, carrier transport and interfacial charge relaxation, as well as trapping at defect centers within the nanoporous semiconductor network. The complex interplay of these microscopic processes, and the vast range of relevant time and length scales, render it difficult to unambiguously identify reaction bottlenecks that limit the overall device performance.[7,8]

The time scale of the initial charge separation at the interface plays a decisive role and has been extensively studied, mainly with all-optical techniques that monitor the transient electronic state of the sensitizer and the appearance of free electrons inside the semiconductor.[9−16] However, very little is known about the underlying transient interfacial charge density redistribution, associated band structure modifications, and their spatiotemporal evolution within the first few nanometers below the surface. The band structure at the interface can be different from the bulk due to local space-charge imbalances that affect all energy levels near the surface. This potential energy landscape can either enhance interfacial charge separation of injected electrons (upward band bending) or favor their confinement and localization near the surface (downward band bending).[17] Since the near-surface region represents a significant volume fraction of nanostructured systems, it is the main gateway between localized photoexcited states on the sensitizers and delocalized charge distributions in the semiconductor that drive chemical reactions.

The hybrid interface between nanostructured ZnO and N3 (*cis*-bis(isothiocyanato)bis(2,2′-bipyridyl-4,4′-dicarboxylato)-ruthenium(II)) dye molecules offers a model system for understanding the complex interaction of photoinduced charge injection, separation, and transfer. ZnO-based nanomaterials are important components in photocatalytic devices,[18] and N3 is one of the most widely studied molecular sensitizers for hybrid light harvesting systems.[19,20] Thus, a more detailed understanding of the photoinduced electronic dynamics in N3/ZnO heterosystems provides technologically pertinent benchmarks for a variety of photoelectrochemical applications.

Received: August 11, 2021
Accepted: December 2, 2021

https://doi.org/10.1021/acs.jpclett.1c02648

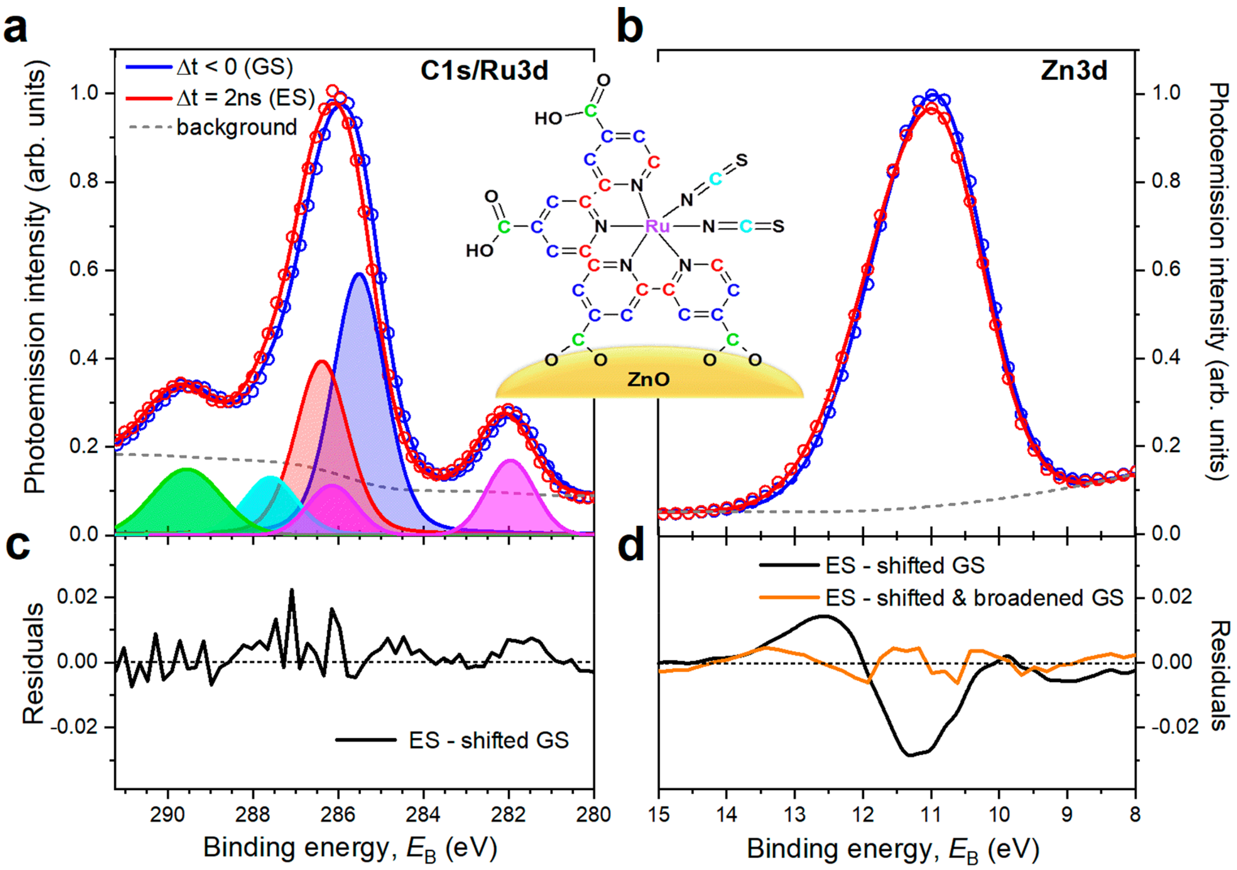

Figure 1. Signatures of photoinduced charge transfer in trXPS spectra of N3/ZnO heterojunction. (a) N3-dye C 1s/Ru 3d and (b) substrate Zn 3d trXPS spectra obtained with $h\nu$ = 888 eV and $h\nu$ = 614 eV, respectively. Blue circles are the ground state (GS) spectra; red circles represent the excited state (ES) measured at a pump−probe delay of Δt = 2 ns after 532 nm laser excitation. Solid lines correspond to constrained multipeak Gaussian fits for C 1s/Ru 3d and fits to an asymmetric Gaussian for Zn 3d. The color-coded schematic of the N3 dye molecular structure in the inset indicates the different contributions to the C 1s/Ru 3d spectrum. (c) Residual after subtracting the C 1s/Ru 3d GS spectrum shifted by ∼180 meV to higher E_B from the ES spectrum. (d) Minimum residual for the Zn 3d photoemission line using the same approach. The distinct bimodal shape indicates significant ES spectral broadening. The orange line is the minimum difference spectrum obtained by including a spectral broadening of ∼65 meV in addition to a rigid shift of ∼60 meV.

Here, we directly monitor the photoinduced electron dynamics and ensuing transient modulations of near-surface potential gradients in the interfacial region of this prototypical hybrid light harvesting system with picosecond time-resolved X-ray photoelectron spectroscopy (trXPS). Our model system consists of an N3 dye monolayer chemisorbed on a sintered film of ZnO nanoparticles with an average particle diameter of ∼15 nm (see the Supporting Information (SI), section A). Element-specific trXPS probes the transient interfacial electronic structure after optical excitation site-selectively from the molecular electron donor (C 1s/Ru 3d) and the semiconductor acceptor (Zn 3d) with picosecond temporal resolution and nanometer spatial sensitivity.

The measurements provide detailed information on the spatial distributions of both electrons and holes across the interface during the photoinduced charge transfer and recombination on time scales ranging from tens of picoseconds up to several microseconds. Nanoscale confinement of photoinjected electrons within <6 nm from the semiconductor surface is deduced from transient changes in the surface potentials, which are revealed by line shape modulations and spectral shifts of the Zn 3d photoemission. The C 1s/Ru 3d response of the molecular donor exhibits an additional transient shift due to the impact of the (electronic) hole located on the photo-oxidized dye. A charged capacitor model is used to describe the charge-separated state at the N3/ZnO interface, from which the average distance of the hole density from the substrate surface is estimated to ∼0.3−1.2 nm. This range is in agreement with the location of the highest occupied molecular orbital (HOMO), from which the injected electron is removed. Furthermore, strong evidence is provided that electron injection into the ZnO conduction band (CB) proceeds via a two-step process involving an intermediate interfacial charge transfer (ICT) configuration. The existence of such transient ICT states has previously been suggested[9−12,21−24] but has been in competition with a two-state injection model, where intramolecular relaxation by intersystem crossing precedes electron transfer to the substrate.[25−27]

The results provide comprehensive insight into the spatiotemporal evolution of the photoinduced interfacial charge redistribution. Both the intermediate ICT configurations as well as the confinement of injected electrons in the defect-rich surface region of the nanostructured substrate significantly increase the odds for charge recombination and, thus, contribute to the challenges of using ZnO as electrode material in solar light harvesting applications. The lifetime of the ICT intermediate as well as the range of electron-dye

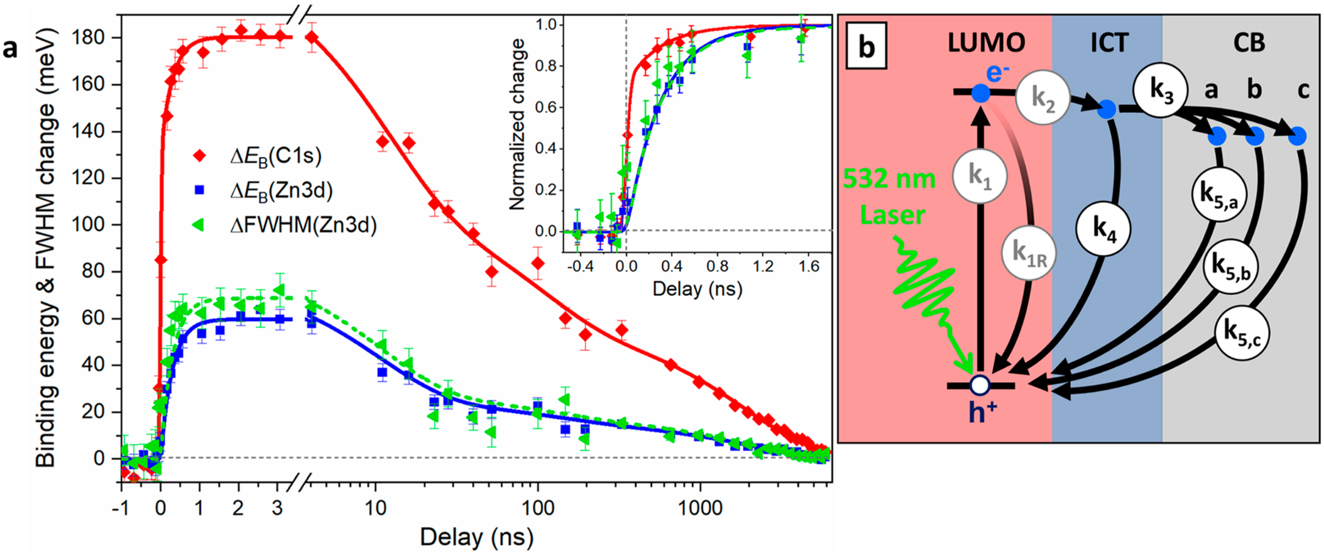

Figure 2. (a) Temporal evolution of the trXPS response. C 1s (red diamonds) and Zn 3d (blue squares) photoelectron energy shifts and Zn 3d photoline fwhm change (green triangles) as a function of pump−probe delay (note the transition from a linear to a logarithmic delay axis for $\Delta t >$ 3 ns). Solid lines are the results of fits to a coupled rate equation model schematically illustrated in (b). Photoinduced HOMO−LUMO excitation (k_1) in the dye (red) is followed by the population (k_2) of an ICT configuration (blue) and by subsequent electron injection (k_3) into the ZnO CB (gray). Recombination of the injected electrons with the dye HOMO holes (h^+) involves three rates ($k_{5,a}$, $k_{5,b}$, $k_{5,c}$), corresponding to the three slopes discernible for delays >4 ns in (a). The inset in (a) (using normalized amplitudes) highlights the delayed onset of the ZnO responses relative to the N3-dye related response due to the intermediate population of the ICT state. The model is described in more detail in section H of the SI.

cation recombination time scales determined here by trXPS are in reasonable to good agreement with values derived in previous time-resolved optical and THz spectroscopy studies.[9,10,14,23]

In the trXPS experiment, the heterojunction is excited by ∼10 ps long laser pulses at a wavelength of 532 nm, and the photoinduced dynamics are probed using a monochromatized soft X-ray pulse train from the Advanced Light Source (ALS), see Experimental Section for details. Figure 1 compares C 1s/Ru 3d (a) and Zn 3d (b) trXPS spectra associated with the N3-dye and the ZnO substrate, respectively. Data (circles) were recorded before (blue) and $\Delta t = 2$ ns after (red) resonant HOMO−LUMO (lowest unoccupied molecular orbital) excitation of the dye with a 532 nm, 1.1 mJ/cm^2 laser pulse, leading to an estimated 6% excitation fraction (see section G of the SI). Details of the fit procedures (solid lines) and the decomposition of the C 1s/Ru 3d spectrum[21,28] are described in section B of the SI. For both regions, the excited-state (ES) spectrum is shifted to higher binding energies (E_B) compared to the ground state (GS) spectrum. However, the ∼180 meV photoinduced shift of the N3-related C 1s/Ru 3d photoemission lines is significantly larger than the corresponding Zn 3d shift of only ∼65 meV.

The photoresponses of the two sides of the heterojunction also differ in their line shape dynamics. The C 1s/Ru 3d ES spectrum is well described by a rigid shift of the GS spectrum. Figure 1(c) shows the difference between the C 1s/Ru 3d ES spectrum and the GS spectrum shifted by 180 meV to higher E_B, indicating good agreement within the signal-to-noise ratio of the experiment. Note that this rigid shift does not exclude smaller differential shifts between C 1s and Ru 3d as previously found for $\Delta t \leq 1$ ps.[21] In contrast, a similar approximation for the ES Zn 3d spectrum by a shifted GS spectrum yields a significant residual (black line in Figure 1(d)), which points toward an additional line shape change. This effect is captured by including a spectral broadening of the GS spectrum in addition to a shift, as indicated by the corresponding orange residual in Figure 1(d). Figure S3 in section B of the SI illustrates and analyzes the signatures of shift and broadening effects in the Zn 3d spectrum in greater detail. We emphasize that no laser-induced changes in the Zn 3d position or shape are observed for bare ZnO electrodes under laser excitation conditions identical to those of the dye-sensitized samples (see SI section D). This excludes photoinduced electron−hole pair generation within ZnO, mediated by defect levels within the 3.30 eV bandgap, as an explanation for the observed Zn 3d trXPS response.[29−31] Thus, the origin of transient modulations in the Zn 3d line shape shown in Figures 1 and 2 must be directly connected to heterogeneous charge transfer across the N3/ZnO interface.

Fitting the pump−probe-delay-dependent C 1s/Ru 3d and Zn 3d photolines with a set of model functions provides the temporal evolution of spectral shifts and peak widths as a function of pump−probe delay (see section B of the SI for details). The results are displayed in Figure 2(a). Time-dependent shifts of the C 1s (red) and Zn 3d (blue) peaks are shown along with changes in the full-width-at-half-maximum (fwhm) of the Zn 3d peak (green). Symbols represent the peak shifts and widths, solid lines indicate fit results based on a coupled rate equation model of the time-dependent electron populations in the N3 LUMO, at the surface (ICT states), and in the ZnO CB. The model is schematically summarized in Figure 2(b) (see section H of the SI for details). It describes a sequential pathway, whereby the initial HOMO−LUMO excitation (k_1) decays to form an ICT configuration (k_2), from which electrons are released into the ZnO CB (k_3). Possible electron-dye cation recombination pathways from all these intermediates are taken into account. In particular, back-transfer and recombination of electrons injected into the ZnO CB is described by three independent exponential decays ($k_{5,a}$,

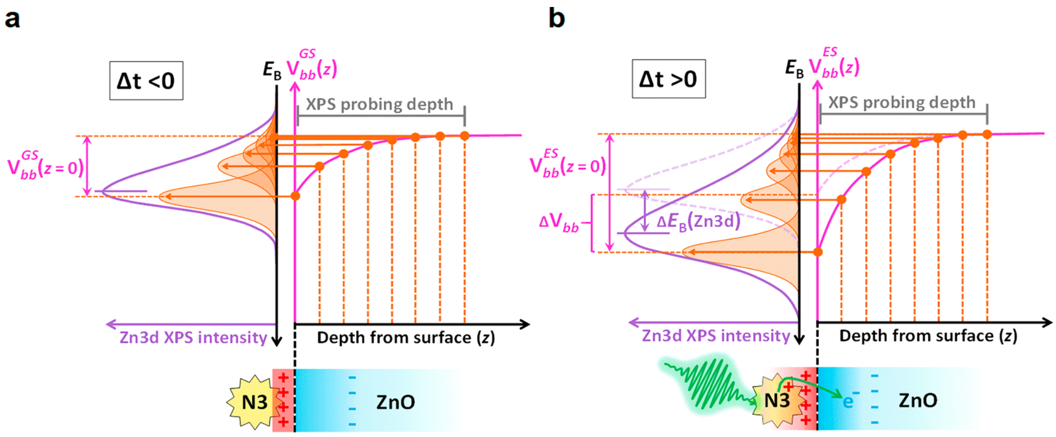

Figure 3. Schematic illustration of band bending effects in the Zn 3d line shape. The near-surface potential $V_{bb}(z)$ (pink) within the ZnO space-charge region determines the binding energies of contributions from various depths (orange) to the overall Zn 3d XPS signal for both the ground state (a) and the photoexcited N3/ZnO junction (b). Light-induced charge injection enhances the pre-existing internal field and induces further downward band bending ΔV_{bb}, which is larger than the apparent Zn 3d peak shift ΔE_B(Zn 3d) due to the averaging over different photoemission signals within the XPS probing depth. The correlation between XPS peak shifts and broadening encodes the spatial profile of $V_{bb}(z)$, which is retrieved by comparison of the Zn 3d photoemission feature to numerical simulations (Figure 4).

$k_{5,b}$, $k_{5,c}$). The C 1s and Ru 3d peaks exhibit identical time-dependent shifts and no broadening within the experimental uncertainty (see SI section B). Thus, we limit our discussion of the molecular response to the energy shifts of the C 1s lines associated with the dye. The inset in Figure 2(a) shows a magnified view of the region near zero pump−probe delay using normalized amplitudes to highlight differences in dynamic trends.

A key observation is that the changes in the Zn 3d shift and fwhm remain correlated throughout the entire lifetime of the photoinduced effects, from their sub-ns emergence to their final disappearance, ~6 μs after optical excitation. The interpretation of these results requires a more detailed understanding of the composition of the Zn 3d spectrum and how it is affected by the photoinduced dynamics. Generally, XPS spectra of condensed phase materials contain contributions that emerge, most intensely, from the surface and, with decreasing intensity, from various depths within the material (Figure 3(a)). Previous steady-state studies have demonstrated that the decomposition of XPS signal contributions from different depths can be used to reconstruct interfacial potential energy surfaces.[32−35] As described in the following, we translate this approach into the time domain to monitor the temporal evolution of the near-surface potentials in the ZnO substrate as a result of the photoexcitation of the interface (Figure 3(b)). The technique is based on modeling the space-charge-induced fields and corresponding electronic structure of the hybrid junction in both the ground and excited states.

The GS band structure of the nanostructured ZnO substrate has been characterized by steady-state ultraviolet photoemission spectroscopy (UPS) and XPS[32] and agrees with previously observed downward band bending for bare and hydroxylated ZnO single crystals under comparable vacuum conditions.[36,37] Subsequent N3 adsorption has no significant impact on the semiconductor band structure (see SI section C). Therefore, the N3/ZnO heterojunction is characterized by the same surface potential as the bare ZnO substrate, which is schematically illustrated in Figure 3(a). The GS band bending $V_{bb}^{GS}(z)$ has a maximum at the surface $V_{bb,max}^{GS} = V_{bb}^{GS}(z = 0) =$ 0.79 ± 0.03 eV and is approximated by a cubic depth profile according to $V_{bb}^{GS}(z) = V_{bb,\max}^{GS} \cdot \left(\frac{z_{bb}^{GS} - z}{z_{bb}^{GS}}\right)^3$, as reported in detail in ref 32. Here, $z_{bb}^{GS} = 5.1 \pm 0.7$ nm indicates the distance from the surface ($z = 0$) at which the electronic bands reach their bulk value. Note that this depth is the asymptotic limit of the band bending region, while the 1/e equivalent decay depth of the potential is $z_{bb}^{dec} \approx 1.5$ nm. This band structure effectively represents a potential well for photoinjected electrons. We note that the significant band bending determined here and in ref 32 is not necessarily expected for nanostructured semiconductors[38] and makes surface properties (rather than those of the bulk) highly relevant for electron transport and photocatalytic activity of nanoporous ZnO.[29] The pronounced band bending $V_{bb}(z)$ inside the ZnO electrode has significant impact on the measured Zn 3d line shape, as the escape depth of the Zn 3d photoelectrons in the soft X-ray region is comparable to z_{bb}^{dec}. The downward band bending results in a depth-dependent binding energy at different distances from the interface. This effect induces notable spectral broadening of the Zn 3d line shape and, conversely, opens up the possibility to reconstruct near-surface potential energy changes from an analysis of the Zn 3d line shape and peak shift. The depth-dependent surface potential analysis also provides access to the corresponding spatial distribution of the photoinjected carrier density $\Delta n_e(z)$ via the Poisson relationship $\frac{\mathrm{d}^2 V_{bb}(z)}{\mathrm{d}z^2} \propto n_e(z)$, where $n_e(z)$ is the electron density in the ZnO near-surface region. The validity of the model illustrated in Figure 3 to assess transient electron density distributions in the substrate CB is confirmed by performing experiments at two significantly different photon energies, leading to different line broadenings and shifts, but the same physical conclusion, as outlined in the following. The shape of the potential has been extensively tested against possible alternatives, as described in ref 32, clearly identifying the cubic depth dependence as the most likely scenario.

As illustrated in Figure 3(b), interfacial charge redistribution initiated by electron injection from the excited N3 dye into the semiconductor amplifies the pre-existing internal electric field, leading to an increased downward band bending of the electronic levels and, therefore, a shift to higher binding energies and further broadening of the Zn 3d envelope. These correlated effects are used to quantify the photoinduced band bending dynamics at the molecule−semiconductor interface. A detailed description of this analysis is provided in section F of the SI. A key benchmark that connects the measured trXPS spectra with the functional form of $V_{bb}^{ES}(z)$ is the relation between the spectral shifts, ΔE_B, and the spectral broadening, Δfwhm, as illustrated in Figure 4. Shown are the observed excited state ΔE_B(Zn 3d) vs Δfwhm relations at X-ray photon energies of $h\nu$ = 614 eV (red diamonds) and $h\nu$ = 320 eV (blue squares), along with the results of a simulation (solid lines). The weak optical excitation of the N3 dyes for our experimental conditions (≈6%, SI section G), induces relatively small modifications of $V_{bb}^{GS}(z)$. We therefore assume the same functional form for the photoexcited state potential of the heterojunction as for the ground state, i.e., $V_{bb}^{ES}(z) = V_{bb,\max}^{ES} \times \left(\frac{z_{bb}^{ES} - z}{z_{bb}^{ES}}\right)^3$. Note that the cubic form of $V_{bb}(z)$ corresponds to a linear depth dependence if the electron density $n_e(z)$ via the Poisson relationship. Using this potential shape and a convolution of spectral contributions from different depths z as described in section F of the SI, a global parameter optimization results in the solid lines shown in Figure 4. Best agreement between the simulation and the two measurements is achieved for $V_{bb,max}^{ES} = 0.89 \pm 0.04$ eV and $z_{bb}^{ES} = 4.1_{-0.8}^{+1.5}$ nm (error limits indicate the parameter range where the χ^2 value of the fit is less than twice its minimum). This means that the interfacial electron injection further enhances the downward bending of the electronic levels below the ZnO surface by ∼100 meV. Simulation results for the upper and lower bounds for z_{bb}^{ES} are indicated by dash-dotted and dashed lines, respectively, in Figure 4, demonstrating the sensitivity of the ΔE_B(Zn 3d) − Δfwhm correlation to small changes in z_{bb}. The two different photon energies used to record the data sets in Figure 4 translate into a ∼40% difference in XPS sampling depth[39] (SI section F). The combination of both data sets therefore provides a rigorous test for evaluating the spatial dependence of $V_{bb}^{ES}(z)$. As expected, the $h\nu$ = 320 eV data exhibit larger peak shifts and less spectral broadening due to the smaller probing depth at this lower photon (and therefore electron kinetic) energy.

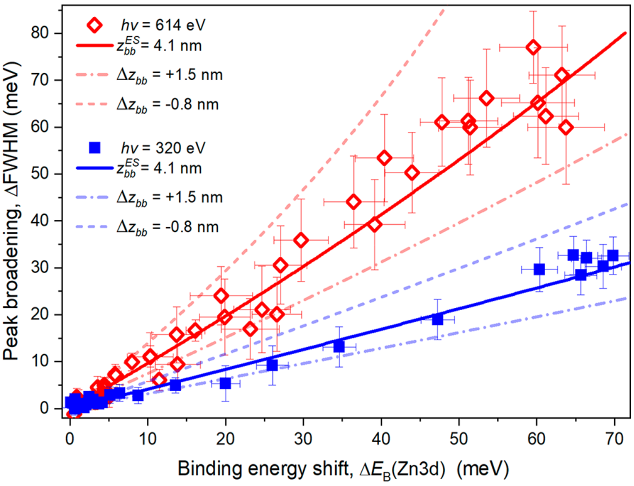

Figure 4. Evidence for nanoscale confinement of injected electrons at the interface. The correlation between the light-induced Zn 3d XPS peak shifts and broadening measured with $h\nu$ = 614 eV (red diamonds) and $h\nu$ = 320 eV (blue squares) is compared to numerical simulations with a cubic band shape approximation for $V_{bb}^{ES}(z)$. A global parameter optimization on both data sets (solid lines) reveals a maximum spatial extent of the potential gradient below the ZnO surface of $z_{bb}^{ES} = 4.1_{-0.8}^{+1.5}$ nm, and a light-induced modulation of the surface potential of $\Delta V_{bb} = 100 \pm 20$ meV. The high spatial sensitivity of the modeling is demonstrated by comparing the data with predicted correlation traces for z_{bb}^{ES} variations according to its indicated uncertainty margins (dashed and dashed-dotted lines). Since the light-induced changes of $V_{bb}(z)$ are directly linked to the injected charge density via the Poisson relation, these limits for the potential depth also restrict the spatial distribution of the injected charge carries $\Delta n_e(z)$ to the same length scale at the N3/ZnO interface.

Due to the Poisson relation between potential gradients and charge carrier densities, the injected charge carrier distribution $\Delta n_e(z)$ must be spatially confined to $z \leq z_{bb}^{ES}$, i.e., to a maximum depth of ∼6 nm below the dye−semiconductor interface. This upper limit for the electron's penetration depth accounts for the uncertainty in the determination of z_{bb}^{ES} based on a planar sample surface model, while an isolated single sphere model would yield an even smaller value.[32] The actual surface topography of the ZnO films likely lies in between these two limiting cases.

We now turn to the interpretation of the transient C 1s peak shifts ΔE_B(C 1s) associated with the molecular component of the hybrid junction. Electronic states in chemisorbed monolayers experience the full change of the surface potential ΔV_{bb}.[40] Thus, the observed maximum C 1s peak shift ΔE_B(C 1s) = 180 meV (Figure 2(a), delay Δt = 2 ns) consists of two contributions, the surface potential change $\Delta V_{bb} = V_{bb,\max}^{ES} - V_{bb,\max}^{GS} \approx 100$ meV and a residual shift $\Delta E_{N3} = \Delta E_B(\text{C 1s}) - \Delta V_{bb} \approx 80$ meV. We attribute ΔE_{N3} to the molecular response, representing the interfacial potential drop (IPD) between the oxidized N3 dye molecules and the ZnO surface. Quantitative analysis of the IPD provides direct access to interfacial charge configurations on a (sub)nm scale. The IPD of a layer of charged molecules adsorbed to a solid substrate is approximated by a modified parallel-plate capacitor model that takes into account the charge density and dielectric properties of the molecules, as well as the average distance of the molecular charges from the surface.[41] Conversely, the distance of the charges from the substrate can be estimated from a known charge density and IPD. As described in section G of the SI, this procedure results in an estimate for the hole distance from the ZnO surface of ∼0.3−1.2 nm. This estimate corresponds approximately to the position of the Ru center atom and NCS groups, where most of the amplitude of the HOMO is located,[21] relative to the surface. In the photo-oxidized state of the dye, the hole density distribution is expected to closely resemble the HOMO density distribution.[21] Values for the total height of the dye with respect to the substrate surface lie between 1.0 and 1.3 nm for different anchoring geometries on TiO_2,[19,42] which is compatible with the retrieved hole-surface distance based on IPDs.

The interpretation of ΔE_{N3} as the result of charge transfer from the dye to the substrate is corroborated by a trXPS study of photoexcited N3 molecules adsorbed on a gold substrate (see SI section I). Here, direct electron injection into the metal substrate and efficient screening of the injected charges is expected, corresponding to an immediate spectroscopic response from the ionized dye. Indeed, the C 1s/Ru 3d photolines in the N3/Au system exhibit an instrument-limited response similar to $\Delta E_{N3}(\Delta t)$ (see SI Figure S10). The molecular response of the N3/ZnO system also appears within the instrument response function (IRF) of the experiment. The IRF-limited onset of the dye oxidation strongly favors the fast population of intermediate ICT configurations, rather than intramolecular relaxation within a two-state model, as the reason for the previously observed delayed generation of free charge carriers in the ZnO CB.[9,10,23]

Closer inspection of the early time dynamics reveals a delayed rise of the ZnO-related trXPS signals compared to ΔE_{N3}; see the inset in Figure 2(a). In this context, it is important to note that the excited electrons have to reside *inside* the ZnO semiconductor to alter the space-charge balance and the resulting internal potential $V_{bb}(z)$.[17,29,30,33,40,43,44] The combination of the instantaneous dye oxidation described above and the delayed response of ΔE_B(Zn 3d) therefore provides clear evidence for a transient retention of the excited charge carriers in ICT states, before their release into the CB, on an overall time scale of $\lesssim$1 ns. These findings align with previous observations of delayed charge separation due to the intermediate population of ICT configurations.[9,10,12,21] Within this framework, ΔE_B(Zn 3d) and (ΔE_B(C 1s) − ΔE_{N3}) are solely governed by the time-dependent electron population in the CB of ZnO, $P_{CB}(t)$, whereas ΔE_{N3} is defined by the net hole population in the N3 monolayer. Since population of ICT states ($P_{ICT}(t)$) from HOMO−LUMO excited states is much faster than both intramolecular relaxation and the instrument response,[10,15,21,45] the hole population on the N3 dye molecules can be approximated by $P_H(t) \approx P_{CB}(t) + P_{ICT}(t)$. Based on these dynamic electron populations (Figure 5), fits to first-order coupled rate equations are used to determine the mean ICT state lifetime from the transient energy shifts at Δt < 3 ns (SI section H). The extracted ICT decay constant of 300 ± 80 ps is consistent with time scales reported previously for injection intermediates at the N3/ZnO interface.[9,10,23,46] We note that $\Delta E_{N3}(t) = \Delta E_B(\text{C 1s})(t) - \Delta E_B(\text{Zn 3d})(t)$ (not shown) exhibits indications for an overshoot of several tens of meV immediately after photoexcitation, which vanishes on the same time scale as the ICT lifetime. This effect is consistent with previous observations that ICT states in the N3/ZnO system may, in addition to charge separation, also decay via electron−hole recombination on the dye.[10] Unfortunately, however, the density of data points in this time delay region is not sufficient to provide a quantitative estimate for the ratio of ICT decay by electron−hole recombination and charge injection into the ZnO CB.

We emphasize that the sensitization time of the ZnO electrodes was restricted to 3 min in order to exclude any surface degradation by dissolution of Zn ions from the electrode and formation of N3−Zn^{2+} aggregates.[15] The observation of ICT state signatures in our work therefore establishes intermediate steps in the charge injection process as an intrinsic property of the pristine N3/ZnO interface. A recent valence photoemission study places the ICT state's center ~0.2 eV above the CB minimum at the surface with a spectral width of ~0.8 eV.[24] Combined with the excited-state downward band bending of ~0.89 ± 0.04 eV deduced here, it follows that even initially injected "hot" electrons are not able to overcome the potential barrier separating the surface and core regions of individual nanoparticles of the ZnO nanoporous network. This distinct near-surface potential landscape points toward an anisotropic carrier mobility, with strong confinement normal to the surface. Time-resolved THz and IR absorption studies[9,12,23] clearly indicate the existence of mobile charge carriers in the ZnO CB as a result of electron injection, but the results presented here show that these electrons do not penetrate into the nanoparticle bulk for particle sizes beyond ~15 nm. Thus, the most likely scenario for charge transport in such semiconductor substrates is lateral carrier diffusion along the interface.[36] This has general implications for ZnO-based photocatalytic devices, since near-interfacial diffusive transport of photoexcited carriers through nanoporous networks may activate additional surface-recombination pathways. These findings represent a possible explanation for the lower efficiencies of N3/ZnO devices compared to their TiO_2-based counterparts. We note that additional measurements on N3/TiO_2 systems would be required for a more quantitative comparison. Generally, however, smaller band bending effects would be expected for TiO_2 nanoparticles due to the significantly higher dielectric constant of TiO_2 compared to ZnO.[23,47]

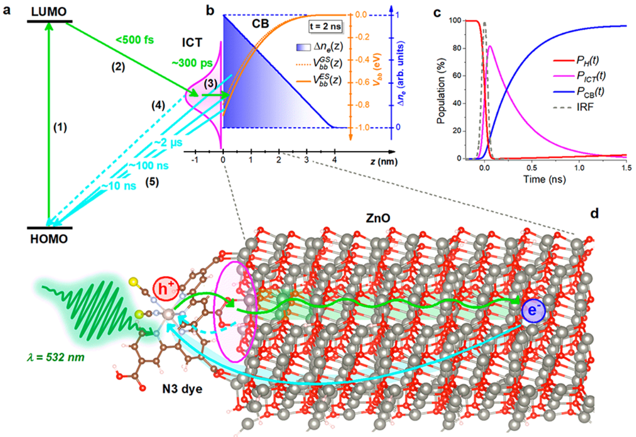

Figure 5. Spatiotemporal dynamics of the light-induced charge redistribution. (a) Schematic of the electron injection and recombination channels involved in the transient charge generation at the N3/ZnO hybrid interface. A lifetime of ~300 ps for the ICT states is derived from a fit of the delayed onset of the Zn 3d response shown in Figure 2(a) to a coupled rate equation model for sequential 2-step injection. The long-term (≥10 ns) relaxation time scales are determined by a fit of the ns−μs dynamics in Figure 2(a) to a triexponential decay. (b) Modulation of the CB minimum within the surface-near region of the ZnO nanoparticles (orange) and spatial distribution of the injected charge density $\Delta n_e(z)$ at t = 2 ns (blue, deduced from numerical modeling of the data as shown in Figure 4). (c) Time-dependent population of HOMO electrons ($P_H(t)$), ICT states ($P_{ICT}(t)$) and the ZnO CB ($P_{CB}(t)$) (IRF = instrument response function; populations are normalized to the number of excited electrons). (d) Illustration of the charge injection and recombination dynamics, using the energetically most favorable N3 adsorption geometry on a model ZnO($10\bar{1}0$) surface.

The long-term dynamics of the Zn 3d and C 1s energy shifts in Figure 2(a) are well approximated by the sum of three exponentially decaying contributions (see SI section H), with relaxation times (relative amplitudes) of 10 ± 5 ns (40%), 100 ± 30 ns (30%), and 2.0 ± 0.3 μs (30%). These few-ns to few-μs time scales fall within the range of recombination times previously observed for N3/ZnO junctions.[14] The appearance of three distinct recombination time scales, rather than a single stretched exponential decay, may point to the existence of distinct recombination pathways rather than a continuous

https://doi.org/10.1021/acs.jpclett.1c02648
J. Phys. Chem. Lett. 2021, 12, 11951−11959

distribution.[48] Further studies on ZnO electrodes with different types of impurities and well-controlled concentrations are necessary to reliably link individual decay times to specific recombination pathways, which is beyond the scope of this study.

The sequence of microscopic processes and their associated length scales that enable charge generation at the photoexcited N3/ZnO hybrid junction is schematically summarized in Figure 5: (a) Ultrafast HOMO−LUMO excitation of the dye (1) is followed by rapid (<500 fs) electron transfer to the ICT state (2). The ICT states depopulate on an overall time scale of ∼300 ps by either transport of electrons into the CB of the ZnO nanoparticles (3), leading to a modulation of the electric field inside the space-charge region, or electron−hole recombination (4). The recombination of injected electrons with the N3 HOMO-hole (5) proceeds through several relaxation pathways involving multiple time scales.[14]

The results presented here demonstrate the capability of trXPS to gain nanoscale insight into transient charge carrier distributions at complex interfaces. Both the injected electron density distribution (Figure 5(b)) and the appearance and location of the HOMO hole remaining on the sensitizer are simultaneously characterized through the near-surface potential $V_{bb}(z)$ and the interfacial potential drop, respectively. Note that, principally, trap states and their spatial distribution within the sample could have an impact on the reconstructed electron densities. However, as discussed in sections C and D of the SI, no direct evidence for trap states has been detected in either the bare or the sensitized sample. The fact that the same cubic potential depth profile, corresponding to a linearly varying electron density distribution, successfully describes the trXPS results for two different photon energies with two significantly different probing depths (Figure 4), further indicates that trap states, if present, are unlikely to lead to significant deviations from the distributions outlined in Figure 5(b).

The delay between the appearance of the HOMO hole and the modifications of $V_{bb}(z)$ provides strong evidence for the intermediate population of ICT configurations (Figure 5(b), (c)), as the root cause for delayed charge injection. Quantitative insight into $V_{bb}(z)$ reveals that the photoinjected electrons themselves enhance the already strong confinement along the surface normal within a <6 nm wide region by increasing the ≈0.79 eV potential well depth of the ground state by an additional ≈100 meV. This finding is crucial for ZnO-based device designs, as the surface region of nanostructured ZnO electrodes seems to play a key role in facilitating charge transport. We note that the introduction of electrolyte environments in working devices may have some impact on the interfacial dynamics. However, as outlined in ref 32, the pronounced band bending in the ground state ZnO substrate is the result of electron transfer doping from surface hydroxyl groups, formed upon contact of background water molecules with the ZnO surface. The study also strongly suggests that under the conditions of the trXPS experiment, the surface is fully hydroxylated. Thus, it is not clear how pronounced the impact of additional electrolyte molecules in the vicinity of the interface would be, but it would likely depend on their chemical nature. Future *in-operando* studies of complex hybrid systems, especially in the presence of electrolytes and with externally biased electrodes, feasible via ambient pressure trXPS, hold great potential to give a more complete picture of the spatiotemporal dynamics of carrier transport across these technologically pertinent interfaces under realistic working conditions.[33,34]

■ EXPERIMENTAL SECTION

Methods. The trXPS experiments were performed at Beamline 11.0.2 of the Advanced Light Source (ALS), using the HPPES (High Pressure Photoemission Spectroscopy) endstation[49] in combination with a previously described time-tagging approach to enable picosecond time-resolved measurements.[44,50,51] The ALS was operated in two-bunch mode with an X-ray pulse spacing of 328.2 ns and an X-ray pulse duration of ∼70 ps. The 532 nm output of the pump laser system provided 10 ps long pulses at a repetition rate of 126.9 kHz and was synchronized to the ALS X-ray pulse train.[50,51] The X-ray beam was focused to a spot size of $A_X = 70 \times 65$ μm^2, whereas the laser spot size was adjusted to $A_L = 165 \times 210$ μm^2. Spatial overlap was achieved and maintained with an accuracy of <10 μm. The pump wavelength of 532 nm matched the absorbance maximum of the N3 dye in the visible regime (see SI Figure S1(c)) and the employed pulse fluence of $F_p = 1.1$ mJ/cm^2 corresponded to an excitation probability of ≈6% (see section G of the SI for details).

Sample Characterization. Details of the nanocrystalline ZnO electrode preparation, the characterization via scanning electron microscopy (SEM), and the sensitization process can be found in section A of the SI.

Statistical Analysis. Details of the composition of the C 1s/Ru 3d XPS spectrum as well as the fit procedures to extract energy shifts and line shape broadening effects from C 1s/Ru 3d and Zn 3d spectra can be found in section B of the SI. An in-depth description of the procedure to retrieve ZnO near-surface potential gradients by numerical simulation of the Zn 3d XPS spectra is given in section F of the SI.

■ ASSOCIATED CONTENT

Supporting Information

The Supporting Information is available free of charge at https://pubs.acs.org/doi/10.1021/acs.jpclett.1c02648.

> (A) Experimental details, sample preparation and characterization; (B) peak fitting analysis of the trXPS spectra; (C) ground state electronic structure of the N3/ZnO interface; (D) control trXPS experiments on bare ZnO electrodes; (E) laser fluence dependence of trXPS effects; (F) retrieving potential gradients by numerical XPS peak simulations; (G) parallel plate capacitor model for interfacial potential drop; (H) rate equation model for 2-step charge injection and recombination; (I) time-resolved XPS of N3 adsorbed to a gold substrate (PDF)

■ AUTHOR INFORMATION

Corresponding Author

Oliver Gessner − *Chemical Sciences Division, Lawrence Berkeley National Laboratory, Berkeley, California 94720, United States;* orcid.org/0000-0003-4709-2822; Email: ogessner@lbl.gov

Authors

Stefan Neppl − *Chemical Sciences Division, Lawrence Berkeley National Laboratory, Berkeley, California 94720, United States;* Present Address: Paul Scherrer Institut, 5232 Villigen, Switzerland; orcid.org/0000-0003-0536-1932

Johannes Mahl − *Chemical Sciences Division, Lawrence Berkeley National Laboratory, Berkeley, California 94720, United States; Physics Department, Universität Hamburg and Center for Free-Electron Laser Science, 22761 Hamburg, Germany*
Friedrich Roth − *Institute of Experimental Physics, TU Bergakademie Freiberg, 09599 Freiberg, Germany*
Giuseppe Mercurio − *Physics Department, Universität Hamburg and Center for Free-Electron Laser Science, 22761 Hamburg, Germany;* Present Address: European XFEL, 22869 Schenefeld, Germany
Guosong Zeng − *Chemical Sciences Division and Liquid Sunlight Alliance, Lawrence Berkeley National Laboratory, Berkeley, California 94720, United States*
Francesca M. Toma − *Chemical Sciences Division and Liquid Sunlight Alliance, Lawrence Berkeley National Laboratory, Berkeley, California 94720, United States;* orcid.org/0000-0003-2332-0798
Nils Huse − *Physics Department, Universität Hamburg and Center for Free-Electron Laser Science, 22761 Hamburg, Germany;* orcid.org/0000-0002-3281-7600
Peter Feulner − *Physics Department, Technische Universität München, 85748 Garching, Germany*

Complete contact information is available at:
https://pubs.acs.org/10.1021/acs.jpclett.1c02648

Author Contributions

#S.N. and J.M. contributed equally to this work.

Notes

The authors declare no competing financial interest.

ACKNOWLEDGMENTS

This work was supported by the Atomic, Molecular, and Optical Sciences Program of the U.S. Department of Energy, Office of Science, Office of Basic Energy Sciences, Chemical Sciences, Geosciences and Biosciences Division, through Contract No. DE-AC02-05CH11231. The research used resources of the Advanced Light Source, which is a DOE Office of Science User Facility under contract no. DE-AC02-05CH11231. J.M. acknowledges support through the ALS Doctoral Fellowship in Residence Program. S.N. acknowledges financial support from the Alexander von Humboldt Foundation and the Helmholtz Association, and P.F. acknowledges financial support from the Deutsche Forschungsgemeinschaft (e-conversion Cluster of Excellence). F.R. acknowledges financial support by the VI 419 of the Helmholtz Association. F.M.T. and G.Z. acknowledge support by the Liquid Sunlight Alliance, which is supported by the U.S. Department of Energy, Office of Science, Office of Basic Energy Sciences, Fuels from Sunlight Hub under Award Number DE-SC0021266. Support by Hendrik Bluhm during the experiments at ALS beamline 11.0.2 is greatly appreciated.

REFERENCES

(1) Hardin, B. E.; Snaith, H. J.; McGehee, M. D. The Renaissance of Dye-Sensitized Solar Cells. *Nat. Photonics* **2012**, *6*, 162−169.

(2) Atwater, H. A.; Polman, A. Plasmonics for Improved Photovoltaic Devices. *Nat. Mater.* **2010**, *9*, 205−213.

(3) Clavero, C. Plasmon-Induced Hot-Electron Generation at Nanoparticle/Metal-Oxide Interfaces for Photovoltaic and Photocatalytic Devices. *Nat. Photonics* **2014**, *8*, 95−103.

(4) Grätzel, M. Solar Energy Conversion by Dye-Sensitized Photovoltaic Cells. *Inorg. Chem.* **2005**, *44*, 6841−6851.

(5) Mubeen, S.; Lee, J.; Singh, N.; Krämer, S.; Stucky, G. D.; Moskovits, M. An Autonomous Photosynthetic Device in Which All Charge Carriers Derive from Surface Plasmons. *Nat. Nanotechnol.* **2013**, *8*, 247−251.

(6) Hodes, G. Perovskite-Based Solar Cells. *Science* **2013**, *342*, 317−318.

(7) Godin, R.; Kafizas, A.; Durrant, J. R. Electron Transfer Dynamics in Fuel Producing Photosystems. *Curr. Opin. Electrochem.* **2017**, *2*, 136−143.

(8) Houle, F. A. Reaction−Transport Coupling in a Nanostructured Porous Electrode. *J. Phys. Chem. C* **2019**, *123*, 14459−14467.

(9) Furube, A.; Katoh, R.; Hara, K.; Murata, S.; Arakawa, H.; Tachiya, M. Ultrafast Stepwise Electron Injection from Photoexcited Ru-Complex into Nanocrystalline ZnO Film via Intermediates at the Surface. *J. Phys. Chem. B* **2003**, *107*, 4162−4166.

(10) Němec, H.; Rochford, J.; Taratula, O.; Galoppini, E.; Kužel, P.; Polívka, T.; Yartsev, A.; Sundström, V. Influence of the Electron-Cation Interaction on Electron Mobility in Dye-Sensitized ZnO and TiO_2 Nanocrystals: A Study Using Ultrafast Terahertz Spectroscopy. *Phys. Rev. Lett.* **2010**, *104*, 197401.

(11) Stockwell, D.; Yang, Y.; Huang, J.; Anfuso, C.; Huang, Z.; Lian, T. Comparison of Electron-Transfer Dynamics from Coumarin 343 to TiO_2, SnO_2, and ZnO Nanocrystalline Thin Films: Role of Interface-Bound Charge-Separated Pairs. *J. Phys. Chem. C* **2010**, *114*, 6560−6566.

(12) Strothkämper, C.; Bartelt, A.; Sippel, P.; Hannappel, T.; Schütz, R.; Eichberger, R. Delayed Electron Transfer through Interface States in Hybrid ZnO/Organic-Dye Nanostructures. *J. Phys. Chem. C* **2013**, *117*, 17901−17908.

(13) Brauer, J. C.; Marchioro, A.; Paraecattil, A. A.; Oskouei, A. A.; Moser, J.-E. Dynamics of Interfacial Charge Transfer States and Carriers Separation in Dye-Sensitized Solar Cells: A Time-Resolved Terahertz Spectroscopy Study. *J. Phys. Chem. C* **2015**, *119*, 26266−26274.

(14) Bauer, C.; Boschloo, G.; Mukhtar, E.; Hagfeldt, A. Electron Injection and Recombination in $Ru(Dcbpy)_2(NCS)_2$ Sensitized Nanostructured ZnO. *J. Phys. Chem. B* **2001**, *105*, 5585−5588.

(15) Horiuchi, H.; Katoh, R.; Hara, K.; Yanagida, M.; Murata, S.; Arakawa, H.; Tachiya, M. Electron Injection Efficiency from Excited N3 into Nanocrystalline ZnO Films: Effect of ($N3-Zn^{2+}$) Aggregate Formation. *J. Phys. Chem. B* **2003**, *107*, 2570−2574.

(16) Asbury, J. B.; Wang, Y.; Lian, T. Multiple-Exponential Electron Injection in $Ru(Dcbpy)_2(SCN)_2$ Sensitized ZnO Nanocrystalline Thin Films. *J. Phys. Chem. B* **1999**, *103*, 6643−6647.

(17) Zhang, Z.; Yates, J. T. Band Bending in Semiconductors: Chemical and Physical Consequences at Surfaces and Interfaces. *Chem. Rev.* **2012**, *112*, 5520−5551.

(18) Ong, C. B.; Ng, L. Y.; Mohammad, A. W. A Review of ZnO Nanoparticles as Solar Photocatalysts: Synthesis, Mechanisms and Applications. *Renewable Sustainable Energy Rev.* **2018**, *81*, 536−551.

(19) Chen, H.; Cole, J. M.; Stenning, G. B. G.; Yanguas-Gil, A.; Elam, J. W.; Stan, L.; Gong, Y. Imaging Dye Aggregation in MK-2, N3, N749, and SQ-2 Dye$\cdots$$TiO_2$ Interfaces That Represent Dye-Sensitized Solar Cell Working Electrodes. *ACS Appl. Energy Mater.* **2020**, *3*, 3230−3241.

(20) Mukaddem, K. T.; Chater, P. A.; Devereux, L. R.; Al Bahri, O. K.; Jain, A.; Cole, J. M. Dye-Anchoring Modes at the Dye$\cdots$$TiO_2$ Interface of N3- and N749-Sensitized Solar Cells Revealed by Glancing-Angle Pair Distribution Function Analysis. *J. Phys. Chem. C* **2020**, *124*, 11935−11945.

(21) Siefermann, K. R.; Pemmaraju, C. D.; Neppl, S.; Shavorskiy, A.; Cordones, A. A.; Vura-Weis, J.; Slaughter, D. S.; Sturm, F. P.; Weise, F.; Bluhm, H.; Strader, M. L.; Cho, H.; Lin, M.-F.; Bacellar, C.; Khurmi, C.; Guo, J.; Coslovich, G.; Robinson, J. S.; Kaindl, R. A.; Schoenlein, R. W.; Belkacem, A.; Neumark, D. M.; Leone, S. R.; Nordlund, D.; Ogasawara, H.; Krupin, O.; Turner, J. J.; Schlotter, W. F.; Holmes, M. R.; Messerschmidt, M.; Minitti, M. P.; Gul, S.; Zhang, J. Z.; Huse, N.; Prendergast, D.; Gessner, O. Atomic-Scale Perspective

of Ultrafast Charge Transfer at a Dye−Semiconductor Interface. *J. Phys. Chem. Lett.* **2014**, *5*, 2753−2759.

(22) Katoh, R.; Furube, A.; Yoshihara, T.; Hara, K.; Fujihashi, G.; Takano, S.; Murata, S.; Arakawa, H.; Tachiya, M. Efficiencies of Electron Injection from Excited N3 Dye into Nanocrystalline Semiconductor (ZrO_2, TiO_2, ZnO, Nb_2O_5, SnO_2, In_2O_3) Films. *J. Phys. Chem. B* **2004**, *108*, 4818−4822.

(23) Tiwana, P.; Docampo, P.; Johnston, M. B.; Snaith, H. J.; Herz, L. M. Electron Mobility and Injection Dynamics in Mesoporous ZnO, SnO_2, and TiO_2 Films Used in Dye-Sensitized Solar Cells. *ACS Nano* **2011**, *5*, 5158−5166.

(24) Borgwardt, M.; Wilke, M.; Kampen, T.; Mähl, S.; Xiao, M.; Spiccia, L.; Lange, K. M.; Kiyan, I. Yu.; Aziz, E. F. Charge Transfer Dynamics at Dye-Sensitized ZnO and TiO_2 Interfaces Studied by Ultrafast XUV Photoelectron Spectroscopy. *Sci. Rep.* **2016**, *6*, 24422.

(25) Anderson, N. A.; Lian, T. ULTRAFAST ELECTRON TRANSFER AT THE MOLECULE-SEMICONDUCTOR NANOPARTICLE INTERFACE. *Annu. Rev. Phys. Chem.* **2005**, *56*, 491−519.

(26) Benkö, G.; Kallioinen, J.; Myllyperkiö, P.; Trif, F.; Korppi-Tommola, J. E. I.; Yartsev, A. P.; Sundström, V. Interligand Electron Transfer Determines Triplet Excited State Electron Injection in RuN3−Sensitized TiO_2 Films. *J. Phys. Chem. B* **2004**, *108*, 2862−2867.

(27) Kallioinen, J.; Benkö, G.; Sundström, V.; Korppi-Tommola, J. E. I.; Yartsev, A. P. Electron Transfer from the Singlet and Triplet Excited States of $Ru(Dcbpy)_2(NCS)_2$ into Nanocrystalline TiO_2 Thin Films. *J. Phys. Chem. B* **2002**, *106*, 4396−4404.

(28) Mayor, L. C.; Saywell, A.; Magnano, G.; Satterley, C. J.; Schnadt, J.; O'Shea, J. N. Adsorption of a Ru(II) Dye Complex on the Au(111) Surface: Photoemission and Scanning Tunneling Microscopy. *J. Chem. Phys.* **2009**, *130*, 164704.

(29) Ozawa, K.; Emori, M.; Yamamoto, S.; Yukawa, R.; Yamamoto, S.; Hobara, R.; Fujikawa, K.; Sakama, H.; Matsuda, I. Electron−Hole Recombination Time at TiO_2 Single-Crystal Surfaces: Influence of Surface Band Bending. *J. Phys. Chem. Lett.* **2014**, *5*, 1953−1957.

(30) Yukawa, R.; Yamamoto, S.; Ozawa, K.; Emori, M.; Ogawa, M.; Yamamoto, Sh.; Fujikawa, K.; Hobara, R.; Kitagawa, S.; Daimon, H.; Sakama, H.; Matsuda, I. Electron-Hole Recombination on ZnO(0001) Single-Crystal Surface Studied by Time-Resolved Soft X-Ray Photoelectron Spectroscopy. *Appl. Phys. Lett.* **2014**, *105*, 151602.

(31) Gierster, L.; Vempati, S.; Stähler, J. Ultrafast Generation and Decay of a Surface Metal. *Nat. Commun.* **2021**, *12*, 978.

(32) Mahl, J.; Gessner, O.; Barth, J. V.; Feulner, P.; Neppl, S. Strong Potential Gradients and Electron Confinement in ZnO Nanoparticle Films: Implications for Charge-Carrier Transport and Photocatalysis. *ACS Appl. Nano Mater.* **2021**, *4*, 12213−12221.

(33) Favaro, M.; Jeong, B.; Ross, P. N.; Yano, J.; Hussain, Z.; Liu, Z.; Crumlin, E. J. Unravelling the Electrochemical Double Layer by Direct Probing of the Solid/Liquid Interface. *Nat. Commun.* **2016**, *7*, 12695.

(34) Lichterman, M. F.; Hu, S.; Richter, M. H.; Crumlin, E. J.; Axnanda, S.; Favaro, M.; Drisdell, W.; Hussain, Z.; Mayer, T.; Brunschwig, B. S.; Lewis, N. S.; Liu, Z.; Lewerenz, H.-J. Direct Observation of the Energetics at a Semiconductor/Liquid Junction by Operando X-Ray Photoelectron Spectroscopy. *Energy Environ. Sci.* **2015**, *8*, 2409−2416.

(35) Shavorskiy, A.; Ye, X.; Karslıoğlu, O.; Poletayev, A. D.; Hartl, M.; Zegkinoglou, I.; Trotochaud, L.; Nemšák, S.; Schneider, C. M.; Crumlin, E. J.; Axnanda, S.; Liu, Z.; Ross, P. N.; Chueh, W.; Bluhm, H. Direct Mapping of Band Positions in Doped and Undoped Hematite during Photoelectrochemical Water Splitting. *J. Phys. Chem. Lett.* **2017**, *8*, 5579−5586.

(36) Ozawa, K.; Mase, K. Metallization of ZnO(10−10) by Adsorption of Hydrogen, Methanol, and Water: Angle-Resolved Photoelectron Spectroscopy. *Phys. Rev. B: Condens. Matter Mater. Phys.* **2010**, *81*, 205322.

(37) Ozawa, K.; Mase, K. Comparison of the Surface Electronic Structures of H-Adsorbed ZnO Surfaces: An Angle-Resolved Photoelectron Spectroscopy Study. *Phys. Rev. B: Condens. Matter Mater. Phys.* **2011**, *83*, 125406.

(38) Hagfeldt, A.; Graetzel, M. Light-Induced Redox Reactions in Nanocrystalline Systems. *Chem. Rev.* **1995**, *95*, 49−68.

(39) Tanuma, S.; Powell, C. J.; Penn, D. R. Calculation of electron inelastic mean free paths (IMFPs) VII. Reliability of the TPP-2M IMFP predictive equation. *Surf. Interface Anal.* **2003**, *35*, 268−275.

(40) Gleason-Rohrer, D. C.; Brunschwig, B. S.; Lewis, N. S. Measurement of the Band Bending and Surface Dipole at Chemically Functionalized Si(111)/Vacuum Interfaces. *J. Phys. Chem. C* **2013**, *117*, 18031−18042.

(41) Lueth, H. *Solid Surfaces, Interfaces and Thin Films*; 5th ed.; Springer: Berlin Heidelberg, 2010; pp 527−528.

(42) Cole, J. M.; Gong, Y.; McCree-Grey, J.; Evans, P. J.; Holt, S. A. Modulation of N3 and N719 Dye···TiO_2 Interfacial Structures in Dye-Sensitized Solar Cells As Influenced by Dye Counter Ions, Dye Deprotonation Levels, and Sensitizing Solvent. *ACS Appl. Energy Mater.* **2018**, *1*, 2821−2831.

(43) Ozawa, K.; Yamamoto, S.; Yukawa, R.; Akikubo, K.; Emori, M.; Sakama, H.; Matsuda, I. Capturing Transiently Charged States at the $C_{60}/TiO_2(110)$ Interface by Time-Resolved Soft X-Ray Photoelectron Spectroscopy. *Org. Electron.* **2016**, *31*, 98−103.

(44) Neppl, S.; Gessner, O. Time-Resolved X-Ray Photoelectron Spectroscopy Techniques for the Study of Interfacial Charge Dynamics. *J. Electron Spectrosc. Relat. Phenom.* **2015**, *200*, 64−77.

(45) Yoshihara, T.; Katoh, R.; Furube, A.; Murai, M.; Tamaki, Y.; Hara, K.; Murata, S.; Arakawa, H.; Tachiya, M. Quantitative Estimation of the Efficiency of Electron Injection from Excited Sensitizer Dye into Nanocrystalline ZnO Film. *J. Phys. Chem. B* **2004**, *108*, 2643−2647.

(46) Anderson, N. A.; Ai, X.; Lian, T. Electron Injection Dynamics from Ru Polypyridyl Complexes to ZnO Nanocrystalline Thin Films. *J. Phys. Chem. B* **2003**, *107*, 14414−14421.

(47) Goossens, A. Potential Distribution in Semiconductor Particles. *J. Electrochem. Soc.* **1996**, *143*, L131.

(48) Phillips, J. C. Stretched Exponential Relaxation in Molecular and Electronic Glasses. *Rep. Prog. Phys.* **1996**, *59*, 1133.

(49) Bluhm, H.; Andersson, K.; Araki, T.; Benzerara, K.; Brown, G. E.; Dynes, J. J.; Ghosal, S.; Gilles, M. K.; Hansen, H.-Ch.; Hemminger, J. C.; Hitchcock, A. P.; Ketteler, G.; Kilcoyne, A. L. D.; Kneedler, E.; Lawrence, J. R.; Leppard, G. G.; Majzlam, J.; Mun, B. S.; Myneni, S. C. B.; Nilsson, A.; Ogasawara, H.; Ogletree, D. F.; Pecher, K.; Salmeron, M.; Shuh, D. K.; Tonner, B.; Tyliszczak, T.; Warwick, T.; Yoon, T. H. Soft X-Ray Microscopy and Spectroscopy at the Molecular Environmental Science Beamline at the Advanced Light Source. *J. Electron Spectrosc. Relat. Phenom.* **2006**, *150*, 86−104.

(50) Neppl, S.; Shavorskiy, A.; Zegkinoglou, I.; Fraund, M.; Slaughter, D. S.; Troy, T.; Ziemkiewicz, M. P.; Ahmed, M.; Gul, S.; Rude, B.; Zhang, J. Z.; Tremsin, A. S.; Glans, P.-A.; Liu, Y.-S.; Wu, C. H.; Guo, J.; Salmeron, M.; Bluhm, H.; Gessner, O. Capturing Interfacial Photoelectrochemical Dynamics with Picosecond Time-Resolved X-Ray Photoelectron Spectroscopy. *Faraday Discuss.* **2014**, *171*, 219−241.

(51) Shavorskiy, A.; Neppl, S.; Slaughter, D. S.; Cryan, J. P.; Siefermann, K. R.; Weise, F.; Lin, M.-F.; Bacellar, C.; Ziemkiewicz, M. P.; Zegkinoglou, I.; Fraund, M. W.; Khurmi, C.; Hertlein, M. P.; Wright, T. W.; Huse, N.; Schoenlein, R. W.; Tyliszczak, T.; Coslovich, G.; Robinson, J.; Kaindl, R. A.; Rude, B. S.; Ölsner, A.; Mähl, S.; Bluhm, H.; Gessner, O. Sub-Nanosecond Time-Resolved Ambient-Pressure X-Ray Photoelectron Spectroscopy Setup for Pulsed and Constant Wave X-Ray Light Sources. *Rev. Sci. Instrum.* **2014**, *85*, 093102.

Nanoscale Confinement of Photo-Injected Electrons at Hybrid Interfaces

SUPPORTING INFORMATION

Stefan Neppl[1,‡,†], *Johannes Mahl*[1,2,†], *Friedrich Roth*[3], *Giuseppe Mercurio*[2,§], *Guosong Zeng*[1,4], *Francesca M. Toma*[1,4], *Nils Huse*[2], *Peter Feulner*[5], *and Oliver Gessner*[1,*]

[1]Chemical Sciences Division, Lawrence Berkeley National Laboratory, Berkeley, CA 94720, USA

[2]Physics Department, Universität Hamburg and Center for Free-Electron Laser Science, 22761 Hamburg, Germany

[3]Institute of Experimental Physics, TU Bergakademie Freiberg, 09599 Freiberg, Germany

[4]Liquid Sunlight Alliance, Lawrence Berkeley National Laboratory, Berkeley, CA 94720, USA

[5]Physics Department, Technische Universität München, 85748 Garching, Germany

[†]these authors contributed equally to this work

[‡]current affiliation: Paul Scherrer Institut, 5232 Villigen, Switzerland

[§]current affiliation: European XFEL, 22869 Schenefeld, Germany

Table of Contents

---

[*]email: ogessner@lbl.gov

A) Experimental details, sample preparation and characterization

ZnO nanoparticles with an average diameter of ~15 nm were prepared according to a procedure based on a zinc acetate dihydrate precursor (Sigma-Aldrich) in ethanoic solution.[1] Approximately 0.2 ml of the resulting colloidal suspension was spin-coated (2,000 rpm) onto cleaned 2 x 5 cm^2 FTO glass slides. The films were subsequently dried at 60 °C and sintered in air at 360 °C for 50 minutes. This procedure yields macroscopically homogenous nanoporous ZnO films (Fig. S1(a)), while preserving the nanoscale surface morphology (Fig. S1(b)). The direct bandgap of $E_g = 3.30 \pm 0.01$ eV (see Fig. S1(c)) determined via the Tauc method[2,3] is consistent with the literature.[4] Sensitization with N3 dyes (cis-bis(isothiocyanato)bis(2,2'-bipyridyl-4,4'-dicarboxylato)-ruthenium(II); Sigma-Aldrich) was carried out in ambient atmosphere by immersing the (still ~80 °C warm) ZnO films in a 0.2 mM ethanoic solution of N3 for 3 min. The resulting dye-sensitized ZnO films were thoroughly rinsed with ethanol to remove excess physisorbed molecules and blown dry in a stream of dry nitrogen. The comparably short sensitization time of 3 min was chosen to avoid the formation of N3/Zn^{2+} surface complexes/aggregates, which exhibit inefficient electron injection properties and modify the surface morphology and electronic structure of the ZnO films due to dissolution of Zn^{2+} ions.[5–8] While this precaution might be less important for bulk-sensitive measurements, such as all-optical studies, it is mandatory for the surface-sensitive trXPS experiments presented here. Samples were kept in the dark prior to transferring them into the vacuum chamber for the trXPS experiments carried out at a base pressure of $\sim 5 \cdot 10^{-8}$ mbar. We note that samples prepared using these or similar techniques have been shown to yield incident photon-to-current conversion efficiencies (IPCE) of ~18% at ~530 nm.[9]

During the trXPS measurements, the sample was continuously scanned at a speed of 275 µm/s, with a 500 µm spacing between neighboring lines to exclude any modification of the ground-state (GS) electronic structure of the N3/ZnO heterojunction due to X-ray- and/or laser-induced damage. For the chosen experimental parameters, we do not observe any changes in the transient trXPS energy shifts or in the GS XPS line shapes and positions for two consecutive scans across the same sample area. We emphasize that fast sample scanning is imperative, since even exposure to synchrotron X-ray radiation itself can alter the GS surface-electronic structure of the ZnO electrodes, as illustrated for the Zn3d photoline in Fig. S1(d). Similar X-ray-induced effects have been observed in synchrotron-based XPS experiments on single crystalline TiO_2 films.[10] The C1s and Zn3d trXPS pump-probe data shown in Fig. 2(a) of the main text have been acquired in an interleaved fashion, i.e. acquiring C1s and Zn3d data at one pump-probe delay before moving to the next one. This procedure mitigates any possible influence of long-term experimental drifts on the quantitative comparison of the C1s and Zn3d trXPS transients in Fig. 2(a) of the main text. X-ray photon energy changes required to switch between C1s and Zn3d regions do not affect the experiment, as an active feedback loop in the beamline stabilizes the X-ray beam pointing. Repeated tests of beam pointing fluctuations indicated a stability and reproducibility of <5 μm in horizontal and vertical directions for the two different X-ray energies.

B) Peak fitting analysis of the trXPS spectra

Fitting of the C1s/Ru3d spectral region

The inset in Fig. 1 of the main text illustrates the molecular structure of the N3 dye. Carbon and ruthenium atoms are color-coded with corresponding colors used for the Gaussian peaks in Fig. 1(a) to indicate the different contributions to the C1s/Ru3d XPS spectrum. These peaks together with the sum of their Shirley backgrounds (dashed gray line) and a constant offset (~0.1) represent the result of a fit (blue line) of the GS spectrum (blue circles). In this fit, the Ru3d doublet (pink)

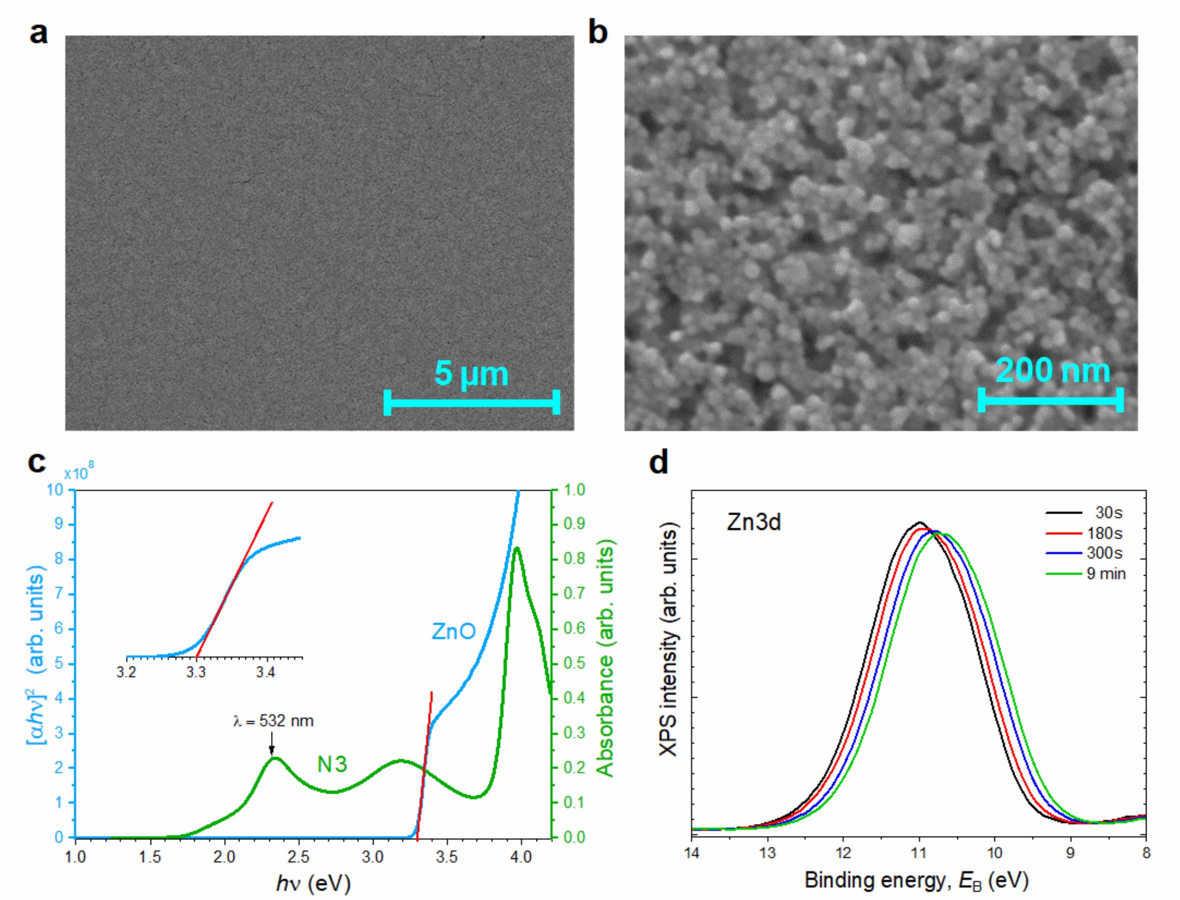

Figure S1. Characterization of ZnO nanoparticle substrates and N3 sensitizer. **a**,**b** SEM images of a ZnO nanoparticle film at different magnifications. **c** UV-Vis absorption spectra of 0.2 mM N3 in ethanol (green) and the bare ZnO film (blue, scaled as indicated). The arrow indicates the pump wavelength (532 nm) used in the trXPS experiments. The inset highlights the determination of the direct bandgap via to the Tauc method (red line). **d** Zn3d XPS spectra at a fixed sample spot as a function of X-ray exposure time.

has a fixed peak area ratio of 3/2 between Ru3d$_{5/2}$ and Ru3d$_{3/2}$ and a fixed energy splitting of 4.2 eV.[11] The Ru3d$_{5/2}$ peak appears at the lowest binding energy of 282.0 eV and the less intense Ru3d$_{3/2}$ peak overlaps with the C1s signals from the bipyridyl rings at 285.5 eV (blue, C**C**C) and 286.4 eV (red, C**C**N). The C1s signal from the thiocyanate groups (cyan, N**C**S) appears as a high binding energy shoulder (287.6 eV) of the main feature, while the carbon in the carboxyl groups (green, C**C**OOH) is subject to valence electron density depletion by the most electronegative environment, leading to the highest binding energy C1s component at 289.5 eV. For the fit procedure, the peak area ratios of the individual carbon peaks are fixed according to their respective number of occurrences within the molecule, i.e. 12:8:2:4 in the order C**C**C:C**C**N:N**C**S:C**C**OOH. Their relative energy separations are fixed to the values reported by Mayor et al,[12] except for the carboxyl group, which is expected to have a substrate dependent binding energy. The spectral widths of the Ru3d doublet and the individual C1s components are free fit parameters, with the two bipyridine C1s peaks constrained to have identical FWHM.[12] For each data set, this GS fit is applied to the average of all data recorded at negative pump-probe delays. Compared to the GS spectrum, the only free parameters when fitting the ES spectra (red circles in Fig. 1(a)) are the relative binding energy shifts of the Ru3d doublet and the entire C1s emission, and the FWHM of the individual peaks as described for the GS. However, in contrast to the Zn3d data, no changes in the spectral widths between the GS and ES spectra are observed within the uncertainty of the fits.

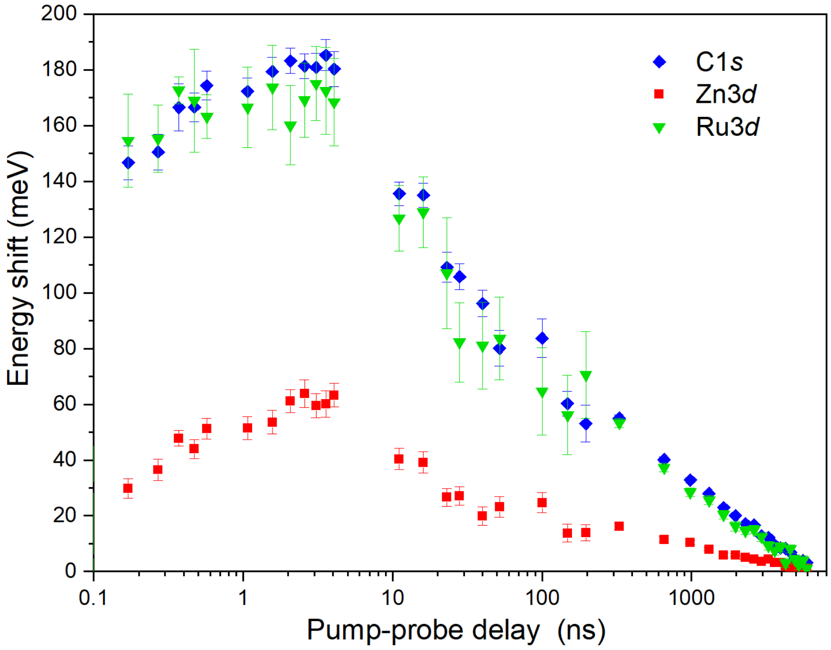

Figure S2. Spectral shifts of C1s, Ru3d, and Zn3d photolines as a function of pump-probe delay. The shifts of C1s (blue diamonds) and Ru3d (green triangles) are independent fit results. They agree within the uncertainty of the measurement, indicating a uniform shift of the entire C1s/Ru3d spectral region associated with the N3 molecule. Zn3d trXPS shifts (red squares) from the ZnO semiconductor substrate are displayed for comparison.

Fig. S2 shows the resulting C1s (blue diamonds) and Ru3d (green triangles) shifts of the ES relative to the GS, which are identical within the experimental range of uncertainty. For improved clarity, only the C1s shifts are shown in Fig. 2(a) of the main text, as their determination is more precise.

Fitting of the Zn3d spectral region

The line-shape of the Zn3d emission is best described by an asymmetric Gaussian function.[13] Fig. 1(b) of the main text shows the GS Zn3d spectrum (blue circles), which is fitted (blue line) with an asymmetric Gaussian peak on top of a polynomial background (gray dashed line). The free parameters of the asymmetric Gaussian peak fit are the peak area, the binding energy position of the maximum, a half-width-at-half-maximum (HWHM) value for the lower binding energy side, and an asymmetry factor α (>1) accounting for the broader peak shape on the higher binding energy side such that FWHM = HWHM(1+α). The fit results are FWHM = 1.53 eV and α = 1.18 for hν = 320 eV, and FWHM = 1.88 eV and α = 1.31 for hν = 614 eV. The difference in the Zn3d line-shape for the two data sets can be explained by the different energy resolution (beamline and analyzer) in the two experiments.

As described for the C1s/Ru3d spectrum, the GS fit for each Zn3d data set is performed on the average of all data with negative pump-probe delays. Each ES spectrum (red circles) is fitted (red line) individually with a variable binding energy position and FWHM parameter, while the peak area and asymmetry factor are fixed to the corresponding GS fit results. Resulting ES peak shifts with respect to the GS (ΔE_B(Zn3d)), as well as the difference between ES and GS FWHM fit results (ΔFWHM(Zn3d)) are shown in Fig. 2(a) of the main text. In addition to Fig. 1(b,d) in the manuscript, Fig. S3 provides a more comprehensive analysis of the photo-induced spectral changes of the Zn3d photoemission. Comparing the GS and ES spectra as recorded (Fig. S3(a)), with the same color coding as described above, both the shift and the broadening become apparent. Shifts to higher E_B are visible for both the low- and the high-energy side of the peak, highlighted in the right and bottom left insets, respectively. Furthermore, the ES peak broadening effect leads to a smaller amplitude of the ES spectrum compared to the GS, as seen in the top left inset in Fig. S3(a). Modelling the photo-induced effect by an E_B shift alone, as shown in Fig. S3(b), results in a distinct residual (bottom). However, a combination of E_B shift and spectral broadening of the GS spectrum (Fig. S3(c)) adequately describes the photo-induced effects in the ES spectrum, which is reflected in a significantly reduced residual. The amplitudes in this residual are similar to the fluctuations observed in difference spectra constructed from separate Zn3d spectra acquired with the same data acquisition time, but without any laser excitation.

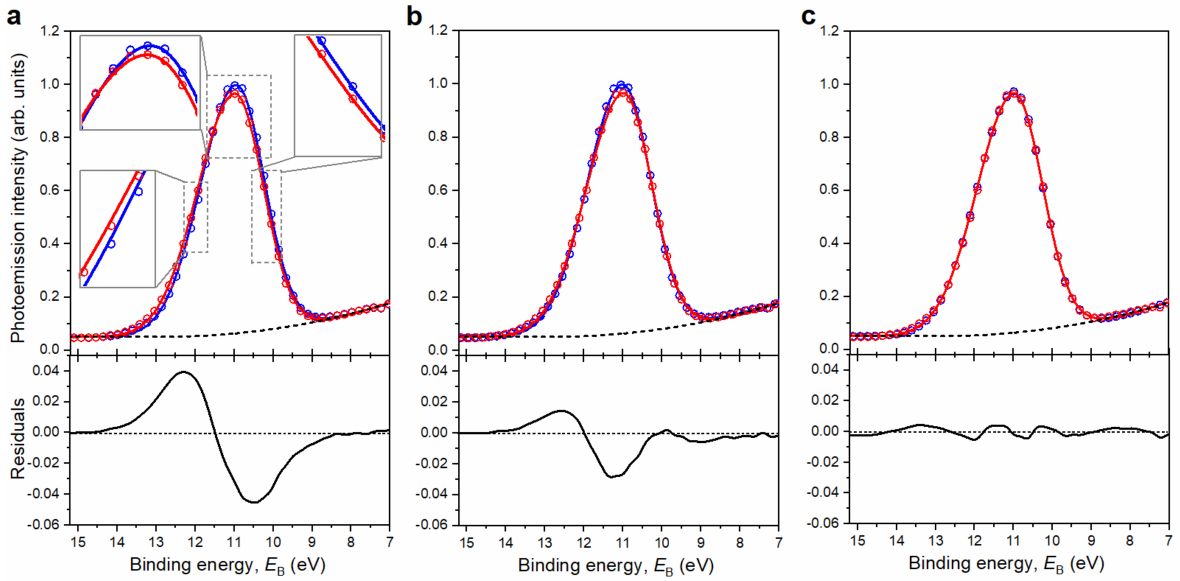

Figure S3. Photo-induced changes in Zn3d spectrum. **a** The data as recorded exhibit a shift towards higher binding energies in the ES (red) compared to the GS (blue) spectrum on both the high (bottom left inset) and low (right inset) binding energy sides of the Zn3d peak. Additionally, a photo-induced peak broadening leads to a decrease in the ES peak amplitude compared to the GS spectrum, visible in the top left inset. **b** A shift alone does not lead to satisfactory overlap of GS and ES spectra, as highlighted by the pronounced residual difference spectrum in the bottom panel. **c** Applying spectral broadening in combination with a binding energy shift to the GS spectrum leads to a good description of ES spectrum, and reduces the residual to a level comparable to the typical differences between two trXPS reference measurements without optical excitation.

C) Ground state electronic structure of the N3/ZnO interface

The GS band bending at the surface $V_{bb,max}^{GS}$, and its spatial profile $V_{bb}^{GS}(z)$ for the hydrated, bare ZnO system has been established by temperature-resolved XPS/UPS experiments on the bare nanoporous ZnO film.[14] In principle, the internal electric fields arising from local space-charge imbalances in the semiconductor surface region may be altered by the adsorption of a sensitizer. This would influence the energy-level alignment and coupling between the electron-donor and the semiconductor acceptor states.[15–18] In the following, we demonstrate that N3 dye adsorption, when performed as described in Section A, does not change the GS band bending for the N3/ZnO heterojunction compared to the hydrated, bare ZnO system.

Fig. S4 shows a series of XPS (Fig. S4(a,b)) and UPS (Fig. S4(c)) spectra of bare ZnO (upper panels) and N3/ZnO films (lower panels). A non-monochromatized, laboratory based MgKα X-ray source ($h\nu$ = 1253.6 eV) is used for the XPS measurements, and the HeI emission from a UV lamp ($h\nu$ = 21.2 eV) for the UPS characterization. Sample charging effects are excluded by reproducing

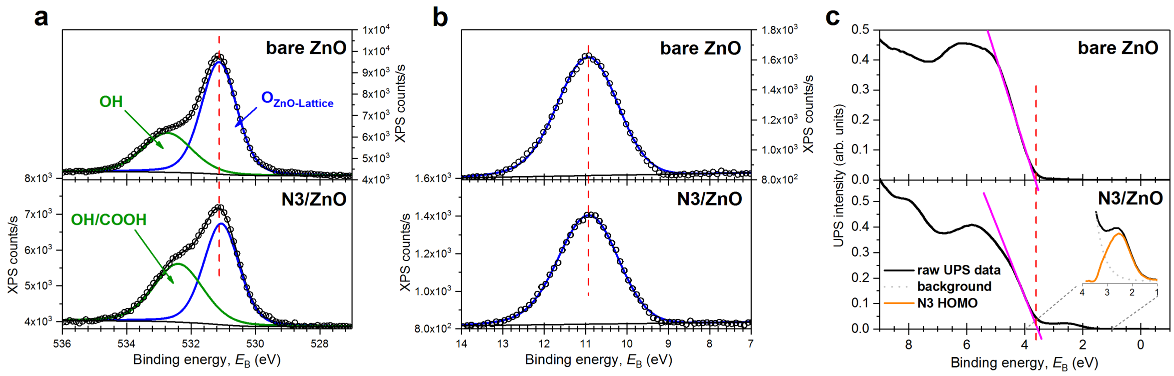

Figure S4. Static XPS and UPS characterization of bare (top) and N3-sensitized (bottom) nanoporous ZnO substrates. **a** O1s XPS spectra composed of ZnO-bulk (blue) and surface-adsorbate (green) contributions. **b** Zn3d XPS photoemission associated with the ZnO electrode. **c** Determination of the VBM at the surface by linear extrapolation of the leading edge of the VB UPS emission (magenta). Top panels show the spectra of the hydrated bare ZnO electrode at room temperature. Spectra obtained from the N3-sensitized electrodes are depicted in the bottom panels. The red, vertical dashed lines highlight the alignment of features at relevant binding energies. The inset in (c) shows a magnified view of the N3 HOMO contribution to the VB emission for the sensitized substrate (orange) and the bare ZnO background (dashed gray).

all spectra independent of the applied photon beam intensity, which was varied by more than one order of magnitude in both experiments. Additional tests were performed to rule out any impact of sample degradation due to prolonged X-ray/UV exposure.

The O1s spectra in Fig. S4(a) consist of a ZnO-lattice contribution (blue) and surface oxygen contributions (green) stemming from hydroxyl and, in the case of N3/ZnO, also carboxyl groups. In contrast, the Zn3d photoemission in Fig. S4(b) is exclusively associated with the semiconductor. For the analysis of the UPS spectra (Fig. S4(c)), a linear fit to the low binding energy edge (magenta line) is extrapolated to zero intensity, which yields the valence band maximum (VBM) position at the surface E_{VBM}^{surf}. Note that in the N3/ZnO heterojunction UPS data, there is an additional contribution from the N3 HOMO (orange peak) that does not affect the valence band position. Dashed red lines in all three panels demonstrate that the positions of the ZnO-lattice associated O1s peak (Fig. S4(a)), the Zn3d peak (Fig. S4(b)) and E_{VBM}^{surf} (Fig. S4(c)) are identical for the hydrated and N3-sensitized ZnO films within the accuracy of the fits. The binding energy axes are calibrated with respect to the Fermi level at E_{F} = 0 eV and the Au4f$_{7/2}$ peak center at 84.00 eV measured for a sputter-cleaned gold substrate with an accuracy of ±10 meV. The identical peak and VBM energy positions for the bare and N3-sensitized ZnO substrates provide strong evidence that the amount of GS band bending is the same in both systems.[18] Therefore, the amplitude and functional shape of $V_{bb}^{GS}(z)$ of the bare ZnO films are assumed to also represent the GS surface electronic structure of the N3/ZnO heterojunction.

D) Control trXPS experiments on bare ZnO electrodes

In order to exclude that photo-induced electron-hole pair generation within the ZnO electrode, e.g. via defect states within the bandgap, contribute to the observed photo-response, trXPS data on bare ZnO are acquired under the same experimental conditions as described in section A. Figure S5 compares Zn3d trXPS data acquired from the bare ZnO substrate (red squares) and the N3-sensitized ZnO nanostructure (blue diamonds). Data for pump-probe delays larger than 100 ps are shown in the main panel, and for near zero delays in the inset. No photo-response is detected for the bare ZnO sample. This result excludes significant contributions of electron-hole pairs generated within the ZnO substrate to the charge dynamics discussed in the main text.

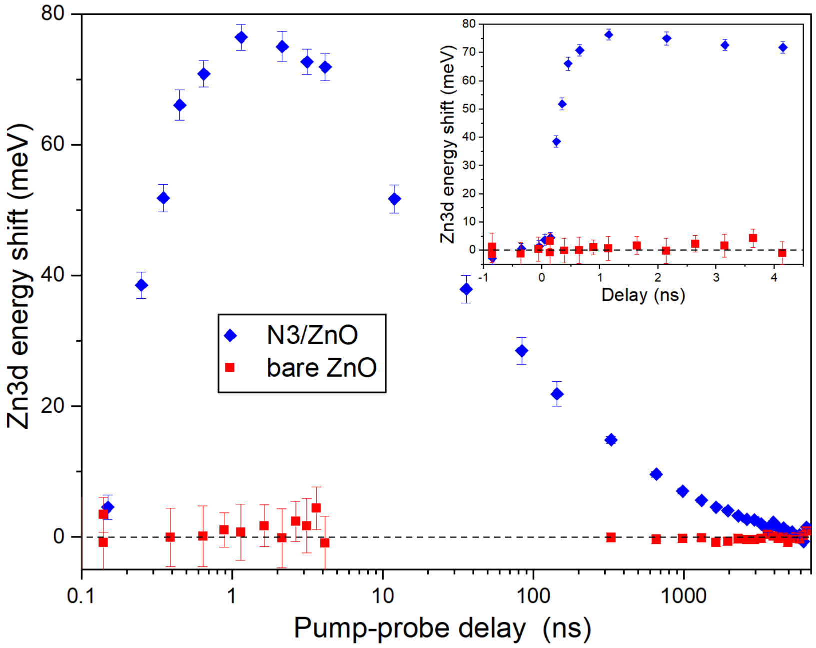

Figure S5. Control experiment with a bare ZnO substrate. Using identical pump laser conditions, the Zn3d spectrum of the N3/ZnO heterojunction (blue diamonds) exhibits a significant photo-response, while the same line of the bare ZnO sample (red squares) is unaffected by the pump pulse. The inset shows a magnified view of data near zero pump-probe delay.

E) Laser fluence dependence of trXPS effects

Fig. S6 shows the observed maximum shifts in the C1s (red) and Zn3d (blue) binding energies as a function of the optical pump pulse fluence. An approximately linear relationship at fluences up to ~1 mJ/cm^2 is contrasted by a clear saturation effect toward higher fluences. The latter is likely, at least in part, caused by photodamage of the dye molecules, which is increasingly hard to control in the regime of 10s of mJ/cm^2. Thus, experiments were performed at a fluence of 1.1 mJ/cm^2, which provides a compromise between a good signal/noise ratio in the trXPS data, and limited saturation/damage effects. Note that the observed trends provide strong evidence that nonlinear effects due to multiphoton absorption by the dye molecules do not contribute significantly to the observed dynamics.

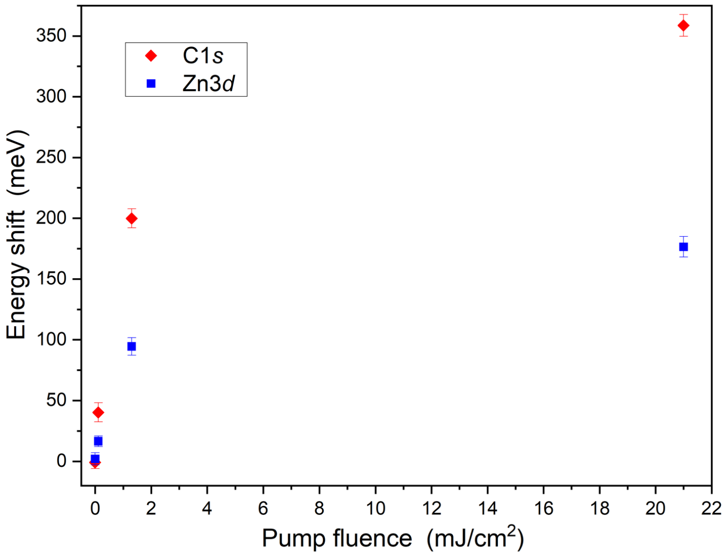

Figure S6. Pump pulse fluence dependence of the maximum energy shift in the C1s (red) and Zn3d (blue) photolines.

F) Retrieving potential gradients by numerical XPS peak simulations

We apply an XPS peak reconstruction technique to retrieve information on the spatial profile of the internal potential $V_{bb}(z)$ from the Zn3d line-shape modifications. Similar methods have been successfully used in static XPS experiments to extract the spatial evolution of GS potential gradients at solid-liquid interfaces and at semiconductor heterojunctions from bias- and angle-dependent changes of XPS peak-shifts and broadening.[19–25] The framework used to reconstruct the Zn3d photoemission peak for the bare ZnO film is described in detail in ref. 14. Briefly, the spectral distribution $D(E_b)$ of the Zn3d emission as a function of binding energy E_b is simulated by a superposition of multiple photoemission lines with the same lineshape but different effective binding energies and amplitudes due to their emergence from different depths z_i of the sample:

$$D(E_b) = \int_{z \in SCR} D_0\big(E_b - E_0 - V_{bb}(z)\big)\, e^{-\frac{z}{IMFP}} dz$$

$$\approx \sum\nolimits_{i(\forall\, z \,\in\, SCR)} D_0(E_b - E_0 - V_{bb}(z_i))\, e^{-z_i/IMFP} \qquad \text{(E1)}$$

Here, E_0 denotes the binding energy at the peak maximum in the absence of any band bending, $D_0(E_b - E_0)$ the corresponding peak shape, $V_{bb}(z)$ the depth-dependent band bending, i.e. the deviation of the potential from the flat-band condition, as illustrated in Fig. 3 of the main text and Fig. S7 below, and IMFP the inelastic mean free path of photoelectrons in the ZnO substrate. The flat-band lineshape $D_0(E_b - E_0)$ is not known a priori. Instead, it is iteratively optimized in the simulations to reproduce the Zn3d photoemission spectra, using the GS FWHM and asymmetry parameters as starting values (see section B). The IMFP is calculated with the Tanuma–Powell–Penn algorithm[26] and determines the spectral weight $e^{-z_i/IMFP}$ of each individual contribution $D_i(E_b) = D_0(E_b - E_0 - V_{bb}(z_i))$ to the overall Zn3d photoemission signal. The spatial sampling step size $z_{i+1} - z_i$ is set to the average interlayer distance along the high-symmetry directions of the ZnO wurtzite lattice of $d_L \approx 0.2$ nm,[27] and the XPS sampling depth in the numerical simulation extends to 3·IMFP. By comparing the peak shifts and FWHM changes of simulated Zn3d spectra $D(E_b)$ to experimental data as a function of pump-probe delay, the dynamic changes of the surface potential $V_{bb}(z)$ including the change at the surface $\Delta V_{bb}(z = 0)$ can be accessed. The width of the space charge region (SCR), d_{SCR}, describes the spatial extent across which $V_{bb}(z)$ values differ from the bulk value. Figure S7(b-d) schematically illustrates instructive cases of broadening of $D(E_b)$, or the lack thereof, depending on the relative length scales of d_{SCR} and IMFP. The largest

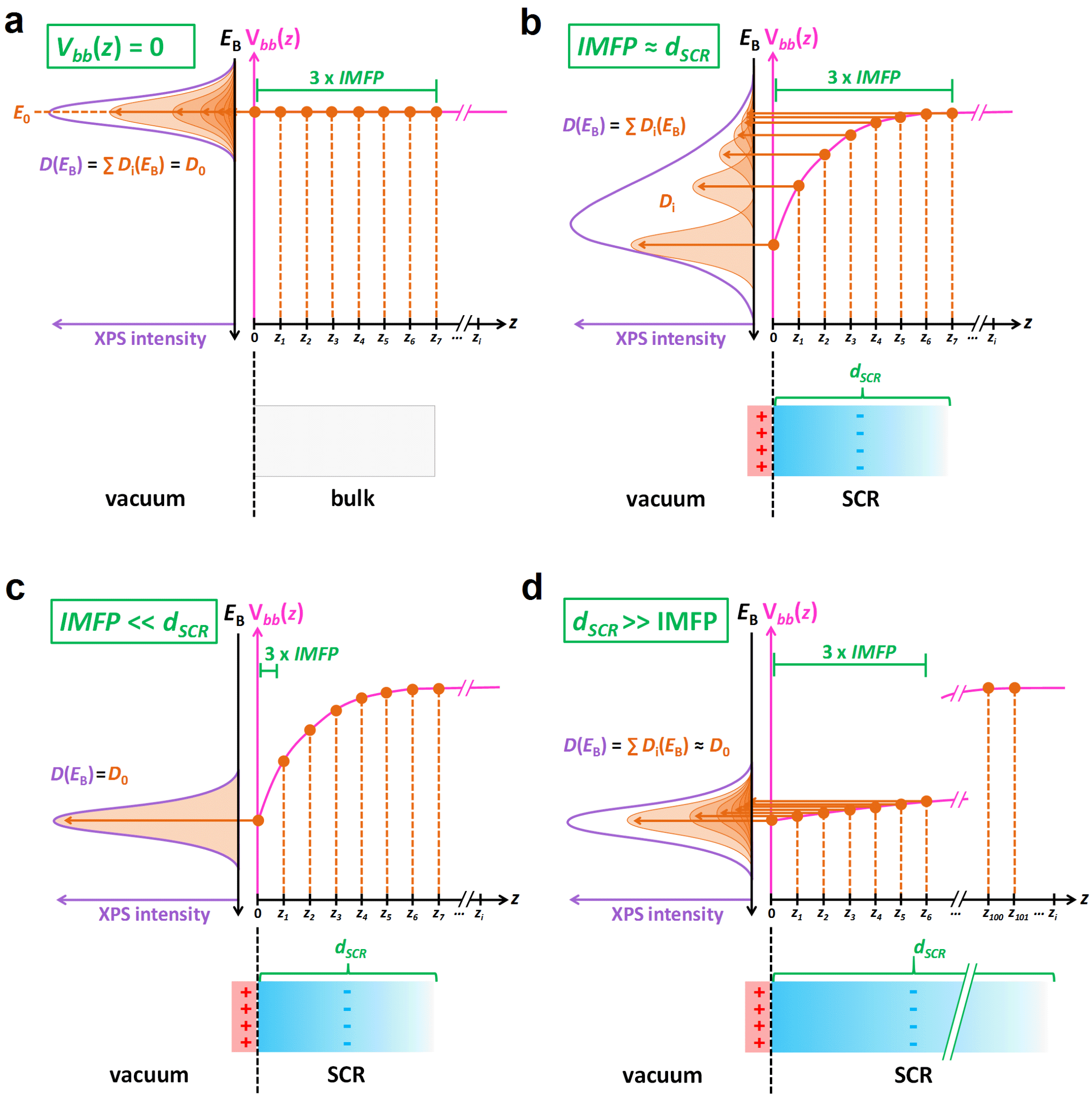

Figure S7. General correlation between the XPS lineshape $D(E_b)$, band-bending potential $V_{bb}(z)$ and *IMFP*. Different scenarios are schematically shown: **a** flatband conditions, **b** a narrow space-charge region (SCR) with downward band bending and *IMFP* ≈ d_{SCR}, **c** the same SCR but *IMFP* << d_{SCR}, and **d** a spatially very far extended SCL relative to *IMFP*. D_i denotes the spectral photoemission contribution emerging from a distance z_i from surface.

modulation of the XPS peak envelope occurs for *IMFP* ≈ d_{SCR} (Fig. S7(b)), when the different contributions D_i have markedly different binding energy positions and significant amplitudes. In this case, $D(E_b)$ will be noticeably broadened compared to flatband conditions. In all other cases illustrated in Fig. S7, $D(E_b) \approx D_0$ and no significant broadening will be observed. Specifically, small IMFPs ($IMFP \approx d_L << d_{\mathrm{SCR}}$, see Fig. S7(c)), comparable with the interlayer lattice spacing d_L, lead to a suppression of contributions from deeper lying atoms and $D(E_b)$ consists only of contributions from the outermost surface without significant binding energy variations. In the other extreme case of a very extended SCR ($d_{\mathrm{SCR}} >> IMFP >> d_L$, see Fig. S7(d)), deeper lying contributions have significant amplitude, but very similar binding energy positions due to the slowly varying internal semiconductor potential $V_{bb}(z)$. Hence, an approximate matching of IMFP and d_{SCR} is necessary to experimentally access $V_{bb}(z)$ through broadening effects in (tr)XPS data. This requirement highlights future prospects of trXPS in the tender/hard X-ray regime to probe light-induced modifications of potential gradients at hybrid systems that feature spatially more extended or buried SCRs compared to the prototypical N3/ZnO system explored here by soft X-ray trXPS.

Fig. S8 displays the results of this envelope reconstruction approach for two exemplary GS spectra acquired at $h\nu = 614$ eV (Fig. S8(a)) and $h\nu = 320$ eV (Fig. S8(c)). For both spectra, the acquired experimental data (black dots) are described by $D(E_b)$, i.e., the SCR simulation (red line). Representative individual contributions D_i at integer values of $z_i \leq 5$ nm are shown as red shaded areas, where the sum of all D_i defines $D(E_b)$ according to Eq. E1. The optimized D_0 flatband line-shape parameters are FWHM = 1.33 eV and α = 1.16 at $h\nu = 320$ eV, and FWHM = 1.59 eV and α = 1.35 at $h\nu = 614$ eV. Figure S8(b,d) shows the depth-dependent relative peak positions, defined by $V_{bb}(z)$ (blue), and the respective weights derived from the IMFP (green). Parameters for $h\nu = 614$ eV and $h\nu = 320$ eV are shown in Fig. S8(b) and Fig. S8(d), respectively. The excellent agreement between the simulated and the measured GS XPS spectra in Fig. S8(a) and (c) demonstrates that a single, global surface potential $V_{bb}(z)$ together with one IMFP for each electron kinetic energy is sufficient to describe both experimental data sets with the envelope reconstruction approach.

We note that we have also evaluated alternative explanations for the observed photoinduced spectral changes, in particular, in the Zn3d line. Among these were an injection yield per excited dye molecule of less than 1 as well as the possibility of spatially inhomogeneous charge injection that, in principle, may lead to separate regions with and without band banding effects. None of these alternatives to the model presented above provides a satisfactory, self-consistent explanation

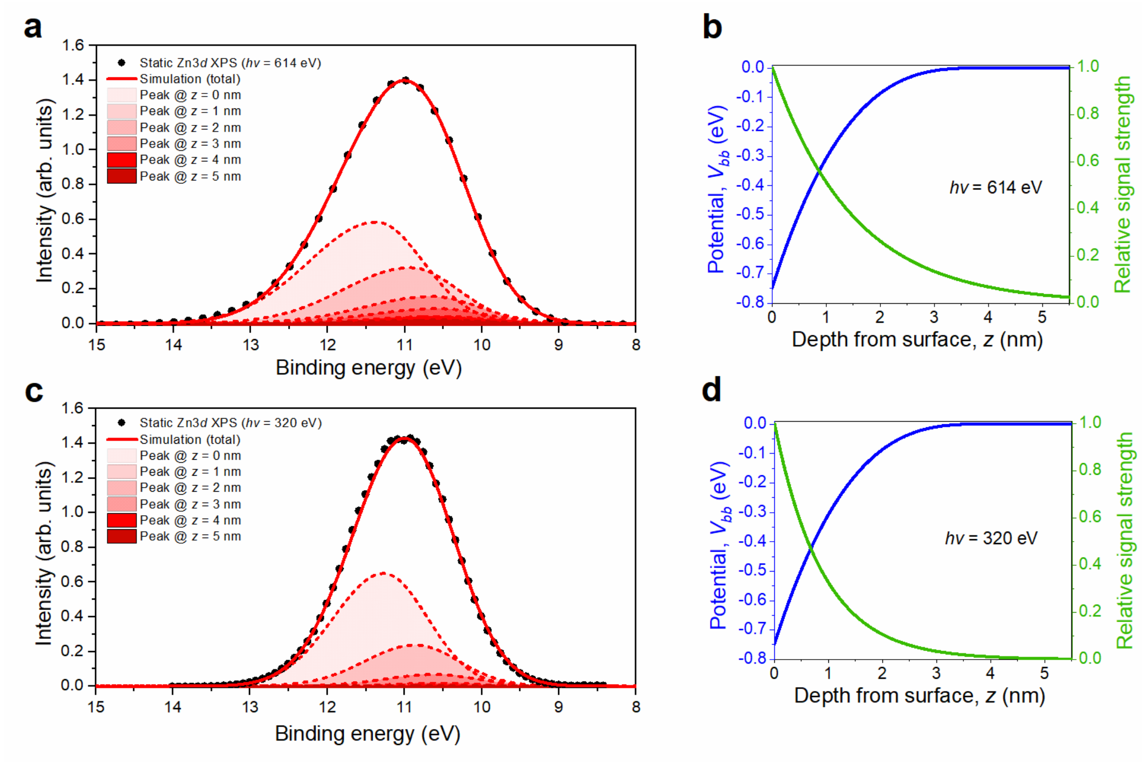

Figure S8. Comparison between measured GS Zn3d spectra and a numerical SCR simulation. **a** Data (black dots) acquired at *hv* = 614 eV and corresponding SCR simulation (red line). Representative contributions D_i from different depths z_i are shown as red-shaded peaks. **b** Near surface potential V_{bb} (blue) and relative XPS signal contributions (green) as a function of depth *z,* which determine the energy position E_B and weight of D_i, respectively. **c** Data and simulation results for *hv* = 320 eV. **d** Depth-dependent potential V_{bb} (blue) and XPS signal contributions (green) that underlie the simulation shown in panel (c).

of the data. For example, a spatially inhomogeneous injection has been approximated by a model with two free fit parameters for the Zn3d line, representing the fraction of regions with injection and the injecting regions' spectral shift. This model did not yield satisfactory fit results. Furthermore, if there were regions of excited dye molecules that do not inject, one would expect fractional line-shape changes in the region of the C1s/Ru3d spectrum since signals from dye molecules in injecting regions would very likely be affected differently than those in non-injecting regions. However, careful analysis of these signals did not reveal any evidence for such effects, but instead the entire C1s/Ru3d undergoes a rigid shift as illustrated in Fig. 1 of the main manuscript. We also emphasize again that we carefully avoided possible complications due to high dye loading by limiting the substrate sensitization time to only 3 minutes, as described in section A.

G) Parallel plate capacitor model for interfacial potential drop

The injected electron in the ZnO CB and the hole remaining in the HOMO of the N3 dye molecule can be viewed as a photo-induced transient dipole that manifests itself as an interfacial potential drop (IPD) within the N3/ZnO system. In a first order description, the injected electron can be assumed to experience metal-like, perfect screening within the ZnO. Within this approximation, the interfacial potential drops between the HOMO hole and the ZnO surface, and is not sensitive to the exact position of the injected electron within the substrate. Experimentally, the IPD is accessible as ΔE_{N3}, i.e. the difference between the C1s/Ru3d shifts, displayed in Fig. 2(a) of the main manuscript, and the Zn3d shift at the surface, i.e. $\Delta V_{bb}(z=0)$. It is important to realize that the detected kinetic energy of Zn3d photoelectrons is not affected by the IPD, despite their passage through it on their way to the detector. The detector and ZnO sample are both grounded and, therefore, share a common Fermi energy level. Hence, the detected kinetic energy of photoelectrons originating from the ZnO substrate is a function of photoelectron binding energy, X-ray photon energy and detector work function only. See e.g. Fig. 2 in ref. 28 for a more detailed explanation. However, photoelectrons emitted by an adsorbate are expected to be affected by the (transient) IPD.[18,29] Similar to static energy shifts induced by interfacial electric fields or surface dipoles as described by Lueth,[30] the IPD can be modeled as a voltage drop across a parallel plate capacitor. Here, the dye HOMO holes and the ZnO surface each constitute one side of the capacitor. For this purpose, the nanoporous structure of the sample is assumed to be approximately described by a (locally) flat surface. Within this approximation, the electric field associated with the IPD is described by $E = \Delta E_{N3}/d_{IPD}$, where d_{IPD} is the distance between the idealized plates, i.e., between HOMO holes and ZnO surface. Using the general relation $C = Q/\Delta E_{N3}$ between the stored charge Q, the voltage drop ΔE_{N3}, and the capacitance C, as well as the parallel-plate capacitor relation $C = \varepsilon_0 \varepsilon_r A/d_{IPD}$, with the vacuum permittivity ε_0, the relative permittivity of the medium between the two plates ε_r, and the area of each individual plate A, and taking into account the interaction of adjacent dipoles, leads to:[28]

$$d_{IPD} = \left(1 + f_{dep}\right) \Delta E_{N3} \varepsilon_0 \varepsilon_r A/Q = \left(1 + f_{dep}\right) \Delta E_{N3} \varepsilon_0 \varepsilon_r/\rho \tag{F1}$$

Here, ρ is the surface charge density $\rho = Q/A$, and the factor $1 + f_{dep}$ is a correction that accounts for the mutual dipole interaction. The so-called depolarization factor f_{dep} for a square array of uniformly arranged charge pairs is given by $f_{dep} \cong 9\alpha\rho^{3/2}/4\pi\varepsilon_0$,[30] with α being the polarizability of the adsorbed molecules. N719, which is very similar to the N3 dye, has a calculated polarizability of $1.06 \cdot 10^{-1}$ nm^3.[31] The surface charge density ρ is estimated by

$$\rho = P_{ex}\, P_{in}\, \rho_M \quad , \tag{F2}$$

where P_{ex} is the molecule excitation probability, P_{in} is the electron injection probability for an excited molecule, and ρ_M is the number of adsorbed molecules per surface area. Values for ρ_M vary between ~0.5 and ~1.0 nm^{-2}, based on experimental (0.55 nm^{-2})[32] and theoretical (0.77 - 1.16 nm^{-2})[33] studies. P_{in} of excited N3 molecules attached to a nanocrystalline film of ZnO has been estimated as being close to unity based on transient optical absorption spectroscopy.[6,34] P_{ex} is defined as

$$P_{ex} = \sigma_{N3}(532\mathrm{nm})\, N_{ph} \quad , \tag{F3}$$

where $\sigma_{N3}(532\mathrm{nm}) \approx 20$ Mbarn is the cross-section of N3 molecules for excitation with 532 nm light,[35] and $N_{ph} = 2.95 \cdot 10^{15}$ cm^{-2} is the number of photons per laser pulse per unit area derived from the laser fluence of 1.1 mJ cm^{-2}. This leads to a fraction of excited molecules $P_{ex} = 5.9\%$ and a surface charge density $\rho = 5.9 \cdot 10^{-2}\, e \cdot$ nm^{-2} (for $\rho_M = 1.0$ nm^{-2}). For this surface charge density, the effect of the depolarization factor f_{dep} is relatively small at 1.4%. The relative permittivity ε_r of a (mono-)layer of molecules is not necessarily related to a macroscopic or bulk-like property.[36] Using values of $\varepsilon_r \approx$ 4-8,[36–40] $\rho_M \approx$ 0.5 - 1.0 nm^{-2}, and $\Delta E_{\mathrm{N3}} = 80$ meV, Eq. F1 leads to a distance between HOMO hole and ZnO surface of 0.3 - 1.2 nm. As noted in the manuscript, these distances are compatible with the height of ~1.0-1.3 nm of N3 dyes anchored to TiO_2 substrates,[41] and the fact that the HOMO holes are primarily located on the Ru centers and NCS groups of the dye molecules.[42]

Within the parallel plate model, the above parameters correspond to an average electric field of ~66 to 260 MV/m within the IPD. Interfacial electric fields in dye-sensitized systems have previously been investigated via the Stark effect in optical absorption spectra.[43–45] Time-resolved Stark effect optical absorption studies found interfacial fields of 35 MV/m[44] and 270 MV/m[45] resulting from photoexcited electron-hole pairs at different ruthenium based sensitizers on TiO_2 in the presence of an electrolyte. The results presented here demonstrate that trXPS provides a complementary route to gain information on interfacial electric fields as well as the spatial distance of transient charge carrier densities relative to the electrode surface.

H) Rate equation model for 2-step charge injection and recombination

Figure S9(a) illustrates the coupled rate equation model used to describe the time-dependent N3 HOMO hole population P_H(t), as well as the electron populations $P_{LUMO}(t)$, $P_{ICT}(t)$ and $P_{CB}(t)$ in the N3 LUMO, in interfacial charge transfer (ICT) states at the surface, and in the ZnO conduction band (CB), respectively. The model is based on the first-order approximation that the time-dependent change of any given electron population P_i is given by the difference between the rate of growth from electron-donating channels and the rate of electron loss into other electron acceptors, whereby the rates are characterized by time-independent rate constants:

$$\frac{d}{dt}P_i(t) = \sum_j k_j^{IN} P_j^{IN}(t) - \sum_m k_m^{OUT} P_i(t) \tag{G1}$$

Here, $P_j^{IN}(t)$ are the time-dependent populations that donate electrons to P_i at rates $k_j^{IN} P_j^{IN}(t)$, and k_m^{OUT} are the time-independent rate constants for the loss of electrons from P_i into other electron acceptors.

The N3 LUMO is populated essentially instantaneously from the HOMO by the optical laser pulse (k_1) and constitutes the first relevant population. The change of P_{LUMO} is proportional to the rate of electron transfer to the surface (k_2) and the recombination rate between the HOMO hole and the LUMO electron (k_{1R}):

$$\frac{d}{dt} P_{LUMO}(t) = -(k_2 + k_{1R})P_{LUMO}(t), \tag{G2}$$

leading to

$$\boldsymbol{P_{LUMO}(t) = P_0 \exp(-[k_2 + k_{1R}]t),} \tag{G3}$$

with $P_{LUMO}(t = 0) = P_0$ as the initial LUMO population created by the pump laser. The corresponding rate equation for $P_{ICT}(t)$ is

$$\frac{d}{dt} P_{ICT}(t) = k_2 P_{LUMO}(t) - (k_3 + k_4)P_{ICT}(t)\,. \tag{G4}$$

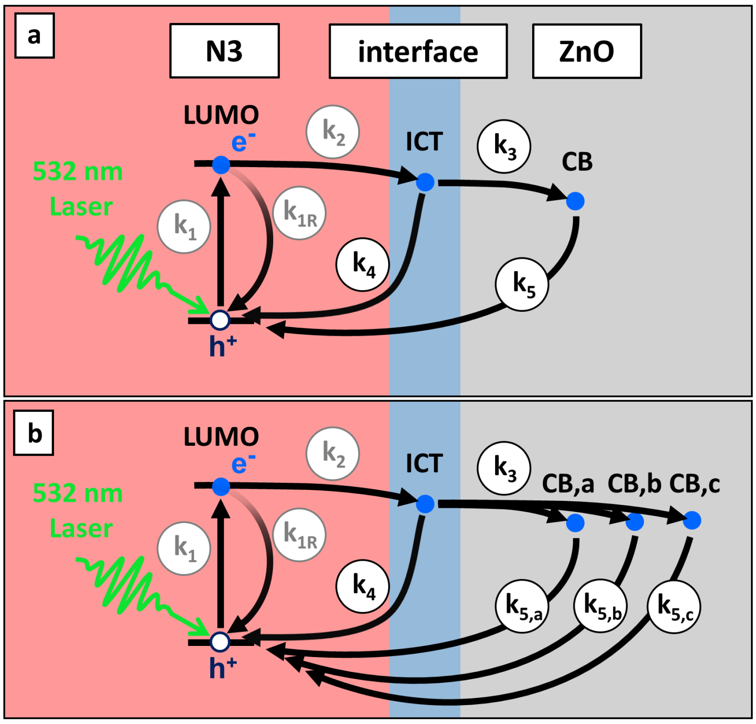

Figure S9. Coupled rate equation model describing photo-induced charge separation, injection and recombination in N3-ZnO heterojunction. **a** Laser light (532 nm, green) is absorbed by N3 dye molecules (red background), leading to a HOMO-LUMO transition (k_1). The electron in the LUMO (e^-) either proceeds to the interface (k_2) to form an interfacial charge transfer (ICT) configuration, or it recombines (k_{1R}) with the hole (h^+). From the ICT configuration, electron injected into the ZnO conduction band (CB) (k_3) is again competing with recombination (k_4). Finally, electrons injected into the ZnO electrode CB recombine with holes in the surface-bound dye molecules with a characteristic rate k_5. This effectively describes a mono-exponential decay behavior from the ZnO CB. **b** A tri-exponential decay can be implemented via three distinct pathways a, b, and c that receive the same total number of electrons with the total rate constant k_3 as in panel (a), while the ratio of the number of electrons per pathway and their decay rates ($k_{5,a}$, $k_{5,b}$, $k_{5,c}$) are different. See text for details. The rates k_1, k_2, and k_{1R} (gray) are not accessible in the experiment and taken from the literature. Rates k_3, k_4, and k_{5a}, k_{5b}, k_{5c} (black) are free fit parameters.

Here, k_3 is the rate of electron injection into the CB from ICT states and k_4 is the recombination rate of ICT electrons with N3 HOMO holes. To solve this equation, we can use Eq. G3 and multiply by $\exp([k_3 + k_4]t)$, after which integration by parts, and the fact that there are no charge carriers at the surface at the moment of excitation, i.e. $P_{ICT}(t = 0) = 0$, leads to

$$\boldsymbol{P_{ICT}(\mathrm{t}) = \frac{k_2\, P_0}{k_3+k_4-\{k_2+k_{1R}\}}[\exp(-[k_2 + k_{1R}]t) - \exp(-[k_3 + k_4]t)]\,.} \quad \text{(G5)}$$

Finally, electrons from the surface-located ICT states are injected into the ZnO CB with a rate of k_3 and recombine from the CB with N3 HOMO holes at a rate of k_5 (Fig. S9(a)), leading to

$$\frac{d}{dt} P_{CB}(t) = k_3 P_{ICT}(t) - k_5 P_{CB}(t)\ . \tag{G6}$$

This equation is solved in a similar fashion as shown above for $P_{ICT}(t)$ and, together with Eq. G5, yields the time-dependent electron population in the ZnO CB:

$$\boldsymbol{P_{CB}}(\mathbf{t}) = \frac{\boldsymbol{k_3\ k_2\ P_0}}{\boldsymbol{k_3+k_4-\{k_2+k_{1R}\}}} \left\{ \frac{\mathbf{exp}(-[\boldsymbol{k_2+k_{1R}}]\boldsymbol{t})-\mathbf{exp}(-\boldsymbol{k_5 t})}{\boldsymbol{k_5-k_2-k_{1R}}} - \frac{\mathbf{exp}(-[\boldsymbol{k_3+k_4}]\boldsymbol{t})-\mathbf{exp}(-\boldsymbol{k_5 t}))}{\boldsymbol{k_5-k_3-k_4}} \right\}. \tag{G7}$$

This solution for $P_{CB}(\mathrm{t})$ effectively incorporates a mono-exponential decay of the ZnO CB population with one rate constant, as shown in Fig. S9(a). The distinctly different timescales for injection and recombination within the system manifest themselves as a plateau for both the C1s and Zn3d trXPS data in Fig. 2(a) of the main text. This difference in timescales enables a simple, straightforward inclusion of the observed multi-exponential decay behavior of the CB electron population in the model.

The trXPS data are best described by a tri-exponential fit. Therefore, as depicted in Fig. S9(b), three different pathways a, b, and c are introduced with independent recombination rates $k_{5,\mathrm{a}}$, $k_{5,\mathrm{b}}$, and $k_{5,\mathrm{c}}$, respectively. These pathways share the electron population provided by the ICT state decay (k_3), using individual amplitude ratios $R_{CB,a}$, $R_{CB,b}$, and $R_{CB,c}$ with respect to the overall electron population, such that

$$\boldsymbol{R_{CB,a}} + \boldsymbol{R_{CB,b}} + \boldsymbol{R_{CB,c}} = \mathbf{1}\ . \tag{G8}$$

The resulting populations $P_{CB,a}(\mathrm{t})$, $P_{CB,b}(\mathrm{t})$, and $P_{CB,c}(\mathrm{t})$ are identical to Eq. G7 except for individual ratios $R_{CB,i}$ as pre-factors and recombination rates $k_{5,\mathrm{i}}$ instead of k_5 such that

$$\boldsymbol{P_{CB,a}}(\mathbf{t}) = \frac{\boldsymbol{R_{CB,a}\ k_3\ k_2\ P_0}}{\boldsymbol{k_3+k_4-\{k_2+k_{1R}\}}} \left\{ \frac{\mathbf{exp}(-[\boldsymbol{k_2+k_{1R}}]\boldsymbol{t})-\mathbf{exp}(-\boldsymbol{k_{5,a} t})}{\boldsymbol{k_{5,a}-k_2-k_{1R}}} - \frac{\mathbf{exp}(-[\boldsymbol{k_3+k_4}]\boldsymbol{t})-\mathbf{exp}(-\boldsymbol{k_{5,a} t}))}{\boldsymbol{k_{5,a}-k_3-k_4}} \right\} \tag{G9}$$

and

$$\boldsymbol{P_{CB,b}}(\mathbf{t}) = \frac{\boldsymbol{R_{CB,b}\ k_3\ k_2\ P_0}}{\boldsymbol{k_3+k_4-\{k_2+k_{1R}\}}} \left\{ \frac{\mathbf{exp}(-[\boldsymbol{k_2+k_{1R}}]\boldsymbol{t})-\mathbf{exp}(-\boldsymbol{k_{5,b} t})}{\boldsymbol{k_{5,b}-k_2-k_{1R}}} - \frac{\mathbf{exp}(-[\boldsymbol{k_3+k_4}]\boldsymbol{t})-\mathbf{exp}(-\boldsymbol{k_{5,b} t}))}{\boldsymbol{k_{5,b}-k_3-k_4}} \right\} \tag{G10}$$

and

$$\boldsymbol{P_{CB,c}}(\mathbf{t}) = \frac{\boldsymbol{R_{CB,c}\ k_3\ k_2\ P_0}}{\boldsymbol{k_3+k_4-\{k_2+k_{1R}\}}} \left\{ \frac{\mathbf{exp}(-[\boldsymbol{k_2+k_{1R}}]\boldsymbol{t})-\mathbf{exp}(-\boldsymbol{k_{5,c} t})}{\boldsymbol{k_{5,c}-k_2-k_{1R}}} - \frac{\mathbf{exp}(-[\boldsymbol{k_3+k_4}]\boldsymbol{t})-\mathbf{exp}(-\boldsymbol{k_{5,c} t}))}{\boldsymbol{k_{5,c}-k_3-k_4}} \right\}. \tag{G11}$$

Because of overall charge neutrality before and after photo-excitation, the HOMO hole population can be expressed through the electron populations above via

$$P_H(\mathrm{t}) = P_{LUMO}(\mathrm{t}) + P_{ICT}(\mathrm{t}) + P_{CB}(\mathrm{t}) \tag{G12}$$

and approximated by

$$P_H(\mathrm{t}) \cong P_{ICT}(\mathrm{t}) + P_{CB}(\mathrm{t}) \tag{G13}$$

since the LUMO population is depleted on timescales that are small compared to the instrument response function.

We emphasize that Fig. S9 illustrates all rates that could principally contribute to the interfacial dynamics, which is more than the number of free fit parameters used and, as outlined in the following, far more than the effective number of free fit parameters relevant for each individual section within the vast range of time-delays included in this study. In more detail: k_1 indicates the initial photoexcitation, which occurs on attosecond timescales, k_2 is the rate of dye oxidation, which is known to be completed within <100 fs (see e.g. Furube et al.[46]). These timescales are far below the temporal resolution of the experiment and, thus, are effectively zero for the purpose of this study. The intramolecular recombination rate k_{1R} is much smaller than the oxidation rate k_2 and has no impact on the fit. In the fit procedure, the three rates k_1, k_2, and k_{1R} (marked gray in Fig. S9) are fixed to literature values. Since the ICT-to-CB injection rate k_3 is much higher than the recombination rates k_4 and k_5 (Fig. S9(a)), the data in Fig. 2(a) reach a plateau at ~1 ns delay and k_3 is effectively the only free fit parameter to describe the early dynamics in Fig. 2(a) for pump-probe delays below 3 ns. Conversely, none of the parameters k_i with i=1...4 have any impact on the slow recombination dynamics at longer delays >3 ns. These are entirely governed by the three recombination rates $k_{5a,b,c}$ (Fig. S9(b)), which are readily apparent from the 3 different decay slopes for delays ≥4 ns in Fig. 2(a). The range of these timescales (~10 ns, ~100 ns, ~2 μs) is in reasonable agreement with the results of Bauer et al.,[9] who report recombination time scales of 290 ns and 2.6 μs. In brief, the number of effective free fit parameters is reduced to 1 for short time delays (≤2 ns) and 3 for long time delays (≥3 ns), whereby each of these contributions are readily apparent from the data in Fig. 2(a): k_3 from the delayed onset of the Zn3d compared to the C1s response, and $k_{5a,b,c}$ from the 3 decay slopes in the logarithmic section of the figure. We therefore trust that the parameter values derived from the fits are meaningful and well-defined. We note that we also tested alternative fit models, such as a stretched exponential and a single-channel sequential recombination, whereby the three observed recombination timescales would be associated with three sequential steps of a single recombination channel. None of the alternatives described the data as well as the model of three independent recombination channels illustrated in Fig. S9(b). This finding is consistent with a picture of (at least) three different recombination channels that may be associated, for example, with different levels occupied by the injected electrons in the substrate. The currently available data, however, do not provide access to this level of detail.

I) Time-resolved XPS of N3 adsorbed to a gold substrate

The difference ΔE_{N3} between the transient energy shifts of the C1s/Ru3d photolines and the surface band bending is interpreted as an interfacial potential drop between the molecular HOMO hole and the semiconductor surface, as described in section G and in the main manuscript. This interpretation is supported by trXPS data of an N3 film drop-cast onto a thin film of gold. The experimental setup used for these measurements is identical to one described in section A. For the N3/Au sample, perfect screening of injected electrons and the absence of any band bending effects in the metal substrate are expected to reduce the photoresponse of the entire sample to the pure molecular response ΔE_{N3}. Figure S10(a) shows the C1s/Ru3d response of the N3/Au sample at a pump-probe delay of $\Delta t = 2$ ns (red) compared to the GS spectrum (blue). Solid lines are the result of the fit procedure described in section B. Subtracting a rigidly (148 meV) shifted GS spectrum from the ES spectrum results in a residual with no discernable structure beyond the signal-to-noise level (Fig. S10(b)), as observed for the N3/ZnO system (Fig. 1(c)). Figure S10(c) shows the temporal evolution of the photoinduced spectral shift. In particular, the inset illustrates the onset of this shift within the instrument response (~70 ps). This is in contrast to the C1s/Ru3d response of the N3/ZnO system, where an additional, slower band bending contribution is present in the overall onset of the C1s/Ru3d response (Fig. 2(a)). The IRF-limited response for the N3/Au system supports the interpretation of ΔE_{N3} as a purely molecular response leading to a potential difference between the molecule itself and the substrate surface. The data shown in Fig. S10(d) verify that the N3/Au photo-response is indeed due to photoexcitation of the N3 dye. At a relatively high laser fluence of 5 mJ/cm^2 and a low scanning speed of 100 µm/s, the dye molecules are gradually and irreversibly damaged, as evidenced by the decreasing amplitude of the C1s/Ru3d shift ($\Delta t = 100$ ps) in subsequent scans on the same sample area. This provides strong evidence that the photo-induced dynamics and associated transient trXPS responses are due to light-harvesting by intact N3 chromophores.

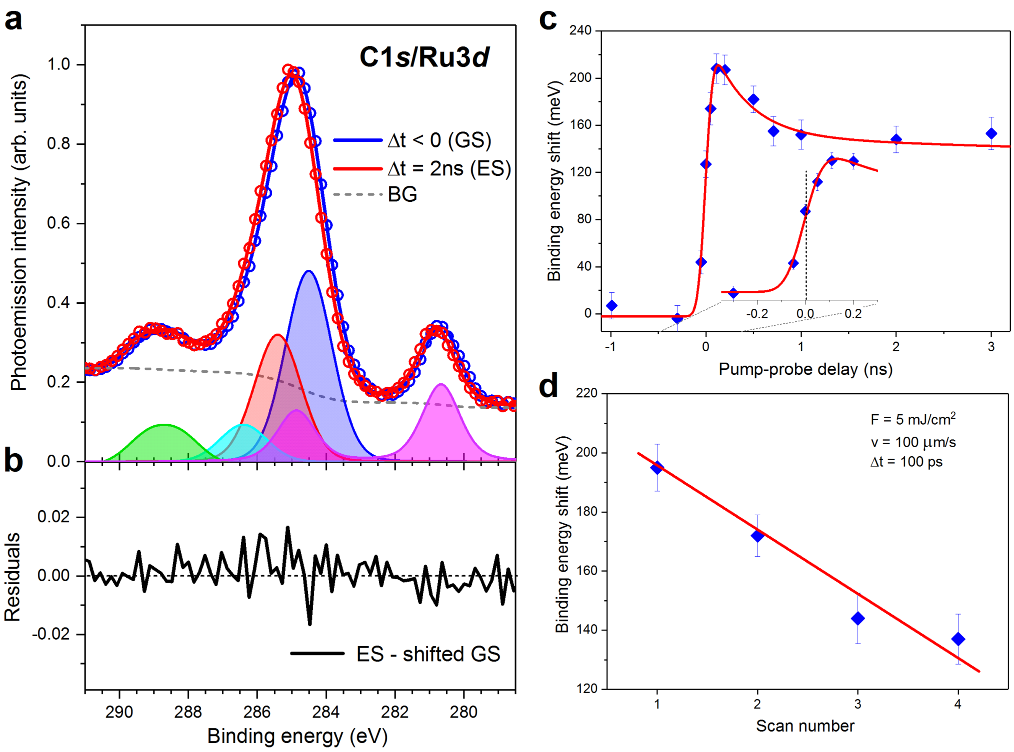

Figure S10. Photoresponse of the C1s/Ru3d lines of N3 adsorbed to a gold substrate. **a** GS (blue) and ES (red) trXPS data (circles) and fits (lines) for the N3/Au system at 2 ns pump-probe delay. **b** Residual trace after modelling the photo-induced effect by a rigid shift of 148 meV. **c** Transient shifts within the first three nanoseconds after photoexcitation. **d** Sample degradation becomes apparent through diminishing maximum binding energy shifts of the C1s/Ru3d photoline when scanning over the same sample area multiple times.

References

(1) Bauer, C.; Boschloo, G.; Mukhtar, E.; Hagfeldt, A. Ultrafast Relaxation Dynamics of Charge Carriers Relaxation in ZnO Nanocrystalline Thin Films. *Chem. Phys. Lett.* **2004**, *387*, 176–181.

(2) Makuła, P.; Pacia, M.; Macyk, W. How To Correctly Determine the Band Gap Energy of Modified Semiconductor Photocatalysts Based on UV–Vis Spectra. *J. Phys. Chem. Lett.* **2018**, *9*, 6814–6817.

(3) Tauc, J.; Grigorovici, R.; Vancu, A. Optical Properties and Electronic Structure of Amorphous Germanium. *Phys. Status Solidi B* **1966**, *15*, 627–637.

(4) Özgür, Ü.; Alivov, Ya. I.; Liu, C.; Teke, A.; Reshchikov, M. A.; Doğan, S.; Avrutin, V.; Cho, S.-J.; Morkoç, H. A Comprehensive Review of ZnO Materials and Devices. *J. Appl. Phys.* **2005**, *98*, 041301.

(5) Chou, T. P.; Zhang, Q.; Cao, G. Effects of Dye Loading Conditions on the Energy Conversion Efficiency of ZnO and TiO_2 Dye-Sensitized Solar Cells. *J. Phys. Chem. C* **2007**, *111*, 18804–18811.

(6) Horiuchi, H.; Katoh, R.; Hara, K.; Yanagida, M.; Murata, S.; Arakawa, H.; Tachiya, M. Electron Injection Efficiency from Excited N3 into Nanocrystalline ZnO Films: Effect of ($N3-Zn^{2+}$) Aggregate Formation. *J. Phys. Chem. B* **2003**, *107*, 2570–2574.

(7) Keis, K.; Bauer, C.; Boschloo, G.; Hagfeldt, A.; Westermark, K.; Rensmo, H.; Siegbahn, H. Nanostructured ZnO Electrodes for Dye-Sensitized Solar Cell Applications. *J. Photochem. Photobiol. Chem.* **2002**, *148*, 57–64.

(8) Neppl, S.; Shavorskiy, A.; Zegkinoglou, I.; Fraund, M.; Slaughter, D. S.; Troy, T.; Ziemkiewicz, M. P.; Ahmed, M.; Gul, S.; Rude, B.; Zhang, J. Z.; Tremsin, A. S.; Glans, P.-A.; Liu, Y.-S.; Wu, C. H.; Guo, J.; Salmeron, M.; Bluhm, H.; Gessner, O. Capturing Interfacial Photoelectrochemical Dynamics with Picosecond Time-Resolved X-Ray Photoelectron Spectroscopy. *Faraday Discuss.* **2014**, *171*, 219–241.

(9) Bauer, C.; Boschloo, G.; Mukhtar, E.; Hagfeldt, A. Electron Injection and Recombination in $Ru(Dcbpy)_2(NCS)_2$ Sensitized Nanostructured ZnO. *J. Phys. Chem. B* **2001**, *105*, 5585–5588.

(10) Ozawa, K.; Emori, M.; Yamamoto, S.; Yukawa, R.; Yamamoto, S.; Hobara, R.; Fujikawa, K.; Sakama, H.; Matsuda, I. Electron–Hole Recombination Time at TiO_2 Single-Crystal Surfaces: Influence of Surface Band Bending. *J. Phys. Chem. Lett.* **2014**, *5*, 1953–1957.

(11) Thompson, A.; Lindau, I.; Attwood, D.; Liu, Y.; Gullikson, E.; Pianetta, P.; Howells, M.; Robinson, A.; Kim, K.-J.; Scofield, J.; Kirz, J.; Underwood, J.; Kortright, J.; Williams, G.; Winick, H. *X-Ray Data Booklet*; 3rd ed.; https://xdb.lbl.gov/xdb-new.pdf; Berkeley, CA, USA, 2009.

(12) Mayor, L. C.; Saywell, A.; Magnano, G.; Satterley, C. J.; Schnadt, J.; O'Shea, J. N. Adsorption of a Ru(II) Dye Complex on the Au(111) Surface: Photoemission and Scanning Tunneling Microscopy. *J. Chem. Phys.* **2009**, *130*, 164704.

(13) King, P. D. C.; Veal, T. D.; Schleife, A.; Zúñiga-Pérez, J.; Martel, B.; Jefferson, P. H.; Fuchs, F.; Muñoz-Sanjosé, V.; Bechstedt, F.; McConville, C. F. Valence-Band Electronic Structure of CdO, ZnO, and MgO from x-Ray Photoemission Spectroscopy and Quasi-Particle-Corrected Density-Functional Theory Calculations. *Phys. Rev. B* **2009**, *79*, 205205.

(14) Mahl, J.; Gessner, O.; Barth, J. V.; Feulner, P.; Neppl, S. Strong Potential Gradients and Electron Confinement in ZnO Nanoparticle Films: Implications for Charge-Carrier Transport and Photocatalysis. *ACS Appl. Nano Mater.* **2021**, *4*, 12213–12221.

(15) Zhang, Z.; Yates, J. T. Band Bending in Semiconductors: Chemical and Physical Consequences at Surfaces and Interfaces. *Chem. Rev.* **2012**, *112*, 5520–5551.

(16) Zojer, E.; Taucher, T. C.; Hofmann, O. T. The Impact of Dipolar Layers on the Electronic Properties of Organic/Inorganic Hybrid Interfaces. *Adv. Mater. Interfaces* **2019**, *6*, 1900581.

(17) Stähler, J.; Rinke, P. Global and Local Aspects of the Surface Potential Landscape for Energy Level Alignment at Organic-ZnO Interfaces. *Chem. Phys.* **2017**, *485–486*, 149–165.

(18) Gleason-Rohrer, D. C.; Brunschwig, B. S.; Lewis, N. S. Measurement of the Band Bending and Surface Dipole at Chemically Functionalized Si(111)/Vacuum Interfaces. *J. Phys. Chem. C* **2013**, *117*, 18031–18042.

(19) Favaro, M.; Jeong, B.; Ross, P. N.; Yano, J.; Hussain, Z.; Liu, Z.; Crumlin, E. J. Unravelling the Electrochemical Double Layer by Direct Probing of the Solid/Liquid Interface. *Nat. Commun.* **2016**, *7*, 1–8.

(20) Lichterman, M. F.; Hu, S.; Richter, M. H.; Crumlin, E. J.; Axnanda, S.; Favaro, M.; Drisdell, W.; Hussain, Z.; Mayer, T.; Brunschwig, B. S.; Lewis, N. S.; Liu, Z.; Lewerenz, H.-J. Direct Observation of the Energetics at a Semiconductor/Liquid Junction by Operando X-Ray Photoelectron Spectroscopy. *Energy Environ. Sci.* **2015**, *8*, 2409–2416.

(21) Minohara, M.; Horiba, K.; Kumigashira, H.; Ikenaga, E.; Oshima, M. Depth Profiling the Potential in Perovskite Oxide Heterojunctions Using Photoemission Spectroscopy. *Phys. Rev. B* **2012**, *85*, 165108.

(22) Sushko, P. V.; Chambers, S. A. Extracting Band Edge Profiles at Semiconductor Heterostructures from Hard-x-Ray Core-Level Photoelectron Spectra. *Sci. Rep.* **2020**, *10*, 13028.

(23) Wippler, D.; Wilks, R. G.; Pieters, B. E.; van Albada, S. J.; Gerlach, D.; Hüpkes, J.; Bär, M.; Rau, U. Pronounced Surface Band Bending of Thin-Film Silicon Revealed by Modeling Core Levels Probed with Hard X-Rays. *ACS Appl. Mater. Interfaces* **2016**, *8*, 17685–17693.

(24) Tsuchiya, T.; Itoh, Y.; Yamaoka, Y.; Ueda, S.; Kaneko, Y.; Hirasawa, T.; Suzuki, M.; Terabe, K. In Situ Hard X-Ray Photoelectron Spectroscopy of Space Charge Layer in a ZnO-Based All-Solid-State Electric Double-Layer Transistor. *J. Phys. Chem. C* **2019**, *123*, 10487–10493.

(25) Shavorskiy, A.; Ye, X.; Karslıoğlu, O.; Poletayev, A. D.; Hartl, M.; Zegkinoglou, I.; Trotochaud, L.; Nemšák, S.; Schneider, C. M.; Crumlin, E. J.; Axnanda, S.; Liu, Z.; Ross, P. N.; Chueh, W.; Bluhm, H. Direct Mapping of Band Positions in Doped and Undoped Hematite during Photoelectrochemical Water Splitting. *J. Phys. Chem. Lett.* **2017**, *8*, 5579–5586.

(26) Tanuma, S.; Powell, C. J.; Penn, D. R. Calculations of Electron Inelastic Mean Free Paths. V. Data for 14 Organic Compounds over the 50-2000 EV Range. *Surf. Interface Anal.* **1994**, *21*, 165–176.

(27) Morkoç, H.; Özgür, Ü. *Zinc Oxide: Fundamentals, Materials and Device Technology*; 2009; Vol. Weinheim, Germany: Wiley-VCH.

(28) Cahen, D.; Kahn, A. Electron Energetics at Surfaces and Interfaces: Concepts and Experiments. *Adv. Mater.* **2003**, *15*, 271–277.

(29) Taucher, T. C.; Hehn, I.; Hofmann, O. T.; Zharnikov, M.; Zojer, E. Understanding Chemical versus Electrostatic Shifts in X-Ray Photoelectron Spectra of Organic Self-Assembled Monolayers. *J. Phys. Chem. C* **2016**, *120*, 3428–3437.

(30) Lueth, H. *Solid Surfaces, Interfaces and Thin Films*; 5th ed.; pp. 527-528; Springer: Berlin Heidelberg, 2010.

(31) Miyashita, M.; Sunahara, K.; Nishikawa, T.; Uemura, Y.; Koumura, N.; Hara, K.; Mori, A.; Abe, T.; Suzuki, E.; Mori, S. Interfacial Electron-Transfer Kinetics in Metal-Free Organic Dye-Sensitized Solar Cells: Combined Effects of Molecular Structure of Dyes and Electrolytes. *J. Am. Chem. Soc.* **2008**, *130*, 17874–17881.

(32) Kavan, L.; Grätzel, M.; Gilbert, S. E.; Klemenz, C.; Scheel, H. J. Electrochemical and Photoelectrochemical Investigation of Single-Crystal Anatase. *J. Am. Chem. Soc.* **1996**, *118*, 6716–6723.

(33) Shklover, V.; Nazeeruddin, M.-K.; Zakeeruddin, S. M.; Barbé, C.; Kay, A.; Haibach, T.; Steurer, W.; Hermann, R.; Nissen, H.-U.; Grätzel, M. Structure of Nanocrystalline TiO_2 Powders and Precursor to Their Highly Efficient Photosensitizer. *Chem. Mater.* **1997**, *9*, 430–439.

(34) Yoshihara, T.; Katoh, R.; Furube, A.; Murai, M.; Tamaki, Y.; Hara, K.; Murata, S.; Arakawa, H.; Tachiya, M. Quantitative Estimation of the Efficiency of Electron Injection from Excited Sensitizer Dye into Nanocrystalline ZnO Film. *J. Phys. Chem. B* **2004**, *108*, 2643–2647.

(35) Grätzel, M. Solar Energy Conversion by Dye-Sensitized Photovoltaic Cells. *Inorg. Chem.* **2005**, *44*, 6841–6851.

(36) Bastide, S.; Butruille, R.; Cahen, D.; Dutta, A.; Libman, J.; Shanzer, A.; Sun, L.; Vilan, A. Controlling the Work Function of GaAs by Chemisorption of Benzoic Acid Derivatives. *J. Phys. Chem. B* **1997**, *101*, 2678–2684.

(37) Rühle, S.; Greenshtein, M.; Chen, S.-G.; Merson, A.; Pizem, H.; Sukenik, C. S.; Cahen, D.; Zaban, A. Molecular Adjustment of the Electronic Properties of Nanoporous Electrodes in Dye-Sensitized Solar Cells. *J. Phys. Chem. B* **2005**, *109*, 18907–18913.

(38) Vilan, A.; Ghabboun, J.; Cahen, D. Molecule−Metal Polarization at Rectifying GaAs Interfaces. *J. Phys. Chem. B* **2003**, *107*, 6360–6376.

(39) Bruening, M.; Cohen, R.; Guillemoles, J. F.; Moav, T.; Libman, J.; Shanzer, A.; Cahen, D. Simultaneous Control of Surface Potential and Wetting of Solids with Chemisorbed Multifunctional Ligands. *J. Am. Chem. Soc.* **1997**, *119*, 5720–5728.

(40) Salomon, A.; Berkovich, D.; Cahen, D. Molecular Modification of an Ionic Semiconductor–Metal Interface: ZnO/Molecule/Au Diodes. *Appl. Phys. Lett.* **2003**, *82*, 1051–1053.

(41) Chen, H.; Cole, J. M.; Stenning, G. B. G.; Yanguas-Gil, A.; Elam, J. W.; Stan, L.; Gong, Y. Imaging Dye Aggregation in MK-2, N3, N749, and SQ-2 Dye···TiO_2 Interfaces That Represent Dye-Sensitized Solar Cell Working Electrodes. *ACS Appl. Energy Mater.* **2020**, *3*, 3230–3241.

(42) Siefermann, K. R.; Pemmaraju, C. D.; Neppl, S.; Shavorskiy, A.; Cordones, A. A.; Vura-Weis, J.; Slaughter, D. S.; Sturm, F. P.; Weise, F.; Bluhm, H.; Strader, M. L.; Cho, H.; Lin, M.-F.; Bacellar, C.; Khurmi, C.; Guo, J.; Coslovich, G.; Robinson, J. S.; Kaindl, R. A.; Schoenlein, R. W.; Belkacem, A.; Neumark, D. M.; Leone, S. R.; Nordlund, D.; Ogasawara, H.; Krupin, O.; Turner, J. J.; Schlotter, W. F.; Holmes, M. R.; Messerschmidt, M.; Minitti, M. P.; Gul, S.; Zhang, J. Z.; Huse, N.; Prendergast, D.; Gessner, O. Atomic-Scale Perspective of Ultrafast Charge Transfer at a Dye–Semiconductor Interface. *J. Phys. Chem. Lett.* **2014**, *5*, 2753–2759.

(43) Oh, D. H.; Sano, M.; Boxer, S. G. Electroabsorption (Stark Effect) Spectroscopy of Mono- and Biruthenium Charge-Transfer Complexes: Measurements of Changes in Dipole Moments and Other Electrooptic Properties. *J. Am. Chem. Soc.* **1991**, *113*, 6880–6890.

(44) Sampaio, R. N.; Li, G.; Meyer, G. J. Continuous Surface Electric Field Contraction Accompanying Electron Transfer from TiO_2 to Oxidized Sensitizers. *ACS Energy Lett.* **2016**, *1*, 846–851.

(45) Ardo, S.; Sun, Y.; Staniszewski, A.; Castellano, F. N.; Meyer, G. J. Stark Effects after Excited-State Interfacial Electron Transfer at Sensitized TiO_2 Nanocrystallites. *J. Am. Chem. Soc.* **2010**, *132*, 6696–6709.

(46) Furube, A.; Katoh, R.; Hara, K.; Murata, S.; Arakawa, H.; Tachiya, M. Ultrafast Stepwise Electron Injection from Photoexcited Ru-Complex into Nanocrystalline ZnO Film via Intermediates at the Surface. *J. Phys. Chem. B* **2003**, *107*, 4162–4166.

5.3 Decomposing Electronic and Lattice Contributions in Optical Pump–X-ray Probe Transient Inner-Shell Absorption Spectroscopy of CuO

The cutting edge of ultrafast X-ray science moves to increasingly high repetition rate and shorter pulse length X-ray sources. High harmonic generation is constantly increasing the spectrally accessible X-ray photon energies, having demonstrated up to 1.5 keV photons,[185] and experimentally useful photon flux at energies <450 eV for X-ray spectroscopy.[186,187] The current minimal achievable pulse duration via high harmonic generation is in the low tens of attoseconds.[188–192] The use of fiber lasers is pushing repetition rates into the megahertz range.[137] Second-generation X-ray free electron lasers[193] are moving towards higher repetition rates with pulse lengths in the few femtoseconds and even sub-femtoseconds regime,[194–196] with corresponding synchronization on the timescale of tens of femtoseconds.[197] These developments have emerged from synchrotron slicing,[198] where femtosecond laser sources were used to isolate a small fraction of an electron bunch in the synchrotron ring that was able to produce femtosecond X-ray pulses with rather limited fluences and kHz repetition rates.

The increasing X-ray repetition rates necessitate the use of pump sources operating with the same repetition rates. Section 4.2 details how this makes residual, non-dissipated heat from the previous pump pulse a potential problem for solid-state experiments, even with femtosecond time resolution. Additionally, in time-resolved experiments with picosecond and lower resolution, higher pump laser fluences make lattice temperature effects more pronounced. The above-described advances in high harmonic generation lead to the accessibility of ultrafast X-ray methods at large scale accelerators, but also increasingly in small-scale laboratories, thereby underscoring the relevance of this topic. Here, existing literature using TRXAS[26] to explore this topic is introduced in more detail, to put the following publication into context. The general goal of all these studies is a better quantitative understanding of thermal effects on ultrafast X-ray spectroscopic measurements with the goal of defining experimental parameters that allow to mitigate such effects or describe them sufficiently well to isolate these signatures from other experimental observables.

Lin *et al.*[63] acquired fs time-resolved XUV data to follow carrier recombination in PbI_2, a synthetic precursor of lead halide perovskites. After the wide bandgap (2.4 eV) SC is excited with 400 nm light (3.1 eV) the iodine 4d level shows signatures of both electrons and holes. All transient effects for pump-probe delays greater than ~4 ps are attributed to lattice temperature effects rather than long-lived electronic effects. An aggregate transient XUV difference spectrum between pump probe delays of 40 to 100 ps qualitatively matches a steady-state difference spectrum between temperatures of 120 and 20 °C (Fig. 6). These results are corroborated by ultrafast electron diffraction (UED) data from which an increase in sample temperature by 133 K was deduced. Furthermore, non-radiative decay is shown to be the dominant pathway by simulating the UED response expected for a full conversion of photon energy to heat. The same simulation demonstrates clear incompatibility of UED data with a radiative decay scenario where only excess photon energy above the bandgap (0.7 eV) is converted to heat. Hayes *et al.*[62] used TRXAS (oxygen and iron K-edges), near-IR and optical ultrafast spectroscopies to investigate photoexcitation of hematite (α-FeO_3). Results of all spectroscopic methods are consistent with lattice heating and subsequent cooling as explanation for any effects at pump-probe delays >100 ps. Specifically, photoinduced changes in the iron K-edge TRXAS 100 ps after excitation with 351 nm light match well with temperature-induced spectral differences between data recorded at sample temperatures of 300 K and 500 K (Fig. 7). Moreover, optical transient absorption data at 20 ps delay after 415 nm excitation qualitatively matches differential optical absorption data for the same temperatures as for the TRXAS data (Fig. 2). Schultze *et al.*[64] studied silicon bandgap modulations due to lattice dynamics. This attosecond time-resolved XUV transient absorption experiment tracks the L-edge absorbance and its derivative on the Si(100) surface. A direct bandgap (3.2 eV) excitation is driven by electron tunneling due to the strong NIR laser light-field. The ~120 meV red-shift of the absorption edge observed after excitation is a combination of a core-level shift, and carrier-carrier interactions causing bandgap narrowing. Relaxation of the excited electrons initially proceeds via carrier-carrier interaction with a ~5 fs time constant followed by electron-phonon coupling with a ~60 fs time constant (Fig. 2D). This ultrafast insight into excited carrier relaxation dynamics shows the relevance of lattice effects even on femtosecond timescales. These three studies provide time-resolved X-ray absorption spectra and qualitative comparisons of individual TRXAS transients with temperature-induced differential XAS data. The following TRXAS study of the oxygen K-edge of CuO adds to these works in that spectroscopic data for an entire time series is modelled by a global fit, utilizing independently acquired temperature-resolved XAS data. This framework provides quantitative access to heat deposition and dissipation in the solid-state sample. Specifically the heat dissipation can be modelled with a resolution of tens of nanometers by exploiting known X-ray penetration and escape depths as well as the laser penetration depth.

Generally, lattice effects can be expected to proceed on longer timescales than electronic effects. Bootstrapping a heat dissipation model with the exclusively temperature-influenced data at longer delays could enable the isolation of electronic effects at earlier delays. This approach could be viable to identify longer-lived electronic effects on the nanosecond timescale. For electronic effects on the sub-picosecond to picosecond timescale, electron-phonon coupling sets in, leading to lattice heating often described with the phenomenological two-temperature model.[199] The coexistence of lattice heating and cooling effects is expected on the pico- to nanosecond timescale depending on the material. Here, an approach that combines the two-temperature model with the presented heat dissipation framework could allow the distinction of temperature-related signatures from laser-induced electronic effects in future experiments. Beyond this application, photoinduced thermal excitations can have utility themselves e.g. to trigger catalytic dynamics.[200]

The following publication is reproduced from ref. 165 with permission from the Royal Society of Chemistry.

Faraday Discussions

Cite this: *Faraday Discuss.*, 2019, **216**, 414

PAPER

View Article Online
View Journal | View Issue

Decomposing electronic and lattice contributions in optical pump – X-ray probe transient inner-shell absorption spectroscopy of CuO†

Johannes Mahl,[ab] Stefan Neppl,‡[a] Friedrich Roth,[cd] Mario Borgwardt,[a] Catherine Saladrigas,[ae] Benjamin Toulson,[a] Jason Cooper,[f] Tahiyat Rahman,[a] Hendrik Bluhm,[ag] Jinghua Guo,[g] Wanli Yang,[g] Nils Huse,[bd] Wolfgang Eberhardt[dg] and Oliver Gessner*[a]

Received 10th December 2018, Accepted 8th January 2019

DOI: 10.1039/c8fd00236c

Electronic and lattice contributions to picosecond time-resolved X-ray absorption spectra (trXAS) of CuO at the oxygen K-edge are analyzed by comparing trXAS spectra, recorded using excitation wavelengths of 355 nm and 532 nm, to steady-state, temperature-dependent XAS measurements. The trXAS spectra at pump-probe time-delays ≥150 ps are dominated by lattice heating effects. Insight into the temporal evolution of lattice temperature profiles on timescales up to 100s of nanoseconds after laser excitation are reported, on an absolute temperature scale, with a temporal sensitivity and a spatial selectivity on the order of 10s of picoseconds and 10s of nanometers, respectively, effectively establishing an "ultrafast thermometer". In particular, for the 532 nm experiment at ~5 mJ cm^{-2} fluence, both the initial sample temperature and its dynamic evolution are well captured by a one-dimensional thermal energy deposition and diffusion model. The thermal conductivity $k = (1.3 \pm 0.4)$ W m^{-1} K^{-1} derived from this model is in good agreement with the literature value for CuO powder, $k_{\text{powder}} =$ 1.013 W m^{-1} K^{-1}. For 355 nm excitation, a quantitative analysis of the experiments is hampered by the large temperature gradients within the probed sample volume owing to the small UV penetration depth. The impact of the findings on mitigating or utilizing

---

[a] *Chemical Sciences Division, Lawrence Berkeley National Laboratory, Berkeley, California, USA. E-mail: ogessner@lbl.gov*

[b] *Physics Department Universität Hamburg, Hamburg, Germany*

[c] *Institute for Experimental Physics, TU Bergakademie Freiberg, Germany*

[d] *Center for Free-Electron Laser Science DESY, Hamburg, Germany*

[e] *Department of Chemistry, University of California, Berkeley, California, USA*

[f] *Joint Center for Artificial Photosynthesis, Lawrence Berkeley National Laboratory, Berkeley, California, USA*

[g] *Advanced Light Source, Lawrence Berkeley National Laboratory, Berkeley, California, USA*

† Electronic supplementary information (ESI) available. See DOI: 10.1039/c8fd00236c

‡ Present Address: Helmholtz-Zentrum Berlin für Materialien und Energie, Berlin, Germany.

photoinduced lattice temperature changes in future X-ray free electron laser (XFEL) experiments is discussed.

1. Introduction

As research in the field of ultrafast X-ray science progresses toward the use of high repetition rate X-ray free-electron lasers[1,2] and high-order harmonic generation (HHG) light sources,[3,4] it is crucial to understand the impact of corresponding high-repetition rate excitation processes on non-replenishing samples that are typical for many applications in materials and chemical sciences. Thermal excitations including phase transitions and their X-ray spectroscopic fingerprints play a particularly important role as they are a ubiquitous, often unintended consequence of virtually all photon absorption processes in condensed phase materials through coupling of electronic and nuclear motion. Understanding and, in many cases, mitigating the impact of thermal excitations on ultrafast X-ray spectroscopy and scattering signals is crucial for the success of a large range of experiments. This applies, in particular, to dynamics that are strongly coupled to thermal excitations[5] and/or that extend beyond the first ~100 fs after photoexcitation where signal contributions from lattice motion due to electron–phonon coupling may become relevant.[6] Despite their importance, systematic studies of the relative contributions and dynamic trends of electronic and lattice excitations in time-resolved X-ray spectroscopy data are scarce to date. Hayes *et al.* found that photoinduced changes in the iron K-edge X-ray absorption spectrum of hematite (α-Fe_2O_3), recorded 100 ps after super-bandgap excitation with 3.5 eV photons, are entirely dominated by lattice heating effects.[7] Lin *et al.* used femtosecond time-resolved XUV absorption spectroscopy to investigate photoinduced dynamics in PbI_2.[8] The transient XUV spectra in this study are well reproduced by lattice temperature dependent changes for pump-probe delays greater than ~4 ps. In an attosecond time-resolved XUV transient absorption experiment on silicon, Schultze *et al.* observed lattice-motion induced band-gap modifications as early as ~60 fs after photoexcitation.[6] Evidently, signal contributions due to lattice motion are an integral part of time-resolved X-ray spectroscopy that can have decisive impact on the feasibility of experiments. It is essential to characterize these signal contributions and to understand their dynamics based on the underlying physics.

Here, we study photoinduced dynamics in the transition metal oxide semiconductor CuO (cupric oxide) using picosecond time-resolved laser-pump – X-ray-probe transient absorption spectroscopy (trXAS). CuO is a p-type semiconductor with possible applications in photocatalytic degradation of organic pollutants,[9,10] hydrogen production from water,[11–13] and as an anode material in lithium batteries.[14] In many of these applications, CuO is used in conjunction with wide band gap semiconductors, such as ZnO and TiO_2, to cover a large portion of the solar spectrum. In the experiments presented here, we study a CuO film that is generated by thermal surface oxidation of a sheet of copper. The trXAS experiments are performed at the oxygen K-edge near ~540 eV using a previously described optical-pump – X-ray-probe picosecond trXAS setup at beamline 8 of the Advanced Light Source (ALS).[15] The pump pulse repetition rate of 127 kHz is comparable to the current 100 kHz design target for the first stage of the Linac Coherent Light Source upgrade (LCLS II). Pump-probe experiments are performed at two different photon energies of 2.33 eV and 3.49 eV. Band gap values for CuO have been reported across a range of ~1.0–2.1 eV,[16–23] thus, both laser wavelengths induce super-bandgap excitations. Relaxation to the conduction band minimum *via* electron-phonon coupling occurs on timescales much smaller than the 70 ps time resolution of the experiment. Therefore, the main difference between measurements with the two different wavelengths is the transfer of an additional 1.2 eV into phonons before relaxation across the band gap, *i.e.*, a potentially higher lattice temperature after excitation with 355 nm, assuming the same number of excitations per unit sample volume (in the following referred to as excitation density). Thus, comparing measurements for both excitation wavelengths (a) using the same excitation density and (b) using the same total excitation energy within the sample volume V $\int_V (\text{photon energy} \times \text{excitation density})$ provides insight into the relative impact of electronic and lattice contributions to the trXAS spectra. Relaxation dynamics are monitored across a pump-probe time-delay range of ~350 ns.

The time-dependent optical-pump – X-ray-probe experiments are complemented by steady-state, temperature-dependent XAS (XAS_{temp}) measurements at sample temperatures between 22 °C and 145 °C, providing a reference for purely temperature-induced effects. The photoinduced changes in the CuO oxygen K-edge trXAS spectra recorded ≥150 ps after photoexcitation with either 355 nm or 532 nm are well reproduced by effects due to increased lattice temperatures. The XAS_{temp} measurements are used to create a "temperature ruler" for the trXAS data, yielding picosecond time-resolved lattice temperature trends. Temperatures for both excitation wavelengths at comparable pump laser fluences of ~5 mJ cm^{-2} exhibit an initial fast decay within ~10s of nanoseconds, followed by a slower cooling trend on ~100s of nanosecond timescales. These dynamics are well reproduced by a one-dimensional thermal diffusion model that explicitly takes into account the depth-dependent intensity distributions of both the UV/vis pump pulses as well as the X-ray probe pulse. Comparison of the 355 nm and 532 nm results illustrates that a detailed modeling of these depth-dependent intensity profiles is crucial for a quantitative understanding of the physics underlying the laser-induced heating and subsequent cooling processes and their impact on the recorded trXAS spectra. The measurements yield a thermal conductivity of the CuO film of $k = (1.3 \pm 0.4)$ W m^{-1} K^{-1}, which is in good agreement with the literature value for CuO powder of 1.013 W m^{-1} K^{-1} in ref. 24 and approximately an order of magnitude smaller than the smallest literature value for bulk CuO of 18 W m^{-1} K^{-1} in ref. 25. The findings are rationalized by surface morphology modifications during the sample preparation by thermal annealing, which have previously been documented using temperature-dependent atomic force microscopy (AFM).[26]

2. Experimental details

2.1 Time-resolved XAS

For the trXAS experiment, a mobile laser-pump – X-ray-probe setup is employed at beamline 8.0.1.2 of the ALS. The setup and its operation have previously been described in detail.[15] Briefly, CuO samples are excited with 10 ps full-width-at-half-maximum (FWHM) laser pulses of either 532 nm (2.33 eV) or 355 nm (3.49 eV) wavelength (photon energy) and interrogated with 70 ps long X-ray pulses from the

ALS. Time-dependent oxygen K-edge absorption spectra are recorded in total fluorescence yield (TFY) mode with a time-sensitive micro-channel plate detector.[27] The detector is capable of distinguishing TFY signals from individual ALS pulses, enabling the simultaneous recording of trXAS spectra at multiple laser-pump – X-ray-probe time delays. The laser system is synchronized to the ALS and operated at ~127 kHz repetition rate. Excited state spectra ("pumped") are compared to ground state reference spectra ("unpumped") by creating difference spectra for each pump-probe delay, $\Delta\text{trXAS}(\Delta t) = \text{trXAS}_{\text{pumped}}(\Delta t) - \text{trXAS}_{\text{unpumped}}$. The sample is raster-scanned with 250 μm s^{-1} scan speed and a 500 μm spacing between neighboring lines to mediate sample damage and thermally induced phase transitions.

2.2 Selection of pump laser fluences

Experiments are performed using pump laser photon energies (wavelengths) of 3.49 eV ($\lambda = 355$ nm) and 2.33 eV ($\lambda = 532$ nm), both of which are beyond the band gap of CuO ($\approx$1.0–2.1 eV (ref. 16–23)). For each laser wavelength, measurements are performed at two different fluences, 1.8 mJ cm^{-2} and 4.6 mJ cm^{-2} for 355 nm as well as 1.7 mJ cm^{-2} and 4.8 mJ cm^{-2} for 532 nm. Fluences are estimated based on the assumption that the FWHM laser focus area contains 50% of the pulse energy. The two higher fluence values are chosen such that both the fluence and the total energy deposited in the sample are the same at each laser wavelength (with the laser spot sizes approximately the same for both colors). The 1.8 mJ cm^{-2} fluence for 355 nm excitation is chosen such that the average laser excitation density within the probed volume is expected to be approximately comparable to that for 532 nm and 4.8 mJ cm^{-2}. The measurement with 1.7 mJ cm^{-2} fluence at 532 nm pump wavelength has been performed as an additional reference point to gauge the impact of the laser fluence on the sample response.

2.3 Temperature-resolved XAS

The trXAS measurements are complemented by temperature-dependent X-ray absorption spectra (XAS_{temp}) recorded at ALS beamline 11.0.2. The XAS_{temp} spectra are acquired in TFY mode using a photodiode covered with an Al filter to suppress background signals from ambient light. The sample is mounted on a button heater stage to control the sample temperature, which is monitored with a thermocouple attached to the front side of the sample. All measurements are performed under 3 mTorr of oxygen, in order to increase the temperature at which the phase transition of CuO to Cu_2O starts to occur.[28,29] Temperature-induced difference spectra $\Delta\text{XAS}_{\text{temp}}$ are calculated by subtracting room temperature (RT) spectra from spectra acquired at elevated temperatures $\Delta\text{XAS}_{\text{temp}}(\Delta T = T - \text{RT}) = \text{XAS}_{\text{temp}}(T) - \text{XAS}_{\text{temp}}(\text{RT})$. For direct comparison of the $\Delta\text{XAS}_{\text{temp}}(\Delta T)$ and the $\Delta\text{trXAS}(\Delta t)$ spectra, RT = 28 °C was used as prolonged laser exposure leads to a slightly increased equilibrium temperature of the sample (see Section 4 for details).

Further details on the sample preparation, trXAS technique, and choice of pump laser fluences are given in the ESI.†

3. Results

Fig. 1a shows static X-ray absorption spectra acquired in total fluorescence yield (TFY, black) and total electron yield (TEY, blue) mode. The spectra agree well with

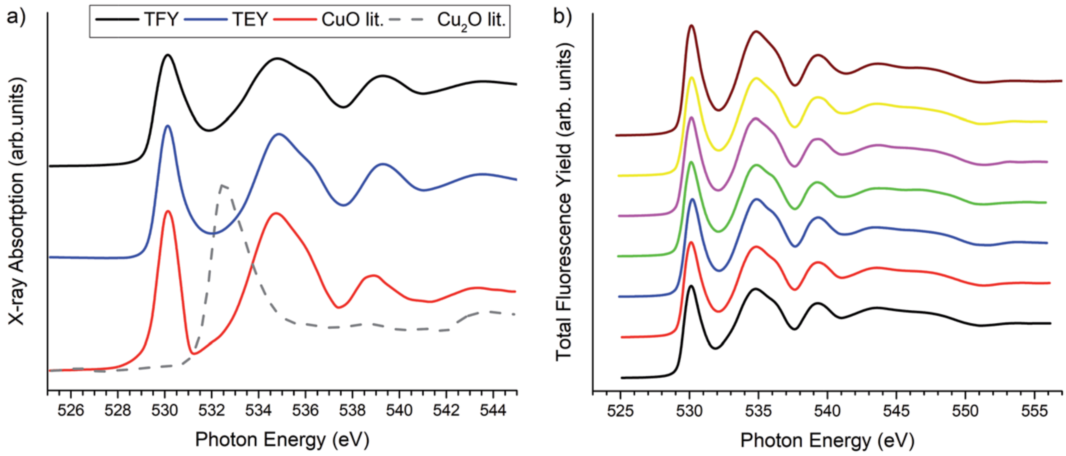

Fig. 1 (a) Comparison of static oxygen K-edge XAS spectra of CuO acquired in TFY (black) and TEY (blue) mode with CuO (red) and Cu_2O (gray, dashed) reference spectra from Jiang *et al.*[30] (b) Static TFY spectra from all samples used for time-resolved measurements. Spectra in (a) and (b) have been offset vertically for improved clarity.

TEY measurements by Jiang *et al.*, shown in red.[30] For comparison, the Cu_2O spectrum from the same study is also included (gray, dashed). The absence of the main Cu_2O resonance feature at 532.5 eV in the black and blue spectra indicates a high purity of the prepared CuO film. The slightly better agreement, concerning the amplitude, between the TEY spectra compared to the TFY spectrum is likely due to saturation and self-absorption effects in the TFY signal.[31] These are minimized by choosing a geometry with a normal X-ray incidence angle and grazing angle X-ray fluorescence detection (~0° and ~82°, respectively, relative to the sample surface normal). Fig. 1b shows static TFY spectra from all samples used for the time-resolved measurements presented here, demonstrating very good reproducibility of the sample preparation and experimental conditions. All spectra are normalized to the same increase between pre- and post-edge signals.

Fig. 2 illustrates the characteristic ΔtrXAS effects of the CuO sample for various pump-probe time delays using the 355 nm, 4.6 mJ cm^{-2} data set as an example. Fig. 2a covers the full spectral range of the measurement, while Fig. 2b provides a magnified view of the first resonance. The static XAS spectrum is overlaid in gray

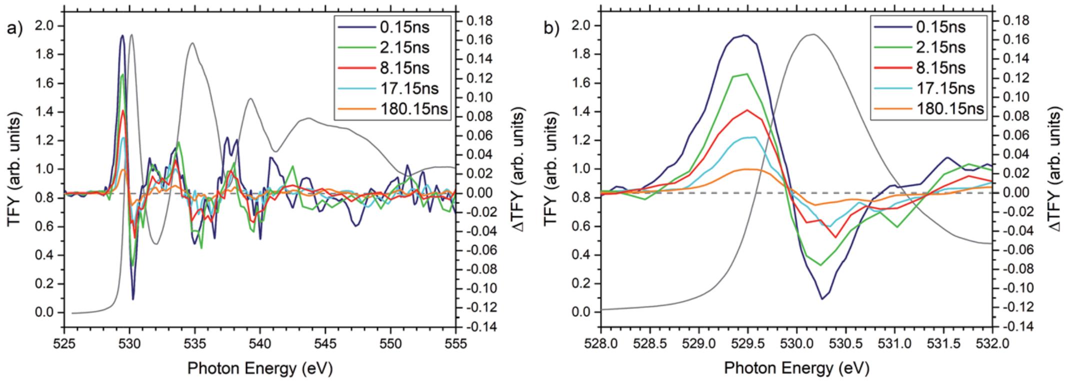

Fig. 2 (a) Overview of the 355 nm 4.6 mJ cm^{-2} trXAS data set. The reference spectrum (gray, left ordinate) is shown along with ΔtrXAS spectra at several pump-probe delays (right ordinate). (b) The lowest energy resonance at 530.1 eV displays the largest relative changes and is analysed in more detail. See text for details.

for reference. The left and right ordinates correspond to XAS and ΔtrXAS spectra, respectively. While the XAS units are arbitrary, they are the same for both the XAS and ΔtrXAS spectra. The blue (0.15 ns) and green (2.15 ns) curves correspond to data from the first and second X-ray pulse after excitation, respectively. In order to investigate smaller differences at longer pump-probe delays, where the ΔtrXAS signals are smaller, signals from multiple ALS bunches are averaged for this figure. The red curve (8.15 ns) is an average of three pulses ($\Delta t = 6.15$–10.15 ns), the cyan curve (17.15 ns) of six pulses ($\Delta t = 12.15$–22.15 ns) and the orange (180.15 ns) of 81 pulses ($\Delta t = 100.15$–260.15 ns). For each of the averaged spectra, the indicated delay is the mean delay of the averaged spectra. The by far strongest effects are observed in the region of the first resonance at ~530.1 eV (Cu e_g ref. 30) which is shown in more detail in Fig. 2b. The difference spectra exhibit a new feature emerging at the low-energy side of the static absorption spectrum (gray) with a peak at ~529.4–529.5 eV. Concurrently, signal is depleted near the static peak maximum with a maximum depletion at ~530.3 eV. The ΔtrXAS spectra exhibit an isosbestic point near ~529.9 eV, which separates the signal enhancement and depletion ranges. At first glance, the difference curves resemble differentials of the static XAS spectrum, which would be an indication that they may be described by a simple energy shift (ΔE) of the XAS spectrum upon photoexcitation, *i.e.* $\Delta\text{trXAS} = \alpha \times [\text{trXAS}(E - \Delta E) - \text{trXAS}(E)]$. However, no combination of parameters α (the fraction of reference spectrum trXAS that is shifted) and ΔE (the shift in X-ray photon energy) can be found that describes the difference spectra reasonably well. This is mostly due to the asymmetry of trXAS signal depletion and emergence, readily apparent in Fig. 2b.

As a first metric to investigate the relaxation dynamics of the photoexcited system, the area underneath the positive peak of the ΔtrXAS spectra in Fig. 2b is plotted as a function of pump-probe delay in Fig. 3. All data sets have been recorded during the same beamtime except for the 355 nm, 1.8 mJ cm^{-2} data. In that case, an additional 355 nm, 4.6 mJ cm^{-2} scan was performed to ensure it matches the data from the previous experiment, and inevitable changes from beamtime to beamtime, such as slight variations of the laser spot size, did not affect the measured signals within the scatter of the data. Each data point in Fig. 3 corresponds to a single pump-probe delay. The amplitudes and dynamic trends of

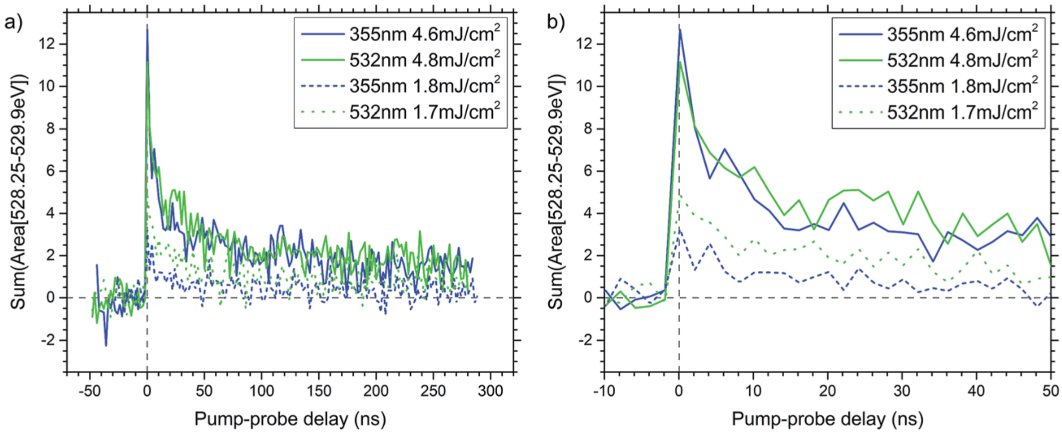

Fig. 3 (a) Time-dependent intensity of the positive ΔtrXAS feature, integrated between 528.25 eV and 529.9 eV (Fig. 2b) for all trXAS data sets. (b) Magnified view for delays up to 50 ns.

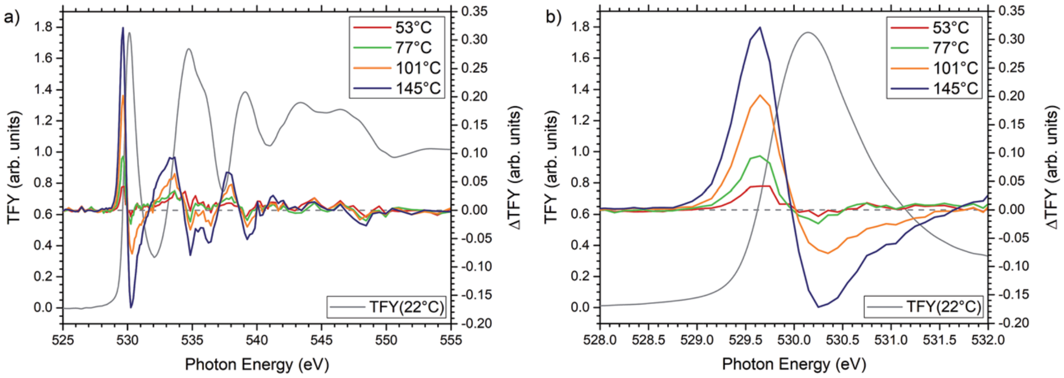

Fig. 4 (a) Temperature-dependent difference spectra ΔXAS_{temp} (colored, right ordinate) together with the reference spectrum XAS_{temp}(22 °C) measured at room temperature (gray, left ordinate). (b) Magnified view near the Cu e_g resonance feature at ~530.1 eV.

the new low-energy feature vary for different excitation wavelengths and fluences. For the highest fluences (4.6–4.8 mJ cm^{-2}), however, they are very similar for both 355 nm and 532 nm excitation. Each of these two data sets display a transient behavior marked by two decay timescales of roughly $t_1 = 10$ ns and $t_2 = 300$ ns. Evidently, the dynamic processes underlying the trXAS signals cannot be characterized by a simple, first-order rate equation. Instead, a more complex description is required that will be derived in Section 4 within the framework of a thermal diffusion model.

Fig. 4 shows the results of the temperature-dependent XAS_{temp} measurements. Fig. 4a shows the room temperature reference spectrum acquired at 22 °C in gray (left ordinate). This reference spectrum is subtracted from spectra acquired at elevated temperatures of 53 °C, 77 °C, 101 °C and 145 °C to generate the color coded ΔXAS_{temp} difference spectra as indicated in the figure legend (right ordinate). Fig. 4b shows a magnified view of the region near the Cu e_g resonance.[30] A comparison of Fig. 2 and 4 reveals striking similarities between the temperature-induced difference spectra $\Delta XAS_{temp}(\Delta T)$ and the photoinduced $\Delta trXAS(\Delta t)$ data. For every resonance peak of the XAS spectrum (~530 eV, ~535 eV and 539 eV), a signal enhancement feature appears at its low-energy side (529.65 eV, 533.50 eV and 537.75 eV) and a depletion feature at its high-energy side (530.3 eV, 535.5 eV and 539.3 eV). Both the positions and relative heights of these features appear to be very similar in both types of measurements. The second resonance around 535 eV has mainly Cu4s and some Cu3d character[30] and consists of two strongly overlapping peaks. Correspondingly, the ΔXAS_{temp} spectra at higher temperatures exhibit a double peaked depletion feature, likely due to overlapping absorption features. As in the case of the ΔtrXAS data, the most distinct features appear in the spectral range of the Cu e_g resonance. Interestingly, the ΔXAS_{temp} spectra also exhibit an isosbestic point separating the positive and negative difference signal for all measured temperatures. It is located at ~530.0 eV, very close to the ~529.9 eV value for the ΔtrXAS curves.

4. Data analysis

Different data sets were recorded with slightly different energy resolutions. In particular, the XAS_{temp} data (Fig. 4) exhibit better energy resolution than the trXAS data. In order to facilitate a quantitative comparison of all observed difference spectra, the energy resolution mismatch is compensated by identifying the ground state XAS spectrum with the lowest energy resolution (532 nm, 4.8 mJ cm^{-2}, further on referred to as XAS$_{\mathrm{ref}}$), and convoluting all other data sets with Gaussian functions that effectively impose a common energy resolution on all ground state and RT spectra. Data analysis is restricted to the energy region between 528.25 and 531.75 eV containing the Cu e$_g$ peak at 530.1 eV. This region exhibits the strongest difference features and small differences in the energy scaling across more extended NEXAFS ranges make a quantitative comparison across larger energy ranges challenging. Due to the asymmetric peak shape, the convolution changes the peak position as well. Therefore, for each ground state spectrum, two free fit parameters are used to match it to XAS$_{\mathrm{ref}}$, the FWHM of the Gaussian convolution function and a rigid shift of the entire spectrum. In order to prevent artifacts due to small peak height variations, all spectra are scaled to the same Cu e$_g$ peak height of 1. The FWHM, energy shift and scaling values derived using the ground state spectra are then applied to both the ground and corresponding excited state spectra to calculate the ΔtrXAS and ΔXAS$_{\mathrm{temp}}$ difference spectra. Fig. 5a shows the ground state (unpumped) reference spectrum XAS$_{\mathrm{ref}}$ (gray, left ordinate) along with ΔtrXAS difference spectra for both excitation wavelengths, 355 nm in blue and 532 nm in green, and two pump laser fluences each at a pump-probe delay of 150 ps (right ordinate). Fig. 5b shows a magnified view of the energy range used for the fit (528.25–531.75 eV). While all data sets show qualitatively similar trends, the best quantitative match is found between the 355 nm, 4.6 mJ cm^{-2} and the 532 nm, 4.8 mJ cm^{-2} data sets. These comparable difference spectra together with the matching peak areas and similar decay behavior illustrated in Fig. 3 strongly suggest that the observed XAS dynamics are primarily defined by the laser fluence, not the photon energy. In contrast, the excitation density within the probed volume appears to play a less prominent role, as evidenced by the significant differences between the traces associated with the 355 nm, 1.8 mJ cm^{-2} and 532 nm, 4.8 mJ cm^{-2} data sets shown in Fig. 3 and 5. In other words, the deposited energy per unit area rather than the number of excitations per unit volume correlates most strongly with the observed transient XAS response, which is a strong indication that thermal effects, rather than the

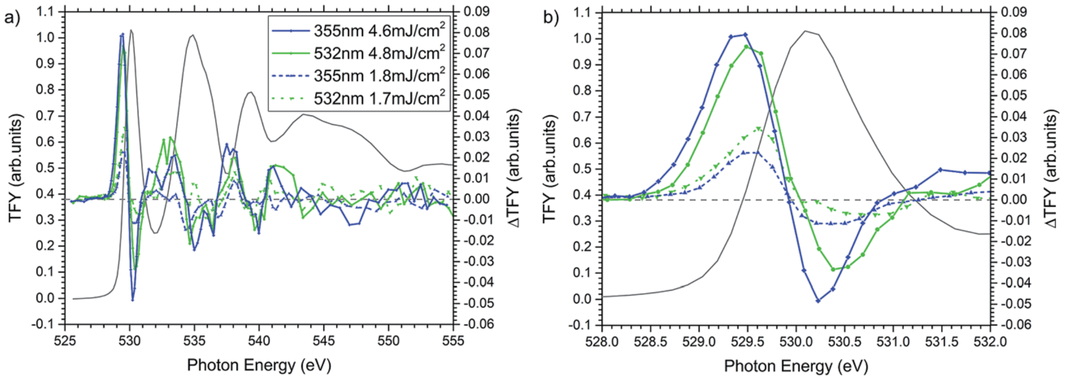

Fig. 5 (a) ΔtrXAS difference spectra at a pump-probe delay of 150 ps for both excitation wavelengths and various pump laser fluences. (b) Spectral region of the lowest energy feature, Cu e$_g$, which is used to adjust all data sets toward a common energy resolution. Data is shown after the convolution procedure is applied. The ground state reference spectrum XAS$_{\mathrm{ref}}$ is shown in gray in both panels.

number of excited electrons, generate the dominant contributions to the ΔtrXAS data.

In order to test this hypothesis, a detailed comparison between the two highest fluence ΔtrXAS data (355 nm, 4.6 mJ cm^{-2} and 532 nm, 4.8 mJ cm^{-2}) and the $\Delta\text{XAS}_\text{temp}$ data is performed for each pump-probe time delay. The comparison is used to generate time-dependent sample temperature profiles for the two trXAS measurements, which are interpreted with the aid of a thermal diffusion model. As demonstrated below, the model reproduces the non-trivial dynamic trends indicated in Fig. 3 and provides access to time-dependent surface- and bulk-temperatures as well as the thermal conductivity of the sample.

In a first step, a linear interpolation of the XAS_temp spectra measured at 22 °C, 53 °C, 77 °C, 101 °C and 145 °C is performed in 1 °C steps in order estimate the shape of the spectra on a finer temperature grid. Spectra for temperature values >145 °C are estimated by a corresponding extrapolation using the 101 °C and 145 °C data. $\Delta\text{XAS}_\text{temp}$ spectra similar to Fig. 4 are generated for all interpolated and extrapolated data beyond 28 °C by subtracting the (interpolated) reference spectrum at 28 °C from the higher temperature spectra. The slightly elevated reference temperature (compared to the nominal 22 °C room temperature) is chosen to account for a slight increase in average temperature during the trXAS measurements that is determined with a thermocouple. The 28 °C spectrum is also used to determine the convolution parameters described above to match the energy resolution of the temperature-dependent and time-dependent spectra.

Two different fit procedures are applied to derive the time-dependent temperature profiles of the sample volumes probed by the trXAS measurements. The first method is easier to implement, but partly neglects inhomogeneous temperature effects, which are fully included in the second method. In the following, we discuss the results achieved by both methods in order to illustrate which effects need to be taken into account and which approximations are applicable when modeling thermal effects in trXAS spectra of condensed phase samples.

In the first method ("homogeneous fit"), the fit routine determines the temperature T for each time delay Δt, for which the absolute difference between the $\Delta\text{XAS}_\text{temp}(T)$ and the $\Delta\text{trXAS}(\Delta t)$ spectra (integrated over the energy range of the Cu e_g resonance) is minimal. Fig. 6a shows the result of this fit procedure for the 532 nm, 4.8 mJ cm^{-2} data set at a pump-probe delay of 150 ps. Depicted are the ΔtrXAS(150 ps) spectrum (green) and the best fit (red) corresponding to the curve $\Delta\text{XAS}_\text{temp}(73\ °\text{C}) = \text{XAS}_\text{temp}(101\ °\text{C}) - \text{XAS}_\text{temp}(28\ °\text{C})$. The residual of the fit is shown as a dashed, black curve. Fig. 6b illustrates the convergence of the fit. The black trace is derived by integrating the absolute value of the residual across the fit energy range for each interpolated $\Delta\text{XAS}_\text{temp}(T)$ spectrum. The minimum position corresponds to the best fit shown in Fig. 6a. The best fit quality varies for different time delays and the corresponding residual curve (as shown in Fig. 6b) is flatter for longer time delays. Nevertheless, the fit always converges to a single temperature to best reproduce the measured $\Delta\text{trXAS}(\Delta t)$ spectrum. Note that the temperature T is the only free parameter of the fit in this method. For any fixed values of T and Δt, the amplitudes of the $\Delta\text{XAS}_\text{temp}(T)$ and $\Delta\text{trXAS}(\Delta t)$ spectra are determined by normalizing the Cu e_g peak heights of the $\text{XAS}_\text{temp}(28\ °\text{C})$ and the ground state trXAS spectra to 1.

Performing this fit for all pump-probe time-delays leads to the time-dependent temperature estimates displayed in Fig. 7. Fig. 7a shows the results for the

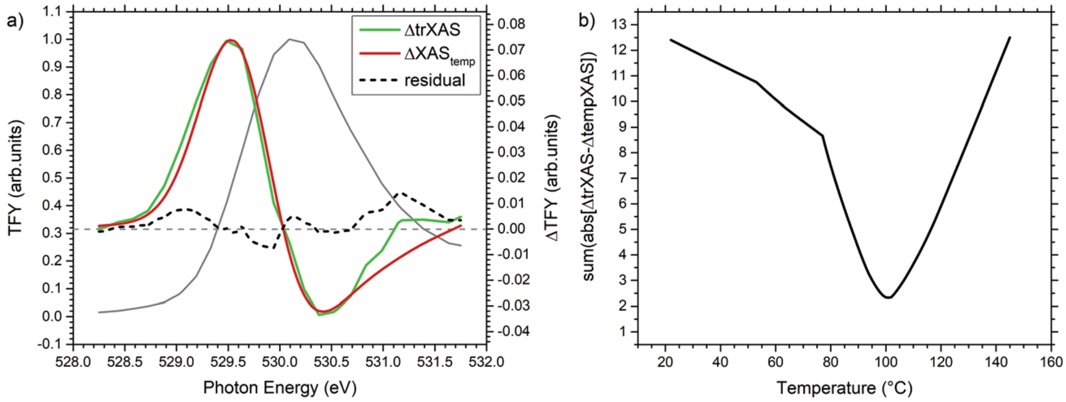

Fig. 6 (a) Photoinduced oxygen K-edge trXAS difference spectrum (ΔtrXAS, green) upon excitation of CuO with 532 nm, ~5 mJ cm^{-2} pulses, probed after 150 ps. The best fit by a temperature-dependent difference spectrum (ΔXAS$_{temp}$) is shown in red, the fit residual in black (dashed). For reference, the ground state XAS spectrum is shown in gray. All difference spectra refer to the right ordinate, the ground state spectrum to the left ordinate. (b) Integral over the absolute value of the fit residual curve in (a) as a function of temperature. The fit routine chooses the minimum of this curve to determine the best ΔXAS$_{temp}$ fit to the ΔtrXAS data.

355 nm, 4.6 mJ cm^{-2} data (blue diamonds), Fig. 7b the corresponding results for the 532 nm, 4.8 mJ cm^{-2} data (green circles). Similar to the traces shown in Fig. 3, the dynamic trends are marked by a fast initial decay within 10s of nanoseconds, followed by a much slower relaxation on 100s of nanosecond timescales. The data are interpreted with the aid of a thermal diffusion model represented by the solid curves in Fig. 7.

The model is based on the assumption that a certain amount of thermal energy is deposited by the pump pulse within a near-surface volume and then propagates further into the bulk by thermal diffusion. Heat transport by convection is neglected, since the experiment is conducted at a pressure of $<5 \times 10^{-9}$ mbar. A simple estimate shows that radiative heat loss is negligible, too. According to the Stefan–Boltzmann law, the total radiated power of a black body at 120 °C is

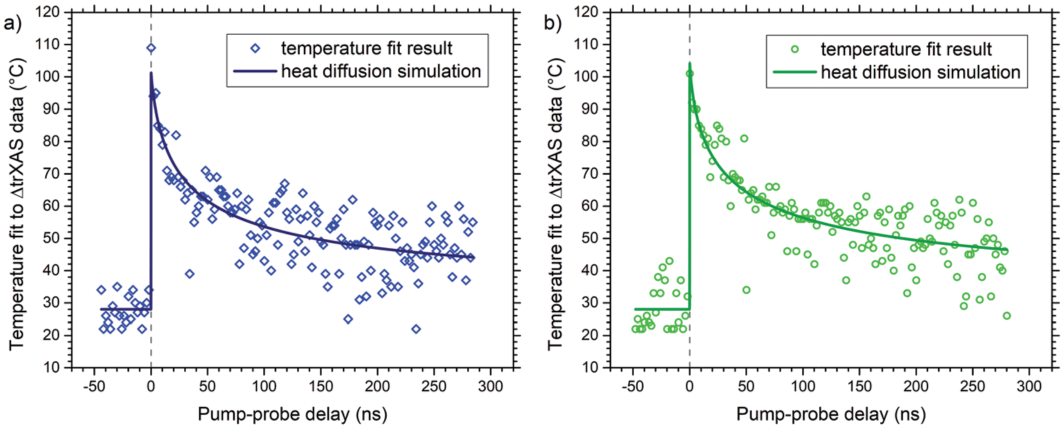

Fig. 7 Time-dependent sample temperatures for excitation with (a) 355 nm (blue diamonds) and (b) 532 nm (green circles) pulses at fluences of ~5 mJ cm^{-2}. Temperatures are derived by a homogeneous temperature fit model that determines a single effective temperature for the probed sample volume. The solid curves are fit results, describing the data within a one-dimensional thermal diffusion model. See text for details.

~1.4 kW m^{-2}. Using a FWHM laser beam size of roughly 250 × 250 μm^2 and a pulse energy of 3 μJ, the fraction of pulse energy emitted within the first 300 ns is 7×10^{-6}, which is negligible within the precision of the experiment. Even when allowing for substantially higher temperatures within the first 150 ps before the first probe pulse arrives, the order of magnitude of this estimate would be unaffected. Heat conduction is modeled as a one-dimensional diffusion process along the surface normal, z. For CuO, the optical penetration depths of 21 nm ($\lambda =$ 355 nm) and 125 nm ($\lambda = 532$ nm)[32,33] as well as the effective X-ray probing depth of 43 nm (ref. 34) (see ESI†) are three to four orders of magnitude smaller than the FWHM of the laser spot (150–250 μm). Furthermore, the diameter of the area probed by the X-ray beam is only about half of the laser spot size. Therefore, the excited and probed sample volumes can be thought of as thin, concentric disks. The characteristic temperature gradients in and around the probed sample volume are thus orders of magnitude larger along the surface normal compared to radial directions parallel to the surface. Consequently, heat transport within the sample may be modeled by diffusion along an insulated cylinder with no lateral heat loss as described by[35–37]

$$\frac{\delta Q}{\delta t} = -k \times A \frac{\delta T(t,z)}{\delta z} . \tag{1}$$

Here, δQ is the amount of thermal energy transferred through a cross-sectional area A per time δt, k is the thermal conductivity and T is the temperature profile as a function of time t and depth z relative to the sample surface. The thermal conductivity is assumed to be constant for simplicity and because slight temperature dependencies would be negligible compared to the overall precision of the analysis presented here. The temperature distribution at time zero $T(t = 0,z)$ is proportional to the derivative of the depth-dependent laser intensity $I_{\text{laser}}(z) = \exp[-z/\delta_{\text{laser}}(\lambda)]$, where δ_{laser} is the laser penetration depth. The amplitude of the resulting exponential function is the initial temperature increase after laser excitation at the surface $\Delta T(t = 0,z = 0)$. This boundary condition leads to

$$T(t=0,z) = \frac{(1-R(\lambda))E_{\text{pulse}}}{2\rho A c(T)\delta(\lambda)_{\text{laser}}} \,\mathrm{e}^{-\frac{z}{\delta(\lambda)_{\text{laser}}}} + \; T_{\text{ref}} \;, \tag{2}$$

where $R(\lambda)$ is the sample reflectivity, E_{pulse} is the laser pulse energy, $\delta_{\text{laser}}(\lambda)$ the 1/e laser penetration depth, ρ the sample density, A is the FWHM laser focus area and $c(T)$ the specific heat capacity.[38] The sample equilibrium temperature $T_{\text{ref}} = 28$ °C is added to the laser-induced temperature jump to convert to an absolute temperature scale $T(t = 0,z)$. Using eqn (2) and the experimental parameters given above, the initial surface temperature estimates are $T(0,0) = 747$ °C for 355 nm (4.6 mJ cm^{-2}) and $T(0,0) = 157$ °C for 532 nm (4.8 mJ cm^{-2}) excitation, respectively.

The subsequent thermal diffusion process is modeled numerically by an iterative computer simulation. Based on an initial temperature profile $T(t = 0,z)$ according to eqn (2), it calculates the amount of heat dQ transferred to and from each volume element $A \times \mathrm{d}z$ within a short time step dt using eqn (1). The slightly modified thermal energy distribution is used to calculate a new temperature profile $T(t + \mathrm{d}t,z)$, which in turn is employed to calculate the depth-dependent heat transfer rates during the next time step and so on. Typical time and depth step sizes are dt = 10 ps and dz = 3 nm, respectively. Convergence of the simulation is tested by varying these step sizes and ensuring that the results are not affected within the overall precision of the method.

For the first, basic temperature analysis presented in Fig. 7, the effective temperature $T_{\text{eff}}(t)$ probed by the X-ray pulse is estimated by multiplying the simulated temperature profile $T(t,z)$ with the probe intensity distribution $I_{\text{X-rays}}(z) \sim \exp[-z/\delta_{\text{X-rays}}]$ and integrating the result over z. Here, $\delta_{\text{X-rays}}$ is the effective 1/e X-ray escape depth described in the ESI.† The free parameters varied during the fit are the amplitude of the initial temperature distribution $T(t = 0,z = 0)$, *i.e.*, the initial surface temperature, and the thermal conductivity k. The best fit results, shown as solid curves in Fig. 7, correspond to thermal conductivities of $k_{355\text{ nm}} = (0.16 \pm 0.06)\text{ W m}^{-1}\text{ K}^{-1}$ and $k_{532\text{ nm}} = (1.3 \pm 0.5)\text{ W m}^{-1}\text{ K}^{-1}$ and initial surface temperatures of $T(0,0)_{355\text{ nm}} = (190 \pm 20)\ ^\circ\text{C}$ and $T(0,0)_{532\text{ nm}} = (120 \pm 11)\ ^\circ\text{C}$. While a substantial difference in the initial surface temperatures is to be expected for the two laser colors due to the factor of ~6 difference in absorption depths, the thermal conductivities should ideally be the same within the precision of the method. In order to improve the temperature dynamics estimates and to get a better understanding of factors affecting the precision of the fit results, a second more advanced temperature modeling and dynamics fit procedure is applied ("inhomogeneous fit").

A key challenge is that each of the XAS_{temp} spectra is acquired at a single temperature that is constant throughout the entire sample, while temperatures in the trXAS experiments vary significantly within the probed sample volume. The first, homogeneous fit method described above hinges on the assumption that an effective temperature T_{eff} can be defined for the probed volume by a weighted average of an extended temperature profile and that the measured $\Delta\text{trXAS}(t)$ spectrum emerging from this volume is well represented by the corresponding $\Delta\text{XAS}_{\text{temp}}(T_{\text{eff}})$ spectrum measured with a homogeneous temperature T_{eff} across the entire sample. However, the temperature dependence of the $\Delta\text{XAS}_{\text{temp}}$ spectra is nontrivial (see Fig. 4) and, generally, the (weighted) average spectrum $\Delta\text{XAS}_{\text{temp}}^{\text{avg}} = \sum_i w_i \Delta\text{XAS}_{\text{temp}}(T_i) \Big/ \sum_j w_j$ of the probed sample volume does not have to be well approximated by the corresponding difference spectrum $\Delta\text{XAS}_{\text{temp}}(T_{\text{eff}})$ measured at the average temperature $T_{\text{eff}} = \sum_i w_i T_i \Big/ \sum_j w_j$. The quality of the approximation is expected to depend strongly on the range of temperatures within the probed volume. For the 532 nm data, the optical penetration depth of 125 nm is significantly larger than the X-ray probing depth of 43 nm, leading to a relatively homogeneous temperature distribution within the probed sample volume and the approximation is expected to hold fairly well. In contrast, for 355 nm excitation, the penetration depth is only 21 nm, much smaller than the X-ray probing depth, resulting in a strongly inhomogeneous temperature distribution within the probed volume, at least for short pump-probe delays. In this case, the approximation is expected to break down.

In order to avoid potential shortcomings of the effective homogeneous temperature approach, a modified inhomogeneous fit procedure is applied that explicitly takes into account both the time- and depth-dependent temperature profiles as well as the complex correlation between local temperatures and corresponding $\Delta\mathrm{XAS}_{\mathrm{temp}}$ profiles. Starting with a thermal conductivity value k and an initial surface temperature $T(0,0)$, the 2D matrix $T(t,z)$ of a time- and depth-dependent temperature profile is calculated using the numerical model based on eqn (1). This provides, in particular, a temperature distribution $T_N(z)$ at the time of arrival of each probe pulse N, *i.e.*, $T_N(z) = T(t_N = t(\text{bunch } N), z)$. The simulated spectrum $\Delta\mathrm{trXAS}_{\mathrm{sim}}(E, t_N)$ for each bunch N is then calculated as the weighted average of the $\Delta\mathrm{XAS}_{\mathrm{temp}}(E, T_N(z))$ spectra using the X-ray intensity distribution $I_{\text{X-rays}}(z) \sim \exp[-z/\delta_{\text{X-rays}}]$ as the weight function:

$$\Delta\mathrm{trXAS}_{\mathrm{sim}}(E, t_N) = \frac{\sum\limits_{z} I_{\text{X-rays}}(z)\Delta\mathrm{XAS}_{\mathrm{temp}}(E, T_N(z))}{\sum\limits_{z'} I_{\text{X-rays}}\left(z'\right)}. \tag{3}$$

During the fit procedure, the values of k and $T(0,0)$ are varied such that the sum of all residuals $R_{\mathrm{total}} = \sum\limits_{N} R_N = \sum\limits_{N}\sum\limits_{E} |\Delta\mathrm{trXAS}_{\mathrm{sim}}(E, t_N) - \Delta\mathrm{trXA}S(E, t_N)|$ for all energies E within the range 528.25–531.75 eV and for all times t_N is minimized. This inhomogeneous fit procedure leads to best fit values of $k_{355\ \mathrm{nm}} = (0.29^{+0.11}_{-0.07})$ W m^{-1} K^{-1} and $k_{532\ \mathrm{nm}} = (1.3 \pm 0.4)$ W m^{-1} K^{-1} for the heat conductivities and $T(0,0)_{355\ \mathrm{nm}} = (230 \pm 30)$°C, $T(0,0)_{532\ \mathrm{nm}} = (123 \pm 10)$ °C for the initial surface temperatures at the two excitation wavelengths. Uncertainties correspond to one sigma standard deviations computed from the fit residuals according to eqn (12) in ref. 39. As expected, the values for 532 nm are very similar to the results derived with the homogeneous, effective temperature fit model, while the values for 355 nm differ considerably.

Fig. 8 shows a comparison of the results from the two modeling procedures for both excitation wavelengths. Gray circles are the result of the homogeneous, single effective temperature fits (same as the data points in Fig. 7) while the black solid lines result from the inhomogeneous fit routine. Similar to the homogeneous fit curves in Fig. 7, the inhomogeneous fit curves in Fig. 8 are generated by multiplying the simulated temperature profiles $T(t,z)$ with the probe intensity distribution $I_{\text{X-rays}}(z) \sim \exp[-z/\delta_{\text{X-rays}}]$ and integrating the results over z. In order to illustrate the effect of varying the thermal conductivity parameter k in the inhomogeneous fit routine, two dashed lines are added, corresponding to the temperature transients computed with half (blue) and double (green) the best fit value of k, while keeping the surface temperatures $T(0,0)$ constant. The curves indicate a pronounced sensitivity of the temperature trends to the absolute value of the thermal conductivity.

Note that the homogeneous and inhomogeneous fit procedures lead to almost identical volume-averaged temperature trends (solid curves in Fig. 7, black curves in Fig. 8). The best fit values for k and $T(0,0)$, however, agree for both fit procedures only for 532 nm excitation, while they differ significantly for the 355 nm data. For the latter, the reconstructed surface temperatures also differ from the volume-averaged ones while they agree reasonably well for the 532 nm measurement. This is illustrated by the red and violet (dotted) curves in Fig. 8, which show the surface temperature trends, $T(t,0)$, for the inhomogeneous and homogeneous fits, respectively. For 532 nm, the two surface temperature curves and the black curve are very similar (Fig. 8b). In contrast, all three curves differ

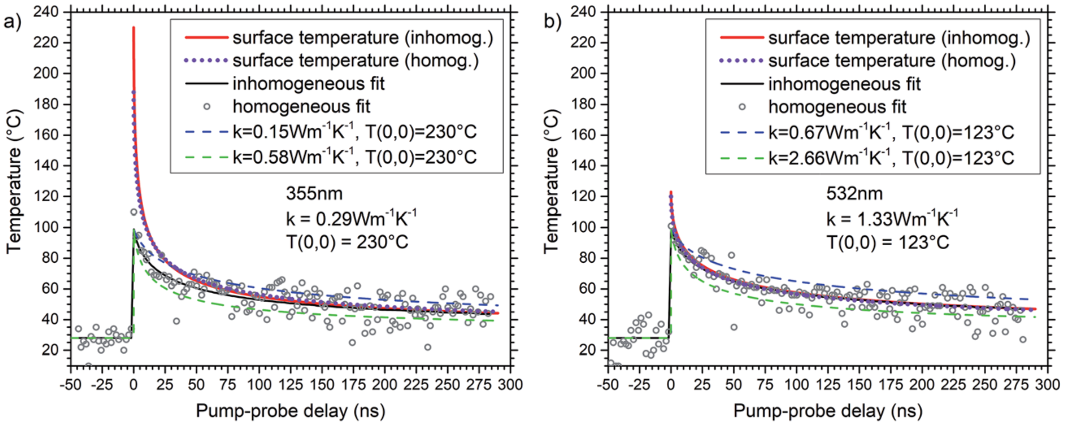

Fig. 8 Temperature dynamics resulting from the two fit models as a function of pump-probe delay for excitation with (a) 355 nm and (b) 532 nm. Singular data points (gray) are the result of the effective, homogeneous temperature model, the black line the result of the inhomogeneous fit model. Red and violet (dotted) lines show the surface temperature dynamics derived from the inhomogeneous and homogeneous fit models, respectively. Blue and green dashed lines indicate the variation of the inhomogeneous fit model results when varying the heat conductance by factors of 1/2 and 2, respectively, compared to the best fit values, while keeping the surface temperature constant.

notably from each other for the 355 nm data set (Fig. 8a). The large differences in the fit results for the 355 nm and 532 nm data are rooted in the different absorption depths of the two excitation wavelengths in relation to the X-ray escape depth. This is illustrated in more detail in Fig. 9, which shows the temperature distributions at time zero (gray lines) and for the first nine probe pulses (colored lines) after excitation, reconstructed with the inhomogeneous fit model. Fig. 9a and b show the results for 355 nm and 532 nm excitation, respectively. For comparison, the X-ray escape profile, offset by the sample equilibrium temperature and scaled to the initial surface temperature, is overlaid as a solid black line in both panels. Note the different ranges of *z*-values in Fig. 9a and b. As expected from the different optical penetration depths, the temperature profiles have much

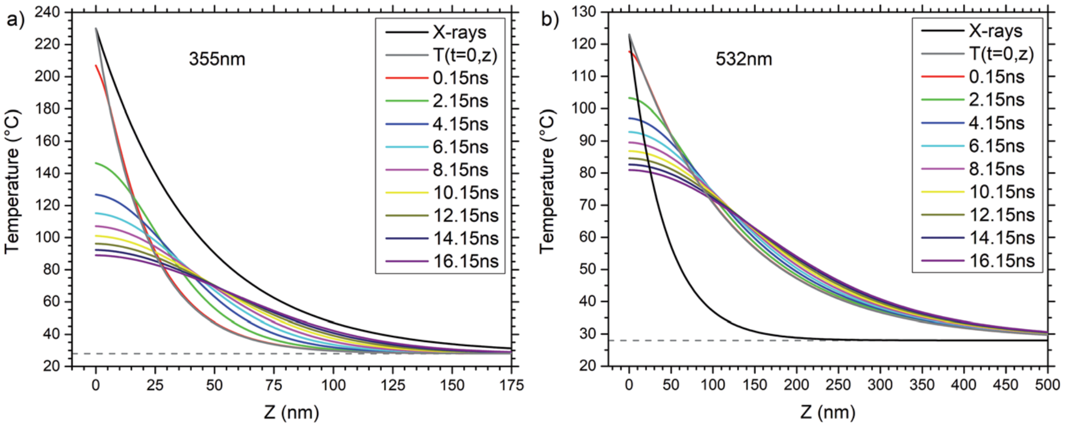

Fig. 9 Time-dependent temperature distributions for (a) 355 nm and (b) 532 nm excitation as a function of distance *z* from the surface along the surface normal. The gray line corresponds to $t \approx 0$ and colored lines to the times of arrival of the first nine X-ray pulses following the laser excitation. For reference, the depth-dependent X-ray probe intensity, offset by the sample equilibrium temperature and scaled to the initial surface temperature, is shown in black.

higher gradients and spread across a larger range of values for the 355 nm experiment compared to the 532 nm experiment. These details, however, are largely obscured in the volume-averaged temperatures "seen" in the experiment. Thus, the striking similarities between the observed volume-averaged temperature dynamics for 355 nm and 532 nm excitation displayed in Fig. 7 and 8 conceal significant differences in the underlying physical phenomena that need to be recovered through careful analysis and modeling. We note that the appearance of significantly higher surface temperatures in the 355 nm experiment compared to the 532 nm experiment is independently corroborated by a more efficient conversion of CuO to Cu_2O upon UV excitation of the sample compared to the visible excitation. This leads to the emergence of an additional signal in the CuO XAS spectrum at the location of the ~532 eV white line of the Cu_2O spectrum (see Fig. 1a), which needs to be suppressed by scanning every sample spot only once in the 355 nm experiment.

5. Discussion

The results presented above strongly suggest that the photoinduced changes in the XAS spectra of CuO beyond ~100 ps pump-probe delay are dominated by thermal effects. This observation is in agreement with the results of Hayes *et al.*[7] and Lin *et al.*[8] for super-bandgap excited α-Fe_2O_3 and PbI_2, respectively. Lin *et al.* excited ~70 nm thick polycrystalline films of PbI_2 (deposited on 50 nm thick silicon nitride) with 400 nm radiation and probed the induced dynamics with femtosecond time-resolved XUV absorption at the iodine 4d level near ~50 eV.[8] Good agreement was found between the photoinduced XUV absorption change after 40–100 ps and a temperature-dependent absorption change induced by heating the sample from 20 °C to 120 °C. A complementary ultrafast electron diffraction experiment by the same group corroborated the finding that temperature effects start to dominate the pump-probe difference spectra after ~4 ps.[8] Hayes *et al.* performed oxygen and iron K-edge trXAS measurements on 20 nm thick films of hematite (α-Fe_2O_3, deposited on 100 nm thick silicon nitride) excited with 400 nm and 351 nm pulses, respectively.[7] The Fe K-edge ΔtrXAS spectrum at 100 ps pump-probe delay is well reproduced by a ΔXAS_{temp} spectrum generated by subtracting a steady-state XAS spectrum recorded at ~30 °C from one acquired at ~230 °C. Corresponding theoretical modeling of the spectra using multiple scattering calculations confirmed that the dominant effects in the ΔtrXAS spectrum are indeed due to thermal effects with contributions from both thermal disorder and lattice distortions.[7]

The study presented here reproduces a predominance of lattice temperature induced effects in picosecond trXAS for another transition metal oxide semiconductor. In addition, it provides further insight into the temporal evolution of lattice temperature profiles after laser excitation on an absolute temperature scale with a temporal sensitivity and a spatial selectivity on the order of 10s of picoseconds and 10s of nanometers, respectively. The results presented in Fig. 7 and 8 indicate that the heat transport dynamics may be approximated by a one-dimensional diffusion model as previously employed in picosecond time-resolved electron diffraction studies of laser-heated metal surfaces.[35] However, comparison of the trXAS results for 355 nm and 532 nm excitation also reveals that a quantitative interpretation of the underlying physics requires detailed understanding and modeling of the relation between the temperature distribution within the sample and the resulting X-ray spectroscopic signatures. In order to understand and predict thermal effects in time-dependent X-ray absorption spectra, it should be ensured that the X-ray probing depth is small compared to the penetration depth of the optical excitation. Otherwise, signal contributions from regions with significantly different temperatures need to be disentangled. This effect is documented by the significant fit-model dependence of both the reconstructed temperature profiles as well as the thermal conductivity k in the 355 nm experiment. In contrast, the corresponding results for the 532 nm measurements are largely model-independent.

Additional evidence that the 532 nm experiment is better understood on a quantitative level is provided by a comparison of the fit results with surface temperature predictions based on eqn (2). The calculated surface temperature after absorption of a 532 nm pump pulse with a fluence of 4.8 mJ cm^{-2} is $T(0,0)_{532\ \mathrm{nm}}(\mathrm{calc}) = 157\ °\mathrm{C}$, which agrees reasonably well with the outcome of the inhomogeneous fit $T(0,0)_{532\ \mathrm{nm}}(\mathrm{fit}) = 123\ °\mathrm{C}$. In contrast, the corresponding values for 355 nm excitation are $T(0,0)_{355\ \mathrm{nm}}(\mathrm{calc}) = 747\ °\mathrm{C}$ and $T(0,0)_{355\ \mathrm{nm}}(\mathrm{fit}) = 230\ °\mathrm{C}$, *i.e.*, the calculated and reconstructed temperature jumps differ by a factor of ~3.6. The reason for this large discrepancy is currently unknown. One contributing factor may be that, despite our best efforts, the convolution methods described in Section 4 could provide an inaccurate modeling of the ΔtrXAS response when the sampled region exhibits a steep-gradient temperature distribution. Another potential issue is that the $\Delta\mathrm{XAS}_{\mathrm{temp}}$ spectra for temperatures above 145 °C have been estimated based on a linear extrapolation of the measurements at 101 °C and 145 °C, which is most likely increasingly inaccurate with increasing temperatures. Interestingly, Hayes *et al.* also observed a significant discrepancy between the estimated temperature rise in their hematite sample based on the absorbed photon energy (~470 °C) and the steady-state temperature rise needed to reproduce the photon-induced change in X-ray absorption (200 °C).[7] In this case, temperature gradients should not play a major role due to the small sample thickness of only 20 nm. Note that in both cases, the hematite experiment using 351 nm excitation and the CuO experiment at 355 nm excitation, the temperature rise estimated by a complete conversion of the absorbed laser pulse energy into heat is much larger than the measured temperature increase based on a comparison to steady-state temperature-dependent $\Delta\mathrm{XAS}_{\mathrm{temp}}$ spectra. Additionally, the estimated temperatures in both cases were significantly higher than the highest temperatures during the steady-state measurements used to determine the $\Delta\mathrm{XAS}_{\mathrm{temp}}$ response. Thus, it could be that this response saturates toward higher temperatures, which would limit their impact on the XAS fingerprint. Further studies with higher reference temperatures are required to gain a better understanding of this regime.

Given the challenges associated with the quantitative analysis of the 355 nm experiment, we restrict a more detailed discussion of the fit results to the 532 nm measurement. The good agreement between the observed and reconstructed temperature dynamics illustrated in Fig. 7b, between the absolute temperature values derived from the absorbed laser pulse energy and the dynamics fit, as well as the model-independence of the fit results for 532 nm excitation suggest that heat transport within the CuO sample is well represented by a thermal diffusion constant $k = (1.3 \pm 0.4)\ \mathrm{W\ m^{-1}\ K^{-1}}$. Literature values for the thermal conductivity of CuO vary across almost two orders of magnitude from 1.013 W m^{-1} K^{-1} in ref. 24 to 18 W m^{-1} K^{-1} in ref. 25 and 33 W m^{-1} K^{-1} in ref. 40 and 78 W m^{-1} K^{-1} in ref. 41. We note, however, that an extensive literature search did not yield any original reference that would describe the experiments used to derive any of these values. Thus, it is not entirely clear whether the large variance is primarily the result of different sample preparation techniques or of uncertainties in the measurements. Notably, however, the smallest value, reported by Samsonov[24] is the only one for which the sample form is indicated as powder. Given that this value is remarkably close to the one derived here and that all other literature values are more than an order of magnitude larger, it appears that the thermal conductivity of the CuO film prepared in this study most closely resembles that of a CuO powder.

At first glance, this result may be surprising as the sample is prepared by annealing a solid sheet of copper. Note, however, that the CuO sample consists of a relatively thin film at the Cu surface and the oxidation process is likely accompanied by significant changes in the surface morphology. Gong *et al.* used annealed sputtering to deposit thin films of copper at temperatures between 200 °C and 400 °C in air and studied the resulting surfaces using X-ray diffraction (XRD), Raman spectroscopy, and atomic force microscopy (AFM).[26] It was concluded that, below 300 °C, Cu is oxidized to Cu_2O and, upon further temperature increase $\geq$300 °C, CuO is formed. In particular, the AFM images reveal substantial surface morphology variations during the phase transitions. During the Cu_2O formation, the surface roughness increases from $\sim$10s to $\sim$100s of nanometer while grains of Cu_2O form and coalesce to typical grain sizes of $\sim$150 nm. At 400 °C, CuO forms in lamellar secondary grains with a thickness of $\sim$5 nm, which are distributed within the larger Cu_2O grains. Based on these observations, it is conceivable that the CuO film prepared here by heating of a Cu surface in air to 500 °C is also marked by a nano-structured morphology rather than a crystalline bulk structure. In this case, the thermal conductivity of the film may be expected to lie closer to the value for a CuO powder than a crystalline bulk sample. Further characterization of the CuO film using alternative techniques may provide additional insight in this regard.

6. Conclusion and outlook

Photoinduced changes in the oxygen K-edge X-ray absorption spectrum of a thin film of CuO have been studied by picosecond time-resolved XAS and complementary steady-state temperature-dependent XAS. The results show that for pump-probe delays $\geq$150 ps, the trXAS spectra are dominated by lattice temperature induced effects for both 355 nm and 532 nm excitation. The laser-induced heating and subsequent sample cooling dynamics at pump laser fluences of $\sim$5 mJ cm^{-2} are well described by a one-dimensional thermal diffusion model that explicitly takes into account the depth-dependence of both the optical excitation and the X-ray probing. A comparison of the measurements with different pump laser wavelengths shows that a detailed modeling of these depth-dependent profiles is crucial for a quantitative understanding of the thermal dynamics in terms of the material properties. *Vice versa*, predicting the impact of thermal excitations on future trXAS studies will require a correspondingly well-developed understanding of the sample properties and nanoscale intensity profiles of pump- and probe-pulse intensities. The thermal conductivity of the

CuO sample used in this study, $k = (1.3 \pm 0.4)$ W m^{-1} K^{-1}, is in good agreement with the literature value for CuO powder, $k_{\text{powder}} = 1.013$ W m^{-1} K^{-1},[24] and approximately an order of magnitude smaller than the smallest literature value for bulk CuO, $k_{\text{bulk}} = 18$ W m^{-1} K^{-1}.[25] This underlines the importance of proper sample characterization prior to a trXAS experiment. A prediction of, for example, how fast thermal excitations in the CuO film may be removed between pump-pulses of a high repetition-rate trXAS experiment would lead to a far too optimistic estimate if it were based on the bulk properties of cupric oxide. Moreover, a predictive understanding of thermal dynamics and their spectral fingerprints is not only important to mitigate sample damage and unwanted signal contributions but also to perform experiments where photoinduced thermal excitations are the actual trigger for the dynamics under investigation.[5] The results presented here demonstrate that a quantitative modeling of thermal effects in trXAS spectra is possible but also that it requires great dedication to detail regarding the material properties and experimental conditions of the pump-probe experiment to make quantitatively accurate predictions.

Conflicts of interest

There are no conflicts to declare.

Acknowledgements

This work was supported by the U.S. Department of Energy, Office of Science, Office of Basic Energy Sciences, Chemical Sciences, Geosciences and Biosciences Division, through Contract No. DE-AC02-05CH11231. This research used resources of the Advanced Light Source, which is a DOE Office of Science User Facility under contract no. DE-AC02-05CH11231. J. M. acknowledges partial support from the ALS Doctoral Fellowship in Residence Program (2017). SN and MB acknowledge support by the Alexander von Humboldt foundation. F. R. acknowledges financial support by VI 419 of the Helmholtz Association. FR and WE were supported by the Helmholtz Research Association (Germany) within the framework program of 'structure of matter'. WE also would like to acknowledge the hospitality of the ALS during some extended visits.

References

1 M. L. Grünbein, J. Bielecki, A. Gorel, M. Stricker, R. Bean, M. Cammarata, K. Dörner, L. Fröhlich, E. Hartmann, S. Hauf, M. Hilpert, Y. Kim, M. Kloos, R. Letrun, M. Messerschmidt, G. Mills, G. Nass Kovacs, M. Ramilli, C. M. Roome, T. Sato, M. Scholz, M. Sliwa, J. Sztuk-Dambietz, M. Weik, B. Weinhausen, N. Al-Qudami, D. Boukhelef, S. Brockhauser, W. Ehsan, M. Emons, S. Esenov, H. Fangohr, A. Kaukher, T. Kluyver, M. Lederer, L. Maia, M. Manetti, T. Michelat, A. Münnich, F. Pallas, G. Palmer, G. Previtali, N. Raab, A. Silenzi, J. Szuba, S. Venkatesan, K. Wrona, J. Zhu, R. B. Doak, R. L. Shoeman, L. Foucar, J.-P. Colletier, A. P. Mancuso, T. R. M. Barends, C. A. Stan and I. Schlichting, *Nat. Commun.*, 2018, **9**, 3487.

2 R. W. Schoenlein, *et al.*, *LCLS-II Science Opportunities, Report SLAC-R-1053*, SLAC National Accelerator Laboratory, Menlo Park CA, https://

portal.slac.stanford.edu/sites/lcls_public/Lists/Publications/DispForm.aspx?ID=1004&ContentTypeId=0x0100D2D2C16F06384A44A845B10E6FC226F600DC7CB9184F2FB34484887A99919A7390, accessed 1 December 2018.

3 S. M. Teichmann, F. Silva, S. L. Cousin, M. Hemmer and J. Biegert, *Nat. Commun.*, 2016, **7**, 11493.

4 D. Popmintchev, B. R. Galloway, M.-C. Chen, F. Dollar, C. A. Mancuso, A. Hankla, L. Miaja-Avila, G. O'Neil, J. M. Shaw, G. Fan, S. Ališauskas, G. Andriukaitis, T. Balčiunas, O. D. Mücke, A. Pugzlys, A. Baltuška, H. C. Kapteyn, T. Popmintchev and M. M. Murnane, *Phys. Rev. Lett.*, 2018, **120**, 093002.

5 H. Öström, H. Öberg, H. Xin, J. LaRue, M. Beye, M. Dell, J. Gladh, M. L. Ng, J. A. Sellberg, S. Kaya, G. Mercurio, D. Nordlund, M. Hantschmann, F. Hieke, D. Kühn, W. F. Schlotter, G. L. Dakovski, J. J. Turner, M. P. Minitti, A. Mitra, S. P. Moeller, A. Föhlisch, M. Wolf, W. Wurth, M. Persson, J. K. Nørskov, F. Abild-Pedersen, H. Ogasawara, L. G. M. Pettersson and A. Nilsson, *Science*, 2015, **347**, 978–982.

6 M. Schultze, K. Ramasesha, C. D. Pemmaraju, S. A. Sato, D. Whitmore, A. Gandman, J. S. Prell, L. J. Borja, D. Prendergast, K. Yabana, D. M. Neumark and S. R. Leone, *Science*, 2014, **346**, 1348–1352.

7 D. Hayes, R. G. Hadt, J. D. Emery, A. A. Cordones, A. B. F. Martinson, M. L. Shelby, K. A. Fransted, P. D. Dahlberg, J. Hong, X. Zhang, Q. Kong, R. W. Schoenlein and L. X. Chen, *Energy Environ. Sci.*, 2016, **9**, 3754–3769.

8 M.-F. Lin, M. A. Verkamp, J. Leveillee, E. S. Ryland, K. Benke, K. Zhang, C. Weninger, X. Shen, R. Li, D. Fritz, U. Bergmann, X. Wang, A. Schleife and J. Vura-Weis, *J. Phys. Chem. C*, 2017, **121**, 27886–27893.

9 S. Harish, J. Archana, M. Sabarinathan, M. Navaneethan, K. D. Nisha, S. Ponnusamy, C. Muthamizhchelvan, H. Ikeda, D. K. Aswal and Y. Hayakawa, *Appl. Surf. Sci.*, 2017, **418**, 103–112.

10 R. Saravanan, S. Karthikeyan, V. K. Gupta, G. Sekaran, V. Narayanan and A. Stephen, *Mater. Sci. Eng., C*, 2013, **33**, 91–98.

11 S. Xu, A. J. Du, J. Liu, J. Ng and D. D. Sun, *Int. J. Hydrogen Energy*, 2011, **36**, 6560–6568.

12 J. Yu, Y. Hai and M. Jaroniec, *J. Colloid Interface Sci.*, 2011, **357**, 223–228.

13 J. Bandara, C. P. K. Udawatta and C. S. K. Rajapakse, *Photochem. Photobiol. Sci.*, 2005, **4**, 857.

14 W. Zhang, G. Ma, H. Gu, Z. Yang and H. Cheng, *J. Power Sources*, 2015, **273**, 561–565.

15 S. Neppl, J. Mahl, A. S. Tremsin, B. Rude, R. Qiao, W. Yang, J. Guo and O. Gessner, *Faraday Discuss.*, 2016, **194**, 659–682.

16 N. Serin, T. Serin, Ş. Horzum and Y. Çelik, *Semicond. Sci. Technol.*, 2005, **20**, 398–401.

17 B. Balamurugan and B. R. Mehta, *Thin Solid Films*, 2001, **396**, 90–96.

18 F. Marabelli, G. B. Parravicini and F. Salghetti-Drioli, *Phys. Rev. B: Condens. Matter Mater. Phys.*, 1995, **52**, 1433–1436.

19 M. T. Nair, L. Guerrero, O. L. Arenas and P. Nair, *Appl. Surf. Sci.*, 1999, **150**, 143–151.

20 S. C. Ray, *Sol. Energy Mater.*, 2001, **68**, 307–312.

21 C. E. Ekuma, V. I. Anisimov, J. Moreno and M. Jarrell, *Eur. Phys. J. B*, 2014, **87**, 23.

22 M. Dahrul, H. Alatas and Irzaman, *Procedia Environ. Sci.*, 2016, **33**, 661–667.
23 J. F. Pierson, A. Thobor-Keck and A. Billard, *Appl. Surf. Sci.*, 2003, **210**, 359–367.
24 G. V. Samsonov, *The Oxide Handbook*, IFI/Plenum, New York, 1973.
25 A. L. Edwards, *A Compilation Of Thermal Property Data For Computer Heat-Conduction Calculations*, Report No. UCRL-50589, 1969.
26 Y. S. Gong, C. Lee and C. K. Yang, *J. Appl. Phys.*, 1995, **77**, 5422–5425.
27 A. S. Tremsin, O. H. Siegmund, J. S. Hull, J. V. Vallerga, J. B. McPhate, J. Soderstrom, J.-W. Chiou, J. Guo and Z. Hussain, *IEEE Nucl. Sci. Symp. Conf. Rec.*, 2006, **2**, 735–739.
28 S. Poulston, P. M. Parlett, P. Stone and M. Bowker, *Surface and Interface Analysis: An International Journal devoted to the development and application of techniques for the analysis of surfaces, interfaces and thin films*, 1996, vol. 24, pp. 811–820.
29 M. Heinemann, B. Eifert and C. Heiliger, *Phys. Rev. B: Condens. Matter Mater. Phys.*, 2013, **87**, 115111.
30 P. Jiang, D. Prendergast, F. Borondics, S. Porsgaard, L. Giovanetti, E. Pach, J. Newberg, H. Bluhm, F. Besenbacher and M. Salmeron, *J. Chem. Phys.*, 2013, **138**, 024704.
31 S. Eisebitt, T. Böske, J.-E. Rubensson and W. Eberhardt, *Phys. Rev. B: Condens. Matter Mater. Phys.*, 1993, **47**, 14103–14109.
32 D. Tahir and S. Tougaard, *J. Phys.: Condens. Matter*, 2012, **24**, 175002.
33 W. K. C. Yung, B. Sun, Z. Meng, J. Huang, Y. Jin, H. S. Choy, Z. Cai, G. Li, C. L. Ho, J. Yang and W. Y. Wong, *Sci. Rep.*, 2016, **6**, 39584.
34 CuO – X-ray attenuation length, http://henke.lbl.gov/optical_constants/atten2.html, accessed 28 November 2018.
35 H. E. Elsayed-Ali and J. W. Herman, *Appl. Phys. Lett.*, 1990, **57**, 1508–1510.
36 J. H. Bechtel, *J. Appl. Phys.*, 1975, **46**, 1585–1593.
37 J. Crank, *The Mathematics of Diffusion*, Oxford University Press, Oxford, England, end edn, 1975.
38 Copper oxide – National Insitute for Standards and Technology, https://webbook.nist.gov/cgi/cbook.cgi?ID=C1317380&Type=JANAFS&Table=on, accessed 28 November 2018.
39 P. J. Cumpson and M. P. Seah, *Surf. Interface Anal.*, 1992, **18**, 345–360.
40 M. Liu, M. Lin and C. Wang, *Nanoscale Res. Lett.*, 2011, **6**, 297.
41 D. Anandan and K. S. Rajan, *Asian J. Sci. Res.*, 2012, **5**, 218–227.

Received 00th January 20xx,
Accepted 00th January 20xx

DOI: 10.1039/x0xx00000x

www.rsc.org/

Decomposing Electronic and Lattice Contributions in Optical Pump – X-ray Probe Transient Inner-Shell Absorption Spectroscopy of CuO - Supplementary Information

Johannes Mahl[a,b], Stefan Neppl[a,c], Friedrich Roth[d,e], Mario Borgwardt[a], Catherine Saladrigas[a,f], Benjamin Toulson[a], Jason Cooper[g], Tahiyat Rahman[a], Hendrik Bluhm[a,h], Jinghua Guo[h], Wanli Yang[h], Nils Huse[b,e], Wolfgang Eberhardt[e,h], and Oliver Gessner[a]

Sample preparation Copper sheet metal is cut to size and the surface roughened with sand paper to create better adhesion of the CuO film grown on the Cu substrate. This is followed by cleaning with micro-soap, acetone and ethanol in this order. The samples are then transferred to a furnace and heated to 500°C for 15 minutes in normal atmosphere. During this procedure, the sample surface oxidizes, creating a layer of CuO.[1–3] After cooling, the sample is gently wiped with an ethanol-soaked lint-free tissue. The heating-cooling-wiping cycle is repeated a total of five times. While the exact value for the final CuO film thickness is unknown, it is large compared to the ~43 nm probing depth of the X-rays (see below), as no significant count rate fluctuations are observed while raster-scanning the sample.

Time-resolved XAS Inside the vacuum system, the pump and probe beams are combined by reflecting the laser beam off a mirror with a hole in the center that allows the X-rays to pass through. Spatial pump-probe overlap is achieved by performing knife-edge scans for both beams using a photodiode with carbon tape attached along horizontal and vertical directions, providing straight edges in both dimensions. The laser pointing is adjusted with a piezo-actuator controlled mirror mount to coincide with the X-rays. The X-ray and laser focus spot sizes are $180 \times 80\,\mu m^2$ and $\sim 250 \times 200\,\mu m^2$ (horizontal × vertical, FWHM), respectively, ensuring that the probed sample area is homogeneously excited. Larger laser spot sizes would unnecessarily increase the total deposited energy (mJ) per shot at a given excitation fluence (mJ/cm^2), leading to additional sample heating and, potentially, damage (see below). The laser spot sizes were approximately the same for both laser colors. Temporal pump-probe overlap is adjusted using a biased photodiode with 30 ps

---

[a] Chemical Sciences Division, Lawrence Berkeley National Laboratory, Berkeley, California, USA
[b] Physics Department Universität Hamburg, Hamburg, Germany
[c] Present Address: Helmholtz-Zentrum Berlin für Materialien und Energie, Berlin, Germany
[d] Institute for Experimental Physics, TU Bergakademie Freiberg, Germany
[e] Center for Free-Electron Laser Science DESY, Hamburg, Germany
[f] Department of Chemistry, University of California, Berkeley, California, USA
[g] Joint Center for Artificial Photosynthesis, Lawrence Berkeley National Laboratory, Berkeley, California, USA
[h] Advanced Light Source, Lawrence Berkeley National Laboratory, Berkeley, California, USA

response time and a digital oscilloscope with 1 GHz bandwidth and 10 GS/s sample rate.

The ALS was operated in multi-bunch mode with 2 ns bunch-to-bunch spacing. Thus, individual TFY spectra have pump-probe delays of $\Delta t_N = t_N - t_0 = \Delta t_0 + 2\,\text{ns} * (N-1)$, where Δt_0 is the pump-probe delay of the first X-ray pulse after the laser pulse and $N = 1,2,3,\ldots$ indicates the N^{th} X-ray pulse following the laser pulse. The minimum pump-probe delay is set to $\Delta t_0 = (150 \pm 30)$ ps for all measurements presented here. The simultaneous recording of trXAS spectra from an extended X-ray pulse train enables the concurrent capture of dynamics across hundreds of nanoseconds, while for delays <2 ns, the pump-probe delay Δt_0 is varied by a programmable, electronic delay line. Excited state spectra ("pumped") are compared to ground state reference spectra ("unpumped") by creating difference spectra for each pump-probe delay, $\Delta\text{trXAS}(\Delta t) = \text{trXAS}_{\text{pumped}}(\Delta t) - \text{trXAS}_{\text{unpumped}}$. Any given pumped spectrum is compared to an unpumped spectrum stemming from the same ALS electron bunch, but acquired one round-trip (656 ns) before laser excitation. This procedure ensures minimum impact of bunch-to-bunch variations in the ALS fill pattern on the ΔtrXAS spectra. Long-term variations of the bunch fill pattern are accounted for using bunch current monitor data supplied by the ALS. Additionally, photon energy dependent variations of the average incident X-ray flux are monitored via a gold mesh placed in the X-ray beam downstream from the last beamline optic.

The main reason for raster scanning the sample during data acquisition is to avoid thermally induced conversion of CuO to Cu_2O, which is particularly noticeable when pumping with 355 nm pulses. High temperatures in conjunction with low partial pressures of oxygen lead to a CuO to Cu_2O phase transition.[4,5] The effect is more pronounced in the 355 nm measurement, most likely due to the smaller penetration depth of 355 nm light compared to 532 nm photons,[6] which leads to higher transient surface temperatures under UV exposure (see section 4 of the main text). The scan speed is chosen such that upon recording of an XAS spectrum on an already laser-scanned sample area, no contributions from the intense Cu_2O white line at 532.5 eV (Fig. 1a) is detected. Note that the scanning procedure is essential to avoid artifacts due to overlapping transient features from CuO and Cu_2O.[7]

Selection of pump laser fluences The 1.8 mJ/cm² fluence for 355 nm excitation is chosen such that the average laser excitation density within the probed volume is expected to be approximately comparable to that for 532 nm and 4.8 mJ/cm². This estimate takes into account the wavelength dependent reflectivities (11.3% and 9.9%, measured independently) and absorbances (1/e penetration depths 21.2 nm and 124.5 nm[2,6]) of the 355 nm and 532 nm pump pulses, respectively, as well as the X-ray penetration and escape depths at the angles of incidence (0˚) and detection (~82±8˚). The 1/e X-ray penetration depth undergoes significant changes around the absorption edge from 320 nm below (<528 eV) to 180 nm above (>543 eV) the edge.[8] For simplicity, the latter value (180 nm) is used as the average penetration depth for the incoming X-rays while the former (320 nm) is used for the 1/e escape depth of the X-ray fluorescence. Multiplying the two exponential decay functions that describe the X-rays entering and escaping the CuO sample and including the entrance and detection angles, leads to an effective 1/e X-ray probing depth of 43 nm. According to this estimate, the excitation densities within the probed volume for 355 nm and 532 nm pump pulses are comparable for a pump fluence ratio $F_{532\,\text{nm}}/F_{355\,\text{nm}} = 1.9^{+1.9}_{-0.4}$. The range of this value is relatively large due to the large angular acceptance of the X-ray fluorescence detector. It includes, in particular, the experimental ratio of 4.8 mJ/cm² / 1.8 mJ/cm² = 2.7.

References

1 L. De Los Santos Valladares, D. H. Salinas, A. B. Dominguez, D. A. Najarro, S. I. Khondaker, T. Mitrelias, C. H. W. Barnes, J. A. Aguiar and Y. Majima, *Thin Solid Films*, 2012, **520**, 6368–6374.
2 D. Tahir and S. Tougaard, *Journal of Physics: Condensed Matter*, 2012, **24**, 175002.
3 Y. S. Gong, C. Lee and C. K. Yang, *Journal of Applied Physics*, 1995, **77**, 5422–5425.
4 S. Poulston, P. M. Parlett, P. Stone and M. Bowker, *Surface and Interface Analysis: An International Journal devoted to the development and application of techniques for the analysis of surfaces, interfaces and thin films*, 1996, **24**, 811–820.
5 M. Heinemann, B. Eifert and C. Heiliger, *Physical Review B*, 2013, **87**, 115111.
6 W. K. C. Yung, B. Sun, Z. Meng, J. Huang, Y. Jin, H. S. Choy, Z. Cai, G. Li, C. L. Ho, J. Yang and W. Y. Wong, *Scientific Reports*, 2016, **6**, 39584.
7 S. Neppl, J. Mahl, A. S. Tremsin, B. Rude, R. Qiao, W. Yang, J. Guo and O. Gessner, *Faraday Discussions*, 2016, **194**, 659–682.
8 CuO - X-ray attenuation length, http://henke.lbl.gov/optical_constants/atten2.html, (accessed 28 November 2018).

6 Conclusion and Outlook

The presented work showcases time-resolved X-ray techniques as useful tools to study charge and energy transfer following photoexcitation with temporal and spatial, i.e. depth, resolution. The first part of the thesis is centered around the N3-ZnO interface as a model heterojunction solar energy harvesting system. The main study (section 5.2) establishes a ~300 ps time delay between photoexcitation and electron injection into the ZnO CB using TRXPS. The nature of this intermediate state is unambiguously assigned to an ICT configuration as the N3 dye oxidation signal (C1s/Ru3d) appears earlier, i.e. within the IRF of the experiment of ~70 ps. Lineshape broadening and shifting of the SC TRXPS response (Zn3d) gives access to the depth-resolved band bending within the SC electrode. Photo-injected electrons enhance the ground state downward band bending by 100 meV within a ~6 nm wide SCL. By applying the Poisson relation, this band bending potential translates into the distribution of photo-injected electrons along the surface normal. Spatial information on the hole remaining on the dye is gained via the excess shift of the C1s/Ru3d photolines after correcting for the band bending changes. Its distance to the ZnO surface as well as the electric field of the associated surface dipole are computed within a parallel-plate capacitor model. The ground-state band bending of the bare nanocrystalline ZnO electrode is discussed in a supporting XPS study (section 5.1). By varying the ZnO surface hydroxylation, i.e. the adsorbate coverage, the band bending changes and can be retrieved from spectral changes in the Zn3d XPS signal. The fully hydroxylated surface has a ~6 nm broad SCL with ~0.8 eV downward bent bands that are best described by a cubic polynomial function. This points towards a linear dependence of the charge distribution via the Poisson relation. The presented (TR)XPS studies demonstrate the method’s capability to investigate the interfacial energy landscape of nanostructures. In principle, any experimental parameter that influences the band bending can be utilized to investigate the ground-state interfacial potential. Transient interfacial charge densities and their redistributions are accessible through band bending variations at different pump-probe delays. A similar method has been used to study the solid/liquid interfaces via ambient pressure XPS.[59–61] By applying a varying bias across the electrode/electrolyte interface of a photoelectrochemical cell, the potential drop within the electrolyte can be accessed. The combination of time-resolved and ambient pressure XPS would be a logical next step to extend the study of interfacial potentials towards *in operando* photovoltaic DSSC and photocatalytic cells. In this setup the ground-state band bending, and electrolyte potential could be determined by varying a bias across the interface. A subsequent pump-probe experiment would investigate transient photoinduced effects with a known ground-state electronic potential at a constant bias voltage. A first step in this direction has been made within the research group by studying a gold NP sensitized nanocrystalline TiO_2 electrode with a water background pressure.[201] Prior results are published on the charge transfer from gold NPs to the TiO_2 electrode following resonant plasmon excitation under UHV conditions.[55]

The proliferation of X-ray sources into labs could accelerate the development of this field. So far experimental time is limited and relatively hard to access at large-scale facilities like synchrotrons and X-ray free electron lasers. Advances in optical parametric amplified laser sources[202,203] enable the generation of soft X-ray radiation covering the water window.[186,204–206] While the brightness of large-scale facilities will not be reached by laboratory sources, especially XPS benefits more from high repetition rates as space charge effects limit the maximum usable X-ray photon flux. The development of ultrafast laser sources with MHz repetition rates may lead to another advent of synchrotron slicing. First implementations of this technique relied on kHz Titanium:Sapphire systems carving out a small portion of the electron bunch to produce a spatially separate femtosecond X-ray pulse during otherwise normal synchrotron operation. MHz sources could be synchronized to the synchrotron ring timing such that they alternate between enough electron bunches to avoid stability issues while other beamlines would suffer only minimal loss of photon flux from the missing carved out electron slice. This would be a viable alternative for femtosecond X-ray experiments requiring high repetition rates but not the kind of peak photon intensities typical for X-ray free electron lasers. An advantage would be the lack of pulse-to-pulse jitter commonly observed especially in self-amplified spontaneous emission X-ray free electron lasers.

The development toward higher repetition rate experiments of laboratory and large-scale facility X-ray techniques make considerations around pump laser-induced sample heating more relevant. Associated lattice effects within time-resolved X-ray spectra may be harder to detect, as higher repetition rates can lead to constantly elevated sample temperatures and therefore saturation effects. The second part of this thesis investigates laser-induced effects in TRXAS on solid-state CuO (section 5.3). A method to model lattice contributions and thereby distinguish them from electronic effects is applied to laser-induced changes in the oxygen K-edge X-ray absorption. TRXAS signals following excitation with 532 nm, 10 ps FWHM laser pulses are modelled within a one-dimensional heat deposition and diffusion approach. Radial diffusion is negligible within the X-ray probed volume because of the significantly larger laser diameter in the interaction region. Both, the picosecond rise and nanosecond decay of the photoinduced effects, are fully captured by this framework within the precision of the experiment. An initial laser-induced temperature profile is propagated in time by iteratively using Fick's Law to describe heat dissipation. For each pump-probe delay, TRXAS data is compared to a modelled spectrum based on temperature-resolved XAS data. The resulting depth- and time-dependent lattice temperature profile is sensitive to increments on the scale of tens of nanometers and tens of picoseconds. The analysis results in a thermal conductivity of (1.3 ± 0.4) $Wm^{-1}K^{-1}$, which is in good agreement with the literature value for CuO powder (1.013 $Wm^{-1}K^{-1}$), and a surface temperature of 120 °C. A general limitation of the TRXAS approach is that the X-ray penetration depth is not as easily tunable as, e.g., the surface sensitivity of TRXPS via the photoelectron energy. The angle of incidence of the X-ray beam on flat (crystalline) surfaces allows for some tuneability while this does not apply to nanostructured samples. This causes issues with TRXAS data following 355 nm excitation, where a comparatively short laser penetration depth leads to pronounced temperature gradients. Estimates for the surface temperature are beyond the range of temperature-resolved XAS data. Extrapolation of the temperature-resolved data cannot fully describe the observed TRXAS effects. Besides enabling the isolation of electronic signals in future experiments, the lattice temperature can also be a driving factor for photocatalytic phenomena. TRXAS is generally well-suited to investigate intermediate species in catalytic reactions as demonstrated in a study of CO dissociation on the Ru(111) surface.[200]

References

(1) *Basic Research Needs for Solar Energy Utilization*; U.S. Department of Energy, 2005; p. 276.

(2) IEA Key World Energy Statistics 2021 – Supply, https://www.iea.org/reports/key-world-energy-statistics-2021/supply (accessed Oct 16, 2021).

(3) Schmela, M. *SolarPower Europe (2021): Global Market Outlook for Solar Power 2021-2025*; 2020.

(4) Cost and Performance Characteristics of New Generating Technologies, Annual Energy Outlook 2021, U.S. Energy Information Administration, https://www.eia.gov/outlooks/aeo/assumptions/ pdf/table_8.2.pdf (accessed Jan 17, 2022).

(5) Studie: Stromgestehungskosten erneuerbare Energien (June 2021), Fraunhofer ISE, https://www.ise.fraunhofer.de/de/veroeffentlichungen/studien/studie-stromgestehungskosten-erneuerbare-energien.html (accessed Feb 12, 2022).

(6) IEA Key World Energy Statistics 2021 – Final consumption, https://www.iea.org/reports/key-world-energy-statistics-2021/final-consumption (accessed Dec 8, 2021).

(7) Wei, J.; Ge, Q.; Yao, R.; Wen, Z.; Fang, C.; Guo, L.; Xu, H.; Sun, J. Directly Converting CO_2 into a Gasoline Fuel. *Nat. Commun.* **2017**, *8*, 15174.

(8) Choi, Y. H.; Jang, Y. J.; Park, H.; Kim, W. Y.; Lee, Y. H.; Choi, S. H.; Lee, J. S. Carbon Dioxide Fischer-Tropsch Synthesis: A New Path to Carbon-Neutral Fuels. *Appl. Catal. B Environ.* **2017**, *202*, 605–610.

(9) Saeidi, S.; Najari, S.; Fazlollahi, F.; Nikoo, M. K.; Sefidkon, F.; Klemeš, J. J.; Baxter, L. L. Mechanisms and Kinetics of CO_2 Hydrogenation to Value-Added Products: A Detailed Review on Current Status and Future Trends. *Renew. Sustain. Energy Rev.* **2017**, *80*, 1292–1311.

(10) McQueen, N.; Gomes, K. V.; McCormick, C.; Blumanthal, K.; Pisciotta, M.; Wilcox, J. A Review of Direct Air Capture (DAC): Scaling up Commercial Technologies and Innovating for the Future. *Prog. Energy* **2021**, *3*, 032001.

(11) Low, J.; Yu, J.; Jaroniec, M.; Wageh, S.; Al-Ghamdi, A. A. Heterojunction Photocatalysts. *Adv. Mater.* **2017**, *29*, 1601694.

(12) Wang, H.; Zhang, L.; Chen, Z.; Hu, J.; Li, S.; Wang, Z.; Liu, J.; Wang, X. Semiconductor Heterojunction Photocatalysts: Design, Construction, and Photocatalytic Performances. *Chem. Soc. Rev.* **2014**, *43*, 5234–5244.

(13) Shockley, W.; Queisser, H. J. Detailed Balance Limit of Efficiency of p-n Junction Solar Cells. *J. Appl. Phys.* **1961**, *32*, 510–519.

(14) Rühle, S. Tabulated Values of the Shockley–Queisser Limit for Single Junction Solar Cells. *Sol. Energy* **2016**, *130*, 139–147.

(15) NREL Best Research-Cell Efficiency Chart, https://www.nrel.gov/pv/cell-efficiency.html (accessed Jan 13, 2022).

(16) Ran, H.; Fan, J.; Zhang, X.; Mao, J.; Shao, G. Enhanced Performances of Dye-Sensitized Solar Cells Based on Au-TiO_2 and Ag-TiO_2 Plasmonic Hybrid Nanocomposites. *Appl. Surf. Sci.* **2018**, *430*, 415–423.

(17) Clavero, C. Plasmon-Induced Hot-Electron Generation at Nanoparticle/Metal-Oxide Interfaces for Photovoltaic and Photocatalytic Devices. *Nat. Photonics* **2014**, *8*, 95–103.

(18) Selopal, G. S.; Wu, H.-P.; Lu, J.; Chang, Y.-C.; Wang, M.; Vomiero, A.; Concina, I.; Diau, E. W.-G. Metal-Free Organic Dyes for TiO_2 and ZnO Dye-Sensitized Solar Cells. *Sci. Rep.* **2016**, *6*, 18756.

(19) Robel, I.; Subramanian, V.; Kuno, M.; Kamat, P. V. Quantum Dot Solar Cells. Harvesting Light Energy with CdSe Nanocrystals Molecularly Linked to Mesoscopic TiO_2 Films. *J. Am. Chem. Soc.* **2006**, *128*, 2385–2393.

(20) Grätzel, M. Solar Energy Conversion by Dye-Sensitized Photovoltaic Cells. *Inorg. Chem.* **2005**, *44*, 6841–6851.

(21) Henderson, M. A. A Surface Science Perspective on TiO_2 Photocatalysis. *Surf. Sci. Rep.* **2011**, *66*, 185–297.

(22) Linsebigler, A. L.; Lu, G.; Yates, J. T. Photocatalysis on TiO_2 Surfaces: Principles, Mechanisms, and Selected Results. *Chem. Rev.* **1995**, *95*, 735–758.

(23) Zewail, A. H. Femtochemistry: Atomic-Scale Dynamics of the Chemical Bond. *J. Phys. Chem. A* **2000**, *104*, 5660–5694.

(24) Siegbahn, K. Electron Spectroscopy for Atoms, Molecules, and Condensed Matter. *Rev. Mod. Phys.* **1982**, *54*, 709–728.

(25) Siegbahn, H. Electron Spectroscopy for Chemical Analysis of Liquids and Solutions. *J. Phys. Chem.* **1985**, *89*, 897–909.

(26) Milne, C. J.; Penfold, T. J.; Chergui, M. Recent Experimental and Theoretical Developments in Time-Resolved X-Ray Spectroscopies. *Coord. Chem. Rev.* **2014**, *277–278*, 44–68.

(27) Cahen, D.; Kahn, A. Electron Energetics at Surfaces and Interfaces: Concepts and Experiments. *Adv. Mater.* **2003**, *15*, 271–277.

(28) Kahn, A. Fermi Level, Work Function and Vacuum Level. *Mater. Horiz.* **2016**, *3*, 7–10.

(29) Neppl, S.; Gessner, O. Time-Resolved X-Ray Photoelectron Spectroscopy Techniques for the Study of Interfacial Charge Dynamics. *J. Electron Spectrosc. Relat. Phenom.* **2015**, *200*, 64–77.

(30) Long, J. P.; Sadeghi, H. R.; Rife, J. C.; Kabler, M. N. Surface Space-Charge Dynamics and Surface Recombination on Silicon (111) Surfaces Measured with Combined Laser and Synchrotron Radiation. *Phys. Rev. Lett.* **1990**, *64*, 1158–1161.

(31) Gießel, T.; Bröcker, D.; Schmidt, P.; Widdra, W. Time-Resolving and Energy-Dispersive Photoelectron Detector for Combined Laser and Synchrotron Radiation Experiments. *Rev. Sci. Instrum.* **2003**, *74*, 4620–4624.

(32) Glover, T. E.; Ackermann, G. D.; Belkacem, A.; Feinberg, B.; Heimann, P. A.; Hussain, Z.; Padmore, H. A.; Ray, C.; Schoenlein, R. W.; Steele, W. F. Measurement of Synchrotron Pulse Durations Using Surface Photovoltage Transients. *Nucl. Instrum. Methods Phys. Res. Sect. Accel. Spectrometers Detect. Assoc. Equip.* **2001**, *467–468*, 1438–1440.

(33) Bröcker, D.; Gießel, T.; Widdra, W. Charge Carrier Dynamics at the SiO_2/Si(100) Surface: A Time-Resolved Photoemission Study with Combined Laser and Synchrotron Radiation. *Chem. Phys.* **2004**, *299*, 247–251.

(34) Pietzsch, A.; Föhlisch, A.; Hennies, F.; Vijayalakshmi, S.; Wurth, W. Interface Photovoltage Dynamics at the Buried BaF_2/Si Interface: Time Resolved Laser-Pump/Synchrotron-Probe Photoemission. *Appl. Phys. A* **2007**, *88*, 587–592.

(35) Ogawa, M.; Yamamoto, S.; Yukawa, R.; Hobara, R.; Lin, C.-H.; Liu, R.-Y.; Tang, S.-J.; Matsuda, I. Oscillatory Relaxation of Surface Photovoltage on a Silicon Surface. *Phys. Rev. B* **2013**, *87*, 235308.

(36) Spencer, B. F.; Graham, D. M.; Hardman, S. J. O.; Seddon, E. A.; Cliffe, M. J.; Syres, K. L.; Thomas, A. G.; Stubbs, S. K.; Sirotti, F.; Silly, M. G.; Kirkham, P. F.; Kumarasinghe, A. R.; Hirst, G. J.; Moss, A. J.; Hill, S. F.; Shaw, D. A.; Chattopadhyay, S.; Flavell, W. R. Time-Resolved Surface Photovoltage Measurements at n-Type Photovoltaic Surfaces: Si(111) and ZnO(10-10). *Phys. Rev. B* **2013**, *88*, 195301.

(37) Tanaka, S.; More, S. D.; Murakami, J.; Itoh, M.; Fujii, Y.; Kamada, M. Surface Photovoltage Effects on p-GaAs (100) from Core-Level Photoelectron Spectroscopy Using Synchrotron Radiation and a Laser. *Phys. Rev. B* **2001**, *64*, 155308.

(38) Yukawa, R.; Yamamoto, S.; Ozawa, K.; Emori, M.; Ogawa, M.; Yamamoto, Sh.; Fujikawa, K.; Hobara, R.; Kitagawa, S.; Daimon, H.; Sakama, H.; Matsuda, I. Electron-Hole

Recombination on ZnO(0001) Single-Crystal Surface Studied by Time-Resolved Soft X-Ray Photoelectron Spectroscopy. *Appl. Phys. Lett.* **2014**, *105*, 151602.

(39) Ogawa, M.; Yamamoto, S.; Fujikawa, K.; Hobara, R.; Yukawa, R.; Yamamoto, Sh.; Kitagawa, S.; Pierucci, D.; Silly, M. G.; Lin, C.-H.; Liu, R.-Y.; Daimon, H.; Sirotti, F.; Tang, S.-J.; Matsuda, I. Relaxations of the Surface Photovoltage Effect on the Atomically Controlled Semiconductor Surfaces Studied by Time-Resolved Photoemission Spectroscopy. *Phys. Rev. B* **2013**, *88*, 165313.

(40) Widdra, W.; Bröcker, D.; Gießel, T.; Hertel, I. V.; Krüger, W.; Liero, A.; Noack, F.; Petrov, V.; Pop, D.; Schmidt, P. M.; Weber, R.; Will, I.; Winter, B. Time-Resolved Core Level Photoemission: Surface Photovoltage Dynamics of the SiO_2/Si(100) Interface. *Surf. Sci.* **2003**, *543*, 87–94.

(41) Furube, A.; Katoh, R.; Hara, K.; Murata, S.; Arakawa, H.; Tachiya, M. Ultrafast Stepwise Electron Injection from Photoexcited Ru-Complex into Nanocrystalline ZnO Film via Intermediates at the Surface. *J. Phys. Chem. B* **2003**, *107*, 4162–4166.

(42) Němec, H.; Rochford, J.; Taratula, O.; Galoppini, E.; Kužel, P.; Polívka, T.; Yartsev, A.; Sundström, V. Influence of the Electron-Cation Interaction on Electron Mobility in Dye-Sensitized ZnO and TiO_2 Nanocrystals: A Study Using Ultrafast Terahertz Spectroscopy. *Phys. Rev. Lett.* **2010**, *104*, 197401.

(43) Stockwell, D.; Yang, Y.; Huang, J.; Anfuso, C.; Huang, Z.; Lian, T. Comparison of Electron-Transfer Dynamics from Coumarin 343 to TiO_2, SnO_2, and ZnO Nanocrystalline Thin Films: Role of Interface-Bound Charge-Separated Pairs. *J. Phys. Chem. C* **2010**, *114*, 6560–6566.

(44) Strothkämper, C.; Bartelt, A.; Sippel, P.; Hannappel, T.; Schütz, R.; Eichberger, R. Delayed Electron Transfer through Interface States in Hybrid ZnO/Organic-Dye Nanostructures. *J. Phys. Chem. C* **2013**, *117*, 17901–17908.

(45) Siefermann, K. R.; Pemmaraju, C. D.; Neppl, S.; Shavorskiy, A.; Cordones, A. A.; Vura-Weis, J.; Slaughter, D. S.; Sturm, F. P.; Weise, F.; Bluhm, H.; Strader, M. L.; Cho, H.; Lin, M.-F.; Bacellar, C.; Khurmi, C.; Guo, J.; Coslovich, G.; Robinson, J. S.; Kaindl, R. A.; Schoenlein, R. W.; Belkacem, A.; Neumark, D. M.; Leone, S. R.; Nordlund, D.; Ogasawara, H.; Krupin, O.; Turner, J. J.; Schlotter, W. F.; Holmes, M. R.; Messerschmidt, M.; Minitti, M. P.; Gul, S.; Zhang, J. Z.; Huse, N.; Prendergast, D.; Gessner, O. Atomic-Scale Perspective of Ultrafast Charge Transfer at a Dye–Semiconductor Interface. *J. Phys. Chem. Lett.* **2014**, *5*, 2753–2759.

(46) Katoh, R.; Furube, A.; Yoshihara, T.; Hara, K.; Fujihashi, G.; Takano, S.; Murata, S.; Arakawa, H.; Tachiya, M. Efficiencies of Electron Injection from Excited N3 Dye into Nanocrystalline Semiconductor (ZrO_2, TiO_2, ZnO, Nb_2O_5, SnO_2, In_2O_3) Films. *J. Phys. Chem. B* **2004**, *108*, 4818–4822.

(47) Tiwana, P.; Docampo, P.; Johnston, M. B.; Snaith, H. J.; Herz, L. M. Electron Mobility and Injection Dynamics in Mesoporous ZnO, SnO_2, and TiO_2 Films Used in Dye-Sensitized Solar Cells. *ACS Nano* **2011**, *5*, 5158–5166.

(48) Borgwardt, M.; Wilke, M.; Kampen, T.; Mähl, S.; Xiao, M.; Spiccia, L.; Lange, K. M.; Kiyan, I. Yu.; Aziz, E. F. Charge Transfer Dynamics at Dye-Sensitized ZnO and TiO_2 Interfaces Studied by Ultrafast XUV Photoelectron Spectroscopy. *Sci. Rep.* **2016**, *6*, 24422.

(49) Anderson, N. A.; Lian, T. Ultrafast Electron Transfer at the Molecule-Semiconductor Nanoparticle Interface. *Annu. Rev. Phys. Chem.* **2005**, *56*, 491–519.

(50) Benkö, G.; Kallioinen, J.; Myllyperkiö, P.; Trif, F.; Korppi-Tommola, J. E. I.; Yartsev, A. P.; Sundström, V. Interligand Electron Transfer Determines Triplet Excited State Electron Injection in RuN3−Sensitized TiO_2 Films. *J. Phys. Chem. B* **2004**, *108*, 2862–2867.

(51) Kallioinen, J.; Benkö, G.; Sundström, V.; Korppi-Tommola, J. E. I.; Yartsev, A. P. Electron Transfer from the Singlet and Triplet Excited States of $Ru(Dcbpy)_2(NCS)_2$ into Nanocrystalline TiO_2 Thin Films. *J. Phys. Chem. B* **2002**, *106*, 4396–4404.

(52) Benkö, G.; Kallioinen, J.; Korppi-Tommola, J. E. I.; Yartsev, A. P.; Sundström, V. Photoinduced Ultrafast Dye-to-Semiconductor Electron Injection from Nonthermalized and Thermalized Donor States. *J. Am. Chem. Soc.* **2002**, *124*, 489–493.

(53) Roth, F.; Borgwardt, M.; Wenthaus, L.; Mahl, J.; Palutke, S.; Brenner, G.; Mercurio, G.; Molodtsov, S.; Wurth, W.; Gessner, O.; Eberhardt, W. Direct Observation of Charge Separation in an Organic Light Harvesting System by Femtosecond Time-Resolved XPS. *Nat. Commun.* **2021**, *12*, 1196.

(54) Roth, F.; Neppl, S.; Shavorskiy, A.; Arion, T.; Mahl, J.; Seo, H. O.; Bluhm, H.; Hussain, Z.; Gessner, O.; Eberhardt, W. Efficient Charge Generation from Triplet Excitons in Metal-Organic Heterojunctions. *Phys. Rev. B* **2019**, *99*, 020303.

(55) Borgwardt, M.; Mahl, J.; Roth, F.; Wenthaus, L.; Brauße, F.; Blum, M.; Schwarzburg, K.; Liu, G.; Toma, F. M.; Gessner, O. Photoinduced Charge Carrier Dynamics and Electron Injection Efficiencies in Au Nanoparticle-Sensitized TiO_2 Determined with Picosecond Time-Resolved X-Ray Photoelectron Spectroscopy. *J. Phys. Chem. Lett.* **2020**, *11*, 5476–5481.

(56) Ozawa, K.; Mase, K. Metallization of ZnO(10-10) by Adsorption of Hydrogen, Methanol, and Water: Angle-Resolved Photoelectron Spectroscopy. *Phys. Rev. B* **2010**, *81*, 205322.

(57) Ozawa, K.; Mase, K. Comparison of the Surface Electronic Structures of H-Adsorbed ZnO Surfaces: An Angle-Resolved Photoelectron Spectroscopy Study. *Phys. Rev. B* **2011**, *83*, 125406.

(58) Mahl, J.; Gessner, O.; Barth, J. V.; Feulner, P.; Neppl, S. Strong Potential Gradients and Electron Confinement in ZnO Nanoparticle Films: Implications for Charge-Carrier Transport and Photocatalysis. *ACS Appl. Nano Mater.* **2021**, *4*, 12213–12221.

(59) Favaro, M.; Jeong, B.; Ross, P. N.; Yano, J.; Hussain, Z.; Liu, Z.; Crumlin, E. J. Unravelling the Electrochemical Double Layer by Direct Probing of the Solid/Liquid Interface. *Nat. Commun.* **2016**, *7*, 1–8.

(60) Shavorskiy, A.; Ye, X.; Karslıoğlu, O.; Poletayev, A. D.; Hartl, M.; Zegkinoglou, I.; Trotochaud, L.; Nemšák, S.; Schneider, C. M.; Crumlin, E. J.; Axnanda, S.; Liu, Z.; Ross, P. N.; Chueh, W.; Bluhm, H. Direct Mapping of Band Positions in Doped and Undoped Hematite during Photoelectrochemical Water Splitting. *J. Phys. Chem. Lett.* **2017**, *8*, 5579–5586.

(61) F. Lichterman, M.; Hu, S.; H. Richter, M.; J. Crumlin, E.; Axnanda, S.; Favaro, M.; Drisdell, W.; Hussain, Z.; Mayer, T.; S. Brunschwig, B.; S. Lewis, N.; Liu, Z.; Lewerenz, H.-J. Direct Observation of the Energetics at a Semiconductor/Liquid Junction by Operando X-Ray Photoelectron Spectroscopy. *Energy Environ. Sci.* **2015**, *8*, 2409–2416.

(62) Hayes, D.; Hadt, R. G.; Emery, J. D.; Cordones, A. A.; Martinson, A. B. F.; Shelby, M. L.; Fransted, K. A.; Dahlberg, P. D.; Hong, J.; Zhang, X.; Kong, Q.; Schoenlein, R. W.; Chen, L. X. Electronic and Nuclear Contributions to Time-Resolved Optical and X-Ray Absorption Spectra of Hematite and Insights into Photoelectrochemical Performance. *Energy Environ. Sci.* **2016**, *9*, 3754–3769.

(63) Lin, M.-F.; Verkamp, M. A.; Leveillee, J.; Ryland, E. S.; Benke, K.; Zhang, K.; Weninger, C.; Shen, X.; Li, R.; Fritz, D.; Bergmann, U.; Wang, X.; Schleife, A.; Vura-Weis, J. Carrier-Specific Femtosecond XUV Transient Absorption of PbI_2 Reveals Ultrafast Nonradiative Recombination. *J. Phys. Chem. C* **2017**, *121*, 27886–27893.

(64) Schultze, M.; Ramasesha, K.; Pemmaraju, C. D.; Sato, S. A.; Whitmore, D.; Gandman, A.; Prell, J. S.; Borja, L. J.; Prendergast, D.; Yabana, K.; Neumark, D. M.; Leone, S. R. Attosecond Band-Gap Dynamics in Silicon. *Science* **2014**, *346*, 1348–1352.

(65) Samsonov, G. V. *The Oxide Handbook*; IFI/Plenum: New York, 1973.

(66) Anpo, M.; Chiba, K.; Tomonari, M.; Coluccia, S.; Che, M.; Fox, M. A. Photocatalysis on Native and Platinum-Loaded TiO_2 and ZnO Catalysts —Origin of Different Reactivities on Wet and Dry Metal Oxides—. *Bull. Chem. Soc. Jpn.* **1991**, *64*, 543–551.

(67) Zhang, Z.; Yates, J. T. Effect of Adsorbed Donor and Acceptor Molecules on Electron Stimulated Desorption: O_2/TiO_2(110). *J. Phys. Chem. Lett.* **2010**, *1*, 2185–2188.

(68) Zhang, Z.; Tang, W.; Neurock, M.; Yates, J. T. Electric Charge of Single Au Atoms Adsorbed on TiO_2(110) and Associated Band Bending. *J. Phys. Chem. C* **2011**, *115*, 23848–23853.

(69) Zhang, Z.; Yates, J. T. Band Bending in Semiconductors: Chemical and Physical Consequences at Surfaces and Interfaces. *Chem. Rev.* **2012**, *112*, 5520–5551.

(70) Mott, N. F. Note on the Contact between a Metal and an Insulator or Semi-Conductor. *Math. Proc. Camb. Philos. Soc.* **1938**, *34*, 568–572.

(71) Schottky, W. Halbleitertheorie Der Sperrschicht. *Naturwissenschaften* **1938**, *26*, 843–843.

(72) Mott, N. F. The Theory of Crystal Rectifiers. *Proc. R. Soc. Lond. A* **1939**, *171*, 27–38.

(73) Schottky, W. Zur Halbleitertheorie der Sperrschicht- und Spitzengleichrichter. *Z. Phys.* **1939**, *113*, 367–414.

(74) Davydov, B. The Rectifying Action of Semiconductors. *Tech. Phys. USSR* **1938**, 87.

(75) Tung, R. T. (董梓則). The Physics and Chemistry of the Schottky Barrier Height. *Appl. Phys. Rev.* **2014**, *1*, 011304.

(76) Tung, R. T.; Kronik, L. Quantitative Explanation of the Schottky Barrier Height. *Phys. Rev. B* **2021**, *103*, 035304.

(77) Choe, D.-H.; West, D.; Zhang, S. Band Alignment and the Built-in Potential of Solids. *Phys. Rev. Lett.* **2018**, *121*, 196802.

(78) Bardeen, J. Nobel Lecture, https://www.nobelprize.org/uploads/2018/06/bardeen-lecture.pdf (accessed May 6, 2020).

(79) Ibach, H. *Physics of Surfaces and Interfaces*; 1st ed.; Chapter 3; Springer: Berlin, Germany, 2006.

(80) Oura, K.; Lifshits, V. G.; Saranin, A. A.; Zotov, A. V.; Katayama, M. *Surface Science: An Introduction*; 1st ed.; Chapter 11; Springer: Berlin, Germany, 2003.

(81) Liqiang, J.; Xiaojun, S.; Jing, S.; Weimin, C.; Zili, X.; Yaoguo, D.; Honggang, F. Review of Surface Photovoltage Spectra of Nano-Sized Semiconductor and Its Applications in Heterogeneous Photocatalysis. *Sol. Energy Mater. Sol. Cells* **2003**, *79*, 133–151.

(82) Goossens, A. Potential Distribution in Semiconductor Particles. *J. Electrochem. Soc.* **1996**, *143*, L131.

(83) Makowski, M. J.; Galhenage, R. P.; Langford, J.; Hemminger, J. C. Liquid-Jet X-Ray Photoelectron Spectra of TiO_2 Nanoparticles in an Aqueous Electrolyte Solution. *J. Phys. Chem. Lett.* **2016**, *7*, 1732–1735.

(84) Lueth, H. *Solid Surfaces, Interfaces and Thin Films*; 5th ed.; Chapter 10; Springer: Berlin Heidelberg, Germany, 2010.

(85) Wang, Y.; Meyer, B.; Yin, X.; Kunat, M.; Langenberg, D.; Traeger, F.; Birkner, A.; Wöll, Ch. Hydrogen Induced Metallicity on the ZnO(10-10) Surface. *Phys. Rev. Lett.* **2005**, *95*, 266104.

(86) Yin, X.-L.; Birkner, A.; Hänel, K.; Löber, T.; Köhler, U.; Wöll, C. Adsorption of Atomic Hydrogen on ZnO(10-10): STM Study. *Phys. Chem. Chem. Phys.* **2006**, *8*, 1477–1481.

(87) Neppl, S.; Mahl, J.; Roth, F.; Mercurio, G.; Zeng, G.; Toma, F. M.; Huse, N.; Feulner, P.; Gessner, O. Nanoscale Confinement of Photo-Injected Electrons at Hybrid Interfaces. *J. Phys. Chem. Lett.* **2021**, 12, 11951-11959.

(88) O'Regan, B.; Grätzel, M. A Low-Cost, High-Efficiency Solar Cell Based on Dye-Sensitized Colloidal TiO_2 Films. *Nature* **1991**, *353*, 737–740.

(89) Gong, J.; Liang, J.; Sumathy, K. Review on Dye-Sensitized Solar Cells (DSSCs): Fundamental Concepts and Novel Materials. *Renew. Sustain. Energy Rev.* **2012**, *16*, 5848–5860.

(90) Nazeeruddin, Md. K.; Baranoff, E.; Grätzel, M. Dye-Sensitized Solar Cells: A Brief Overview. *Sol. Energy* **2011**, *85*, 1172–1178.

(91) Greijer Agrell, H.; Lindgren, J.; Hagfeldt, A. Coordinative Interactions in a Dye-Sensitized Solar Cell. *J. Photochem. Photobiol. Chem.* **2004**, *164*, 23–27.

(92) Tachibana, Y.; Moser, J. E.; Grätzel, M.; Klug, D. R.; Durrant, J. R. Subpicosecond Interfacial Charge Separation in Dye-Sensitized Nanocrystalline Titanium Dioxide Films. *J. Phys. Chem.* **1996**, *100*, 20056–20062.

(93) Germanova, K.; Hardalov, C.; Strashilov, V.; Georgiev, B. An Improved Apparatus for Surface Photovoltage Studies with a Bimorphous Piezoelectric Kelvin Probe. *J. Phys. E: Sci. Instrum.* **1987**, *20*, 273–276.

(94) Lägel, B.; Baikie, I. D.; Petermann, U. A Novel Detection System for Defects and Chemical Contamination in Semiconductors Based upon the Scanning Kelvin Probe. *Surf. Sci.* **1999**, *433–435*, 622–626.

(95) Streicher, F.; Sadewasser, S.; Lux-Steiner, M. Ch. Surface Photovoltage Spectroscopy in a Kelvin Probe Force Microscope under Ultrahigh Vacuum. *Rev. Sci. Instrum.* **2009**, *80*, 013907.

(96) Shearer, M. J.; Li, M.-Y.; Li, L.-J.; Jin, S.; Hamers, R. J. Nanoscale Surface Photovoltage Mapping of 2D Materials and Heterostructures by Illuminated Kelvin Probe Force Microscopy. *J. Phys. Chem. C* **2018**, *122*, 13564–13571.

(97) Meyer, G. J.; Lisensky, G. C.; Ellis, A. B. Evidence for Adduct Formation at the Semiconductor-Gas Interface. Photoluminescent Properties of Cadmium Selenide in the Presence of Amines. *J. Am. Chem. Soc.* **1988**, *110*, 4914–4918.

(98) Gatos, H. C.; Lagowski, J. Surface Photovoltage Spectroscopy—A New Approach to the Study of High-Gap Semiconductor Surfaces. *J. Vac. Sci. Technol.* **1973**, *10*, 130–135.

(99) Spencer, B. F.; Cliffe, M. J.; Graham, D. M.; Hardman, S. J. O.; Seddon, E. A.; Syres, K. L.; Thomas, A. G.; Sirotti, F.; Silly, M. G.; Akhtar, J.; O'Brien, P.; Fairclough, S. M.; Smith, J. M.; Chattopadhyay, S.; Flavell, W. R. Chemically-Specific Time-Resolved Surface Photovoltage Spectroscopy: Carrier Dynamics at the Interface of Quantum Dots Attached to a Metal Oxide. *Surf. Sci.* **2015**, *641*, 320–325.

(100) Kamrla, R.; Trützschler, A.; Huth, M.; Chiang, C.-T.; Schumann, F. O.; Widdra, W. SiO_2/Si(001) Studied by Time-Resolved Valence Band Photoemission at MHz Repetition Rates: Linear and Nonlinear Excitation of Surface Photovoltage. *J. Vac. Sci. Technol. A* **2019**, *37*, 021101.

(101) Neppl, S.; Shavorskiy, A.; Zegkinoglou, I.; Fraund, M.; Slaughter, D. S.; Troy, T.; Ziemkiewicz, M. P.; Ahmed, M.; Gul, S.; Rude, B.; Zhang, J. Z.; Tremsin, A. S.; Glans, P.-A.; Liu, Y.-S.; Wu, C. H.; Guo, J.; Salmeron, M.; Bluhm, H.; Gessner, O. Capturing Interfacial Photoelectrochemical Dynamics with Picosecond Time-Resolved X-Ray Photoelectron Spectroscopy. *Faraday Discuss.* **2014**, *171*, 219–241.

(102) Sell, K.; Barke, I.; Polei, S.; Schumann, C.; Oeynhausen, V. von; Meiwes-Broer, K.-H. Surface Photovoltage of Ag Nanoparticles and Au Chains on Si(111). *Phys. Status Solidi B* **2010**, *247*, 1087–1094.

(103) Shavorskiy, A.; Neppl, S.; Slaughter, D. S.; Cryan, J. P.; Siefermann, K. R.; Weise, F.; Lin, M.-F.; Bacellar, C.; Ziemkiewicz, M. P.; Zegkinoglou, I.; Fraund, M. W.; Khurmi, C.; Hertlein, M. P.; Wright, T. W.; Huse, N.; Schoenlein, R. W.; Tyliszczak, T.; Coslovich, G.; Robinson, J.; Kaindl, R. A.; Rude, B. S.; Ölsner, A.; Mähl, S.; Bluhm, H.; Gessner, O. Sub-Nanosecond Time-Resolved Ambient-Pressure X-Ray Photoelectron Spectroscopy Setup for Pulsed and Constant Wave X-Ray Light Sources. *Rev. Sci. Instrum.* **2014**, *85*, 093102.

(104) Neppl, S.; Mahl, J.; Tremsin, A. S.; Rude, B.; Qiao, R.; Yang, W.; Guo, J.; Gessner, O. Towards Efficient Time-Resolved X-Ray Absorption Studies of Electron Dynamics at Photocatalytic Interfaces. *Faraday Discuss.* **2016**, *194*, 659–682.

(105) Reprinted from Journal of Electron Spectroscopy and Related Phenomena, 200, Stefan Neppl and Oliver Gessner, Time-Resolved X-Ray Photoelectron Spectroscopy Techniques for the Study of Interfacial Charge Dynamics, 64-77, Copyright (2015), with Permission from Elsevier.

(106) March, A. M.; Stickrath, A.; Doumy, G.; Kanter, E. P.; Krässig, B.; Southworth, S. H.; Attenkofer, K.; Kurtz, C. A.; Chen, L. X.; Young, L. Development of High-Repetition-Rate

Laser Pump/X-Ray Probe Methodologies for Synchrotron Facilities. *Rev. Sci. Instrum.* **2011**, *82*, 073110.

(107) Lima, F. A.; Milne, C. J.; Amarasinghe, D. C. V.; Rittmann-Frank, M. H.; Veen, R. M. van der; Reinhard, M.; Pham, V.-T.; Karlsson, S.; Johnson, S. L.; Grolimund, D.; Borca, C.; Huthwelker, T.; Janousch, M.; van Mourik, F.; Abela, R.; Chergui, M. A High-Repetition Rate Scheme for Synchrotron-Based Picosecond Laser Pump/X-Ray Probe Experiments on Chemical and Biological Systems in Solution. *Rev. Sci. Instrum.* **2011**, *82*, 063111.

(108) Oelsner, A.; Rohmer, M.; Schneider, C.; Bayer, D.; Schönhense, G.; Aeschlimann, M. Time- and Energy Resolved Photoemission Electron Microscopy-Imaging of Photoelectron Time-of-Flight Analysis by Means of Pulsed Excitations. *J. Electron Spectrosc. Relat. Phenom.* **2010**, *178–179*, 317–330.

(109) Tremsin, A. S.; Siegmund, O. H. W.; Hull, J. S.; Vallerga, J. V.; McPhate, J. B.; Soderstrom, J.; Chiou, J. W.; Guo, J. H.; Hussain, Z. High Resolution Photon Counting Detection System for Advanced Inelastic X-Ray Scattering Studies. *IEEE Nucl. Sci. Symp. Conf. Rec.* **2006**, *2*, 735–739.

(110) Thompson, A.; Lindau, I.; Attwood, D.; Liu, Y.; Gullikson, E.; Pianetta, P.; Howells, M.; Robinson, A.; Kim, K.-J.; Scofield, J.; Kirz, J.; Underwood, J.; Kortright, J.; Williams, G.; Winick, H. *X-Ray Data Booklet*; 3rd ed.; https://xdb.lbl.gov/xdb-new.pdf; Berkeley, CA, USA, 2009.

(111) Taucher, T. C.; Hehn, I.; Hofmann, O. T.; Zharnikov, M.; Zojer, E. Understanding Chemical versus Electrostatic Shifts in X-Ray Photoelectron Spectra of Organic Self-Assembled Monolayers. *J. Phys. Chem. C* **2016**, *120*, 3428–3437.

(112) Gleason-Rohrer, D. C.; Brunschwig, B. S.; Lewis, N. S. Measurement of the Band Bending and Surface Dipole at Chemically Functionalized Si(111)/Vacuum Interfaces. *J. Phys. Chem. C* **2013**, *117*, 18031–18042.

(113) Thränhardt, A.; Kuckenburg, S.; Knorr, A.; Meier, T.; Koch, S. W. Quantum Theory of Phonon-Assisted Exciton Formation and Luminescence in Semiconductor Quantum Wells. *Phys. Rev. B* **2000**, *62*, 2706–2720.

(114) Rossi, F.; Kuhn, T. Theory of Ultrafast Phenomena in Photoexcited Semiconductors. *Rev. Mod. Phys.* **2002**, *74*, 895–950.

(115) Semenov, A. D.; Nebosis, R. S.; Gousev, Yu. P.; Heusinger, M. A.; Renk, K. F. Analysis of the Nonequilibrium Photoresponse of Superconducting Films to Pulsed Radiation by Use of a Two-Temperature Model. *Phys. Rev. B* **1995**, *52*, 581–590.

(116) Chen, J. K.; Tzou, D. Y.; Beraun, J. E. A Semiclassical Two-Temperature Model for Ultrafast Laser Heating. *Int. J. Heat Mass Transf.* **2006**, *49*, 307–316.

(117) Singh, N. Two-Temperature Model of Nonequilibrium Electron Relaxation: A Review. *Int. J. Mod. Phys. B* **2010**, *24*, 1141–1158.

(118) Carpene, E. Ultrafast Laser Irradiation of Metals: Beyond the Two-Temperature Model. *Phys. Rev. B* **2006**, *74*, 024301.

(119) Hodak, J.; Martini, I.; Hartland, G. V. Ultrafast Study of Electron–Phonon Coupling in Colloidal Gold Particles. *Chem. Phys. Lett.* **1998**, *284*, 135–141.

(120) Elsayed-Ali, H. E.; Norris, T. B.; Pessot, M. A.; Mourou, G. A. Time-Resolved Observation of Electron-Phonon Relaxation in Copper. *Phys. Rev. Lett.* **1987**, *58*, 1212–1215.

(121) Hodak, J. H.; Martini, I.; Hartland, G. V. Spectroscopy and Dynamics of Nanometer-Sized Noble Metal Particles. *J. Phys. Chem. B* **1998**, *102*, 6958–6967.

(122) Lui, C. H.; Mak, K. F.; Shan, J.; Heinz, T. F. Ultrafast Photoluminescence from Graphene. *Phys. Rev. Lett.* **2010**, *105*, 127404.

(123) Reich, S.; Dworzak, M.; Hoffmann, A.; Thomsen, C.; Strano, M. S. Excited-State Carrier Lifetime in Single-Walled Carbon Nanotubes. *Phys. Rev. B* **2005**, *71*, 033402.

(124) Jiang, J.; Saito, R.; Grüneis, A.; Chou, S. G.; Samsonidze, Ge. G.; Jorio, A.; Dresselhaus, G.; Dresselhaus, M. S. Photoexcited Electron Relaxation Processes in Single-Wall Carbon Nanotubes. *Phys. Rev. B* **2005**, *71*, 045417.

(125) Hartland, G. V. Electron-Phonon Coupling and Heat Dissipation in Metal Nanoparticles. *Int. J. Nanotechnol.* **2004**, *1*, 307–327.

(126) Jiang, Y.; Wang, H.-Y.; Xie, L.-P.; Gao, B.-R.; Wang, L.; Zhang, X.-L.; Chen, Q.-D.; Yang, H.; Song, H.-W.; Sun, H.-B. Study of Electron−Phonon Coupling Dynamics in Au Nanorods by Transient Depolarization Measurements. *J. Phys. Chem. C* **2010**, *114*, 2913–2917.

(127) Groeneveld, R. H. M.; Sprik, R.; Lagendijk, A. Ultrafast Relaxation of Electrons Probed by Surface Plasmons at a Thin Silver Film. *Phys. Rev. Lett.* **1990**, *64*, 784–787.

(128) Groeneveld, R. H. M.; Sprik, R.; Lagendijk, A. Femtosecond Spectroscopy of Electron-Electron and Electron-Phonon Energy Relaxation in Ag and Au. *Phys. Rev. B* **1995**, *51*, 11433–11445.

(129) Sun, C.-K.; Vallée, F.; Acioli, L. H.; Ippen, E. P.; Fujimoto, J. G. Femtosecond-Tunable Measurement of Electron Thermalization in Gold. *Phys. Rev. B* **1994**, *50*, 15337–15348.

(130) Waldecker, L.; Bertoni, R.; Hübener, H.; Brumme, T.; Vasileiadis, T.; Zahn, D.; Rubio, A.; Ernstorfer, R. Momentum-Resolved View of Electron-Phonon Coupling in Multilayer WSe_2. *Phys. Rev. Lett.* **2017**, *119*, 036803.

(131) Faure, J.; Mauchain, J.; Papalazarou, E.; Marsi, M.; Boschetto, D.; Timrov, I.; Vast, N.; Ohtsubo, Y.; Arnaud, B.; Perfetti, L. Direct Observation of Electron Thermalization and Electron-Phonon Coupling in Photoexcited Bismuth. *Phys. Rev. B* **2013**, *88*, 075120.

(132) M. Lange, K.; Kothe, A.; F. Aziz, E. Chemistry in Solution: Recent Techniques and Applications Using Soft X-Ray Spectroscopy. *Phys. Chem. Chem. Phys.* **2012**, *14*, 5331–5338.

(133) Eidam, T.; Hanf, S.; Seise, E.; Andersen, T. V.; Gabler, T.; Wirth, C.; Schreiber, T.; Limpert, J.; Tünnermann, A. Femtosecond Fiber CPA System Emitting 830 W Average Output Power. *Opt. Lett.* **2010**, *35*, 94–96.

(134) Saraceno, C. J.; Emaury, F.; Schriber, C.; Hoffmann, M.; Golling, M.; Südmeyer, T.; Keller, U. Ultrafast Thin-Disk Laser with 80 µJ Pulse Energy and 242 W of Average Power. *Opt. Lett.* **2014**, *39*, 9–12.

(135) Brons, J.; Pervak, V.; Fedulova, E.; Bauer, D.; Sutter, D.; Kalashnikov, V.; Apolonskiy, A.; Pronin, O.; Krausz, F. Energy Scaling of Kerr-Lens Mode-Locked Thin-Disk Oscillators. *Opt. Lett.* **2014**, *39*, 6442–6445.

(136) Hädrich, S.; Krebs, M.; Hoffmann, A.; Klenke, A.; Rothhardt, J.; Limpert, J.; Tünnermann, A. Exploring New Avenues in High Repetition Rate Table-Top Coherent Extreme Ultraviolet Sources. *Light Sci. Appl.* **2015**, *4*, e320–e320.

(137) Hädrich, S.; Rothhardt, J.; Krebs, M.; Demmler, S.; Klenke, A.; Tünnermann, A.; Limpert, J. Single-Pass High Harmonic Generation at High Repetition Rate and Photon Flux. *J. Phys. B At. Mol. Opt. Phys.* **2016**, *49*, 172002.

(138) Chiang, C.-T.; Huth, M.; Trützschler, A.; Kiel, M.; Schumann, F. O.; Kirschner, J.; Widdra, W. Boosting Laboratory Photoelectron Spectroscopy by Megahertz High-Order Harmonics. *New J. Phys.* **2015**, *17*, 013035.

(139) Vernaleken, A.; Weitenberg, J.; Sartorius, T.; Russbueldt, P.; Schneider, W.; Stebbings, S. L.; Kling, M. F.; Hommelhoff, P.; Hoffmann, H.-D.; Poprawe, R.; Krausz, F.; Hänsch, T. W.; Udem, T. Single-Pass High-Harmonic Generation at 20.8 MHz Repetition Rate. *Opt. Lett.* **2011**, *36*, 3428–3430.

(140) Ruehl, A.; Marcinkevicius, A.; Fermann, M. E.; Hartl, I. 80W, 120fs Yb-Fiber Frequency Comb. *Opt. Lett.* **2010**, *35*, 3015–3017.

(141) Lide, D. R. (ed.) *CRC Handbook of Chemistry and Physics*; 90th ed. (CD-ROM version); CRC Press/Taylor and Francis: Boca Raton, FL, USA, 2010.

(142) Gilbert, B.; Frandsen, C.; Maxey, E. R.; Sherman, D. M. Band-Gap Measurements of Bulk and Nanoscale Hematite by Soft X-Ray Spectroscopy. *Phys. Rev. B* **2009**, *79*, 035108.

(143) Nakano, Y.; Saeki, S.; Morikawa, T. Optical Bandgap Widening of p-Type Cu_2O Films by Nitrogen Doping. *Appl. Phys. Lett.* **2009**, *94*, 022111.

(144) Nair, M. T. S.; Guerrero, L.; Arenas, O. L.; Nair, P. K. Chemically Deposited Copper Oxide Thin Films: Structural, Optical and Electrical Characteristics. *Appl. Surf. Sci.* **1999**, *150*, 143–151.
(145) Ray, S. C. Preparation of Copper Oxide Thin Film by the Sol–Gel-like Dip Technique and Study of Their Structural and Optical Properties. *Sol. Energy Mater. Sol. Cells* **2001**, *68*, 307–312.
(146) Tahir, D.; Tougaard, S. Electronic and Optical Properties of Cu, CuO and Cu_2O Studied by Electron Spectroscopy. *J. Phys. Condens. Matter* **2012**, *24*, 175002.
(147) Mang, A.; Reimann, K.; Rübenacke, St. Band Gaps, Crystal-Field Splitting, Spin-Orbit Coupling, and Exciton Binding Energies in ZnO under Hydrostatic Pressure. *Solid State Commun.* **1995**, *94*, 251–254.
(148) Serpone, N.; Lawless, D.; Khairutdinov, R. Size Effects on the Photophysical Properties of Colloidal Anatase TiO_2 Particles: Size Quantization versus Direct Transitions in This Indirect Semiconductor. *J. Phys. Chem.* **1995**, *99*, 16646–16654.
(149) NIST Chemistry WebBook, SRD 69: Hematite (Fe_2O_3), https://webbook.nist.gov/cgi/cbook.cgi?ID=C1317608&Type=JANAFS&Table=on (accessed Feb 12, 2022).
(150) NIST Chemistry WebBook, SRD 69: dicopper oxide, https://webbook.nist.gov/cgi/cbook.cgi?ID=C1317391&Units=SI&Mask=2&Type=JANAFS&Table=on#JANAFS (accessed Feb 12, 2022).
(151) NIST Chemistry WebBook, SRD 69: copper oxide, https://webbook.nist.gov/cgi/cbook.cgi?ID=C1317380&Type=JANAFS&Table=on (accessed Feb 12, 2022).
(152) Madelung, O.; Rössler, U.; Schulz, M. *Zinc Oxide (ZnO) Debye Temperature, Heat Capacity, Density, Melting Point, Vapor Pressure, Hardness: Datasheet from Landolt-Börnstein - Group III Condensed Matter · Volume 41B: "II-VI and I-VII Compounds; Semimagnetic Compounds";* Springer-Verlag: Berlin Heidelberg.
(153) Smith, S. J.; Stevens, R.; Liu, S.; Li, G.; Navrotsky, A.; Boerio-Goates, J.; Woodfield, B. F. Heat Capacities and Thermodynamic Functions of TiO_2 Anatase and Rutile: Analysis of Phase Stability. *Am. Mineral.* **2009**, *94*, 236–243.
(154) Glasscock, J. A.; Barnes, P. R. F.; Plumb, I. C.; Bendavid, A.; Martin, P. J. Structural, Optical and Electrical Properties of Undoped Polycrystalline Hematite Thin Films Produced Using Filtered Arc Deposition. *Thin Solid Films* **2008**, *516*, 1716–1724.
(155) Caglar, M.; Ilican, S.; Caglar, Y. Influence of Dopant Concentration on the Optical Properties of ZnO: In Films by Sol–Gel Method. *Thin Solid Films* **2009**, *517*, 5023–5028.
(156) Wang, Z.; Helmersson, U.; Käll, P.-O. Optical Properties of Anatase TiO_2 Thin Films Prepared by Aqueous Sol–Gel Process at Low Temperature. *Thin Solid Films* **2002**, *405*, 50–54.
(157) Dosch, H.; Höfer, T.; Peisl, J.; Johnson, R. L. Synchrotron X-Ray Scattering from the Al(110) Surface at the Onset of Surface Melting. *Europhys. Lett. EPL* **1991**, *15*, 527–533.
(158) Kofman, R.; Cheyssac, P.; Aouaj, A.; Lereah, Y.; Deutscher, G.; Ben-David, T.; Penisson, J. M.; Bourret, A. Surface Melting Enhanced by Curvature Effects. *Surf. Sci.* **1994**, *303*, 231–246.
(159) Ketteler, G.; Weiss, W.; Ranke, W.; Schlögl, R. Bulk and Surface Phases of Iron Oxides in an Oxygen and Water Atmosphere at Low Pressure. *Phys. Chem. Chem. Phys.* **2001**, *3*, 1114–1122.
(160) Schmidt-Whitley, R. D.; Martinez-Clemente, M.; Revcolevschi, A. Growth and Microstructural Control of Single Crystal Cuprous Oxide Cu_2O. *J. Cryst. Growth* **1974**, *23*, 113–120.
(161) Asadian, M. Thermodynamic Analysis of ZnO Crystal Growth from the Melt. *J. Cryst. Process Technol.* **2013**, *3*, 75–80.
(162) Cao, H.; Liu, X. Activating Titanium Oxide Coatings for Orthopedic Implants. *Surf. Coat. Technol.* **2013**, *233*, 57–64.

(163) Primo, A.; Corma, A.; García, H. Titania Supported Gold Nanoparticles as Photocatalyst. *Phys. Chem. Chem. Phys.* **2011**, *13*, 886–910.

(164) Umrath, W.; Adam, H.; Bolz, A.; Boy, H.; Dohmen, H.; Gogol, K.; Jorisch, W.; Moenning, W.; Mundinger, H.-J.; Otten, H.-D.; Scheer, W.; Seiger, H.; Schwarz, W.; Stepputat, K.; Urban, D.; Wirtzfeld, H.-J.; Zenker, H.-J. *Fundamentals of Vacuum Technology*; Cologne, 2007.

(165) Mahl, J.; Neppl, S.; Roth, F.; Borgwardt, M.; Saladrigas, C.; Toulson, B.; Cooper, J.; Rahman, T.; Bluhm, H.; Guo, J.; Yang, W.; Huse, N.; Eberhardt, W.; Gessner, O. Decomposing Electronic and Lattice Contributions in Optical Pump – X-Ray Probe Transient Inner-Shell Absorption Spectroscopy of CuO. *Faraday Discuss.* **2019**, *216*, 414–433.

(166) Crank, J.; Nicolson, P. A Practical Method for Numerical Evaluation of Solutions of Partial Differential Equations of the Heat-Conduction Type. *Mathematical Proceedings of the Cambridge Philosophical Society* **1947**, *43*, 50–67.

(167) Crank, J. *The Mathematics of Diffusion*; 2nd ed.; Oxford University Press: Oxford, England, 1975.

(168) Elsayed-Ali, H. E.; Herman, J. W. Picosecond Time-resolved Surface-lattice Temperature Probe. *Appl. Phys. Lett.* **1990**, *57*, 1508–1510.

(169) Bechtel, J. H. Heating of Solid Targets with Laser Pulses. *J. Appl. Phys.* **1975**, *46*, 1585–1593.

(170) CXRO database: X-ray attenuation length, http://henke.lbl.gov/optical_constants/atten2.html (accessed Jan 11, 2022).

(171) Tanuma, S.; Powell, C. J.; Penn, D. R. Calculations of Electron Inelastic Mean Free Paths. V. Data for 14 Organic Compounds over the 50–2000eV Range. *Surf. Interface Anal.* **1994**, *21*, 165–176.

(172) Tanuma, S.; Powell, C. J.; Penn, D. R. Calculations of Electron Inelastic Mean Free Paths. IX. Data for 41 Elemental Solids over the 50eV to 30keV Range. *Surf. Interface Anal.* **2011**, *43*, 689–713.

(173) Wang, Z. L. Nanostructures of Zinc Oxide. *Mater. Today* **2004**, *7*, 26–33.

(174) Wang, Z. L. ZnO Nanowire and Nanobelt Platform for Nanotechnology. *Mater. Sci. Eng. R Rep.* **2009**, *64*, 33–71.

(175) Waugh, K. C. Methanol Synthesis. *Catal. Today* **1992**, *15*, 51–75.

(176) Sun, Y.; Chen, L.; Bao, Y.; Zhang, Y.; Wang, J.; Fu, M.; Wu, J.; Ye, D. The Applications of Morphology Controlled ZnO in Catalysis. *Catalysts* **2016**, *6*, 188.

(177) Eranna, G.; Joshi, B. C.; Runthala, D. P.; Gupta, R. P. Oxide Materials for Development of Integrated Gas Sensors—A Comprehensive Review. *Crit. Rev. Solid State Mater. Sci.* **2004**, *29*, 111–188.

(178) Rim, Y. S.; Bae, S.-H.; Chen, H.; De Marco, N.; Yang, Y. Recent Progress in Materials and Devices toward Printable and Flexible Sensors. *Adv. Mater.* **2016**, *28*, 4415–4440.

(179) Look, D. C. Recent Advances in ZnO Materials and Devices. *Mater. Sci. Eng. B* **2001**, *80*, 383–387.

(180) Vanmaekelbergh, D.; Vugt, L. K. van. ZnO Nanowire Lasers. *Nanoscale* **2011**, *3*, 2783–2800.

(181) Fang, X.; Bando, Y.; Gautam, U. K.; Zhai, T.; Zeng, H.; Xu, X.; Liao, M.; Golberg, D. ZnO and ZnS Nanostructures: Ultraviolet-Light Emitters, Lasers, and Sensors. *Crit. Rev. Solid State Mater. Sci.* **2009**, *34*, 190–223.

(182) Sirkeli, V. P.; Hartnagel, H. L. ZnO-Based Terahertz Quantum Cascade Lasers. *Opto-Electron. Rev.* **2019**, *27*, 119–122.

(183) Quintana, M.; Edvinsson, T.; Hagfeldt, A.; Boschloo, G. Comparison of Dye-Sensitized ZnO and TiO_2 Solar Cells: Studies of Charge Transport and Carrier Lifetime. *J. Phys. Chem. C* **2007**, *111*, 1035–1041.

(184) Bersch, E. Energy Level Alignment In Metal/Oxide/Semiconductor and Organic Dye/Oxide Systems, Ruttgers University, 2008.

(185) Popmintchev, T.; Chen, M.-C.; Popmintchev, D.; Arpin, P.; Brown, S.; Ališauskas, S.; Andriukaitis, G.; Balčiunas, T.; Mücke, O. D.; Pugzlys, A.; Baltuška, A.; Shim, B.; Schrauth, S. E.; Gaeta, A.; Hernández-García, C.; Plaja, L.; Becker, A.; Jaron-Becker, A.; Murnane, M. M.; Kapteyn, H. C. Bright Coherent Ultrahigh Harmonics in the keV X-Ray Regime from Mid-Infrared Femtosecond Lasers. *Science* **2012**, *336*, 1287–1291.

(186) Teichmann, S. M.; Silva, F.; Cousin, S. L.; Hemmer, M.; Biegert, J. 0.5-keV Soft X-Ray Attosecond Continua. *Nat. Commun.* **2016**, *7*, 1–6.

(187) Attar, A. R.; Bhattacherjee, A.; Pemmaraju, C. D.; Schnorr, K.; Closser, K. D.; Prendergast, D.; Leone, S. R. Femtosecond X-Ray Spectroscopy of an Electrocyclic Ring-Opening Reaction. *Science* **2017**, *356*, 54–59.

(188) Gaumnitz, T.; Jain, A.; Pertot, Y.; Huppert, M.; Jordan, I.; Ardana-Lamas, F.; Wörner, H. J. Streaking of 43-Attosecond Soft-X-Ray Pulses Generated by a Passively CEP-Stable Mid-Infrared Driver. *Opt. Express* **2017**, *25*, 27506–27518.

(189) Goulielmakis, E.; Schultze, M.; Hofstetter, M.; Yakovlev, V. S.; Gagnon, J.; Uiberacker, M.; Aquila, A. L.; Gullikson, E. M.; Attwood, D. T.; Kienberger, R.; Krausz, F.; Kleineberg, U. Single-Cycle Nonlinear Optics. *Science* **2008**, *320*, 1614–1617.

(190) Zhao, K.; Zhang, Q.; Chini, M.; Wu, Y.; Wang, X.; Chang, Z. Tailoring a 67 Attosecond Pulse through Advantageous Phase-Mismatch. *Opt. Lett.* **2012**, *37*, 3891–3893.

(191) Li, J.; Ren, X.; Yin, Y.; Zhao, K.; Chew, A.; Cheng, Y.; Cunningham, E.; Wang, Y.; Hu, S.; Wu, Y.; Chini, M.; Chang, Z. 53-Attosecond X-Ray Pulses Reach the Carbon K-Edge. *Nat. Commun.* **2017**, *8*, 1–5.

(192) Cousin, S. L.; Di Palo, N.; Buades, B.; Teichmann, S. M.; Reduzzi, M.; Devetta, M.; Kheifets, A.; Sansone, G.; Biegert, J. Attosecond Streaking in the Water Window: A New Regime of Attosecond Pulse Characterization. *Phys. Rev. X* **2017**, *7*, 041030.

(193) Geloni, G.; Huang, Z.; Pellegrini, C. The Physics and Status of X-Ray Free-Electron Lasers (Chapter 1). *X-Ray Free Electron Lasers Appl. Mater. Chem. Biol.* **2017**, 1–44.

(194) Coffee, R. N.; Cryan, J. P.; Duris, J.; Helml, W.; Li, S.; Marinelli, A. Development of Ultrafast Capabilities for X-Ray Free-Electron Lasers at the Linac Coherent Light Source. *Philos. Trans. R. Soc. Math. Phys. Eng. Sci.* **2019**, *377*, 20180386.

(195) Helml, W.; Maier, A. R.; Schweinberger, W.; Grguraš, I.; Radcliffe, P.; Doumy, G.; Roedig, C.; Gagnon, J.; Messerschmidt, M.; Schorb, S.; Bostedt, C.; Grüner, F.; DiMauro, L. F.; Cubaynes, D.; Bozek, J. D.; Tschentscher, T.; Costello, J. T.; Meyer, M.; Coffee, R.; Düsterer, S.; Cavalieri, A. L.; Kienberger, R. Measuring the Temporal Structure of Few-Femtosecond Free-Electron Laser X-Ray Pulses Directly in the Time Domain. *Nat. Photonics* **2014**, *8*, 950–957.

(196) Duris, J.; Li, S.; Driver, T.; Champenois, E. G.; MacArthur, J. P.; Lutman, A. A.; Zhang, Z.; Rosenberger, P.; Aldrich, J. W.; Coffee, R.; Coslovich, G.; Decker, F.-J.; Glownia, J. M.; Hartmann, G.; Helml, W.; Kamalov, A.; Knurr, J.; Krzywinski, J.; Lin, M.-F.; Marangos, J. P.; Nantel, M.; Natan, A.; O'Neal, J. T.; Shivaram, N.; Walter, P.; Wang, A. L.; Welch, J. J.; Wolf, T. J. A.; Xu, J. Z.; Kling, M. F.; Bucksbaum, P. H.; Zholents, A.; Huang, Z.; Cryan, J. P.; Marinelli, A. Tunable Isolated Attosecond X-Ray Pulses with Gigawatt Peak Power from a Free-Electron Laser. *Nat. Photonics* **2020**, *14*, 30–36.

(197) Schulz, S.; Grguraš, I.; Behrens, C.; Bromberger, H.; Costello, J. T.; Czwalinna, M. K.; Felber, M.; Hoffmann, M. C.; Ilchen, M.; Liu, H. Y.; Mazza, T.; Meyer, M.; Pfeiffer, S.; Prędki, P.; Schefer, S.; Schmidt, C.; Wegner, U.; Schlarb, H.; Cavalieri, A. L. Femtosecond All-Optical Synchronization of an X-Ray Free-Electron Laser. *Nat. Commun.* **2015**, *6*, 1–11.

(198) Schoenlein, R. W.; Chattopadhyay, S.; Chong, H. H. W.; Glover, T. E.; Heimann, P. A.; Shank, C. V.; Zholents, A. A.; Zolotorev, M. S. Generation of Femtosecond Pulses of Synchrotron Radiation. *Science* **2000**, *287*, 2237–2240.

(199) Allen, P. B. Theory of Thermal Relaxation of Electrons in Metals. *Phys. Rev. Lett.* **1987**, *59*, 1460–1463.

(200) Öström, H.; Öberg, H.; Xin, H.; LaRue, J.; Beye, M.; Dell'Angela, M.; Gladh, J.; Ng, M. L.; Sellberg, J. A.; Kaya, S.; Mercurio, G.; Nordlund, D.; Hantschmann, M.; Hieke, F.; Kühn, D.; Schlotter, W. F.; Dakovski, G. L.; Turner, J. J.; Minitti, M. P.; Mitra, A.; Moeller, S. P.; Föhlisch, A.; Wolf, M.; Wurth, W.; Persson, M.; Nørskov, J. K.; Abild-Pedersen, F.; Ogasawara, H.; Pettersson, L. G. M.; Nilsson, A. Probing the Transition State Region in Catalytic CO Oxidation on Ru. *Science* **2015**, *347*, 978–982.

(201) Fraund, M.; Borgwardt, M.; Mahl, J.; Brausse, F.; Roth, F.; Blum, M.; Gessner, O. Towards Real-Time Monitoring of Interfacial Chemical Dynamics with Time-Resolved X-Ray Photoelectron Spectroscopy. *22nd International Conference on Ultrafast Phenomena (2020)*; Optica Publishing Group, 2020.

(202) Fuji, T.; Ishii, N.; Teisset, C. Y.; Gu, X.; Metzger, T.; Baltuska, A.; Forget, N.; Kaplan, D.; Galvanauskas, A.; Krausz, F. Parametric Amplification of Few-Cycle Carrier-Envelope Phase-Stable Pulses at 2.1µm. *Opt. Lett.* **2006**, *31*, 1103–1105.

(203) Silva, F.; Teichmann, S. M.; Cousin, S. L.; Hemmer, M.; Biegert, J. Spatiotemporal Isolation of Attosecond Soft X-Ray Pulses in the Water Window. *Nat. Commun.* **2015**, *6*, 1–6.

(204) Popmintchev, D.; Galloway, B. R.; Chen, M.-C.; Dollar, F.; Mancuso, C. A.; Hankla, A.; Miaja-Avila, L.; O'Neil, G.; Shaw, J. M.; Fan, G.; Ališauskas, S.; Andriukaitis, G.; Balčiunas, T.; Mücke, O. D.; Pugzlys, A.; Baltuška, A.; Kapteyn, H. C.; Popmintchev, T.; Murnane, M. M. Near- and Extended-Edge X-Ray-Absorption Fine-Structure Spectroscopy Using Ultrafast Coherent High-Order Harmonic Supercontinua. *Phys. Rev. Lett.* **2018**, *120*, 093002.

(205) Johnson, A. S.; Austin, D. R.; Wood, D. A.; Brahms, C.; Gregory, A.; Holzner, K. B.; Jarosch, S.; Larsen, E. W.; Parker, S.; Strüber, C. S.; Ye, P.; Tisch, J. W. G.; Marangos, J. P. High-Flux Soft X-Ray Harmonic Generation from Ionization-Shaped Few-Cycle Laser Pulses. *Sci. Adv.* **2018**, *4*, eaar3761.

(206) Schmidt, C.; Pertot, Y.; Balciunas, T.; Zinchenko, K.; Matthews, M.; Wörner, H. J.; Wolf, J.-P. High-Order Harmonic Source Spanning up to the Oxygen K-Edge Based on Filamentation Pulse Compression. *Opt. Express* **2018**, *26*, 11834–11842.

Acknowledgements

Many people contributed to the work presented here and helped, taught, and encouraged me during this journey for which I want to express my appreciation. I am deeply grateful to have been part of a large and inspiring scientific community at the Advanced Light Source specifically and Lawrence Berkeley National Laboratory in general that had a transformative impact on me.

First, I would like to thank Dr. Oliver Gessner for providing the opportunity to conduct research in his lab at the Chemical Sciences Division of Lawrence Berkeley National Laboratory (LBNL). I enjoyed our group meetings, and personal discussions on general topics of science as well as all other more specific topics reflected in this thesis that are too many to name. I am very grateful for his supervision of my studies, general advice, letting me explore different scientific questions, help with the beamtimes, enabling me to participate in collaborations and conferences, and for his patience especially helping to shape my scientific writing. I want to thank Prof. Nils Huse for supervising my thesis, proof-reading, guidance with many different aspects of the dissertation and his general positive attitude. I would also like to thank Dr. Stefan Neppl for teaching me most of what I know about experimental physics and introducing me to many aspects of solid-state and specifically surface science during countless discussions. I will never forget the sometimes seemingly endless shifts at the ALS but most importantly the feeling of happiness when these efforts were rewarded with functioning experiments and a lot of interesting data. Stefan, I am very grateful for the camaraderie during and many years before my PhD, both in the lab and as a friend. For their extensive collaboration, both while coming to the ALS in Berkeley and inviting me to participate in experiments at FLASH in Hamburg, I would like to thank Friedrich Roth and Prof. Wolfgang Eberhardt. I really appreciated the exposure to a very related yet different science and environment there. I would also like to sincerely thank the members of my dissertation committee, Prof. Arwen Pearson, Prof. Michael Rübhausen, and Prof. Gabriel Bester.

For being wonderful office mates and making everyday life at the lab fun with many interesting conversations that taught me much of what I learned during graduate school, I would like to thank Dipanwita Ray, Kirk Larsen, Camila Bacellar, Mike Ziemkiewicz, Adam Chatterley, Florian

Lackner, Catherine Saladrigas, Mario Borgwardt, Ben Toulson, Felix Brausse, Matthew Fraund, and Tahiyat Rahman. Many thanks to Friedrich Roth, Mario Borgwardt, Felix Brausse and Matthew Fraund for conducting really interesting TRXPS experiments and collaborating at the beamline. For helping out at the beamline, letting us borrow hardware, and sharing their knowledge about lasers, I would like to thank Ben Toulson and Catherine Saladrigas. Tahiyat Rahman helped out with several beamtimes and coded an important part of the general TRXAS data analysis. Andrey Shavorskiy implemented a crucial part of the TRXPS data acquisition, and I would like to thank him especially for being available to help get things running remotely while he had already left LBNL. Many thanks to Lukas Wenthaus and Giuseppe Mercurio for making those beamtimes at FLASH a lot of fun. Special thanks to David Kilcoyne for his mentorship, uplifting presence, and proof-reading manuscripts. I would also like to thank Ben Ortega, Larry Guo, Pat Young, Angela Green, Angie Wu, and Deborah Reed for quick, effective, and uncomplicated help with administrative questions.

Without the staff of the Advanced Light Source the data presented in this thesis could have not been acquired. I am especially thankful for the responsive beamline support at all hours of the day and night by Hendrik Bluhm and Monika Blum at beamline 11.0.2 and Wanli Yang, Yi-Sheng Liu, and Ruimin Qiao at beamline 8.0.1. I want to sincerely thank Jinghua Guo for mentoring my Advanced Light Source Fellowship. In terms of the data acquisition software for both experiments I am indebted to the ALS beamline controls staff, especially Brian Smith, Lee Yang, Earl Cornell and Ed Domning, for providing the TRXPS software and their general coding tips, sharing code for all sorts of experimental hardware as well as practical help interfacing with the ALS EPICS system that enabled the TRXAS software. Jonah Weber and Michael Chin were going out of their way to provide customized hardware for interfacing with the ALS master clock and helping with electronic questions around making sure we have a reliable signal for our timing system. Monroe Thomas deserves many thanks for making sure we could always get any piece of heavy equipment where it needed to be. David Malone, Douglas Taube, and Greta Toncheva provided great actionable and constructive help at the ALS regarding general safety, everything around chemicals, and the laser, respectively, and all contribute to the amazing culture at LBNL. Many different members of the ALS, building 2, and general LBNL machine shops, the ALS electrical shop, and shipping and receiving helped solving countless little problems in an uncomplicated fashion and made conducting experiments at the ALS a real pleasure. Thank you all. The user experience at the ALS would have

not been the same without Bruce Rude. He is always willing to help and has knowledge about hardware in general, vacuum, pumps and who to ask to get ahead that never failed us.

Finally, I would like to thank my family and friends for all their unwavering support and encouragement. You make my world go round.